University of East Anglia

The effect of matrix stiffness on vascular smooth muscle cell contractility

---

Sultan Ahmed

A thesis submitted for the degree of Doctor of Philosophy (Ph.D.)

University of East Anglia

School of Pharmacy

May 2021

Abstract

Vascular smooth muscle cells (VSMCs) typically line the medial layer of the arterial wall, and exist in a quiescent contractile phenotype to regulate vessel tone. However, during ageing and early cardiovascular disease (CVD) development, the arterial wall becomes more rigid, and under these conditions, VSMC de-differentiate into the synthetic proliferative phenotype where they instead contribute to vessel repair. Arterial stiffness is a key predicative biomarker of CVD and our work focuses on the response of the VSMCs to the less compliant extracellular matrix (ECM). We hypothesise aberrations in VSMC structure and function in response to matrix stiffness, and speculate that this may contribute to the pathological vessel wall remodelling typically observed within CVD.

To test this, we fabricated polyacrylamide gels with rigidities representative of both physiological (12kPa) and pathological (72kPa) stiffness. Our work presents an increase in VSMC force generation in response to matrix stiffness via traction force microscopy (TFM). We show this to occur via novel mechanisms and, importantly, highlight the key mechanosensors mediating this. When seeded on that 72kPa hydrogel, quiescent VSMCs were shown to undergo hypertrophy causing increased DNA damage. Our study identifies stretch activated channels (SACs) and N-acetyltransferase 10 (NAT10) as critical mechanosensors that facilitate this, as inhibition of both restored healthy morphology. Importantly, we highlight Piezo1 as a novel SAC within stiffness-induced VSMC dysregulation. Using qPCR, we show Piezo1 gene expression to increase in response to matrix rigidity, and also reveal that its knockdown, via siRNA-mediated methods, can reduce DNA damage accumulation. Due to this, we predict there to be an intricate crosstalk between the cytoskeletal networks and key mechanosensors present at the cell membrane, and introduce Piezo1 and NAT10 as therapeutic targets for stiffness-induced quiescent VSMC dysregulation.

Contents

List of Figures

List of Tables

Acknowledgements

To begin with, I would like to thank my supervisor Dr Derek Warren for your invaluable support and guidance over the last three years. I am extremely grateful for your help as well as your remarkable ability to have put up with my endless questions on a daily basis. You have an incredible ability to make people feel comforted and confident about their abilities, and I couldn't be happier to see how much your lab has grown since I started. Your positivity and warm character have made the last three years extremely enjoyable and without you, none of this would have been possible. I couldn't have wished for a better supervisor. My gratitude also extends to Professor Sam Fountain, my secondary supervisor, for your great advice and feedback through the course of my project, and more importantly, for making me feel like a part of your own lab from the beginning of my PhD. Furthermore, I would like to also thank Dr Paul Thomas for your incredible patience in teaching and assisting me with all microscopy techniques used within my PhD. Additionally, I am immensely appreciative to Dr Tracey Swingler for her continuous support with my qPCR studies. I would also like to acknowledge the British Heart Foundation for the financial support given for my project and the University of East Anglia for giving me a home to perform my research.

Next, I would like to thank the entire Warren lab, past and present, for their friendship, support and memories. In particular, to Teclino Afewerki. I am so appreciative of our friendship and for all of the memories you have provided me with. There is no single individual who I would have rather spent my late nights in the lab with, joked with about our mutual failures, or had the privilege to work alongside. Your positivity is incredibly contagious and I will miss it in my day-to-day life. Next, I will like to thank Dr Robert Johnson. Despite missing the opportunity to spend as much time in the lab with you because of the lockdown, it was really enjoyable to make the most of it. You have been an amazing addition to our lab and have given me far more help than I could have asked for, and for that, I am so grateful. It will always be "Post-doc appreciation month" in the Warren lab. Alongside this, I would like to give thanks to all my project students throughout the last 3 years. In particular, I would like to thank my cousin, Shofi Alom, for his continued help throughout my project. I've been very lucky to have my own family join my lab for two summers, and during this time, immensely help me with my PhD project (even if it meant the both of us mutually suffering mountains of data analysis). The time spent was incredibly fun and I'm really glad to have shared it with you.

I would like to also extend my appreciation to Dr Anastasia Sobolewski and her group for allowing me to be an "honorary" member of your lab. I genuinely loved the opportunity to

work alongside you all and will greatly miss the laughs shared over the last three years. Thank you for always making me feel included, and for always caring so much. Additionally, I would like to thank, in particular, my two friends, Sathuwarman Raveenthiraraj and Vaisakh Puthusserypady for their support over the last few years. I couldn't think of two better people to live with during my PhD and I'm grateful to have had the chance to experience this phase with you both. All the nights spent eating takeaways, watching movies or playing squash have kept me sane throughout this time and I can't wait to catch up with you both once this pandemic is all over.

Finally, I would like to thank the two most important people in my life. My brother and my mother. They have been my two pillars of support throughout this entire journey. To my brother, I am appreciative of how much effort you've put into helping me, whether it was numerously assisting me in moving back and forth, for continuously checking up on me or for always being readily available whenever I needed you. I couldn't have asked for a better brother. To my mother, you have been my motivation for the last six years. I am so appreciative of you for always praying for me. Thank you for always believing in me and, more importantly, for making me believe in myself. I am immensely grateful for how much you've supported me, even when I was so far away from you. I am extremely lucky to have an incredible mother who cares so much for me. This PhD is a small reflection of the amazing job you have done. To you both, I can say that the culmination of my accomplishments is the result of the love and support you have shown me.

Abbreviations

53BP1 - p53-binding protein 1

ACE - Angiotensin-converting enzyme

AFM - Atomic force microscopy

Ang II – Angiotensin II

APES - (3-Aminopropyl)triethoxysilane

APS - Ammonium persulfate

ARP 2/3 - Actin Related Protein 2/3

ATR1 - Angiotensin II type 1 receptor

BSA - Bovine Serum Albumin

CVD – Cardiovascular disease

Carbachol - Carbamoylcholine chloride

CT - Cycle threshold

DAG – Diacylglycerol

DAPI - Diamidino-2-Pheylindoledihydrochloride

DDR - DNA damage response

DMSO - Dimethyl sulfoxide

DNAse I - Deoxyribonuclease I

EC - Extracellular cadherin

ECIS - Electric-cell-substrate impedance sensing

ECM – Extracellular matrix

eNOS - Endothelial NO synthase

F-actin – Filamentous actin

FAK - Focal adhesion kinase

FBS - Fetal Bovine Serum

G-actin – Globular actin

GEF - Guanine nucleotide exchange factor

GFP – Green fluorescent protein

GOI – Genes of interest

GTP - Guanosine 5'-Triphosphate

H3K9ace - Histone 3 Lysine-9 acetylation

HGPS - Hutchinson-Gilford progeria syndrome

HRP - Horseradish peroxidase

INM - Inner nuclear membrane

IP3 - Inositol triphosphate

IT - Integrin

KASH - Klarsicht, Anc-1, Syne-1 homology

LIMK1 - LIM kinase 1

LIMK2 - LIM kinase 2

LINC - Linker of nucleoskeleton and cytoskeleton

MAP - Microtubule associated protein

MLC - Myosin light chain

MLCK - Myosin light chain kinase

MLCP - Myosin light chain phosphatase

NAT10 - N-Acetyltransferase 10

NHEJ - Non-homologous end joining

NM-myosin II - Non-muscle myosin II

NO - Nitric oxide

NP-40 - Nonidet P-40

N.T. - Non-targeted

ONM - Outer nuclear membrane

PAX – Paxillin

PBS - Phosphate Buffered Saline

PFA - Paraformaldehyde

PIP2 - Phosphatidylinositol 4,5-bisphosphate

PKC – Protein kinase C

PKG - Protein kinase G

PLC - Phospholipase C

pMLC - Phosphorylated myosin light chain

PTEN - Phosphatase and tensin homologue

PTM - Post-translational modification

PWV – Pulse wave velocimetry

qPCR - Quantitative polymerase chain reaction

ROCK - Rho-associated protein kinase

ROI - Region of interest

RT – Room temperature

SAC - Stretch-activated ion channel

SDS - Sodium Dodecyl Sulfate

SHR - Spontaneously hypertensive rats

SM-myosin II - Smooth muscle myosin II

SR - Sarcoplasmic reticulum

TEMED - Tetramethylethylenediamine

TF – Traction force

TFM – Traction force microscopy

TLN – Talin

TRP - Transient receptor potential

TRPC - Transient receptor potential-canonical

TS – Traction stress

VCL – Vinculin

VRAC - Volume regulated anion channel

VSMC – Vascular smooth muscle cell

VGCC - Voltage-gated calcium channel

WASP - Wiskott–Aldrich syndrome protein

ZYX - Zyxin

Chapter 1: Introduction

1.1 Cardiovascular disease

1.1.1 Cardiovascular disease overview

Cardiovascular disease (CVD) is a major risk factor to health worldwide, placing a great burden on numerous healthcare systems and leading to significant morbidity (1). Within the United Kingdom, it is the leading cause of mortality, establishing an urgent need for better prevention and treatment therapies (2). The term CVD holds host to multiple pathologies, including but not limited to, coronary heart disease (CHD) and peripheral arterial disease (3). These conditions present mutual risk factors such as hypertension and atherosclerosis, and its prevalence is observed in both industrial and developing countries (4). CVD incidence can be attenuated via careful risk reduction in the form of diet and exercise, however the largest contributing factor to it is the unavoidable process of ageing.

1.1.2 Role of ageing in CVD

The average lifespan of humans is progressively increasing, and it is estimated by 2030, 20% of the population will be aged 65 or older. This age group has been shown to be the most vulnerable to complications in cardiovascular health, with almost 50% of deaths attributed towards it (5-7). Ageing is mediated through a variety of environmental and genetic factors, and causes the body to decline in its ability to perform crucial physiological processes (5, 8). This can lead to harmful compensatory mechanisms by inducing aberrant structural changes within the vasculature. Typically, within healthy physiology, the arterial system is very compliant. Arterial compliance is the ability of the vessels to distend in order to increase blood volume in response to pressure. It is classically defined as the change in volume (ΔV)/ change in pressure (ΔP) (9). The inverse of this is arterial stiffness which acts as a key predicative biomarker of ageing and CVD development (10). Arterial stiffness has been found to impede the control of blood flow from the left ventricle of the heart to the microcirculation of different organs (11). This is due to a reduction in aortic compliance, which causes the left ventricle to increase the density of muscle mass to compensate. Whilst this mediates short-term solutions via adjusting end-systolic volume and prolonging systolic contraction, it ultimately diminishes cardiac performance leading to ventricular hypertrophy (12, 13). As a result, ageing causes damage to the vasculature, making it unable to efficiently regulate the demands it faces.

1.1.3 The cause and implications of arterial stiffness in CVD

Arterial stiffness serves as the most common biomarker amongst numerous CVD subpopulations (14-16). Within normally physiology, the pulse pressure is able to expand the healthy arterial wall, allowing blood velocity to decrease due to a transfer of kinetic energy. However, when the vascular wall becomes more rigid, it impedes its expansion and prevents any control of blood flow (**Figure 1.1**). As a result, when the blood enters the microcirculation of the heart and lungs, it causes damage due to the high pulse pressure becoming unmanageable for the more fragile vessels (17). Typically, individuals at risk of CVD have defects in the repair mechanisms and this accelerates the pathological reorganisation of the vasculature (18).

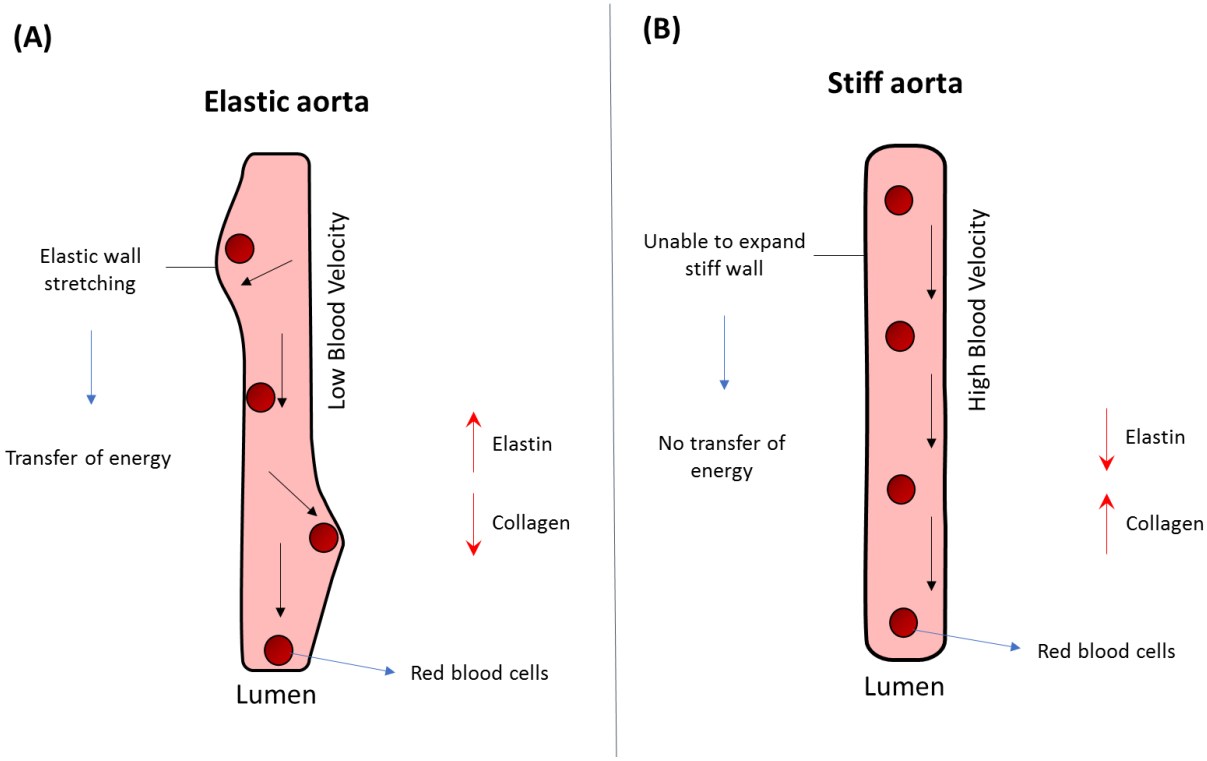

Figure 1.1: Illustration showing the impact of matrix stiffness on blood velocity. **(A)** shows blood flow within a physiological elastic artery and **(B)** depicts a stiffened artery during cardiovascular disease.

The most common way to measure arterial stiffness is via pulse wave velocimetry (PWV). This gold standard works by eliciting a pressure wave along the vascular bed, and recording the transit time it takes for it to go between two electrodes. The speed of the pressure wave is calculated by diving the distance between the electrodes by the time taken, and this represents the PWV value (19). Typically, the speed of the pressure wave increases within a stiffened artery, and therefore individuals with a greater risk of CVD have a higher

PWV value (20). However, despite providing an accurate assessment of arterial stiffness, this method does not give any indication to what factors may contribute to its prevalence.

The dogmatic view previously considered the occurrence of arterial stiffness to be solely due to changes in extracellular matrix (ECM) composition, specifically elastin degradation and enhanced collagen production (21). Under physiological conditions, elastin is the primary component within elastic fibres, and works to provide high pliability to the arterial wall to allow it to recoil (22). Collagen, on the other hand, forms stiff fibres that provide structural reinforcement and prevent arterial rupture from high pressures (23). Alterations in the synthesis and degradation of both proteins during early CVD development, however, leads to a stiffer and less compliant vessel. Despite this, numerous studies have reported inconsistent collagen levels, with multiple showing no changes (24-28), and others even demonstrating a decrease in its density during CVD (29, 30). As a result, earlier studies hypothesised that this was not sufficient to independently drive these pathological changes. Therefore, other factors have been considered since, and these include cell-matrix interactions, endothelial contributions, and more recently vascular smooth muscle cells (VSMCs) (31).

1.2 Arterial structure

The arterial structure is comprised of several key components that help to carefully regulate vascular function, and they can be spatially categorised within three different layers of the elastic wall (**Figure 1.2**). The tunica intima is the innermost layer, and it is constituted by endothelial cells along with collagen fibrils and a basal membrane. Each of the layers within the arterial wall are mechanosensitive, and during CVD development, endothelial cells remodel the ECM to allow VSMCs to migrate to the tunica intima (32). The outer layer is referred to as the tunica adventitia, and it primarily comprised of fibrous connective tissue. It works to provide structural support to the vascular wall, and does this by preventing pulsatile pressure-induced expansion (33). The third and intermediate layer is the tunica media, which is primarily comprised of VSMCs along with elastin and collagen fibrils (34). VSMCs regulates vascular tone via contractile activity, and this mediates effective responses to mechanical stimuli (35). During CVD, each of the layers undergo structural remodelling, and our work focuses on the VSMC response to enhanced matrix stiffness.

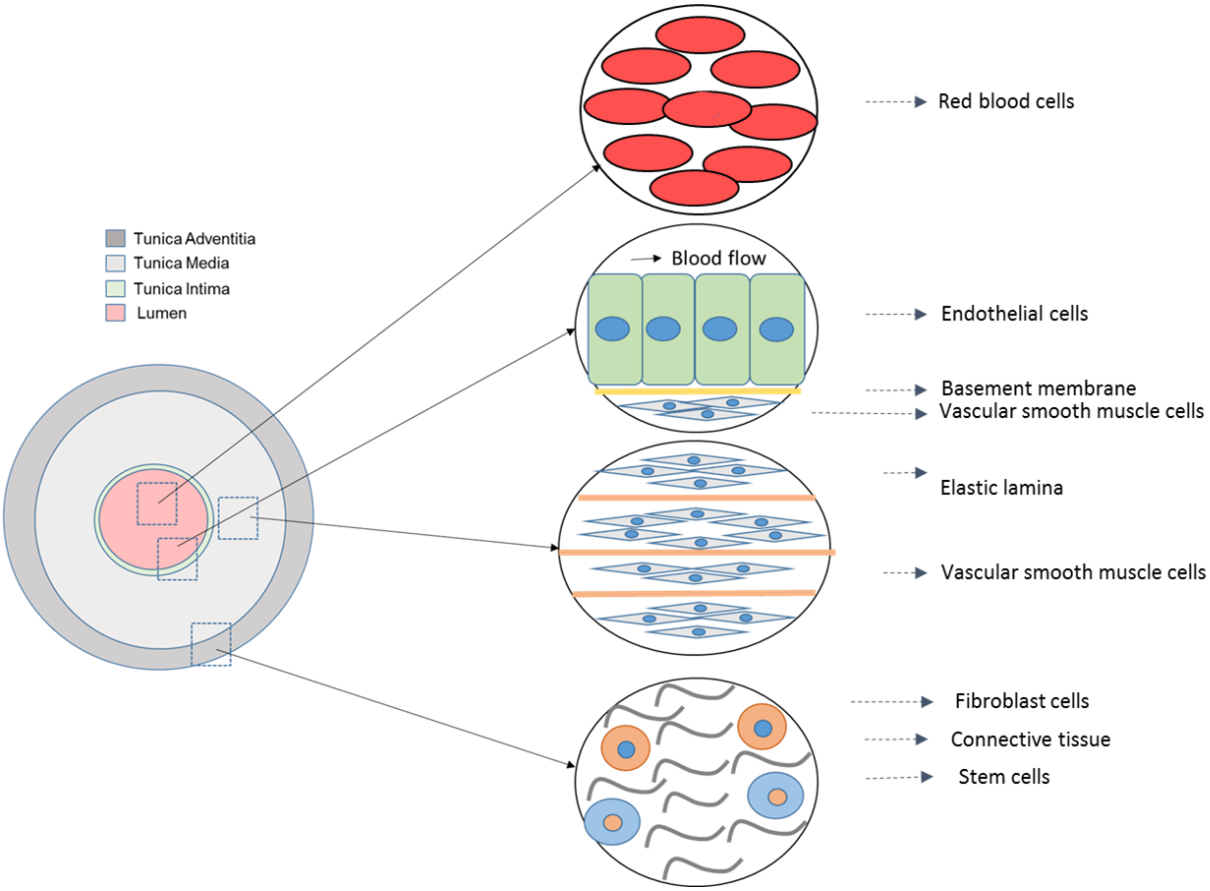

Figure 1.2: Schematic diagram showing the structural organisation of the arterial wall. Adapted from (10).

1.3 VSMC phenotypic regulation within CVD

A cells phenotype is primarily controlled by signalling input and a subset of nuclear genes specific to its lineage. VSMCs are derived from distinct regions during embryonic development, and are typically found in a quiescent contractile state within the tunica media once matured (36). Within the arterial wall, they exist as the predominant cell type and are arranged in a fibrous helix (35). Under healthy conditions, VSMCs work to regulate vascular tone via contractile activity, however during CVD development, they display remarkable plasticity and transition to the synthetic proliferative phenotype (37, 38). This phenomenon is regarded as “de-differentiation”, and *in vitro* culture work demonstrates this as VSMCs exhibit accelerated growth and a loss of contractile properties (39). Additionally, *in vivo* studies supplement this as similar effects are shown in models of mechanical injury (40, 41).

As a result, VSMC phenotypic transition is observed within development and disease associated vessel remodelling, where they alter ECM deposition via proliferative and migratory functions.

The quiescent contractile phenotype of VSMCs is characterised by the expression of key contractile marker proteins. Examples are smooth muscle myosin II (SM-myosin II), α-smooth muscle actin, and smoothelin (42). There are also a variety of additional myosin isoforms expressed within smooth muscle, including non-muscle and embryonic types, but these show a significant decrease during early development (43). During de-differentiation, however, VSMCs present augmented expression of non-muscle myosin II (NM-myosin II) and a decrease in SM-myosin II levels (42) (**Figure 1.3**). Biochemical and structural studies have revealed that myosin II possesses two heavy chains which are physically linked to an essential and regulatory light chain. Both light chain isoforms bind to the IQ motifs within the heavy chain, and the regulatory light chain induces enzymatic activity to mediate contraction (44). Previous work with tissue has shown that SM-myosin II function is more active in regions of fast phasic contraction as they revealed a higher immune-reactivity (45). This is in contrast to NM-myosin II, which has been shown to contribute to slower tonic contractions which generate less contractile force (45, 46). As a result, changes in gene expression induced from the synthetic phenotype causes a loss of contractile properties within VSMCs.

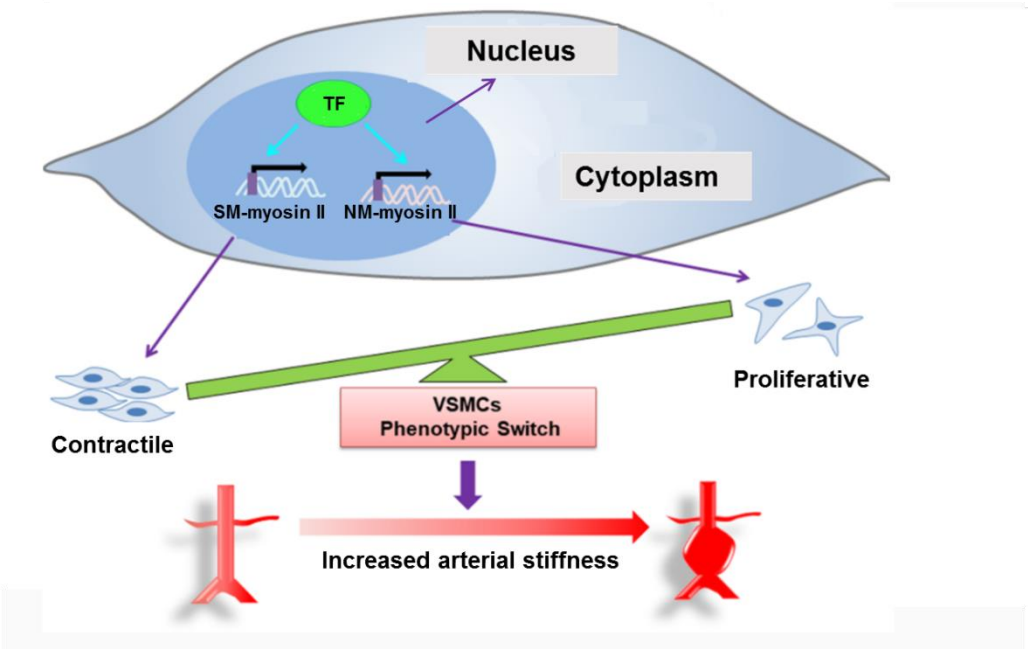

Figure 1.3: Illustration showing how increased arterial stiffness can cause VSMC phenotypic modulation. Depicts how the synthetic proliferative state is accompanied with augmented expression of key genes such as NM-myosin II. NM-myosin II: Non-muscle myosin II; SM-myosin II: Smooth muscle myosin II; TF: Transcription factor; VSMC; Vascular smooth muscle cell. Adapted from (47).

1.4 VSMC cytoskeleton

There are three filamentous components that made up the VSMC cytoskeleton, and these are the intermediate filaments, microtubules, and actin (10). Cytoskeletal remodelling occurs to mediate numerous processes, and this maintains healthy function of the cell. The intermediate filaments provide structural support to the VSMC by maintaining its 3-D cell integrity. Within the quiescent contractile phenotype, the intermediate filaments are comprised of two proteins; desmin and vimentin. Vimentin exists as the major component within large arteries, however desmin shows higher expression levels in VSMCs of smaller distal arteries (48-50).

Microtubules filaments are structurally arranged by α-/β-tubulin proteins to form long polymers that are prone to dynamic regulation (51). Within VSMCs, the properties of the microtubule network are not clearly defined due to immense difficulty in staining dense tissues (52). However, it has previously been revealed that microtubule depolymerisation can cause vasoconstriction of VSMCs (53). Additionally, within other mammalian cell types, microtubules are shown to regulate contractile and migratory function via coordination with the actin cytoskeleton (54, 55).

The third component, actin, primarily works to transmit mechanical signals to the ECM via cell-matrix adhesions. Monomeric globular actin (G-actin) units come together to form filamentous actin (F-actin), and transition between both states is regulated by actin-binding proteins (56) (**Figure 1.4**). Actin polymerisation begins with the formation of stable actin trimer and its expansion is facilitated by two groups of actin polymerisation nucleators, mDia1/2 and the ARP2/3 complex (57-59). mDia1/2 polymerises actin linearly by binding to the barbed end whilst the ARP2/3 complex promotes branched polymerisation of the actin filaments at a 70° angle (60, 61). VSMCs display remarkable plasticity under stiffened conditions, and the cellular machinery undergoes rapid changes in response to phenotypic switching (62). The contractile phenotype is responsible for regulating vessel tone and presents a stable actin cytoskeleton whilst the synthetic phenotype demands a dynamic actin cytoskeleton to facilitate repair (52, 62, 63). To mediate this, cofilin can regulate actin dynamics by severing the filamentous actin structures (64). Within differentiated VSMCs, actin acts as the most abundant cytoskeletal protein and makes up ~20% of the total protein content (65). There are four populations of actin isoforms within VSMCs, and these are α-smooth muscle actin (SMA) (40%), β-non-muscle actin (20%), γ-SMA, and γ-cytoplasmic actin (combined 20%) (66). Out of these, α- and γ-SMA primarily contribute to the contractile properties of the VSMCs, causing increased tension via myosin association (67). Mechanical cues from the intracellular/extracellular environment causes alterations in the actin

cytoskeletal structure, which facilitates regulation of VSMC contraction, migration and survival (68).

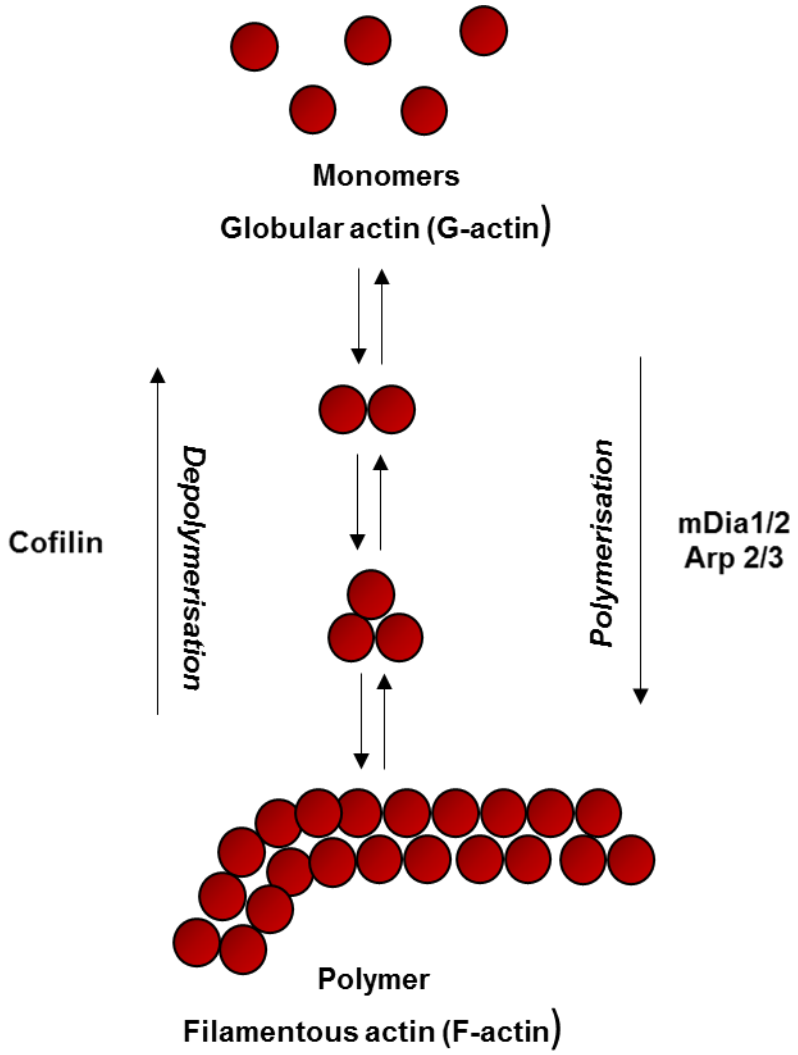

Figure 1.4: Schematic diagram showing VSMC actin polymerisation and key proteins involved in the process. ARP 2/3: Actin Related Protein 2/3; VSMC; Vascular smooth muscle cell.

1.5 VSMC contraction

VSMCs have a variety of functions within the arterial wall, however their primary role is to regulate vessel tone via contractile activity. Within the cell, exerting force maintains numerous functions such as migration, gene regulation and effectively coordinating with

other cytoskeletal networks (69-71). The contractile mechanism can be subdivided into two signalling routes, referred to as the calcium-dependent and independent pathways and these synergistically work together (**Figure 1.5**).

1.5.1 Calcium-dependent pathway

The calcium-dependent pathway works by increasing intracellular calcium concentration within VSMCs. This pathway can be triggered by mechanical/electrical/chemical stimuli which enables fast phasic contraction along the arterial wall. Calcium-induced contraction can be facilitated by ion channels located on the membrane or via release from the intracellular sarcoplasmic reticulum (72). Entry of calcium from the extracellular matrix occurs via depolarisation of numerous types (L-type, P/Q-type and V-type) of voltage-gated calcium channels (VGCCs) or through mechanical induced-opening of non-selective cation channels (73).

In contrast, release of calcium from the intracellular stores is mediated by the Gαq pathway, which begins with ligand binding to the G-protein coupled receptors at the cell membrane. A common agonist found within the vasculature is Angiotensin II and it works via this pathway to constrict vessel diameter (74). Once the receptor is bound, Gαq is transitioned to its GTP-bound state where it can activate phospholipase C (PLC). PLC then hydrolyses phosphatidylinositol 4,5-bisphosphate (PIP2) into two substrates, inositol triphosphate (IP3) and diacylglycerol (DAG). The sarcoplasmic reticulum (SR) has IP3 receptors present on its membrane, and when bound, it causes the efflux of calcium ions into the cytosol (75, 76).

Once in the cytosol, 4 calcium ions can bind to calmodulin to form a complex, which results in the activation of multiple downstream kinases (77). A key target, specifically, is myosin light chain kinase (MLCK) which works by phosphorylating the myosin regulatory light chain on two residues, serine-19 and threonine-18 (78, 79). The former residue allows enhanced Mg^{2+}-ATPase activity, and this is further augmented by the threonine-18 residue. The resulting hydrolysis of the phosphate group releases energy, and this allows the myosin head to pull the actin filament, in a term called actomyosin activity, to initiate the cross-bridge cycle and induce contraction (79).

1.5.2 Calcium-independent pathway

In the absence of external stimuli, the myosin regulatory light chain maintains a low level of phosphorylation. This allows a slower tonic form of contraction that persistently facilitates minor changes in vessel tone (80). Within VSMCs, the small GTPase Rho and its downstream effect Rho-associated protein kinase (ROCK), have been shown to regulate the lower tonic force generation independently of calcium. Outside of contractile function, Rho/ROCK pathway also regulates other cellular processes such as cell growth, protein synthesis and transcriptional activity by phosphorylating key substrates such as phosphatase and tensin homologue (PTEN) (81).

Rho GTPase exists within the Ras superfamily, and it cycles between a GTP/GDP bound state via guanine nucleotide exchange factor (GEF) and GTPase-activating protein activity (82). When inactive, GDP-Rho is localised at the cell membrane, however it is translocated to the cytosol via Rho GDP dissociation inhibitor (83). The $G_{12/13}$ family of G proteins then stimulates Rho into its GTP-bound state via activation of p115 RhoGTPase GEFs, which perform GTP for GDP exchange (84, 85). Once activated, GTP-Rho can return and anchor itself to the membrane via C-terminal geranyl-geranylated tail, where it can stimulate downstream substrates, one of which is ROCK (83, 86).

ROCK is categorised as a Serine/Threonine kinase, and exists as two isoforms both with molecular weight of ~160kDa (87). These are human ROCK1 and ROCK2, and the different genes encoding them are found on chromosome 18 and 2, respectively. Both are found expressed within VSMCS and are comprised of the same structural template, with a 65% amino acid sequence identity. Its arrangement consists of N-terminal kinase domain, a central coiled-coil domain and C-terminal pleckstrin homology and cysteine rich domain (88). As mentioned before, ROCK has multiple effects within VSMCs, however this review will focus on its effects within contractility.

It can work via two ways; the first is an indirect effect on force generation via the inhibition of cofilin. ROCK phosphorylates LIM kinase 1 (LIMK1) and 2 (LIMK2), and this induces further downstream phosphorylation of cofilin. Cofilin is an actin-depolymerising factor, and its function can be abolished via phosphorylation. As a result, this maintains stress fibre formation allowing for increased contractility (89). The second method is via direct inhibition of myosin light chain phosphatase (MLCP). MLCP is structurally comprised of a catalytic domain, variable subunit and most importantly, a myosin binding region (80). This region is critical as it can regulate the action of the phosphatase via the phosphorylation of the Threonine-695/697, Serine-849/854 and Threonine-850/855 residues present within it (83, 90). MLCP typically dephosphorylates the myosin light chain (MLC) diminishing

contractile function; however, its activity can be inhibited by ROCK phosphorylation on the myosin binding subunit, resulting in a higher level of basal phosphorylated MLC and increased contraction (90).

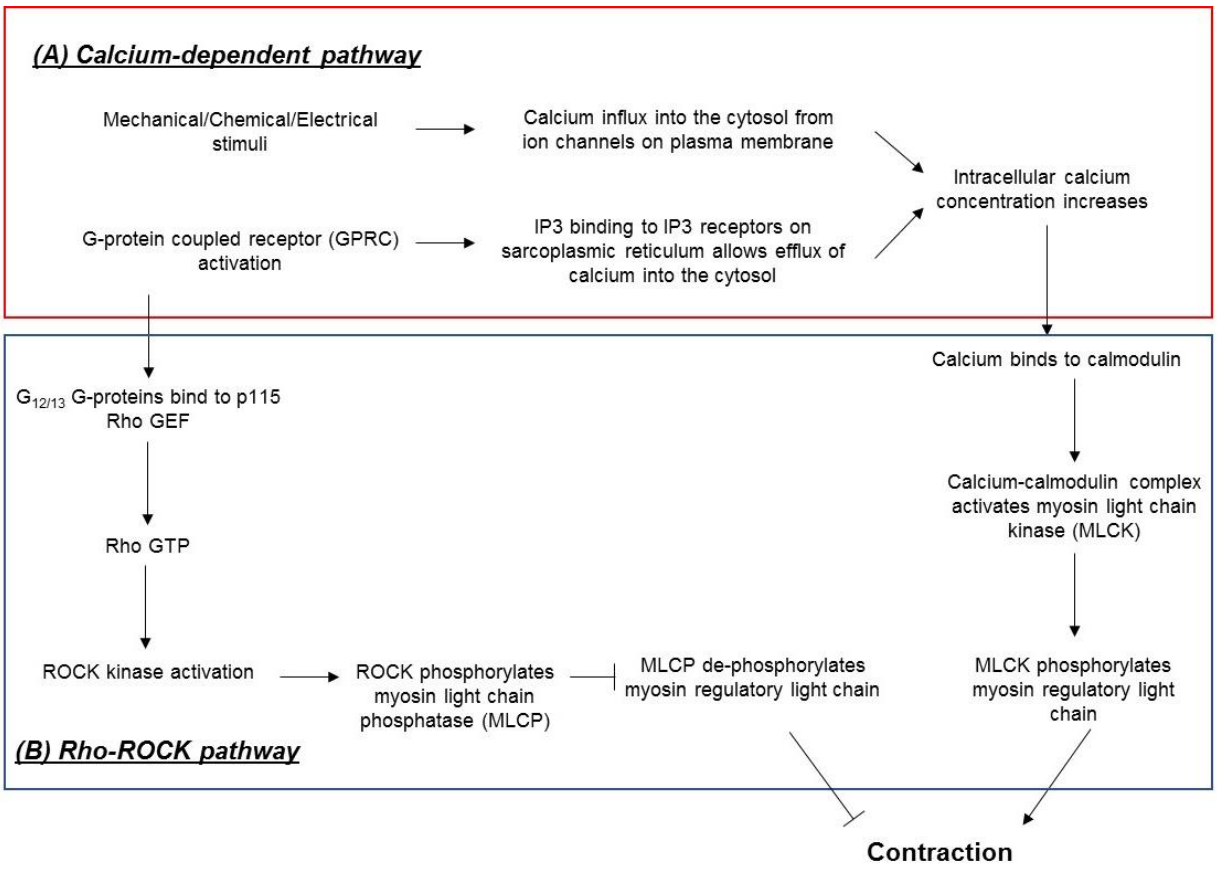

Figure 1.5: Contractile mechanism of VSMCs, showing synergistic cooperation between both pathways. **(A)** the calcium-dependent pathway works via an influx of extracellular calcium to induce fast phasic contractions whilst **(B)** the Rho-ROCK pathway functions independently of calcium to maintain slower tonic contractions. IP3: inositol triphosphate; Rho GEF: RhoGTPase guanine nucleotide exchange factors; GTP; Guanosine 5'-Triphosphate; ROCK; Rho-associated protein kinase; VSMC: Vascular smooth muscle cells. Adapted from (10).

1.6 Membrane-connections to the actin cytoskeleton

The actin cytoskeleton uses and is regulated by different membrane anchors both within and outside of the cell (**Figure 1.6**). Typically, VSMC makes connective junctions to the extracellular matrix or to neighbouring cells, and this allows for bidirectional transmission of signalling cues (91). Within this review, the different mechanical links to the actin cytoskeleton will be discussed in further detail.

1.6.1 Cell-cell adhesions

Within the vasculature, VSMCs can form cell-cell adhesions with each other, as well as other neighbouring cell types such as endothelial cells. The primary molecule that mediates this is cadherin, and N-cadherin is the pre-dominant isoform that is expressed within VSMCs (92). It regulates crucial cellular processes such as VSMC proliferation and apoptosis (93, 94). Its structure is constituted by three domains; an N-terminal domain, a central transmembrane anchoring domain, and a cytoplasmic tail (95). The large N-terminal domain facilitates homodimer formation with a neighbouring cell via the linkage of their five extracellular cadherin (EC) repeat regions (92, 95). Specifically, both cells exchange a beta strand within their EC1 domain in a process referred to as trans-binding, and this interaction is stabilised by calcium (96-98). Importantly, the cytoplasmic tail of N-cadherin is physically linked to the actin cytoskeleton via the recruitment of α-catenin, and this facilitates mechanical signals between cell-cell adhesions and the contractile apparatus (99).

Recently, there has been increasing evidence that N-cadherin plays a role in mechanotransduction to induce changes in adhesion strength and actomyosin activity (100-102). Within VSMC cells, cell-cell adhesions contribute to myogenic vasomotor tone regulation in healthy conditions, as well as atherosclerotic intimal thickening during CVD development (103, 104). However, further work is required to clarify the mechanisms in which N-cadherin-based mechanosignalling influences VSMC function.

1.6.2 Cell-ECM adhesions

Cell-ECM adhesions, otherwise termed focal adhesions, allow the cell to anchor itself to its extracellular environment. Focal adhesions span the plasma membrane, and integrins act as the core of the complex. Integrins structure consists of an α and β subunit, and both subunits contribute to the formation of the ligand binding- and cytosolic-domain (105). The ligand binding domain facilitates interaction with extracellular components, whilst the cytosolic tail allows anchorage to the actin cytoskeleton (106). This enables a bi-directional exchange of mechanical cues and regulatory signals, which is transmitted via key mechanosensing proteins within the adhesion complex (107, 108).

Prior to signal transduction, focal adhesions must mature and this involves the recruitment of cytosolic components (109). Talin and α-actinin are a few of the initial proteins that are employed to the cytoplasmic domain of integrin, and once bound, talin can induce recruitment of additional proteins. These include vinculin, paxillin, and focal adhesion kinase (FAK) amongst others, that form a series of connected elements that lead to the actin

cytoskeleton (110, 111). Vinculin, in particular, acts as a key mechano-regulator, and physically links the focal adhesion complex to the cytoskeleton. When inactive, the head and tail domain of vinculin maintains autoinhibition, however this can be disrupted via binding with talin/α-actinin (112, 113). Vinculin binds to talin's rod domain which becomes exposed until mechanical stress, and also physically links to filamentous actin allowing force transduction to the ECM to occur (112, 113).

It is not yet fully understood the full range of processes that occur during focal adhesion maturation, however known processes include stress-induced activation of focal adhesion proteins, stimulation of receptor tyrosine kinases and phosphatases, and remodelling of the cytoskeleton (114-116). These processes regulate cell-matrix adhesions, allowing them to maintain a mechanical balance within the dynamic ECM of the vasculature.

1.6.3 The linker of nucleoskeleton and cytoskeleton complex

The nucleus is subjected to mechanical tension and its structure allows transmission of biophysical signals from actomyosin-generated force. Within the nuclear envelope, the inner nuclear membrane (INM) and outer nuclear membrane (ONM) form a double lipid bilayer, and this is divided by a ~40 nm perinuclear space (117). The mechanical cues transmitted between the actin cytoskeleton and nuclei are facilitated by the linker of nucleoskeleton and cytoskeleton (LINC) complex. This complex is comprised by the Nesprin-family members found on the ONM and SUN-domain containing proteins residing on the INM (118). Both groups of proteins span the nuclear envelope and are mechanically linked within the perinuclear space, via the coupling of the Klarsicht, Anc-1, Syne-1 homology (KASH) domain of Nesprin 1/2 to the SUN domain of the SUN 1/2 proteins (118, 119). Importantly, the Nesprin 1/2 protein can directly associate with the actin filaments via its calponin-homology domain to directly regulate cytoskeletal organisation (120). This allows the nuclei to translate key mechanosignalling input from the cytosol and extracellular space in order for it to respond appropriately.

One way in which it does this is via the reorganisation of the nuclear lamina meshwork. The lamina network consists of A-/B-type lamin intermediate proteins along with lamina-associated proteins, and works to provide nuclear stability (121). The SUN 1/2 proteins present on the INM physically associates with A-type lamin A/C, and as a result, its disruption via mechanical overload can alter VSMC morphology and adhesion organisation (118, 122). Additionally, the LINC complex regulates actomyosin-derived forces, as disrupting Nesprin 1/2 and lamin A/C function was found to enhance actomyosin activity in

skeletal muscle progenitor and endothelial cells (123, 124). However, the role of the LINC complex may be cell-type specific as differential lamin A/C-induced effects were shown in the actomyosin activity of fibroblast cells (123). The extent in which the LINC complex participates in VSMC mechanotransduction is currently unknown, however it is speculated to influence actomyosin activity due to being key regulators of Rac1 and Rho GTPases (122, 125).

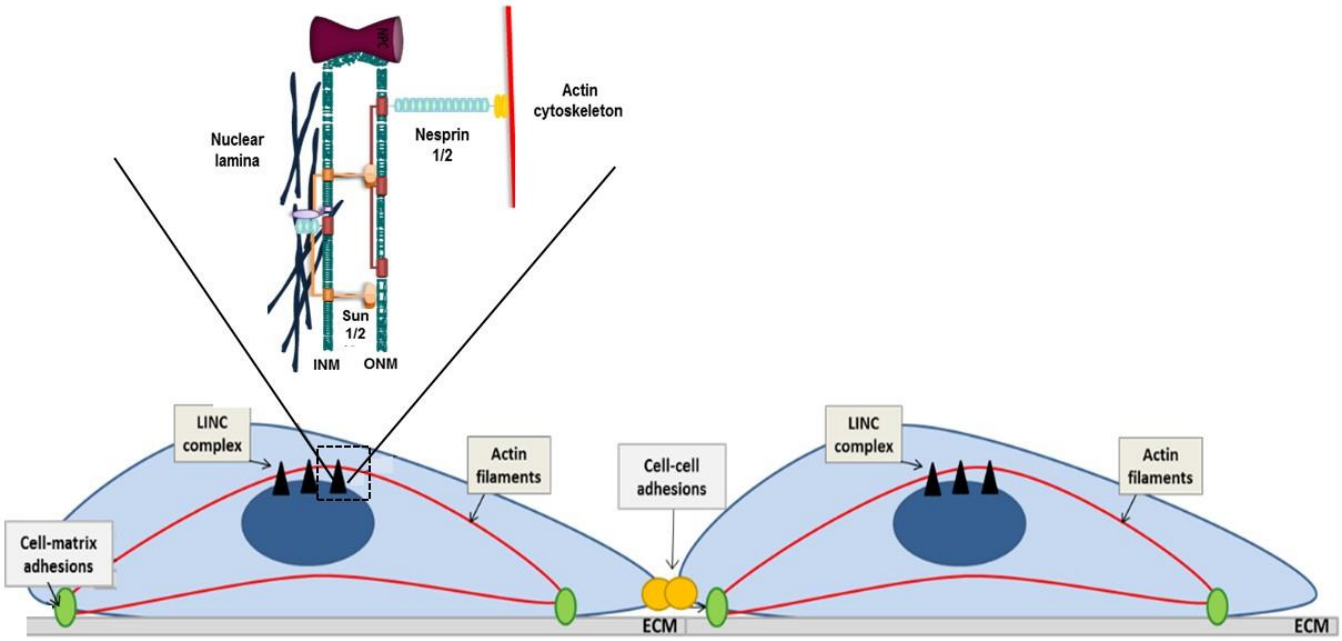

Figure 1.6: Schematic diagram showing organisation of LINC complex and adhesion complexes within VSMCs. ECM: Extracellular matrix; INM: Inner nuclear membrane; ONM: Outer nuclear membrane; VSMC: Vascular smooth muscle cell. Adapted from (10).

1.7 VSMC ageing and regulatory mechanisms

1.7.1 Stiffness-induced DNA damage

VSMC ageing is commonly observed within CVD, and is typically associated with a variety of key functional changes. Importantly, ageing can induce a switch to the proliferative phenotype and cause altered mechanosensitivity, eventually leading to pre-mature senescence of the VSCMs (126). Within aged/CVD models, VSMCs typically undergo phenotypic transition, and migrate to the tunica intima where they proliferate to help form an atherosclerotic plaque in response to injury (127). However, during CVD development,

vascular tissues present remodelling, and increased collagen-1 density were shown to produce smaller and stiffer matrix pores (128, 129). Within these conditions, VSMCs are forced to move via these tighter gaps to the tunica intima, which could subject the stiff nuclei to mechanical stress (130) (**Figure 1.7**). The nucleus presents itself as the stiffest organelle within the cell, with almost 5 times more rigidity than the cell itself (131). Cancer models have previously shown that altered ECM composition can enhance DNA damage accumulation, as the nuclei has to physically squeeze through the less porous matrix during cell migration (132). This is supported by previous work which shows incidence of nuclear rupture is augmented when cells are seeded on stiffer 2D substrates (133). Disruption of nuclear integrity is typically accompanied by DNA damage accumulation, and this has been shown in multiple studies (133, 134).

Importantly, VSMC ageing can be triggered by many factors with DNA damage being one of the most prevalent. DNA damage can occur in many forms and includes strand breaks, telomere shortening and base oxidation (135). In severe cases, plaque rupture within atherosclerosis can occur and *in vitro*/*in vivo* work have shown that VSMCs are unable to compensate as they display poor proliferation rates and undergo premature senescence (136, 137). Additionally, VSMCs derived from atherosclerotic plaques present an increase in DNA damage with disease severity, and this is shown via augmented γ-H2AX levels and increased tail lengths on a Comet assay (138). Due to this, DNA damage has been shown to accelerate VSMC ageing and senescence, and if not efficiently repaired, can lead to vascular inflammation, arterial dysfunction and CVD development (135). In summation, the cause of VSMC ageing-induced DNA damage accumulation remains unknown. It has previously been shown that unrestrained actomyosin activity can induce DNA damage accumulation in other cell types (139-141). Coupled to this, VSMCs have shown to present enhanced actomyosin activity and traction force generation within stiffer matrices (142), however further work is required to determine whether actomyosin activity can drive DNA damage accumulation within VSMCs.

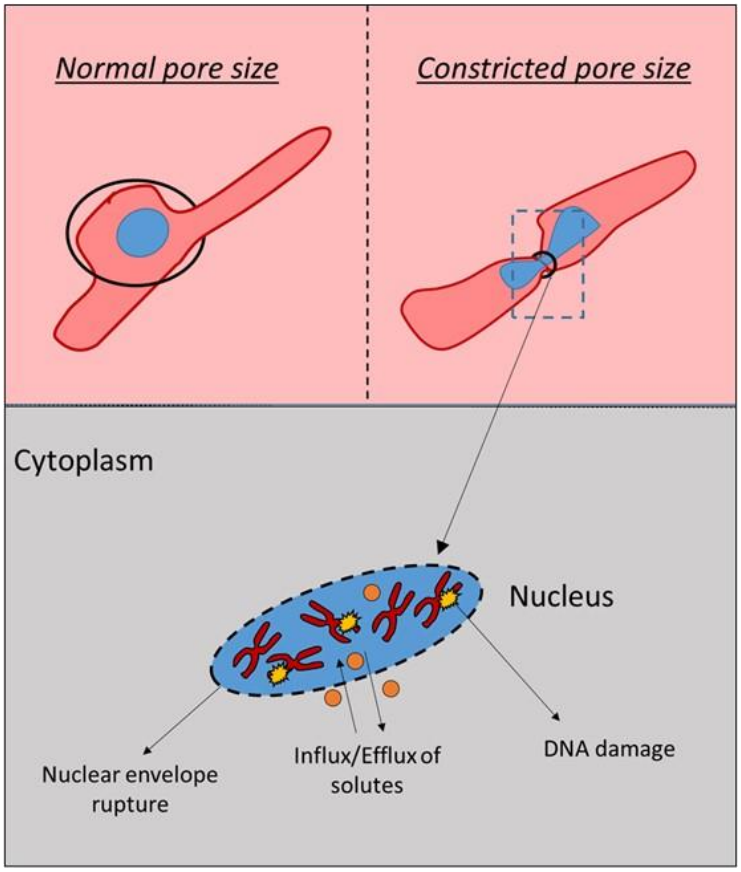

Figure 1.7: Diagram showing constricted VSMC migration through smaller pores leading to nuclear rupture. VSMC: Vascular smooth muscle cell. Adapted from (69).

1.7.2 NAT10 and protein acetylation

Within the vessel wall, VSMCs work to maintain vessel tone, however under stiffer conditions, they reveal a dysregulation of their core functions including increased contractility (142). Previously, it's been shown that unrestrained actomyosin activity induces DNA damage in multiple cell types, and as discussed before, DNA damage drives VSMC ageing (139-141). Importantly, multiple cytoskeletal proteins have emerged as novel regulatory components of actin stress fibre formation and cell contractility (70, 143, 144). In order to do this, many undergo conformational changes in their organisation and recent work has revealed acetylation of key lysine residues to help facilitate this.

Acetylation acts as an important post-translational modification (PTM) for multiple cytosolic proteins, and emerging studies have identified N-Acetyltransferase 10 (NAT10) as

a critical histone acetyltransferase that is involved within this. NAT10 is a part of the Gcn5-related N-acetyltransferases family and controls multiple processes within the cell such as maintaining telomerase activity, transcription and cytokinesis (145-149). Importantly, tubulin has been established as a key substrate for NAT10, and loss of NAT10 activity has been shown to induce reorganisation of the microtubule network (146, 150). Prior studies have shown microtubule acetylation to inversely correlate with cell contractility within fibroblast cells (70). We speculate this to be a regulatory mechanism by NAT10 as utilisation of Remodelin, a specific NAT10 inhibitor, has revealed a link between microtubule reorganisation and rescue from nuclear deformation (150). Nuclear deformation is a common consequence of mechanical overload, and in support of this, NAT10 inhibition was also shown to reduce genomic instability and delay senescence within aged VSMCs (151).

Another key protein that regulates VSMC function is vimentin. Vimentin is an intermediate filament protein that is highly expressed within VSMCs (48). It has previously been shown to regulate VSMC contractility via polymerisation of its intermediate filament network (143, 144, 152-155). Importantly, it has been shown to be acetylated on several lysine residues, specifically lysine 120, which has induced enhanced migration in other cell types (156). Prior studies have shown Remodelin treatment to decrease vimentin levels (157), and as a result, vimentin expression may be upregulated by NAT10 during CVD, and this may increase VSMC migration leading to early VSMC senescence and accelerated ageing.

1.7.3 Epigenetic regulation

Heritability determinants have been shown to contribute to complex CVD conditions such as atherosclerosis, hypertension and diabetes, however, variability in disease severity may be a result of epigenetic changes that target chromatin structure as opposed to DNA sequence (158, 159). Epigenetic regulation can either be in the form of DNA methylation which characterise long-term changes, as well as more transient histone modifications (160). Methylation tags on the DNA sequence may promote regulation of histone structure, and thus perpetuate a sequence of chromatin modifications. Such post-translational histone changes include phosphorylation, ubiquitination, acetylation and methylation (161, 162). Out of these, acetylation of the histone H3/H4 tails, specifically on its lysine residue, serves as the most consistent sign of promoting transcription, whilst histone deacetylation typically induces chromatin condensation (160, 163, 164). However, whilst this is the general case, epigenetic modifications are far more complex and can induce differential effects. An example is methylation of the histone tails which can cause gene silencing on H3K27

residues, as well as activation via H3K4 residues (160), with further information shown on **Table 1.1**.

Table 1.1: Histone methylation sites showing most common effects and chromatin regions currently known. Adapted from (160).

Histone protein	Residue position	Modification	Transcriptional effect
H3	Lysine 4	Di-methyl	Gene activation
H3	Lysine 4	Tri-methyl	Gene activation
H3	Lysine 9	Mono-methyl	Gene silencing
H3	Lysine 9	Di-methyl	Gene silencing
H3	Lysine 9	Tri-methyl	Gene activation/silencing
H3	Lysine 27	Mono-methyl	Gene silencing
H3	Lysine 27	Tri-methyl	Gene silencing
H3	Lysine 79	Di-methyl	Gene activation
H3	Lysine 79	Tri-methyl	Gene activation
H4	Lysine 20	Di-methyl	Gene silencing
H4	Lysine 20	Tri-methyl	Gene silencing

Within VSMCs, many smooth muscle differentiation marker genes contain CArG boxes within their promoter regions, and are regulated by serum-response factor as well epigenetic histone markers (165). During CVD development, VSMCs switch to the synthetic proliferative phenotype which is accompanied by changes in the expression of key contractile marker proteins (166). The mechanical pressure induced by alterations in ECM composition can be transmitted to the nuclear lamina which potentially triggers epigenetic changes (130, 131). Previous work has shown aged VSMC samples from atherosclerotic model's present DNA hypomethylation which can activate a number of gene clusters (167). Dysregulation of this can cause aberrant cellular effects and key inducers such as angiotensin II and DNA damage have previously been shown to trigger VSMC senescence via epigenetic changes (135). In support of this, prior research has revealed Angiotensin II stimulation can induce opening of chromatin via histone acetylation, whilst other studies show compressive forces to VSMCs reduce actomyosin activity and suppress transcription in VSMCs (168, 169). As a result, it becomes clear that intra/extracellular mechanical

tension can regulate gene expression during phenotypic switching, and this may accelerate VSMC ageing within the stiffened environment.

1.8 VSMC mechanotransduction

1.8.1 Mechanotransduction overview

The mechanical stimuli that arise from a cell's microenvironment can be translated to biochemical processes within the cell, via a process referred to as mechanotransduction. Within the vasculature, this is essential in allowing the VSMCs to timely adapt to the dynamic changes of the vascular wall (170). Mechanotransduction facilitates regulation of VSMC function, adjusting crucial processes such as actomyosin activity, adhesion organisation and phenotypic switching (171). Mechanosensors facilitate transmission of mechanical cues from the ECM, and are defined as proteins that present a specific modification in response to intra/extracellular tension. Alterations in these proteins can vary, and positive signatures of a successful mechanosensor include post-translational modifications, protein localisation and new binding partners (170). Key mechanosensors within VSMCs include stretch-activated ion channels (SACs), cytoskeletal filaments and cytosolic/nuclear proteins, as shown by **Figure 1.8**, and activation of each can trigger specific response pathways within the cell (171, 172).

In order to effectively respond to the ECM, cells tune their mechanical properties by actively exerting and resisting forces both to and from their microenvironment. The force generated from the actin cytoskeleton is transmitted via focal adhesion complexes, enabling "inside-out" and "outside-in" signalling (173). This induces appropriate changes in gene expression which causes structural remodelling of the cytoskeleton. As a result, VSMCs can mediate essential maintenance of the healthy vascular wall, as well as initiate damage repair during disease development (174). Within the arterial wall, each of the three layers present roles in mechanotransduction (32). However, this review focuses upon the VSMCs that lines the tunica media, and the mechanotransduction that takes place under both physiological and pathological conditions.

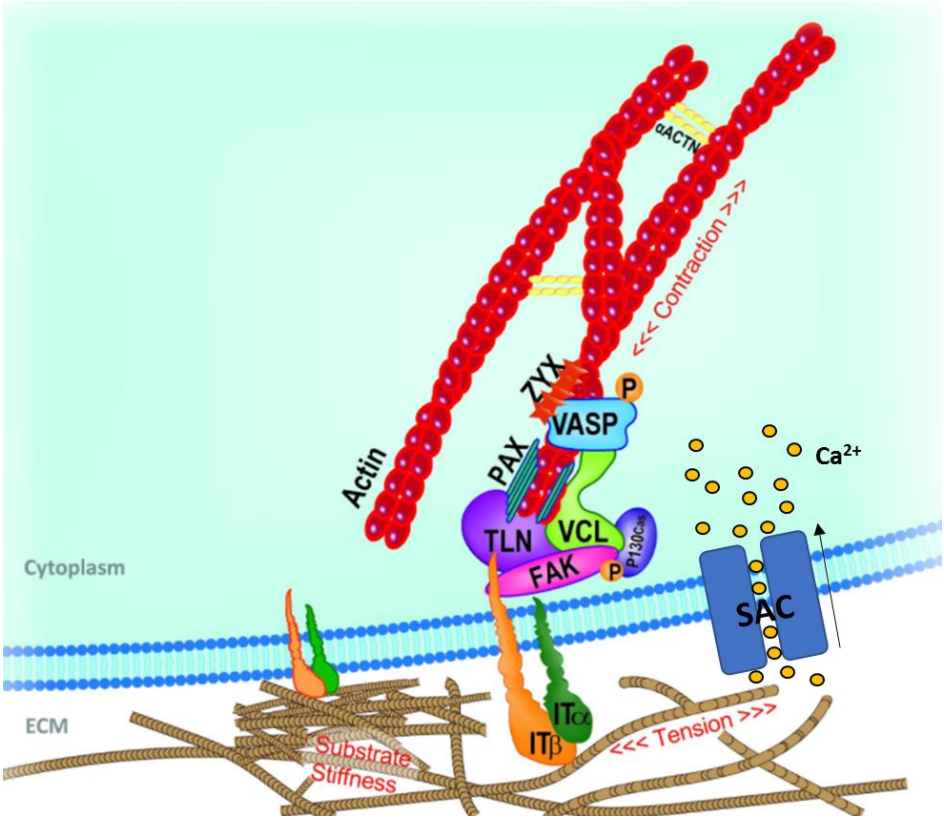

Figure 1.8: Schematic diagram showing key mechanosensors present at the cell membrane of VSMCs. Substrate stiffness is sensed by cell-matrix adhesions which results in the recruitment of subsequent focal adhesion proteins. Vinculin, via talin, binds to the actin cytoskeleton allow transfer of mechanical cue between the cytoplasm and ECM. ECM: Extracellular matrix; FAK: Focal adhesion kinase; IT: Integrin; PAX: Paxillin; SAC: Stretch-activated channel; TLN: Talin; VCL: Vinculin; VSMC: Vascular smooth muscle cell; WASP: Wiskott–Aldrich syndrome protein; ZYX: Zyxin. Adapted from (170).

1.8.2 Elastic arteries and the role of stretch

The cardiac cycle is cyclical in nature, and the blood that is ejected from the left ventricle creates numerous mechanical stimuli that vascular smooth muscle is subjected to. Examples are circumferential wall tension and vascular shear strain, however, VSMCs are pre-dominantly exposed to cyclic stretch from pulsatile blood pressure (35, 174). The occurrence of cyclic stretch is periodic within the cardiac cycle, due to the systolic and diastolic phase causing an increase and subsequent decrease in blood flow, respectively (175). The healthy arterial wall is abundant in elastin, and when stretched, it can stimulate the activation of key signalling molecules such as protein kinase C (PKC) and Akt. These mechanosensors can regulate important cellular functions such as migration and

proliferation (35). A crucial component recently identified in this response are SACs, which mediate calcium entry into the cytosol to regulate VSMC contraction (176, 177).

SACs exist on the cell membrane and work to regulate the myogenic response, via calcium entry and depolarisation (177). This allows VSMCs to translate mechanical stretch into force generation, however the exact signal transduction mechanisms are not fully clarified. Despite this, numerous studies have identified mechano-sensitive ion currents within VSMCs, and several channels have been implicated to contribute towards this (178). One such family are the transient receptor potential-canonical (TRPC) channels. The TRPC are part of the transient receptor potential (TRP) superfamily, comprising one of its six subfamilies, and possesses a structure of four subunits with 6 membrane-spanning helices in each (179, 180). Within VSMCs, TRPC channels have been found to cause depolarisation, which allow for vessel tone regulation and control of systemic blood pressure (181, 182). Specifically, the non-selective cation channel TRPC6 has previously been found to augment cytosolic calcium concentration via release from the SR to increase VSMC contraction (183). This channel works via the PKC pathway, and requires phosphorylation of the Threonine 69 residue found on one of its subunits, to exert its effects (184).

Another mechanosensitive family are the Piezo non-selective cation channels consisting of Piezo1 and Piezo2, with the former revealing roles in vascular development and blood pressure management. Cryogenic electron microscopy has revealed that Piezo1 exists in a trimeric form, resembling three-bladed propellor-like structure, with an ion-conducting pore module in its centre (185). Its electrophysiological properties reveal an influx of Na^+, K^+, $Ca^{2+,}$ and Mg^{2+} ions, with Ca^{2+} showing favourable permeability (186). Piezo1 is highly expressed within endothelial and smooth muscle cells, and work to mediate blood vessel development and structural maintenance (187-189). Importantly, it has been shown to contribute to arterial remodelling within hypertensive models, and therefore Piezo1 presents a crucial role within the mechano-responses of VSMCs in both physiological and pathological conditions (189).

1.8.3 The role of matrix stiffness in CVD

During CVD development, the arterial wall loses elasticity and becomes stiffer due to a variety of contributing factors (31). As a result of key mechanosensors, such as the focal adhesion complexes, VSMCs are able to sense the rigid matrix and respond by exerting actomyosin-derived forces to the ECM (173). This usually allows for regulation of the vessel tone, however during pathological remodelling, the vascular wall becomes progressively less

compliant (12). The resulting reduction in elasticity diminishes stretch signals that normally arise from blood flow, and causes a switch between transient stretch signals to sustained stiffness signalling.

Decreased aortic compliance typically occurs in the early stages of numerous CVDs such as atherosclerosis, restenosis and diabetes (63). Atherosclerosis progression, in particular, has shown a clear correlation with arterial compliance (190). It is an inflammatory condition that acts as the underlying cause of heart attacks and cardiac death, and works by eliciting aberrant functions from both the intimal and medial layers (63, 191). This results in the formation of an atherosclerotic plaque, which consists of a soft lipid core (~5kPa) surrounded by a stiff fibrous cap (~60-250 kPa) (192). As a result, the mechanical rigidity of the microenvironment possesses abnormal heterogeneity, and VSMCs can sense this to perform directional cellular migration via durotaxis (192, 193). Durotaxis differentiates from chemotaxis and haptotaxis as it does not require soluble chemical signals or adhesive ligand densities, respectively (193). Previously, it has been shown that VSMCs undergo directed migration on gels coated with fibronectin (194). Fibronectin is abundant within atherosclerotic lesions, and this suggests that a stiffness gradient may contribute to how VSMCs migrate to the intimal layer within atherosclerosis.

Additionally, VSMC phenotypic switching and enhanced proliferation has been observed within atherosclerosis (14, 190). As mentioned before, phenotypic regulation is modulated by a variety of environmental cues, and ECM composition has been implicated to play a crucial role (195). Within atherosclerotic plaques, there is a degradation of elastin as well as augmented collagen-1 deposition (142). Previous studies have shown that increases in collagen-1 density can induce a reduction in the expression of key contractile marker proteins, such as SM-myosin II (195). This suggests that the augmentations in the stiffness and nanotopography of the ECM can direct a proliferative change to the synthetic phenotype of VSMCs (196).

Despite this, our understanding of matrix rigidity and the numerous effects it has on VSMC function remains limited. Previously, it has been shown that VSMCs reveal increased intracellular tension and larger cell-matrix adhesion formation when seeded on stiffer substates (31, 197). Alongside this, VSMC stiffness is augmented within multiple CVDs, such as diabetes and hypertension, and this can be attenuated via actin inhibitors (31, 198). This gives indication that matrix stiffness may increase actomyosin activity within VSMCs, and this leads to increased cell stiffness. To support this, an increase in matrix rigidity from 10 kPa to 25 kPa has previously been found to evoke larger traction force generation within fetal aortic VSMCs (142). Importantly, when increased to 135 kPa, VSMCs lose their ability

to displace the matrix, and therefore cannot generate sufficient force to manipulate the ECM under enhanced stiffness (142). This was also shown in 3D models where VSMCs no longer retained the ability to physically contract their substrate when surrounded by collagen-1 fibrils (199).

From this, it is possible that the rigid ECM is no longer remodelled by VSMC actomyosin activity due to a stiffness-dependent reduction in contractile marker protein expression (200). This can prevent VSMCs from generating sufficient traction force to deform the stiff substrate, as previously observed, making the extracellular environment non-compliant (142). However, it remains unclear whether the absence of substrate deformation is due to a reduction in actomyosin activity or an unmanageable increase in matrix rigidity. A previous study utilising young and old soleus muscle feed arteries examined the vasoconstrictor response of each. This study found that the vasoconstrictor response of the aged vessels significantly decreased in comparison to its counterpart, suggesting impairments in the intrinsic actomyosin activity of the VSMCs (200). However, due to the fact that aged arteries are stiffer and less prone to deformation, the actomyosin response may remain intact (201). In agreement with this, VSMCs within aged arteries show enhanced ROCK activity as well as higher mechanical loads at their cell-matrix adhesions (200). Due to this, further work is required to clarify the extent in which matrix stiffness may influence actomyosin signalling within VSMCs.

1.9 Hypothesis and Project Aims

The arterial wall undergoes stiffening during CVD development, and this has several implications on VSMC, the pre-dominant cell type within the aorta (31, 142, 197). However, prior work investigating VSMC function has primarily been performed on either plastic/glass or gels unrepresentative of the aortic wall and as a result, we speculate that employing materials that mimic both the healthy and stiffened aortic wall will reveal novel mechanistic insights. We hypothesise that matrix stiffness will result in altered VSMC mechanotransduction and this will affect:

- Morphological characteristics
- Cytoskeletal function and organisation
- Contractile activity

The specific objectives within this project were:

1) To characterise the impact of matrix stiffness on synthetic VSMC organisation and traction force generation.

2) To explore the effect of various contractile agonist and antagonists on quiescent VSMC morphology and whether matrix stiffness induces a differential response.

3) To determine the effect of matrix stiffness on quiescent VSMC volume and the underlying mechanism behind it.

4) To study the role of NAT10 in VSMC morphology and DNA damage regulation.

By furthering our understanding of the altered mechanotransduction that VSMCs undergo within the pathological environment, this work will aid in identifying future therapeutic targets for stiffness-related vascular diseases.

Chapter 2: Materials and Methods

2.1 Laboratory Consumables

All laboratory consumables and equipment utilised throughout the course of this project, unless otherwise indicated, have been listed within the tables below. If excluded, they are presented clearly later on within this chapter. All diluted reagents, unless stated differently, were made using distilled water.

2.1.1 Chemicals and reagents

Table 2.1: Laboratory chemicals and reagents used.

Chemical/reagent	Source	Product/Catalogue number
Smooth Muscle Cell Growth Medium	Sigma	311-500
Smooth Muscle Cell Growth Supplement	Sigma	311-GS
Smooth Muscle Cell Basal Medium	Sigma	310-500
Keratinocyte Calcium-Free Basal Medium	Sigma	132-500
Earle's Balanced Salts	Sigma	E6267
Trypsin-EDTA solution	Sigma	T3924
Dimethyl sulfoxide (DMSO)	Sigma	D8418
Fetal Bovine Serum (FBS)	Fisher Scientific	26140079
(3-Aminopropyl)triethoxysilane (APES)	Sigma	A3648
Glutaraldehyde solution	Sigma	G6257
Ammonium persulfate (APS)	Sigma	A3678
Tetramethylethylenediamine (TEMED)	Thermo Scientific	17919
Acrylamide Solution (40%/Electrophoresis)	Fisher Scientific	BP1402-1
Bis-acrylamide Solution (2% w/v/Electrophoresis)	Fisher Scientific	BP1404-250
Isopropanol	Fisher Scientific	10674732
Chloroform	Fisher Scientific	10102190
Ethanol absolute ≥99.8%	VWR	20821.330
FluoSpheres™ Carboxylate-Modified Microspheres, 0.5 µm, red fluorescent (580/605), 2% solids	Thermo Scientific	F8812
Triton™ X-100	Sigma	X100
Collagen I, rat tail	Thermo Scientific	A1048301

Table 2.1: Laboratory chemicals and reagents used.

Sulfo-SANPAH, primary amine-nitrophenylazide crosslinker	Abcam	ab145610
Dulbecco's Phosphate Buffered Saline (PBS)	Sigma	D8537
Paraformaldehyde (PFA)	Sigma	P6148
Nonidet P-40 (NP-40) Surfact-Amps™ Detergent Solution (10% (w/v) aqueous solution)	Thermo Scientific	85124
Bovine Serum Albumin (BSA)	Sigma	A2153
VectaShield® HardSet™ Antifade Mounting Medium with DAPI)	Vector	H-1500
VectaSheild® Hardset™ Antifade Mounting Medium	Vector	H-1400
HiPerFect Transfection Reagent	Qiagen	301705
Flexitube siRNA (5 nmol)	Qiagen	1027417
Sodium Dodecyl Sulfate (SDS)	Fisher Scientific	10090490
2-Mercaptoethanol	Sigma	M3148
Glycerol, 99+%	Fisher Scientific	10795711
Bromophenol Blue sodium salt	Sigma	B8026
Tris Base	Fisher Scientific	10376743
TruPAGE™ Precast Gels, 4-20%	Sigma	PCG2004
Methanol	Fisher Scientific	10284580
TruPAGE™ Tris-MOPS SDS Express Running Buffer, 20X	Sigma	PCG3003
TruPAGE™ Transfer Buffer, 20X	Sigma	PCG3011
Skim milk powder	Oxoid	LP0031
Tris Buffered Saline, with Tween® 20 (TBST), pH 8.0	Sigma	T9039
Cytiva Amersham™ ECL™ Prime Western Blotting Detection Reagent	Fisher Scientific	10308449
Nuclease-free water	Sigma	W4502
qPCRBIO Probe Mix Lo-Rox	PCR Biosystems	PB20.21
Invitrogen™ TRIzol™ Reagent	Fisher Scientific	12044977
9x Invitrogen™ Random Primers	Fisher Scientific	48190011
SuperScript™ II Reverse Transcriptase (including 0.1M DTT & 5X first-strand buffer)	Fisher Scientific	18064014
100 µM DNTP Mix	Bioline	BIO-39053

2.1.2 Lab consumables

Table 2.2: Details of laboratory apparatus used.

Lab apparatus	Source	Product number
Thermo Scientific™ BioLite Cell Culture Treated Flasks	Fisher Scientific	11884235
Cryogenic vial 1.2 ml, Sterile	Fisher Scientific	1050025
Parafilm	Sigma	P7793
30 mm Coverslips	VWR	631-0174
13 mm Coverslips	VWR	631-0149
6 Well Plates	Thermo Scientific	130184
24 Well Plates	Fisher Scientific	930186
Immun–Blot® PVDF Membrane	Bio-Rad	162-0177
VisiPlate-24 Black, Black 24-well Microplate with Clear Bottom	PerkinElmer	1450-605
1.5 ml Natural Flat Cap Microcentrifuge Tubes	Starlab	S1615-5500
Microscopic Slides with Ground Edges	Fisher Scientific	12373118
25x Fisherbrand™ 96-Well Nonskirted PCR Plates, Natural	Fisher Scientific	14230232
250x Fisherbrand™ Flat and Domed 8-Cap Strips, Flat Cap Strips	Fisher Scientific	11859251
MicroAmpTM Optical 96-Well Reaction Plate (Applied Biosystems N8010560)	Applied Biosystems	N8010560
MicroAmpTM Optical Adhesive Film	Applied Biosystems	4311971
10 µl Graduated TipOne Filter Tip (Sterile), Racked (10x96)	Starlab	S1121-3810
20 µl Bevelled TipOne Filter Tip (Sterile), Racked (10x96)	Starlab	S1120-1810
200 µl Graduated TipOne Filter Tip (Sterile), Racked (10x96)	Starlab	S1120-8810
1000 µl XL Graduated TipOne Filter Tip (Sterile), Racked (10x96)	Starlab	S1122-1830
Sterile Graduated Transfer Pipettes	Fisher Scientific	13469108

2.1.3 Lab instruments

Table 2.3: Laboratory instruments used within project.

Instrument	**Source**
Plate Reader	CLARIOstar
Benchtop UV Transilluminator	UVP
UV Cabinet	Fisher Scientific
Magnetic Stirrer with Heating	Starlab
Vortex	Starlab
Centrifuge 5810 R	Eppendorf
2720 Thermal Cycler	Applied Biosystems
7500 Real Time PCR System	Applied Biosystems
ChemiDoc XRS+ System	Bio-Rad
Trans-Blot® Turbo™ Transfer System	Bio-Rad

2.2 Cell culture

All cells were grown in T75 flasks and kept in humidified incubators set at 37°C, with a 5% CO_2 atmosphere. At 70-80% confluency, culture medium was removed and cells were washed with Earle's balanced salts solution. Cells were then detached from cell flask during passaging via trypsin-EDTA treatment for 3-5 minutes at 37°C. Smooth muscle cell growth medium was used to inactivate trypsin-EDTA and cells were split 1:2 into fresh T75 culture flasks.

Cell stocks were created by suspending cells in VSMC freezing medium (10% DMSO and 90% FBS) within a cryogenic vial to be initially frozen at -80°C, with long-term storage at -180°C, in a liquid nitrogen vapour phase.

2.2.1 Human VSMCs

Our study utilised two isolates of human VSMCs. 354 human VSMCs were purchased from Thermo Scientific (C0075C) whilst 35F human VSMCs were a kind gift from Professor Catherine Shanahan (Kings College London, UK). Both were cultured in smooth muscle cell growth medium containing smooth muscle cell growth supplements. The 354 VSMC isolate was pre-dominantly used throughout this project due to accessibility and time restraints. However, when using 35F VSMCs, they are clearly mentioned within this thesis as isolate-2.

2.2.2 Polyacrylamide hydrogels

2.2.2.1 Coverslip activation

Using parafilm, the top surface of the coverslip (13/30 mm) was covered with APES, used neat, for 5 minutes. Next, coverslips were rinsed two times with 1-2 ml of distilled water. Coverslips were then immersed in 0.05% glutaraldehyde solution for 30-60 minutes. After, coverslips were rinsed twice more with distilled water before being air dried. Within our lab, activated coverslips remained functional for two weeks and could be stored at room temperature (RT).

2.2.2.2 Hydrogel fabrication

Appropriate ratios of acrylamide and bis-acrylamide were mixed in distilled water. The standard ratios and their corresponding Young's modulus were previously determined in Dr Warren's lab, shown in **Table 2.4** (202). Within this project, we fabricated polyacrylamide hydrogels with an average Young's modulus of 2, 12 and 72 kPa, however the acrylamide/bis-acrylamide ratios of alternative elastic values can be found in earlier work (203). In order to ensure consistency between hydrogels, 50 ml of hydrogel stock solutions were made in bulk and stored in 4°C. Once made, hydrogel polymerisation was initiated via the addition of 1:100 APS (10%) and 1:1000 TEMED. For experiments mapping cellular traction forces, 1:1000 FluoSpheres are combined before the addition of TEMED. 25 µL (for 13 mm coverslips) to 50 µL (for 30 mm coverslips) of the mix was placed on the centre of a glass slide and the activated coverslip was placed face down on the solution for 5-10 minutes. This step was performed carefully to prevent air bubbles forming ensuring intact hydrogel fabrication. After, the glass slides were slowly peeled off the coverslip leaving a newly formed polyacrylamide hydrogel on its surface. The coverslip, hydrogel side up, was kept in water/PBS at 4°C for a maximum duration of 2 weeks.

Table 2.4: Composition of acrylamide/bis-acrylamide stock solution for 2, 12 and 72 kPa hydrogels in a 50 ml volume.

	2 kPa	**12 kPa**	**72 kPa**
Acrylamide Solution	6.250 ml	9.375 ml	12.500 ml
Bio-Acrylamide Solution (2%) W/V	2.000 ml	3.000 ml	10.000 ml
Dd$H_2$0	41.750 ml	37.625 ml	27.500 ml

2.2.2.3 Hydrogel functionalisation for cell culture

To facilitate cell attachment to the hydrogels, coating with an ECM protein is required. For this model, any ECM component will suffice, however, we utilised collagen-1. In order to do this, we covalently linked the collagen-1 to the polyacrylamide hydrogel via

Sulfo-SANPAH, a protein cross linker. Sulfo-SANPAH was diluted 1:3000 to give a concentration of 6 mM and 1-2 ml of this was then used to treat each hydrogel. Using a Benchtop UV Transilluminator, the well plate was exposed to 365 nm UV light for 5 minutes in order to activate the cross-linking agent. Indication of activation can be visually assessed as cross-linking solution turns from bright red to dark red. After activation, the well plate was UV sterilised using a UV cabinet for an additional 30 minutes. Following this, every step of the functionalisation protocol was performed in the tissue culture hood. The Sulfo-SANPAH was removed and the hydrogels were washed twice with sterile PBS. The hydrogel was then treated with 0.1 mg/ml of collagen-1 and incubated at 4°C for a period of 10 minutes. Hydrogels were then washed twice more with sterile PBS. Cells were then seeded on the

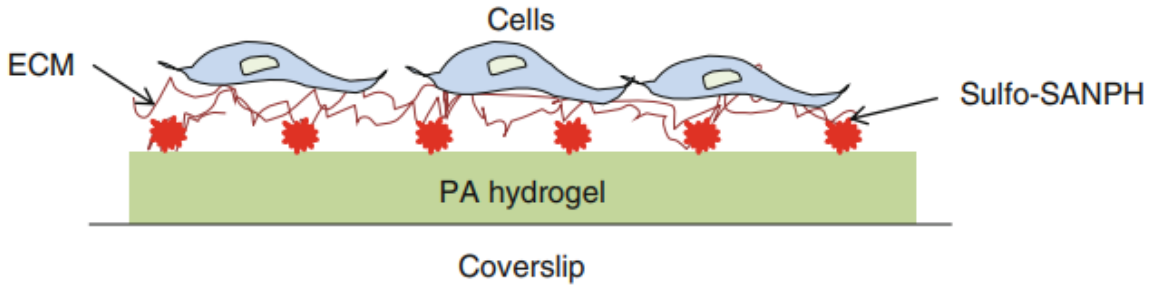

polyacrylamide hydrogels with smooth muscle growth/basal medium and cultured in a humidified incubator at 37°C, 5% CO_2. A schematic diagram of the final set up is shown (**Figure 1**).

Figure 2.1: Final set up of functionalised polyacrylamide hydrogels with cells attached. Adapted from (202).

2.2.3 SiRNA target knockdown

Target knockdown via the transfection of siRNA was performed using HiPerFect, following manufactures instructions. Briefly, siRNA was combined with basal media (100 µl) to give a final concentration of 0.4 µM. 24 µl of HiPerFect was then added to this and the resuspended solution was left to incubate at RT for 10 minutes, prior to being added dropwise to VSMCs cultured with 2 ml of growth media within a 6-well plate. All siRNA-targeted knockdowns were performed by Dr Robert Johnson within the Warren lab.

2.2.4 Cell treatments

A variety of different compounds were utilised throughout this project to test VSMC response within physiological and pathological environments. To do this, they were diluted to appropriate working concentrations, as indicated by **Table 2.5**, with smooth muscle growth/basal medium. Pre-existing medium was removed and replaced with drug solution for a duration defined by each experiment.

Table 2.5: Details of laboratory compounds utilised.

Compound	**Source and product number**	**Working concentration**
Angiotensin II	Sigma A9525	0.01-100 μM (Serial dilution)
Carbamoylcholine chloride (Carbachol)	Sigma C4282	0.01-100 μM (Serial dilution)
Irbesartan	Sigma I2286	0.023-230 nM (Serial dilution)
Atropine	Sigma A0132	0.036-360 nM (Serial dilution)
Y-27632 dihydrochloride	Sigma Y0503	5 μM
InSolution Y-27632	Sigma 688001	5 μM
Blebbistatin	Sigma B0560	40 μM
Atorvastatin calcium salt trihydrate	Sigma PZ0001	0.5 μM
Remodelin Hydrobromide	Sigma SML1112	1 μM
GsMTx-4, mechanosensitive and stretch-activated ion channel inhibitor	Abcam ab141871	0.05-500 nM (Serial dilution)
SAR-7334	Tocris 5831	0.1 nM-10 μM

2.3 Biochemical techniques

2.3.1 Whole cell lysate preparation

Samples were obtained by lysing cells in 4x Laemmli's Buffer, comprised of: SDS (8%), 2-mercaptoethanol (20%), glycerol (40%), bromophenol blue (0.008%) and Tris-HCl (0.125 mM). Prior to loading, samples were boiled at 95°C for 5 minutes.

2.3.2 Western Blot analysis

Samples (20 µL) were loaded onto TruPAGE 4-20% Precast gradient gels and subsequently underwent SDS-PAGE at 120 V for 2-3 hours, in the presence of TruPAGE running buffer, diluted to 1x concentration.

The separated proteins were subsequently transferred onto PVDF membrane using the Trans-Blot Turbo transfer system set at 25 V for 40 minutes. To do this, membranes were first wetted in Methanol briefly, and then placed in TruPAGE transfer buffer (1x) along with filter paper. Membranes were then blocked in 5% skimmed-milk powder prepared in TBST, for 1 hour at RT. After, the membranes underwent a 5-minute wash in TBST three times prior to being incubated in primary antibody, prepared in 5% BSA/TBST, overnight at 4°C. The following antibodies were used: anti-Piezo1 (used 1:1000) and anti-GAPDH (used 1:2000). After incubation with the primary antibody, membranes underwent a further 5-minute TBST wash three times before undergoing a 2-hour incubation with the appropriate horseradish peroxidase (HRP) conjugated secondary antibody, used 1:4000 in 5% milk/TBST.

Finally, membranes were washed with TBST for 5 minutes six times, and then treated with a 1:1 solution of Amersham ECL Prime Western Blotting Detection reagents. Chemiluminescence was detected on a ChemiDoc XRS+ system, and densitometric readings of blot intensities were quantified using FIJI. Within this project, all western blots presented were performed by Dr Robert Johnson within the Warren lab.

2.4 Molecular biology techniques

2.4.1 RNA isolation

Initially, all surfaces on the work bench were decontaminated using 70% ethanol. VSMCs from a confluent hydrogel plate were lysed using 500 µL of TRIzol reagent per hydrogel. The TRIzol solution was pipetted several times to facilitate full dissociation of nucleoprotein complexes, before being transferred to an Eppendorf tube. Next, 200 µL of chloroform was added and samples were vortexed for 15 seconds followed by a 2-minute incubation at RT. The samples were then centrifuged for 15 minutes/18,500 xg/4°C, with the resulting upper aqueous layer being collected and combined with 500 µL of isopropanol. A second vortex was performed on the samples and they were spun down once more for 10 minutes/18,500 xg/4°C. The supernatant was then removed and the resulting pellet was washed with 200 µL of 70% of ethanol, before undergoing a final centrifugation for 2 minutes/18,500 xg/4°C. The ethanol was removed and the RNA pellet was left to air-dry for 30 minutes, before being re-suspended in 20 µL of molecular grade water. The Nanodrop 2000 software was used to assess the concentration and purity of RNA samples, before storing at -80°C.

2.4.2 Reverse transcription (cDNA synthesis)

Total RNA of each sample was diluted to 1 µg/9 µL, with the addition of 2 µL of random primers before centrifugation for 2 minutes/18,500 xg/4°C. RNA was then incubated at 70°C for ten minutes using a Thermal Cycler. After, 4 µL of 5X first strand, 2 µL of 0.1 M DDT, 1 µL of Superscript II reverse transcriptase, dNTPs (100 µM), and molecular grade water was added to each sample. The randomly-primed RNA mix was then incubated for a further 60 minutes at 42°C, followed by heat inactivation for 10 minutes at 70°C. The total cDNA produced was diluted 1:100 in molecular grade water to obtain the required concentration necessary.

2.4.3 Quantitative polymerase chain reaction (qPCR)

All primer sets used within this project were examined via *Taq*-based PCR. Forward/reverse sequences of all genes of interest (GOI) were designed in the Assay design

centre of Roche Life Science, and then subsequently ordered from Sigma, (**Table 2.6)**. Corresponding probes were purchased from Universal ProbeLibrary on Sigma. Prior to qPCR, primer pellets were diluted to 10 µM and kept at -20°C.

A reaction mix was prepared using the following quantities per gene: 125 µL of qPCRBIO Probe Mix Lo-Rox, 7 µL each of diluted forward/reverse primers, 3.75 µL of corresponding probe, and 81 µL of water. Each mix had 10 µL of diluted cDNA added to it. Using a 7500 Real Time PCR System, PCRs were performed at 50°C for 2 minutes followed by 95°C for 10 minutes (Holding stage). Next, 40 cycles were performed at 95°C for 15 seconds before cooling to 60°C for 1 minute (Cycling stage). The 7500 software automatically determined the cycle threshold (CT) of each sample and mRNA expression was quantified from standard curves generated for each gene before being normalised to the internal control, ATP5B, from the same sample. Following this, the delta-delta CT method was used to determine fold changes.

Table 2.6: Primer sequences of genes of interest.

Gene	Forward sequence	Reverse sequence	Probe number (Universal Probe Library)	Scale (µM)	Purification	State
AQP1	gcccgagttcacaccatc	atcctctcaggcatcacctc	#48	0.025	Desalt	Dry
AQP4	tctggtacacaaaggtccaca	caggcaatgagagctgcac	#60	0.025	Desalt	Dry
PIEZO1	gcatccacatccctctcatc	ctgtctgcctcggcatct	#24	0.025	Desalt	Dry
PIEZO2	cccactgggaagtgtacagg	tgcacagtcaaaggctatcaa	#40	0.025	Desalt	Dry
TRPC1	tgatcgttttggtcgatgatt	agcttcttttggactacggttg	#24	0.025	Desalt	Dry
TRPC2	atcgggcactgtccactatc	aggaaagtgcagcaccaaag	#49	0.025	Desalt	Dry
TRPC3	aaaagggcttcgcagaattt	ttcctggccattggctact	#40	0.025	Desalt	Dry
TRPC4	gtatcgcttcaccaggttcc	caataggggtaagaacacagcat	#9	0.025	Desalt	Dry
TRPC5	ctgtcagcattgcgttctg	tggtaactggttcaacaacacc	#43	0.025	Desalt	Dry
TRPC6	tgcgtgtgctacaaacttca	atttactggtttgctccatgc	#60	0.025	Desalt	Dry
α-SMA	cctatccccgggactaagac	aggcagtgctgtcctcttct	#78	0.025	Desalt	Dry
ACAN	cctccccttcacgtgtaaaa	gctccgcttctgtagtctgc	#76	0.025	Desalt	Dry
BGN	ctcccagacctcaagctcct	tgggacagaagtcgttgaca	#9	0.025	Desalt	Dry
CNN	gctgtcagccgaggttaaga	cctcgatccactctctcagc	#32	0.025	Desalt	Dry
DCN	caaattcccggattaaaaggt	caggaaacttgtgcaagcag	#88	0.025	Desalt	Dry
LUM	cgaaagcagtgtcaagacagtaa	ggccactggtaccaccaa	#72	0.025	Desalt	Dry
VCAN	gcacctgtgtgccaggata	acgacagggattagagtgacatt	#54	0.025	Desalt	Dry
MAC2	aaaggcaggttataaggcacaa	cttctggacagccaagtgc	#3	0.025	Desalt	Dry
MYH11	gagctccagggcttttatca	actccattcccaagggtttc	#1	0.025	Desalt	Dry
MYH9	ctcgcgctggtactcctc	gctggatttgagatctttgaggt	#38	0.025	Desalt	Dry
TAGLN2	ccatatgcaggtcccctgt	gctttggctttggtgagc	#83	0.025	Desalt	Dry

2.5 Microscopy

All fluorescent images presented within this project were captured using a Zeiss Axiovert 200M, Zeiss Axioplan 2ie or Zeiss LSM510-META. Software programs used to capture images were AxioVision and LSM 510. Unless otherwise stated, all images of VSMCs were captured at the equatorial plane using an X20 objective.

2.5.1 Widefield and confocal microscopy

Within fluorescence, a source of light typically excites a fluorescent molecule before being emitted at a longer wavelength, which can be captured by either a widefield or confocal microscope. The photon is typically absorbed by the fluorescent molecule, causing it to rise from a ground state, resulting in a loss of vibrational energy. This causes an emission of the photon sensed by the detector generating a corresponding image.

Widefield microscopy uses LED illumination focused by the objective lens to illuminate the sample. The emitted fluorescence is separated from the excited wavelengths using a dichroic filter cube, and then focused towards the detector, a CCD camera in this case, via the same objective lens (**Figure 2.2A**).

In contrast, confocal microscopy uses light emitted by a laser to excite samples. Unlike widefield imaging, it utilises a second objective lens to direct emitted light towards a narrow pinhole, with a detector positioned behind. The detector utilised within confocal microscopes is a photomultiplier (PMT) (**Figure 2.2B**), and the image is generated solely from the software used. The photons are counted by the PMT via multiple scans, and the software is able to recognise the location of the photon via the relative position of the laser during its scan. As a result, this allows for better resolution images with less background fluorescence (204).

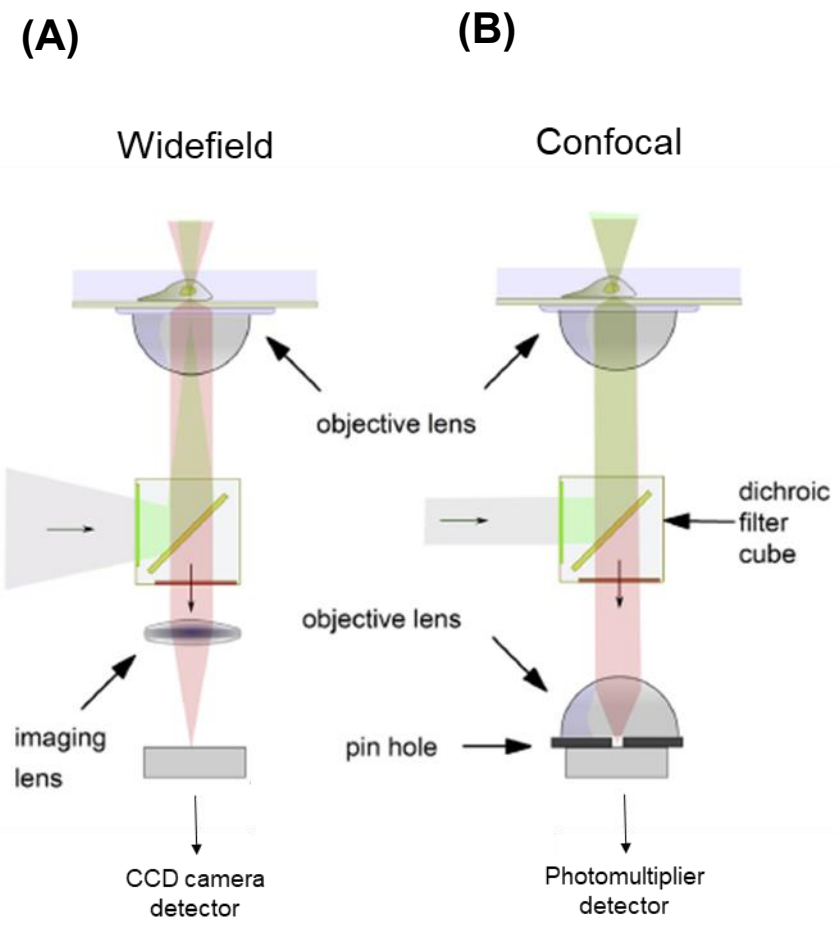

Figure 2.2: Microscopy set up. Diagram showing **(A)** widefield and **(B)** confocal microscopes. Excitation beams are presented in green and emission fluorescence is depicted in red. Adapted from (204).

2.5.2 Immunofluorescence

2.5.2.1 Antibody staining

For the contractility assay, specific compounds were serially diluted 1:10 for treatment prior to immunofluorescence. Following cell treatment, VSMCs cultured on polyacrylamide hydrogels were washed twice with PBS and then fixed with 4% PFA for 10 minutes at RT. After, cells were washed twice more with PBS and membranes were permeabilised with 0.5% NP40 for 3-5 minutes at RT. Cells were then blocked in 3% BSA/PBS, for at least 45 minutes at RT before staining with primary antibody overnight at 4°C. All antibodies were diluted with 3% BSA/PBS, unless otherwise stated, and further details can be found in **Table 2.7**. The following day, cells were washed with 3% BSA/PBS,

and then treated with fluorophore-conjugated secondary antibodies/rhodamine phalloidin for 2 hours at RT in the absence of light. VSMC nuclei were stained with either an anti-lamin A/C antibody or via mounting medium with Diamidino-2-Pheylindoledihydrochloride (DAPI) prior to imaging.

Table 2.7: Details of primary antibodies used within project.

Primary Antibodies	**Dilution**
Mouse monoclonal anti-vinculin antibody (Sigma V4505)	1:200
Rabbit phospho-Myosin Light Chain 2 (Ser19) antibody (Cell Signalling Technology 3671S)	1:100
Mouse monoclonal anti-Lamin A/C antibody (Sigma SAB4200236)	1:200
Rabbit anti-Histone H3 (acetyl K9) antibody (Abcam 4441)	1:200
Phospho-Histone H2A.X (Ser139/Tyr142) antibody (Cell Signalling Technology 5438S)	1:100
53BP1 antibody (Cell Signalling Technology 4937S)	1:100
Rabbit polyclonal Piezo1 antibody (Novus, NBP1-78537)	1:1000
Rabbit monoclonal GAPDH (Cell Signalling Technology 2118)	1:2000

Table 2.8: Details of secondary antibodies used within project.

Secondary Antibodies	**Dilution**
Goat anti-Rabbit IgG (H+L) Highly Cross-Adsorbed Secondary antibody, Alexa Fluor 488 (Invitrogen A-11034)	1:400
Goat anti-Mouse IgG (H+L) Cross-Adsorbed Secondary antibody, Alexa Fluor 488 (Invitrogen A-11001)	1:400
Goat anti-Mouse IgG (H+L) Highly Cross-Adsorbed Secondary antibody, Alexa Fluor 568 (Invitrogen A-11031)	1:400
Rhodamine phalloidin (Life technologies R415)	1:400
Deoxyribonuclease I (DNAse I), Alexa Fluor™ 488 Conjugate (ThermoFisher D12371)	1:1000

2.5.2.2 Plate reader

VSMCs were stained with rhodamine phalloidin and DNAse I Alexa Fluor™ 488 conjugate using the immunofluorescence protocol previously described. After incubating in secondary solution for 2 hours, polyacrylamide gels were washed twice with PBS and transferred to a black-walled 24-wellplate with further PBS to immerse the cells. The fluorescent intensity of both filamentous and monomeric actin was then measured using a CLARIOstar plate reader.

2.5.2.3 Optical sectioning

VSMCs were stained with rhodamine phalloidin and anti-lamin A/C and optical sectioned (z-stack) images were acquired on the Zeiss LSM510-META laser scanning confocal microscope using a 20x 0.75 objective. VSMCs were sectioned by capturing consecutive images (scan speed, 8), whilst alternating the focal plane. Pinhole size was set to optimal for each laser and gain/offset was adjusted accordingly to clearly visualise VSMCs. Unless otherwise stated, z-stacks images presented were captured at 1.4 μm intervals, spanning the entire cell and nuclear structure.

2.5.3 Traction force microscopy (TFM)

2.5.3.1 Principles of TFM

TFM remains the gold standard for assessing cellular traction force amongst a wide variety of techniques. When cells exert traction force (TF)/traction stress (TS), they pull on their extracellular matrix via focal adhesion anchors. Within TFM, cells are seeded on polyacrylamide hydrogels with fluorescent beads embedded, and traction force causes movement of these beads (**Figure 2.3**). This can be tracked using Image J software, revealing important information in ECM compliance and cellular traction force generation.

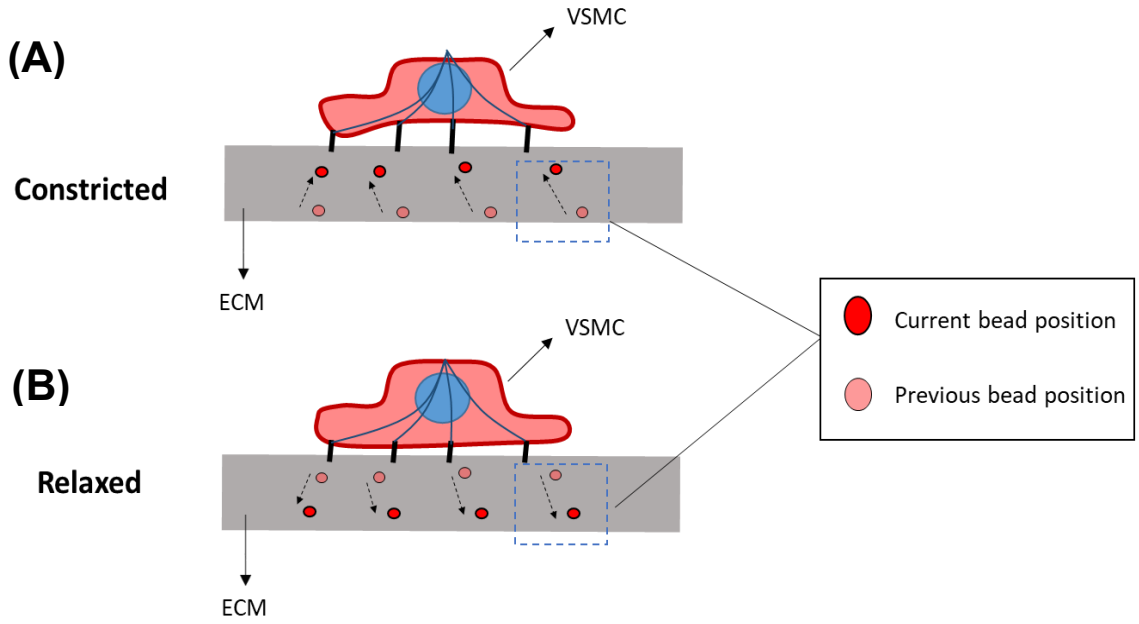

Figure 2.3: TFM fluorescent bead displacement. Diagram showing **(A)** constricted and **(B)** relaxed VSMCs. TFM: Traction force microscopy; VSMCs: Vascular smooth muscle cells.

2.5.3.2 TFM imaging

Imaging was performed using a Zeiss Axiovert 200M widefield microscope, with a live cell imaging system to capture 20x magnification images. VSMCs were grown on polyacrylamide hydrogels overnight and were continually maintained at 37°C with 5% CO_2 during imaging. For experiments using agonist/antagonists, compounds were added 30 minutes prior to cell lysis. Cell lysis was performed on pre-constricted VSMCs via the addition of 0.5% Triton X-100, and images were taken before and after lysis to monitor bead displacement from lysis-mediated relaxation. Each sample was imaged in ~ 8 positions, for a total of 15 cycles with 2-minute intervals.

2.6 Image processing

Within this project, image analysis was performed on Image J or Volocity 6.3, with all exported images saved as TIFF files for processing.

2.6.1 Analysing morphology

2.6.1.1 Cell and nuclear morphology

Within this section, we measured the area and aspect ratio of the cell and nuclei. The aspect ratio is defined by:

(major axis length of approximate ellipse/minor axis length of approximate length)

Therefore, the aspect ratio is equal to 1 when an object is perfectly circular and increases from 1 with augmentations in deformations (when the object becomes elongated). To calculate the area and aspect ratio, VSMCs were stained with rhodamine phalloidin and Image J software was used to manually draw around individual cells using the free hand region of interest (ROI) function. Prior to this, optically sectioned images were processed to display all cells clearly within a single stack (*Image – Stacks – Z project; Projection type = Max intensity*). As images were captured with 20X magnification, scale of images was adjusted accordingly (*Analyse – Set scale; Distance in pixels = 1, Known distance = 0.323*) and measurements were set to obtain required information (*Analyse – Set measurements; Tick Area & Shape descriptors*). With nuclear area and aspect ratio, staining was performed as mentioned before and images captured were converted to an 8-bit format (*Image – Type – 8-bit*), inverted (*Edit – Invert*), with threshold adjusted to ensure clear visibility of nuclei (*Image – Adjust – Threshold*). Each nucleus was then selected with the wand (tracing tool) function and measured. An illustration of nuclear morphology analysis is shown in more detail in **Figure 2.4**. Optically sectioned images were processed to present maximum intensity and scale/measurements were set, as previously described within Image J.

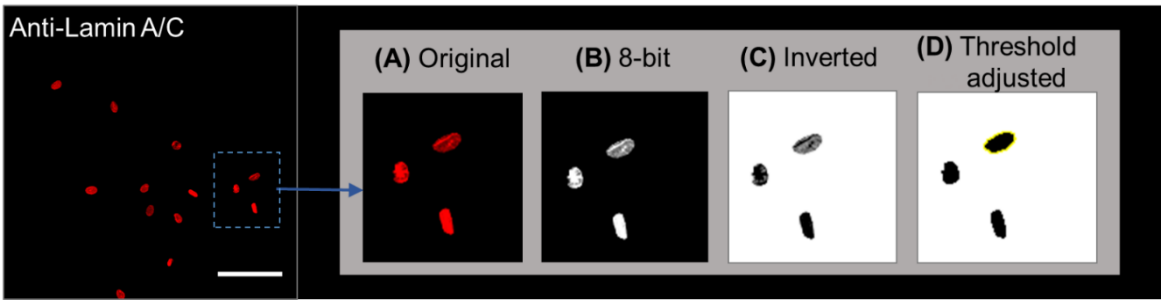

Figure 2.4: Analysis of VSMC nuclear morphology using anti-lamin A/C (red) staining. Image J software was used to perform analysis. Scale bar represents 100 μM. **(A)** Cropped image of VSMC nuclei. **(B)** Image was converted to an 8-bit format and **(C)** inverted to increase contrast. **(D)** Threshold was adjusted to enhance the image and individual nuclei were then selected to measure morphology. VSMC: Vascular smooth muscle cell.

To investigate cell/nuclear height, number of stacks showing visibility of cell/nucleus within optically sectioned images were calculated within Image J and this was multiplied by the stack interval distance (**Figure 2.5**).

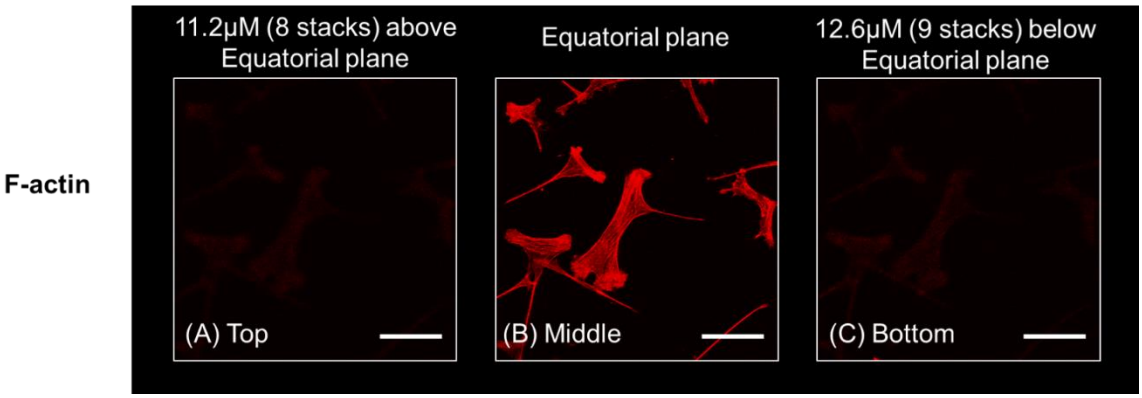

Figure 2.5: Analysis of VSMC height using rhodamine phalloidin (red) staining. Image J software was used to perform analysis. Scale bar represents 100 μM. Images present rotation of equatorial plane from **(A)** the top, **(B)** middle and **(C)** bottom of the cell. Number of stacks between the top and bottom of the cell were calculated and multiplied by stack interval distance to obtain cell height. VSMC: Vascular smooth muscle cell.

For volume analysis, Volocity 6.3 software was used as it measures both cell and nuclear parameters by fluorescence detection. Individual cells were analysed by manually drawing an ROI around their perimeter, which generated the volume. As individual nuclei were not physically touching, measurements were automated, presenting the corresponding list of nuclear volumes for each image.

2.6.1.2 Vinculin morphology

Anti-vinculin was used to measure focal adhesion morphology within Image J. To do this, vinculin-stained images were converted to an 8-bit format, inverted, and threshold was adjusted to ensure clear visibility of focal adhesions, as previously described in section 2.6.1.1 for nuclear morphology. Additionally, scale and measurements were set identically to before. The free-hand ROI function was then used to draw around individual cells and focal adhesion morphology was then analysed for selected cells (*Analyse – Analyse particles; Size = 0.20-7.01, Show = Masks, Tick Display results, Exclude on edges & Include holes*) (**Figure 2.6**).

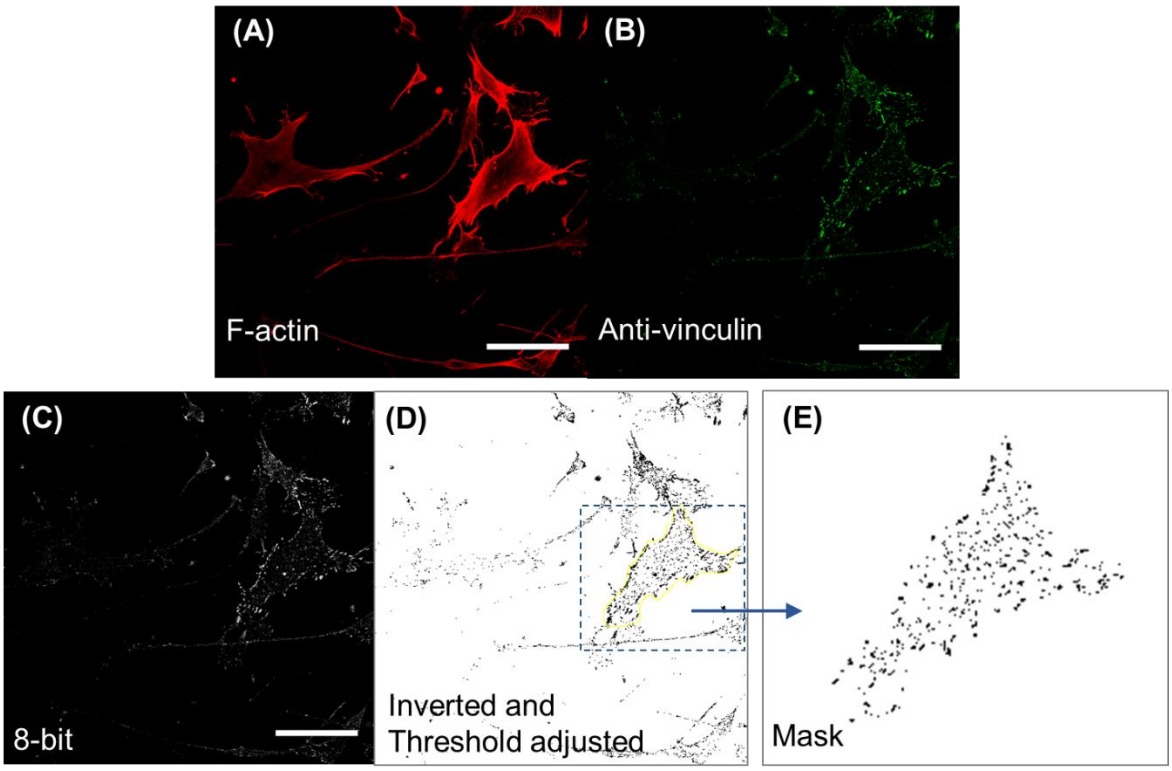

Figure 2.6: Analysis of VSMC focal adhesions. Image J software was used to perform analysis. Scale bar represents 100 µM. Representative images show **(A)** VSMC actin filaments (F-actin) and **(B)** focal adhesions stained using rhodamine phalloidin and anti-vinculin, respectively. **(C)** Anti-vinculin image was converted to an 8-bit format and **(D)** inverted with threshold adjusted to increase contrast. **(E)** Shows mask that is generated when measuring focal adhesions within an individual cell. VSMC: Vascular smooth muscle cell.

2.6.2 DNA damage

Our studies utilised anti-H2AX and anti-53BP1 antibodies to investigate DNA damage within VSMCs. Image J software was used to assess DNA damage foci size and

number, this was done via the following steps. Images were converted to an 8-bit format, inverted, and threshold was adjusted to clearly visualise foci, as described previously in section 2.6.1.1 for nuclear morphology. Scale was set identically to before and measurements were adjusted accordingly (*Analyse – Set measurements; Tick Area*). Corresponding anti-lamin A/C image was used to indicate where foci for individual nuclei resided, and this was done by generating an overlay on top of the DNA damage-stained window (*Image – Overlay – Add Image; Opacity = 50%*). Using the freehand ROI function, individual nuclei were manually drawn around and foci were then analysed with the *"*Analyse particles" function, using identical settings established previously in section 2.6.1.2 (**Figure 2.7**).

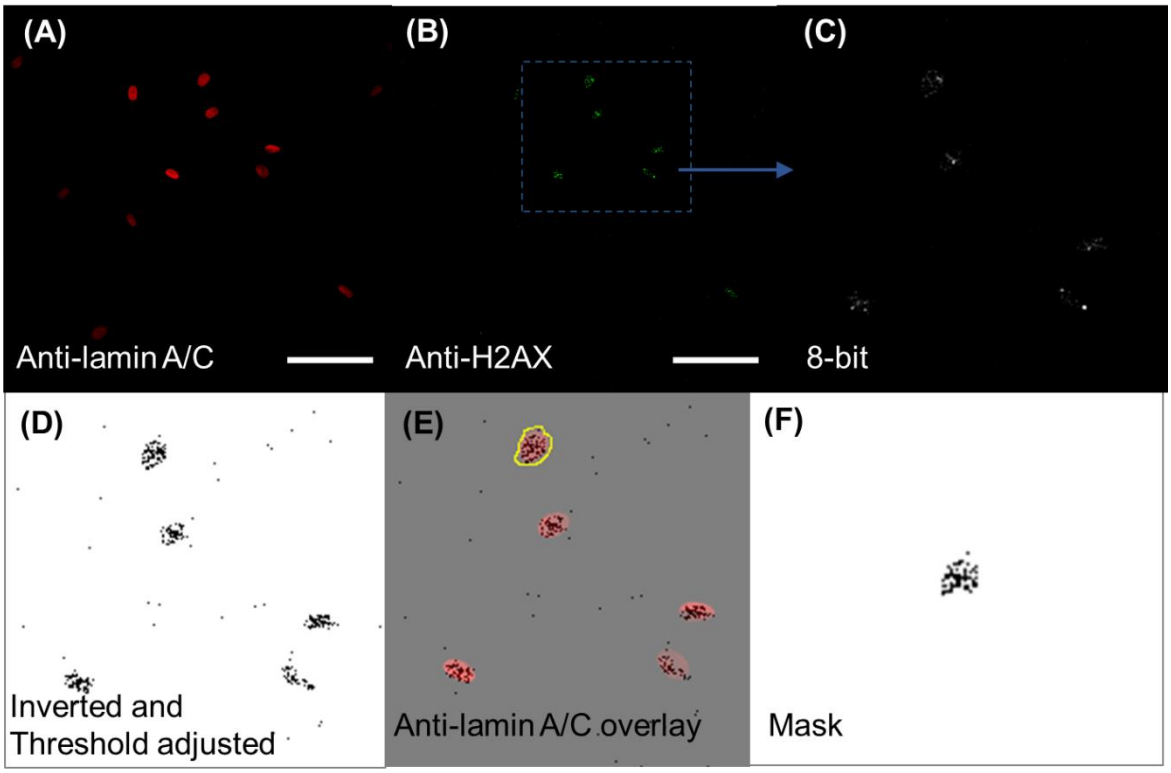

Figure 2.7: Analysis of VSMC DNA damage foci. Image J software was used to perform analysis. Scale bar represents 100 µM. Representative images show **(A)** VSMC nuclei and **(B)** H2AX foci stained using anti-lamin A/C and anti-H2AX, respectively. **(C)** Anti-H2AX image was converted to an 8-bit format and **(D)** inverted with threshold adjusted to increase contrast. **(E)** Shows overlay with anti-lamin A/C image and **(F)** presents mask that is generated when measuring H2AX foci within an individual cell. VSMC: Vascular smooth muscle cell.

2.6.3 Actin alignment

Rhodamine phalloidin was used to assess VSMC F-actin alignment. If optically sectioned, the image file was processed to present maximum intensity, as previously described in section 2.6.1.1 for cell morphology. Following this, the Orientation J Plugin was used to measure actin alignment (*Plugins – OrientationJ – OrientationJ Measure*). Using the freehand ROI function, the cell perimeter was manually drawn around and used to generate the corresponding coherence value of the actin filaments. Visual representation of F-actin alignment is also shown via the Plugin (*Plugins – OrientationJ – OrientationJ Analysis*) (**Figure 2.8**).

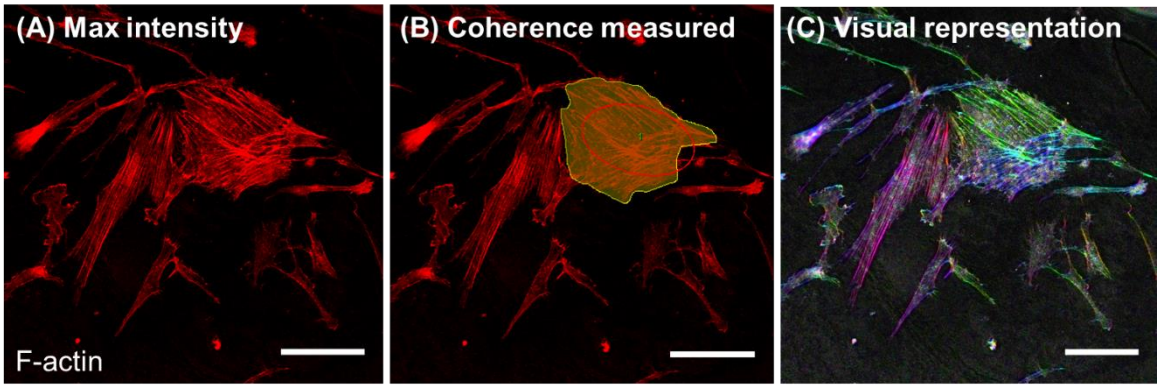

Figure 2.8: Analysis of VSMC F-actin alignment. Image J software was used to perform analysis. Scale bar represents 100 μM. Representative images show **(A)** VSMC F-actin stained using rhodamine phalloidin. **(B)** ROI drawn around single VSMC to measure F-actin alignment (Orientation J measure Plugin). **(C)** Visual representation of F-actin alignment (Orientation J analysis Plugin). VSMC: Vascular smooth muscle cell.

2.6.4 Mean and total fluorescent intensity

The mean fluorescent intensity of both pMLC and epigenetic experiments were calculated using Image J software. The freehand ROI function was used to manually draw around individual cells/nuclei and scale was set as mentioned before in section 2.6.1.1. Importantly, measurements were adjusted to be able to generate the mean fluorescent intensity (*Analyse – Set measurements; Tick Area & Mean gray value*). Following this, total fluorescent intensity was calculated by taking the mean value and multiplying by the cell/nuclear area.

2.6.5 TFM analysis

2.6.5.1 Bead displacement

The drift within the movie sequence of beads was corrected by using the StackReg Plugin on Image J (*Plugins – StackReg; Transformation = Rigid body*). Measurements of bead displacement were then performed using the first and last image of the stacks collected. Using the PIV Plugin, we obtained the displacement field from the bead images (*Plugins – iterative PIV (Basic); Remove 3rd pass parameters*). Once obtained, the plot function of the PIV Plugin was used to visualise the displacement field and a phase image was overlaid on top. **Figure 2.9A**). The freehand ROI function was used to manually draw around the displacement field of each cell, with displacement data saved as an Excel file (*Analyse – Tools – Save XY Coordinates*). The sum total of the displacement dataset was then calculated to obtain the integrated displacement generated from each cell.

2.6.5.2 Traction stress and force

Traction stress uses Pascals (Pa), the standard unit of pressure, to quantify the stress placed onto a material. To analyse traction stress, the FTTC Plugin was utilised to reconstruct the heat map from the displacement data file (*Plugins – FTTC – FTTC; Adjust Young's modulus of the gel (in Pascal*). Generated data was then visualised as its own heat map, via the plot function of the FTTC Plugin, and the corresponding phase image was overlaid (**Figure 2.9B**). Traction stress of each cell was then obtained in the same manner as displacement data. The dataset was sorted from largest to smallest within the Excel file to obtain the total and maximum traction stress of every cell.

Traction force uses Newtons as its standard unit of measurement, and it is directly related to pressure (Pa) as shown via the equation below. Our project derives integrated traction force from total traction stress and the area of the traction stress heat map (spread of traction stress) produced by the cell. The following equation: *(kPa = N/m^2)* was rearranged to calculate integrated traction force:

Integrated traction force (μN):

*[Heat map area (μm^2) * Total traction stress (Pa)] * 10^{-9}*.

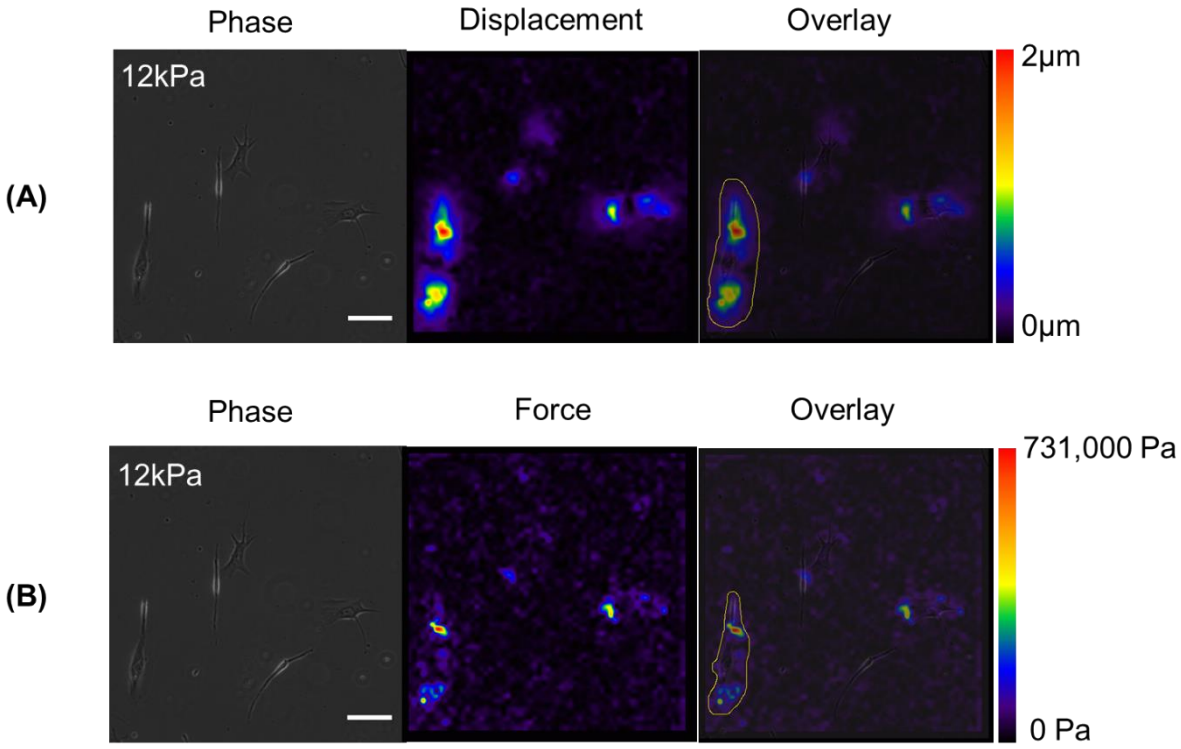

Figure 2.9: Analysis of TFM. Image J software was used to perform analysis. Scale bar in phase image represents 100 µM. Representative images show **(A)** displacement field with phase image overlay. **(B)** Force field with phase image overlay. TFM: Traction force microscopy.

2.6.5.3 Calculated traction stress/force formulas

Our TFM model was developed by plotting VSMC area against integrated-TS/TF. The gradient of the graphs was calculated and the resulting formula of each cell line was tested and further refined by compiling both groups of isolate data.

Isolate 1:

Calculated Integrated-TS (Equation 1A) = 2665.7(cell area) + 2000000

Calculated Integrated-TF (Equation 1B) = 0.0748(cell area) – 88.001

Isolate 2:

Calculated Integrated-TS (Equation 2A) = 2685.4(cell area) + 887197

Calculated Integrated-TF (Equation 2B) = 0.066(cell area) – 55.784

Refined:

Calculated Integrated-TS (Equation 3A) = 2683.7(cell area) + 1000000

Calculated Integrated-TF (Equation 3B) = 0.0663(cell area) – 57.384

2.7 Statistical analysis

To determine statistical significance between two groups of data, a paired Students t-test was performed. For comparison between multiple groups, results were subjected to a one-way/two-way ANOVA, followed by a post-hoc Bonferroni's multiple comparison test. Trend line differences were investigated via a linear regression analysis and EC50 values of sigmoidal dose curves were derived through non-linear regression analysis. All statistical analysis was performed using GraphPad Prism 5. Error bars represent the standard error of the mean (SEM), with bar charts displaying the mean value. P values are represented as followed: (* p = <0.05), (** p = <0.001) and (*** p = <0.0001).

Chapter 3: Characterising the impact of matrix stiffness on synthetic VSMC morphology and traction force

3.1 Introduction

Decreased vascular compliance is a risk factor in the development of cardiovascular disease, including atherosclerosis and hypertension (205, 206). Previously, rodent models of hypertension have presented a 4-fold increase in aortic stiffness compared to age matched controls (207). However, our understanding of the mechanisms contributing to decreased vascular compliance and its resulting impact on cell function remains limited. VSMCs are the predominant cell type within the medial layer of the arterial wall and normally exist in a quiescent, contractile phenotype, where they maintain vascular tone via actomyosin-derived contractile forces (208). However, VSMCs present high plasticity and can undergo a transition to a synthetic, migratory phenotype commonly found in CVDs, such as atherosclerosis and diabetes (37, 38). Previous work conducted in our laboratory investigated synthetic VSMC morphology and traction stress changes. These studies demonstrate the effect of nuclear envelope proteins on VSMC structure and function (207). However, the effect of matrix stiffness and the employment of materials that fully mimic the physiological/pathological rigidities of VSMCs have yet to be described.

Emerging evidence has illustrated that Rho/ROCK activation is prevalent at ECM adhesions in response to matrix stiffness. This signalling increases actomyosin activity via actin polymerisation and myosin light chain phosphorylation (209). VSMCs apply force to the ECM, termed integrated-traction force, and this is augmented via actin cytoskeletal reorganisation and enhanced actomyosin activity. Recent studies have shown matrix stiffness promotes enhanced adhesion and actomyosin activity, to strengthen traction force in other cell types (210-213). Our knowledge of the balance and regulation between actomyosin activity, traction force magnitude and adhesion organisation in response to matrix stiffness within VSMCs requires further investigation. In this chapter, we investigate the impact of matrix stiffness on synthetic VSMC traction force generation and the underlying changes that drive this.

3.2 Aim of this chapter

This chapter aims to investigate the impact of enhanced matrix stiffness on VSMC organisation and traction force generation. Within this chapter, we will study the relationship between synthetic VSMC spreading and traction force generation. Additionally, we will observe how the contractile machinery and focal adhesion organisation responds to matrix rigidity in order to better define the relationship between these factors.

3.3 Hypothesis

We hypothesise that enhanced matrix stiffness will alter VSMC morphology, focal adhesion organisation and contractile machinery structure. We believe that the changes observed will facilitate a higher traction force generation within the stiffer environment, and our work will identify novel mechanisms that will allow this.

3.4 Results

3.4.1 Optimisation of polyacrylamide hydrogel fabrication

To model a representative physiological and pathological stiffness of the aorta, we first optimised the fabrication of polyacrylamide hydrogels of 2 (soft), 12 (physiological) and 72 kPa (pathological) stiffness. This process involved comparing 3 different fabrication methods. ***Method 1*** consisted of gel fabrication directly into a well plate followed by isopropanol treatment to ensure an even surface. However, as shown by *Method 1* of (**Figure 3.1A**), this resulted in a white precipitate indicating unsuccessful formation. The reason for this is because it would interfere with the downstream microscopy later within the protocol when we stained our seeded cells. Next, in ***Method 2***, we aimed to reduce precipitant formation by activating coverslips with APES followed by fixation with glutaraldehyde. These activated coverslips were transferred to a fresh multiwell plate. Gel fabrication was performed directly on top of the coverslips within the well plate. This resulted in a thin layer of gel with minimal precipitation formation as shown by ***Method 2*** of (**Figure 3.1A**).

However, measurement of the focal heights of these gels using a CLARIOstar plate reader showed large variation between the focal planes (**Figure 3.1B**). Despite being non-significant, further work was performed to minimise this variation. The reason for this was because the variation in the focal heights may have affected the fluorescence emitted during the plate reader assay. Additionally, the thickness of the gel is crucial in determining its mechanical properties, and as a result, we wanted to ensure the focal heights remained consistent between experiments.

Gel fabrication was then performed using a glass slide and the activated adhesive coverslip was placed directly on the gel solution. In this case, a glass slide was used as it would ensure an even surface for the polyacrylamide gels to form against. The gels formed from ***Method 3*** were fuller in appearance (**Figure 3.1A**) and measurement of the focal planes showed much less variation (**Figure 3.1B**). Once optimised, these polyacrylamide hydrogels were utilised for experiments performed within the remainder of the research project.

(A)

2kPa 12kPa 72kPa

Method 1 – Gels were found to form a white precipitate.

Method 2 – A light layer of the gel seemed to form on the untreated coverslip

Method 3 – Full gels formed on the treated coverslips.

(B)

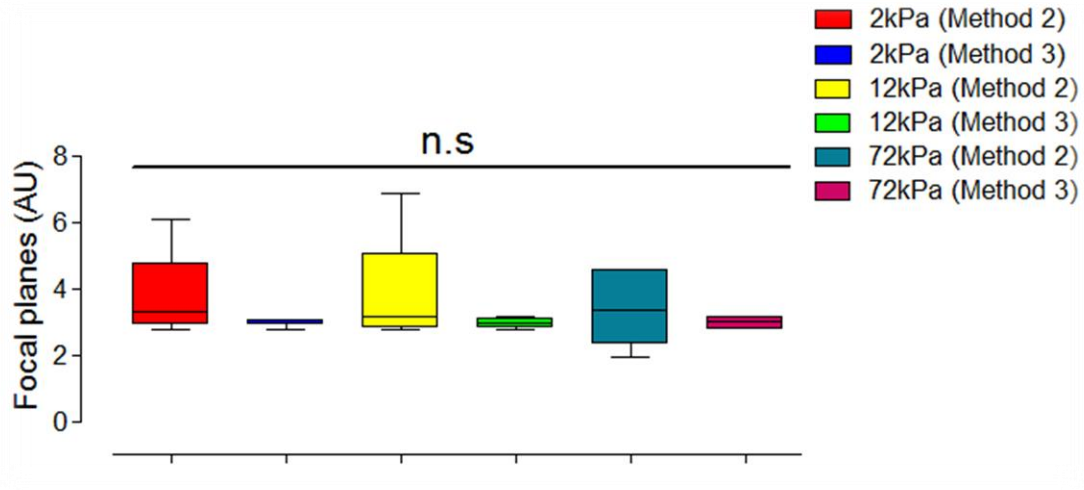

Figure 3.1: Optimisation of polyacrylamide hydrogel fabrication. (A) Representative images of polyacrylamide hydrogel fabrication under different conditions. CLARIOstar plate reader was used to measure **(B)** the focal planes of polyacrylamide hydrogels from second and third method. Data is based on 6 polyacrylamide hydrogels fabricated from 6 independent experiments. Statistical significance was determined using a one-way ANOVA to show differences in focal planes with varying stiffness (non-significant; p = >0.05), followed by a Bonferroni's multiple comparison test.

3.4.2 Effect of matrix stiffness on cell morphology and actin cytoskeleton organisation

We set out to validate previous findings showing that matrix stiffness induces cell spreading (214, 215). VSMCs were seeded on collagen-1 coated polyacrylamide hydrogels, with an average Young's modulus of 2 (soft), 12 (physiological) and 72 kPa (pathological). To maintain them in the synthetic phenotype, VSMCs were grown in the presence of high serum. F-actin staining with rhodamine phalloidin was performed on VSMCs prior to immunofluorescence microscopy. In agreement with prior research, VSMCs possessed significantly larger cell areas on the 72 kPa polyacrylamide hydrogel (2710±157.6 μM) than on 2 (1869±151.1 μM) or 12kPa (1846±1294 μM) matrices (**Figure 3.2A & B**). Subsequent analysis using Image J software revealed the stiffer environment showed no impact on cell aspect ratio (**Figure 3.2A & C**).

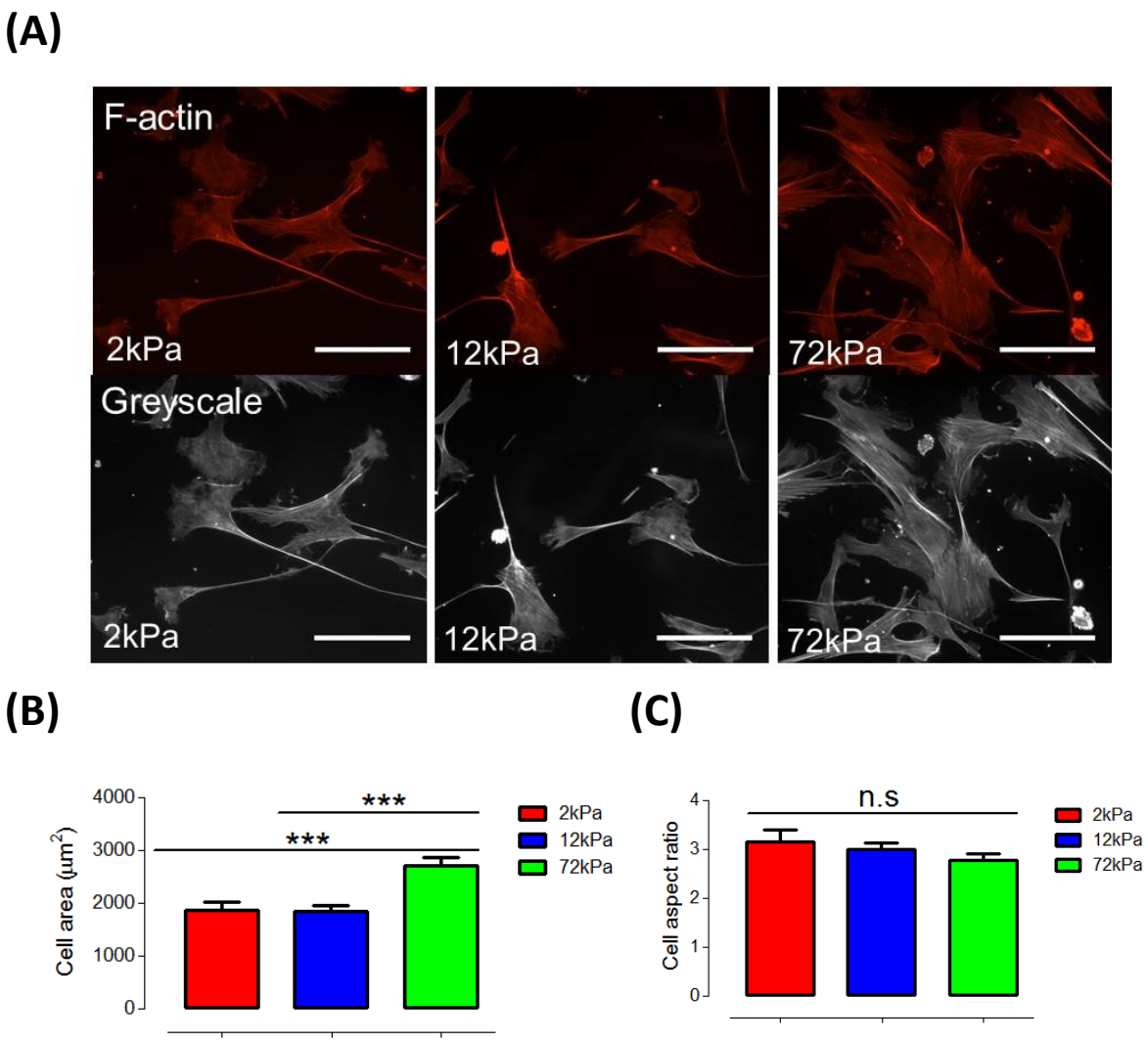

Figure 3.2: The impact of matrix stiffness on VSMC morphology. (A) Representative immunofluorescence images showing VSMC actin filaments (F-actin) stained using rhodamine phalloidin (red) and grey-scale images of F-actin (grey) on 2 kPa, 12 kPa and 72 kPa polyacrylamide hydrogels. Scale bar represents 100 μm. Image J software was used to manually measure the **(B)** cell area and **(C)** cell aspect ratio of the VSMCs. Data are based on the measurement of >150 VSMCs from 3 independent experiments. Statistical significance was determined using a one-way ANOVA to show differences in cell area (*** p = <0.0001) and cell aspect ratio (non-significant; p = >0.05) with varying stiffness, followed by a Bonferroni's multiple comparison test. VSMC: Vascular smooth muscle cell.

As the actin cytoskeleton defines cell morphology, we speculated that F-actin organisation would present alterations in response to matrix stiffness. VSMC filamentous and monomeric/globular actin were stained with rhodamine phalloidin and FITC conjugated DNAse I, respectively. Fluorescent intensity was then measured using a CLARIOstar plate reader (**Figure 3.3A**) and this revealed a significant increase in the F/G actin ratio when

seeded on the 72kPa polyacrylamide hydrogel (2.165±0.4083) compared to 2kPa (0.866±0.1546) or 12kPa (1.614±0.2258) gels. Therefore, matrix stiffness increases levels of filamentous actin.

Previous work has shown ECM stiffness augmentation can cause a corresponding increase in actin filament alignment of fibroblast cells (216). Based on this evidence, we next investigated to see if filamentous actin alignment of VSMC show any change in response to matrix rigidity. VSMCs were cultured for 24 hr and 72 hrs and then stained with rhodamine phalloidin prior to immunofluorescence microscopy. Using Image J software, F-actin alignment of VSMCs on the 72 kPa polyacrylamide hydrogel were also found significantly higher at 24hrs (0.599±0.0232) and 72hrs (0.564±0.0441) when comparing to 2kPa (24hrs: 0.377±0.0339; 72hrs: 0.379±0.0475) and 12kPa (24hrs: 0.508±0.0319; 72hrs: 0.543±0.0484) once more (**Figure 3.3B & C**). Comparison of 24hr and 72hr time points revealed no difference in F-actin alignment for VSMCs seeded on 2, 12 or 72kPa polyacrylamide hydrogels (**Figure 3.3D**).

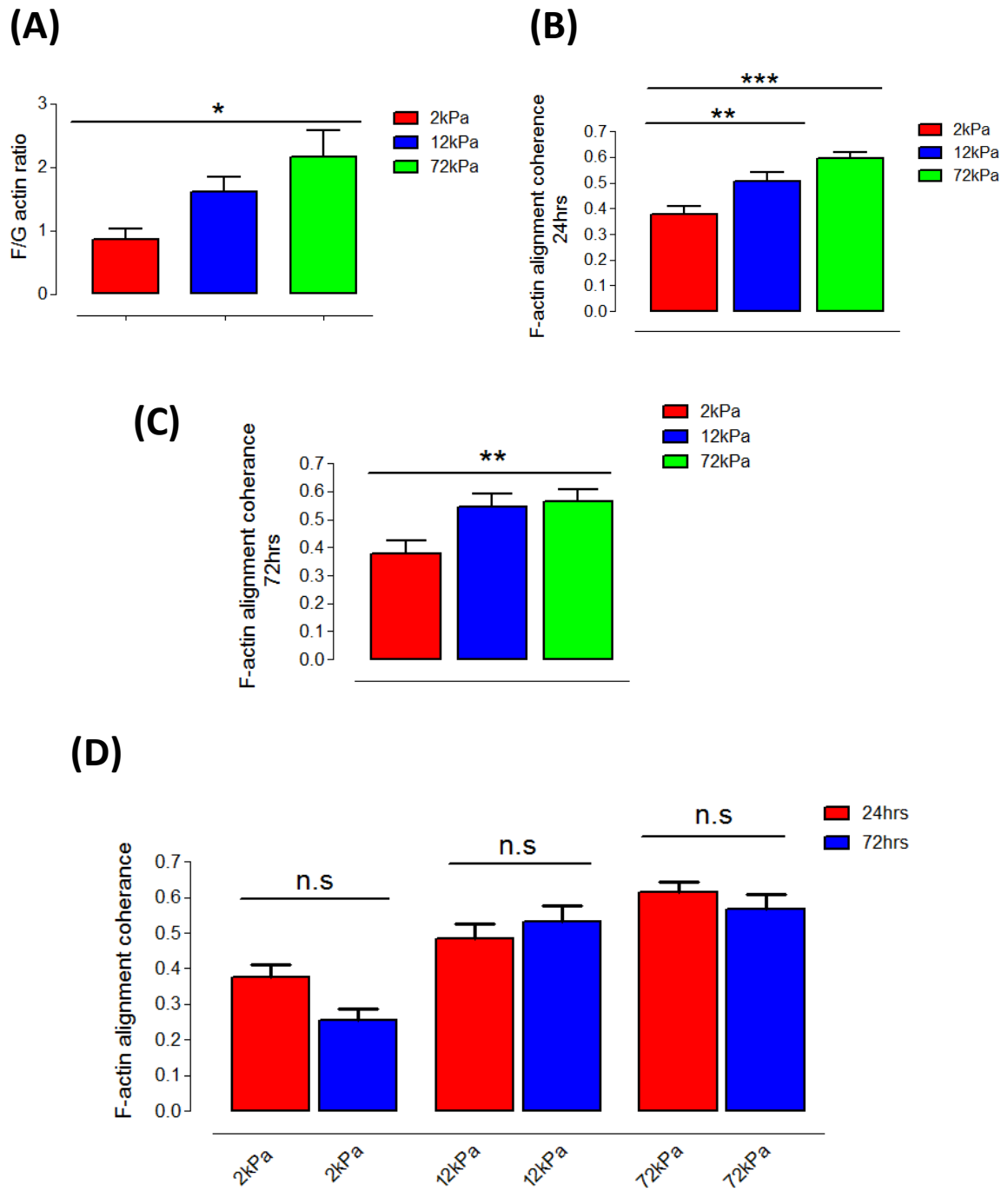

Figure 3.3: Actin organisation of VSMCs in response to matrix stiffness. CLARIOstar plate reader was used to measure the ratio between **(A)** filamentous and globular actin of VSMCs, stained with rhodamine phalloidin and DNAse I respectively. Data are based on the measurements of ~35 polyacrylamide hydrogels from 6 independent experiments. Image J software was used to manually measure the filamentous actin alignment at **(B)** 24 hours, **(C)** 72 hours and **(D)** a comparison of both time points is shown. Data, in this case, are based on the measurement of >50-100 VSMCs from 2 independent experiments. Statistical significance was determined using a one-way ANOVA to show differences in F/G actin ratio (* p = <0.05) and actin alignment at 24 hours (** p = <0.001, *** p = <0.0001) and 72 hours (** p = <0.001), followed by a Bonferroni's multiple comparison test. Additionally, a paired Student's t test was performed (24 hours vs 72 hours) (non-significant; p = >0.05). VSMC: Vascular smooth muscle cell.

3.4.3 VSMC nuclear morphology alterations caused from matrix stiffness

Prior research performed within our laboratory has shown that ageing promotes VSMC nuclear morphology defects (217). As arterial stiffness is a predicative biomarker of ageing as well as CVD (10), we next hypothesised that nuclear morphology would show significant changes in response to matrix stiffness. To test this, nuclei from VSMCs were stained with DAPI and immunofluorescence microscopy was used to determine the nuclear changes associated with matrix rigidity (**Figure 3.4A**). Image J software measured nuclear parameters to reveal VSMC nuclei area were significantly larger on the 72 kPa matrix as opposed to 2 or 12 kPa polyacrylamide hydrogels (**Figure 3.4A** & **B**). In addition, nuclear aspect ratio was also shown to be significantly smaller in cells cultured on a 12 kPa substrate compared to those on a 72 kPa substrate, meaning VSMC nuclei become more rounded as substrate stiffness increases. Analysis of the nuclear/cell area ratio revealed that, on 72 kPa hydrogels, VSMCs show a significantly lower value than 2 kPa counterparts (**Figure 3.4C**). This suggests that stiffness has a greater influence on spreading of the cytoplasm than on the nucleus.

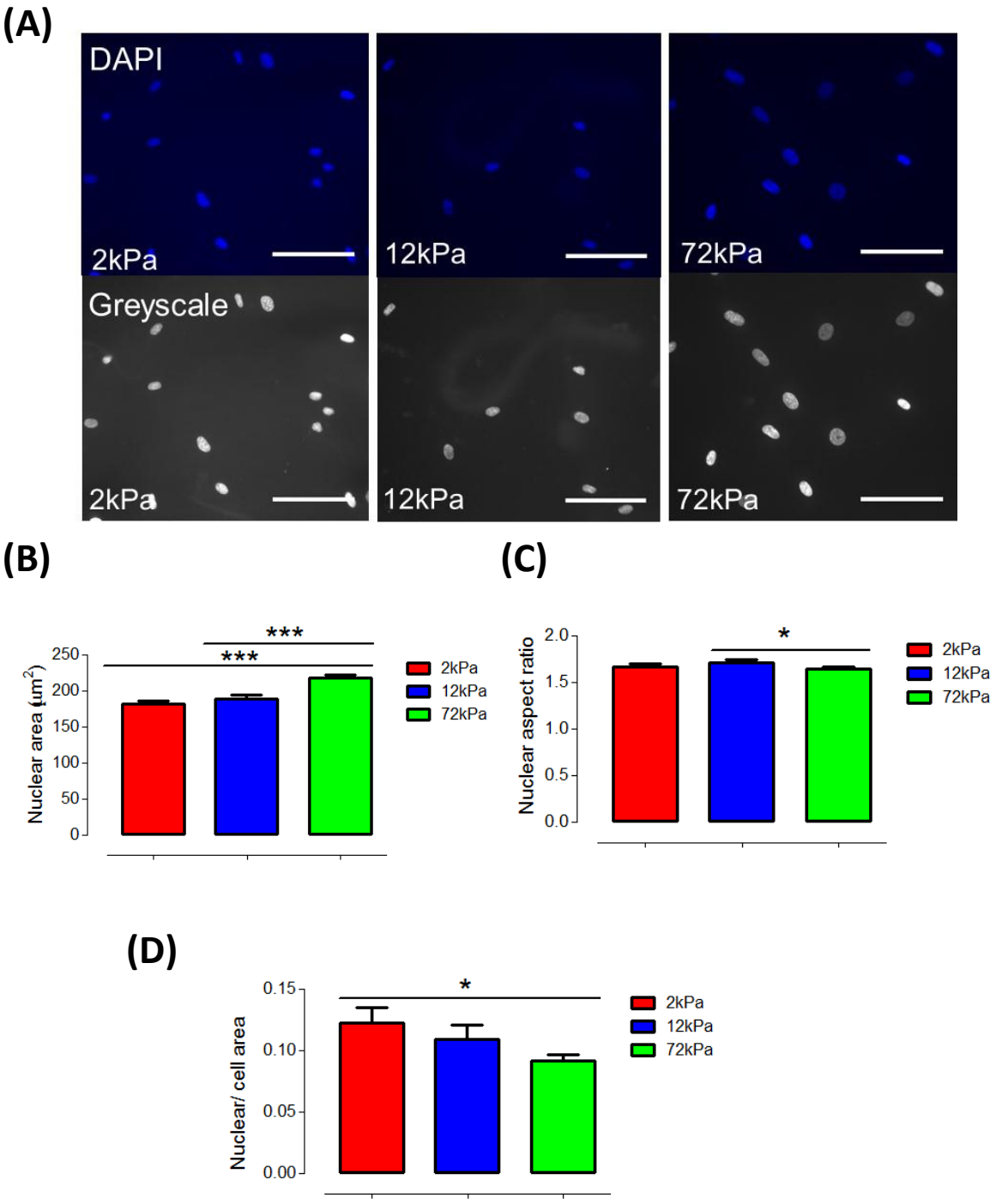

Figure 3.4: The impact of matrix stiffness on VSMC nuclear morphology. (A) Representative immunofluorescence images showing VSMC nuclei stained using DAPI (blue) and grey-scale images of nuclei (grey) on 2 kPa, 12 kPa and 72 kPa polyacrylamide hydrogels. Scale bar represents 100 μm. Image J software was used to manually measure the **(B)** nuclear area and **(C)** aspect ratio of the VSMCs. **(D)** shows the ratio between nuclear area and cell area. Data are based on the measurement of >150 VSMCs from 3 independent experiments. Statistical significance was determined using a one-way ANOVA to show differences in nuclear area (*** p = <0.0001), nuclear aspect ratio (* p = <0.05) and nuclear to cell area ratio (* p = <0.05) with varying stiffness, followed by a Bonferroni's multiple comparison test. VSMC: Vascular smooth muscle cell.

3.4.4 Matrix stiffness-induced changes in VSMC phosphorylated myosin light chain levels

The actin cytoskeleton associates with phosphorylated myosin light chain (pMLC) to form the actomyosin complex. This allows the ATPase activity of myosin to pull the actin thin filaments resulting in contraction (80). Levels of pMLC is an independent marker of actomyosin activity. Based on our previous findings, we expected to see an increase in pMLC intensity as a result of matrix stiffness. VSMCs were grown on collagen-1 coated polyacrylamide hydrogels, with an average Young's modulus of 2 (soft), 12 (physiological) and 72 kPa (pathological). PMLC was stained with anti-pMLC and immunofluorescence microscopy was then performed. However, analysis revealed that pMLC mean intensity showed significant decreases as matrix rigidity increased (**Figure 3.5A** & **B**).

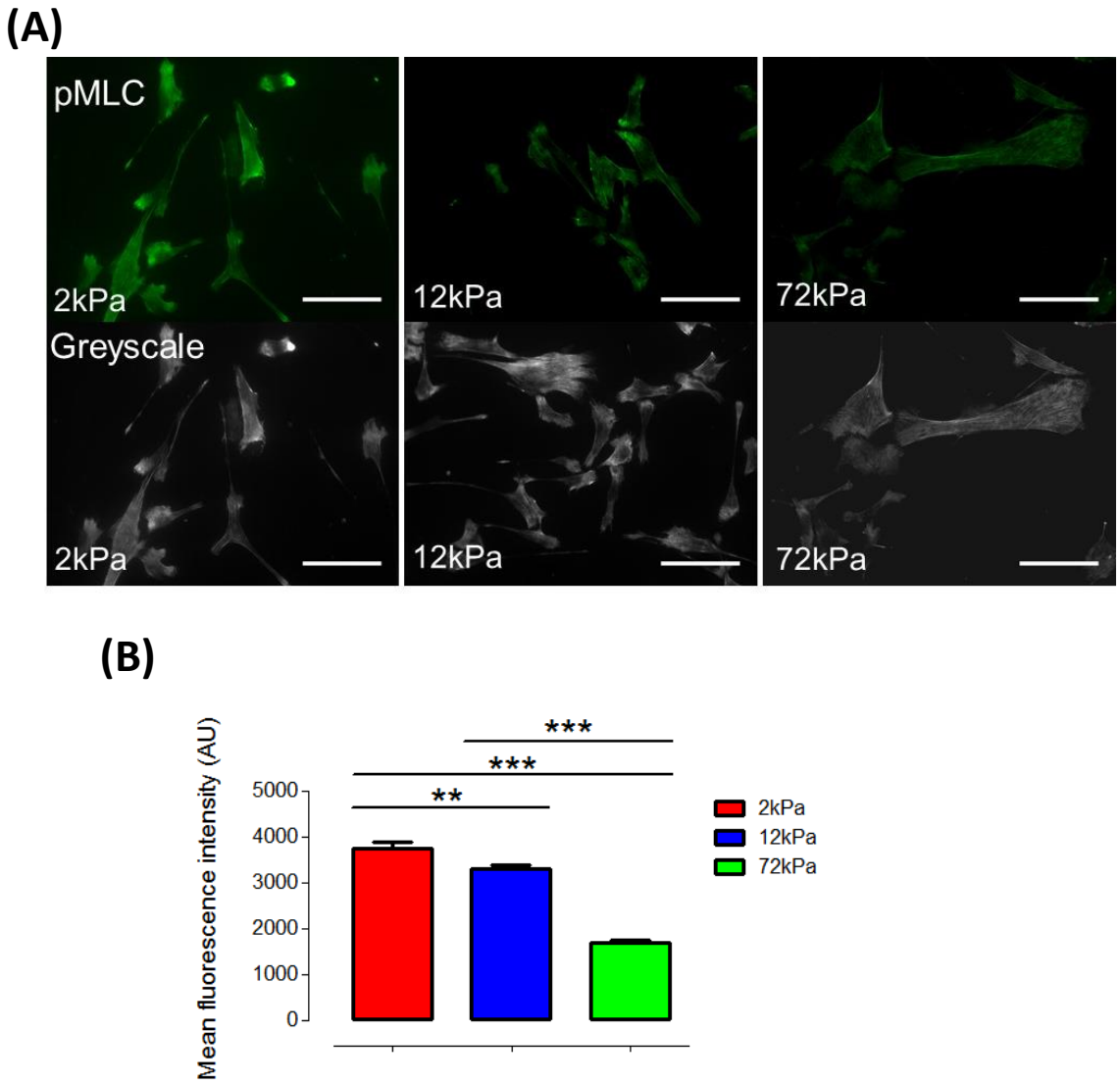

Figure 3.5: Matrix stiffness causes a decrease in VSMC mean pMLC levels. (A) Representative immunofluorescence images showing VSMC phosphorylated myosin light chain stained with anti-pMLC (green) and grey-scale images of phosphorylated myosin light chain (grey) on 2 kPa, 12 kPa and 72 kPa polyacrylamide hydrogels. Scale bar represents 100 µm. Image J software was used to manually measure the **(B)** mean pMLC fluorescent intensity. Data represent the measurement of ~100 VSMCs from 3 independent experiments. Statistical significance was determined using a one-way ANOVA for pMLC mean intensity (** p = <0.001, *** p = <0.0001) in response to matrix stiffness, followed by a Bonferroni's multiple comparison test. pMLC: Phosphorylated myosin light chain; VSMC: Vascular smooth muscle cell.

Following from this, our subsequent analysis pre-dominantly looked at the 12 kPa and 72 kPa responses as our primary focus were on the changes observed as the aorta became stiffer from the physiological rigidity. In contrast to our results shown in the mean pMLC intensity (**Figure 3.5A & B**), subsequent analysis showed levels of total pMLC levels remained unchanged between 12 kPa (physiological) and 72 kPa (pathological) polyacrylamide hydrogels (**Figure 3.6A**). Further investigation confirmed VSMC spreading strongly correlated with total pMLC intensity with both 12 kPa (R^2 = 0.87) and 72 kPa (R^2 = 0.94) stiffness (**Figure 3.6B** & **C**) and compiled data is shown (**Figure 3.6D**). This indicated that total pMLC intensity increases with augmentations in VSMC spreading.

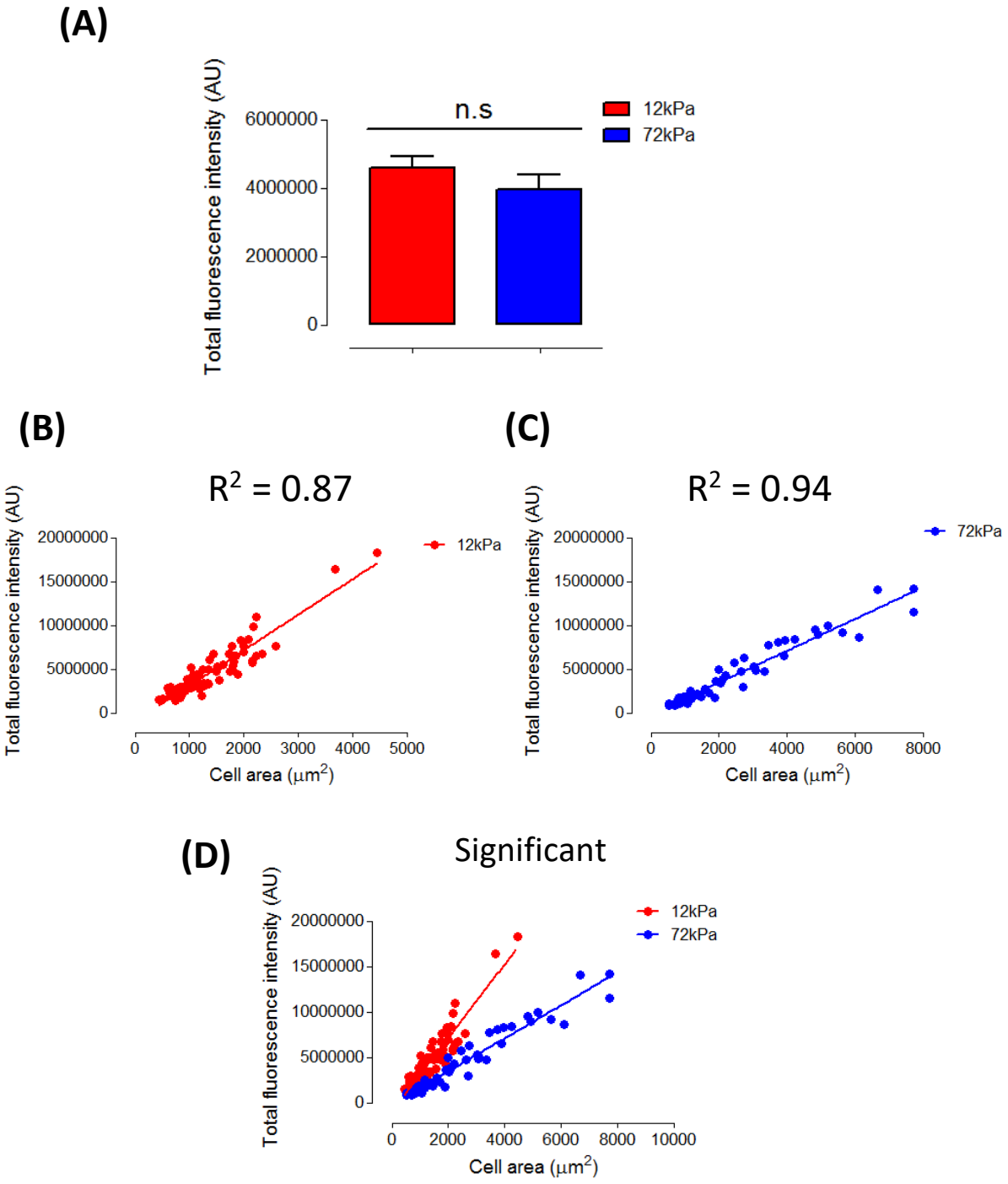

Figure 3.6: Relationship between VSMC cell area and total pMLC levels. Image J software was used to manually measure the **(A)** total pMLC fluorescent intensity of VSMCs on 12 kPa and 72 kPa polyacrylamide hydrogels. Additionally, it was used to manually measure VSMC cell area and the relationship between cell area and total fluorescent intensity is shown for **(B)** 12 kPa, **(C)** 72 kPa as well as **(D)** an overlay of both. Data represent the measurement of ~100 VSMCs from 3 independent experiments. Statistical significance was determined using a paired Student's *t* test for the total fluorescent intensity (12 kPa vs 72 kPa) (non-significant; p = >0.05) as well as a linear regression analysis for the relationship between cell area and total pMLC fluorescent intensity (*** p = <0.0001). pMLC: Phosphorylated myosin light chain; VSMC: Vascular smooth muscle cell.

3.4.5 The relationship between VSMC traction force and cell area

After observing no change in total pMLC intensity via matrix stiffness (**Figure 3.6A**), we next investigated the impact of matrix stiffness on VSMC traction force generation. Traction force of VSMCs facilitates mechanotransduction via mechanical sensing of the external environment. This causes downstream regulation of focal adhesion dynamics and of the actin cytoskeleton structure (69). Existing work has shown that increased stiffness causes a corresponding augmentation in cellular traction force (218, 219). To confirm these findings, we performed TFM on VSMCs that were grown on collagen-1 coated polyacrylamide hydrogels, with an average Young's modulus of 12 (healthy) and 72 kPa (stiff). Our study employed two isolates of VSMCs for the TFM work performed and therefore these will either be referred to as "isolate-1" or "isolate-2" within this chapter.

The ability of isolate-1 VSMCs to displace fluorescent beads embedded within the polyacrylamide hydrogels was reduced on 72 kPa compared to 12 kPa hydrogels (**Figure 3.7A** + **B**). However, maximum and integrated traction stress was observed to be higher on the 72 kPa hydrogel (**Figure 3.7C** +**D**). Next, we looked at the traction force by normalising the area of traction stress distribution. The resulting traction force calculated was also shown to be significantly higher on the stiffer gel (**Figure 3.7E**). These data confirm previous findings that matrix rigidity influences VSMC traction force (218, 219).

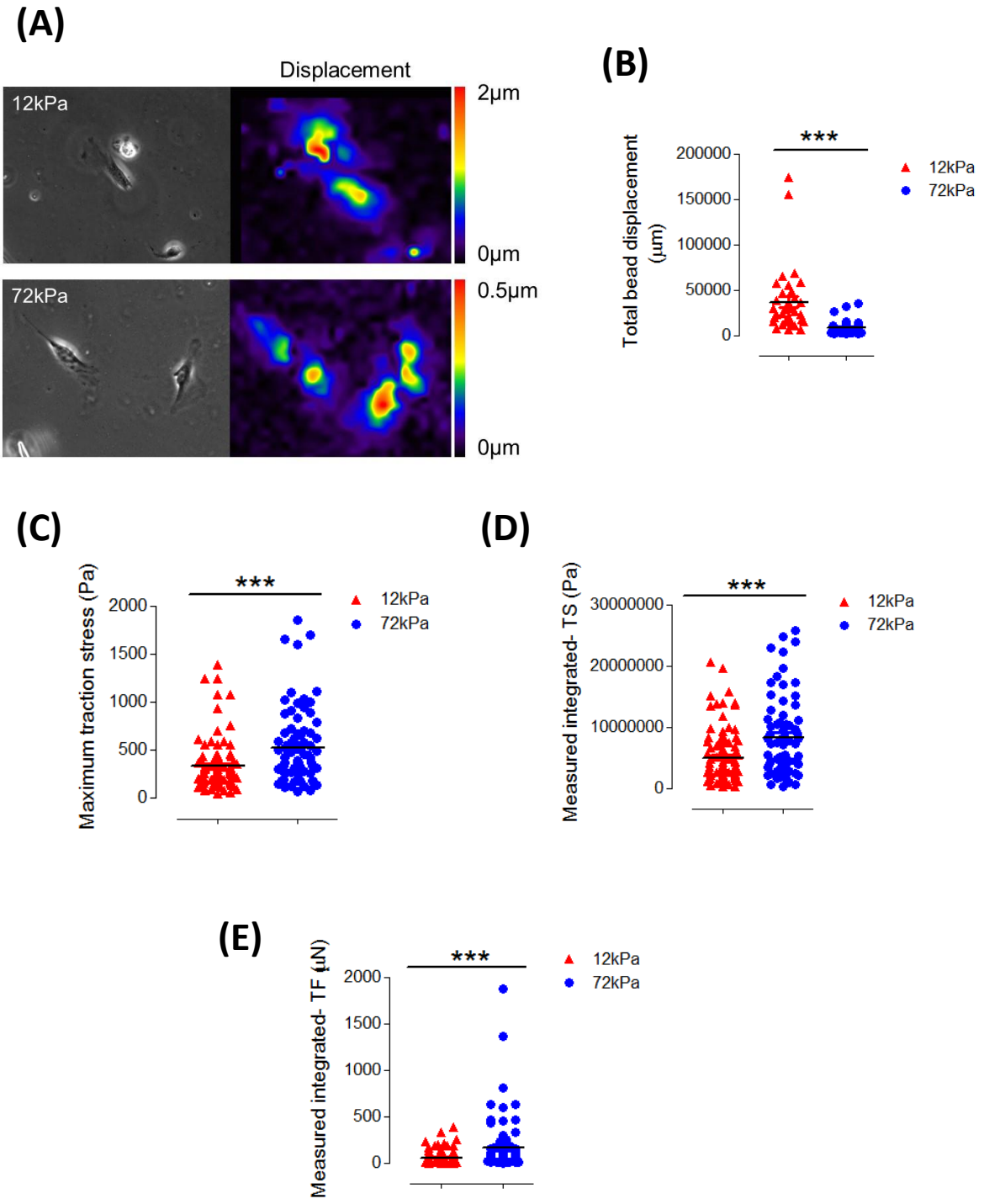

Figure 3.7: Matrix rigidity influences isolate-1 VSMC traction stress/force. (A) Representative bead displacements maps of isolate-1 VSMCs grown on 12 kPa and 72 kPa polyacrylamide hydrogels. Graphs show **(B)** integrated bead displacements, **(C)** maximum-TS magnitude, **(D)** integrated-TS magnitude and **(E)** integrated-TF magnitude generated for VSMCs grown on 12 kPa and 72 kPa polyacrylamide hydrogels. Image J software was used to measure the bead displacements and traction stress generation of the VSMCs. Data represent the measurement of ~100 VSMCs from 6 independent experiments. Statistical significance was determined using a paired Student's *t* test (12kPa vs 72kPa) (*** p = <0.0001). TF: Traction force; TS: Traction stress; VSMC: Vascular smooth muscle cell.

The above data demonstrates that matrix stiffness increases both VSMC spreading (**Figure 3.2A** & **B**) and integrated traction stress/force magnitude (**Figure 3.7D** & **E**). Endothelial cell spreading has previously been reported to be correlate with traction force on micropost arrays and soft 1 kPa hydrogels (219, 220). We next speculated that matrix rigidity influences the relationship between VSMC spreading and traction stress/force magnitude. Analysis confirmed a moderate correlation between VSMC spreading and integrated-TS magnitude on both 12 kPa (R^2 = 0.40) and 72 kPa (R^2 = 0.33) hydrogels (**Figure 3.8A**). However, the relationship between VSMC spreading and integrated-TS magnitude was not significantly altered by matrix stiffness. This is reiterated by the relationship between VSMC spreading and integrated-TF magnitude (**Figure 3.8C**), which showed no significant difference between 12 kPa (R^2 = 0.31) and 72 kPa (R^2 = 0.50) polyacrylamide hydrogels.

As this relationship was stiffness-independent, we speculated that the integrated-TS/TF magnitude could be calculated from the VSMC area. To test this idea, both 12 kPa and 72 kPa data sets were compiled (**Figure 3.8B** & **D**) and the gradient of the trend lines were determined. This allowed us to derive formulas to calculate:

Integrated-TS – Equation 1A: (*2665.7(cell area) + 2000000*) and

Integrated TF – Equation 1B: (*0.0748(cell area) –88.001*).

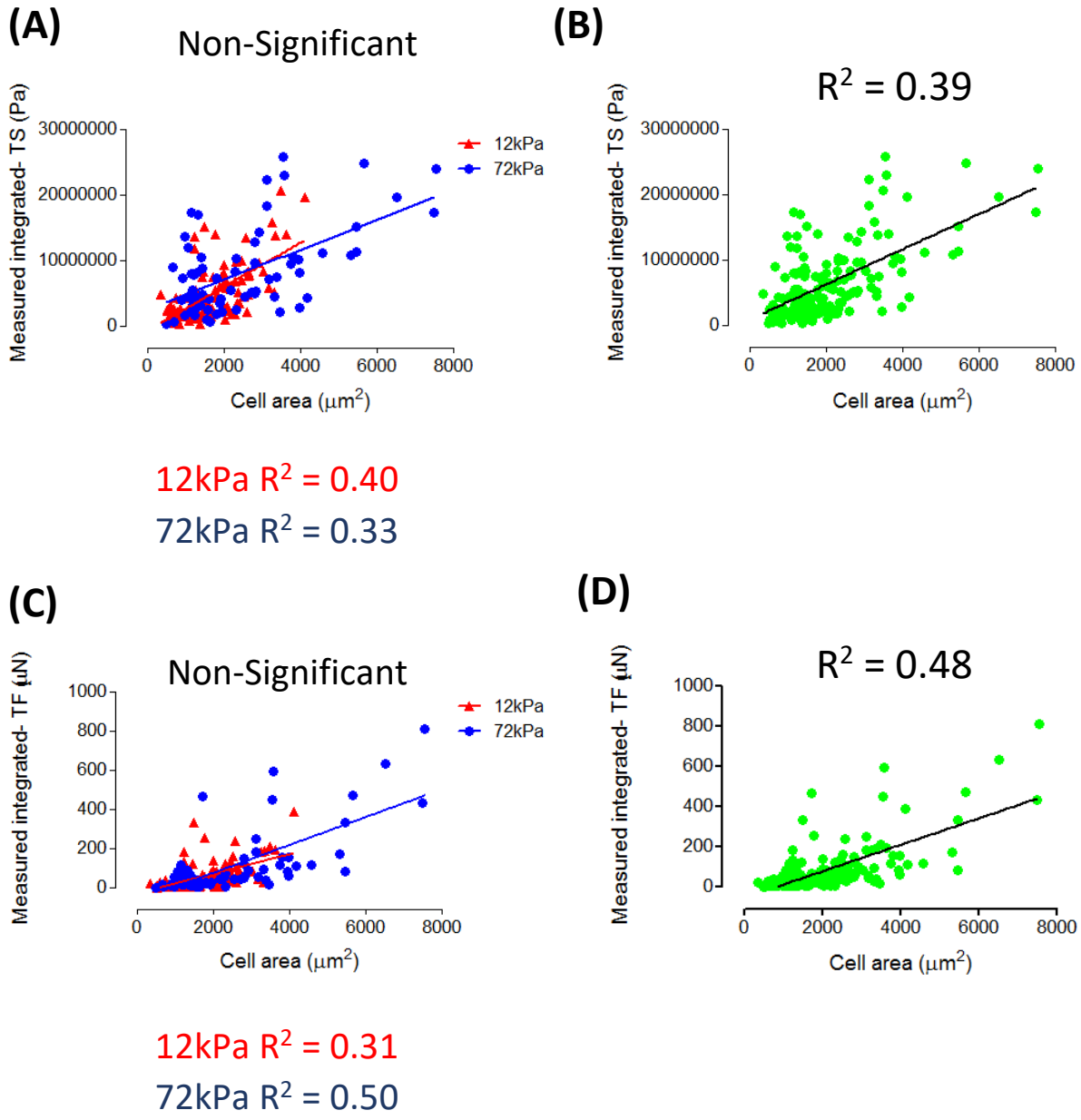

Figure 3.8: Isolate-1 VSMC spreading/integrated-TS/TF magnitude relationship is matrix rigidity independent. (A) Graph shows distribution of integrated-TS magnitude plotted against isolate-1 VSMC area on 12 kPa and 72 kPa polyacrylamide hydrogels and **(B)** combined distribution of this is shown. **(C)** Graph shows distribution of integrated-TF magnitude plotted against isolate-1 VSMC area on 12 kPa and 72 kPa polyacrylamide hydrogels and **(D)** combined distribution of this is also shown. Data represent the measurement of ~100 VSMCs from 6 independent experiments. Statistical significance was determined using linear regression analysis (non-significant; p = >0.05). TF: Traction force; TS: Traction stress; VSMC: Vascular smooth muscle cell.

To test our hypothesis further, we used the second independent aortic VSMC isolate. The work performed here was assisted by our project student Panashe Mabeza. The second isolate recapitulated previous findings with bead displacement reduced and traction stress and force increased by matrix rigidity (**Figures 3.9A-E**).

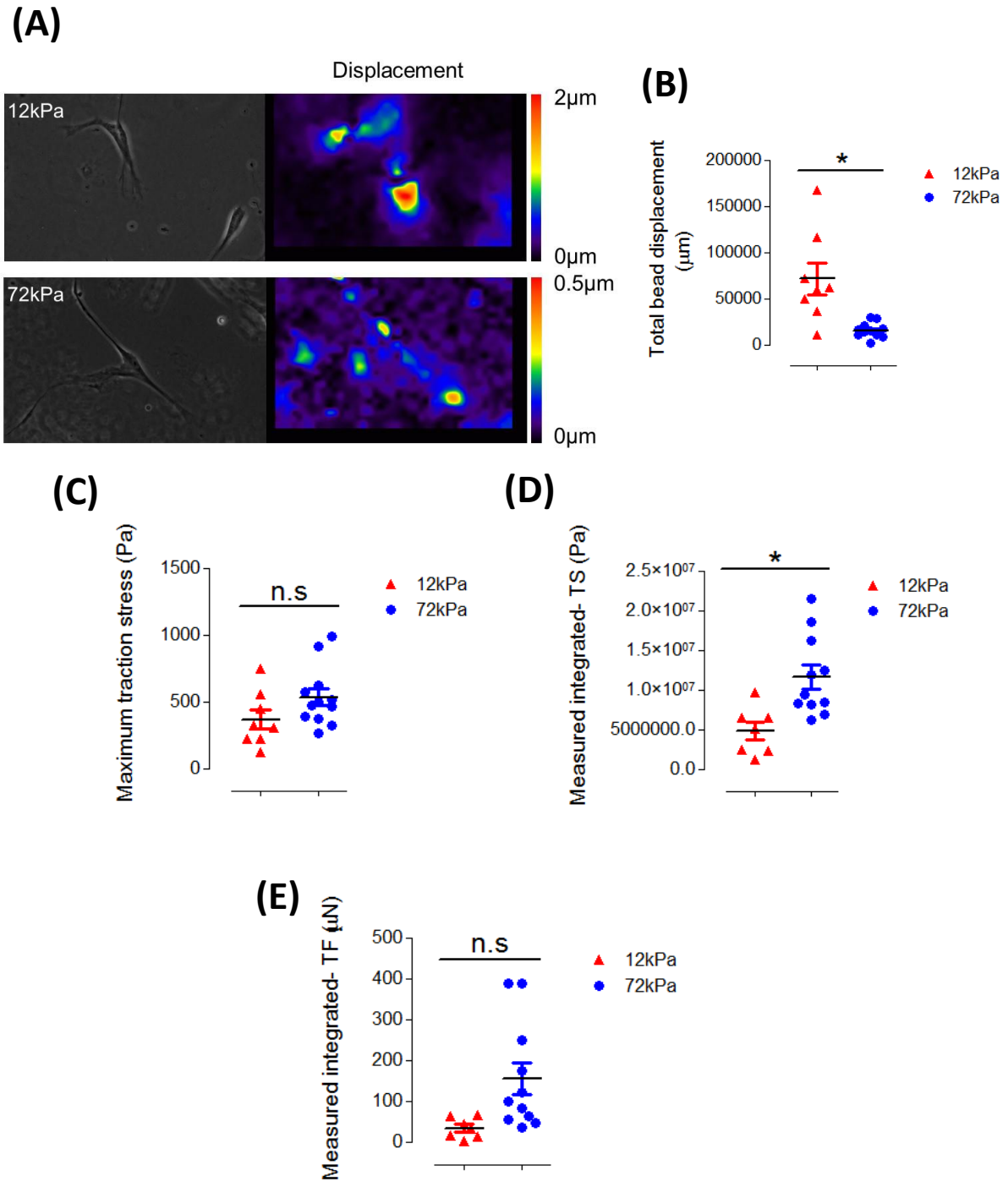

Figure 3.9: Matrix rigidity influences isolate-2 VSMC traction stress/force. (A) Representative bead displacements maps of isolate-2 VSMCs grown on 12 kPa and 72 kPa polyacrylamide hydrogels. Graphs show **(B)** integrated bead displacements, **(C)** maximum-TS magnitude, **(D)** integrated-TS magnitude and **(E)** integrated-TF magnitude generated for VSMCs grown on 12 kPa and 72 kPa polyacrylamide hydrogels. Image J software was used to measure the bead displacements and traction stress generation of the VSMCs. Data represent the measurement of ~15 VSMCs from 2 independent experiments. Statistical significance was determined using a paired Student's *t* test (12 kPa vs 72 kPa) (non-significant; p = >0.05, * p = <0.05). TF: Traction force; TS: Traction stress; VSMC: Vascular smooth muscle cell.

Similarly to isolate-1, trend line formulas for:

Integrated-TS – Equation 2A: (*2685.4(cell area) + 887197*) and

Integrated-TF – Equation 2B: (*0.066(cell area) – 55.784*),

were generated for the second isolate by compiling 12 kPa and 72 kPa data sets and plotting their distribution against VSMC area (**Figure 3.10A** & **B**).

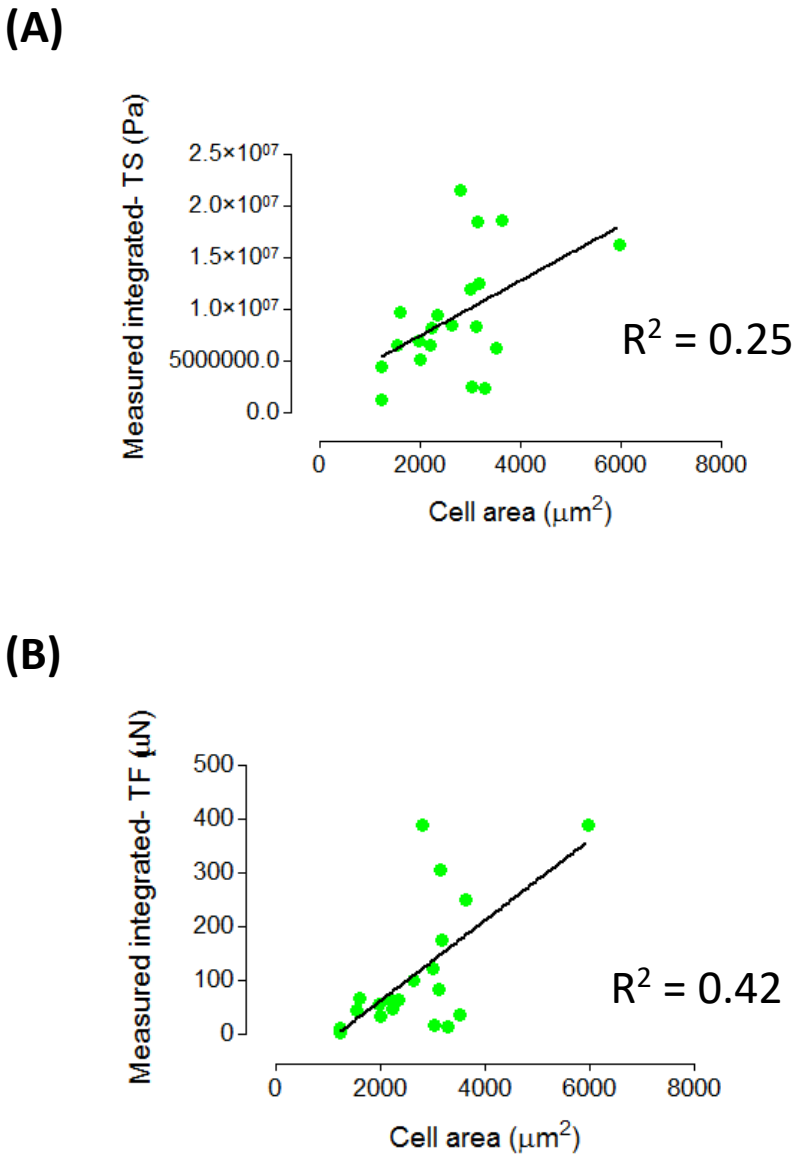

Figure 3.10: Isolate-2 VSMC spreading/integrated-TS/TF magnitude relationship is matrix rigidity independent. Graph shows distribution of VSMC area plotted against **(A)** integrated-TS magnitude and **(B)** integrated-TF magnitude. Data represent the measurement of ~20 VSMCs from 2 independent experiments. Statistical significance was determined using linear regression analysis. TF: Traction force; TS: Traction stress; VSMC: Vascular smooth muscle cell.

3.4.6 Refinement of calculated traction stress and traction force formulas

Using the trend-line formulas generated from counterpart isolates, we now estimated the integrated-TS of both isolates from a measurement of cell spreading. Comparison showed no significant differences between measured and calculated integrated-TS for

isolate-1 and 2 (**Figure 3.11A** & **B**). The same was performed for integrated-TF of both isolates and this similarly showed no significant differences (**Figure 3.11C** & **D**).

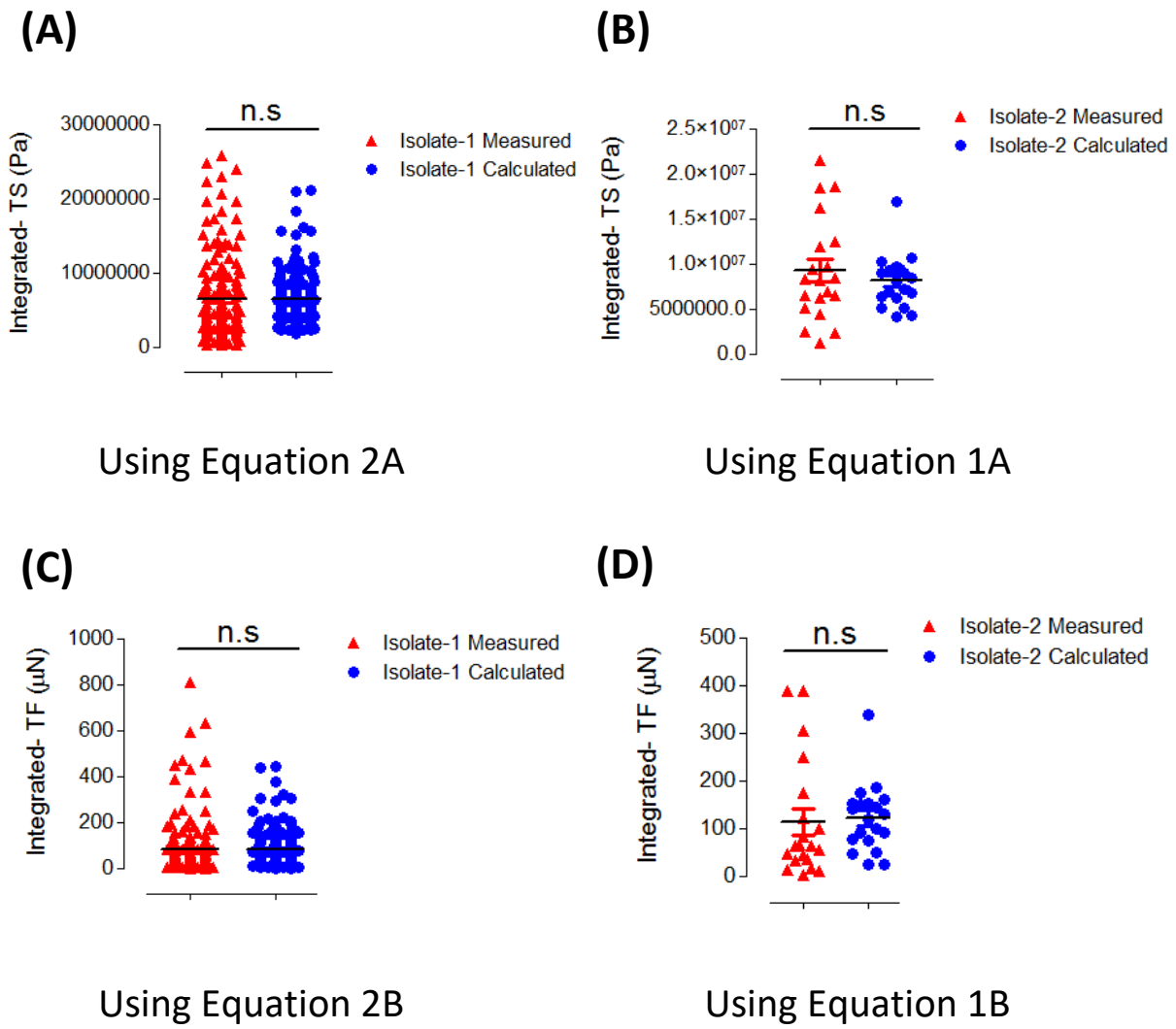

Figure 3.11: Comparison of measured vs calculated integrated-TS/TF of VSMCs. Within this figure, calculated integrated-TS/TF uses trend-line formula previously generated from other isolates distribution of integrated-TS/TF against cell area. Graphs shows measured vs calculated integrated-TS of VSMCs from **(A)** Isolate-1 and **(B)** Isolate-2. **(C)** Isolate-1 and **(D)** Isolate-2 measured vs calculated integrated-TF is also shown. Data from Isolate-1 was based on the measurement of ~100 VSMCs from 6 independent experiments whilst data from Isolate-2 was based on the measurement of ~15 VSMCs from 2 independent experiments. Statistical significance was determined using a paired Student's t test (Isolate 1 vs Isolate 2) (non-significant; p = >0.05). TF: Traction force; TS: Traction stress; VSMC: Vascular smooth muscle cell.

Next, we aimed to refine our models and compared the VSMC spreading/measured integrated-TS relationship between the two independent isolates (**Figure 3.12A**). Isolate 1 (R^2 = 0.39) and 2 (R^2 = 0.25) were found to be non-significant when compared and due to this, we compiled data sets of both isolates (**Figure 3.12B**) (R^2 = 0.31). The gradient was then calculated and an overall trend line formula was derived for:

Integrated-TS – Equation 3A: (*2683.7(cell area)* + *1000000*).

Using the refined equation, measured integrated-TS of both isolates were compiled and compared against calculated-TS, revealing data values to be within similar range with no significant differences (**Figure 3.12C**).

Following this, we sought to similarly optimise our integrated-TF equation. VSMC spreading/measured integrated-TF relationship of isolate-1 (R^2 = 0.48) and isolate-2 (R^2 = 0.42) were compared and no significant differences were revealed (**Figure 3.12D**). Both isolate data sets were then compiled (**Figure 3.12E**) (R^2 = 0.48) and by calculating the gradient, the resulting trend line formula was calculated for:

Integrated-TF – Equation 3B: (*0.0663(cell area) – 57.384*).

Next, measured integrated-TF of both isolates were collated and compared against calculated integrated-TF using the optimised equation (**Figure 3.12F**). Data was shown to be in close agreement with no significant differences between measured and calculated integrated-TF.

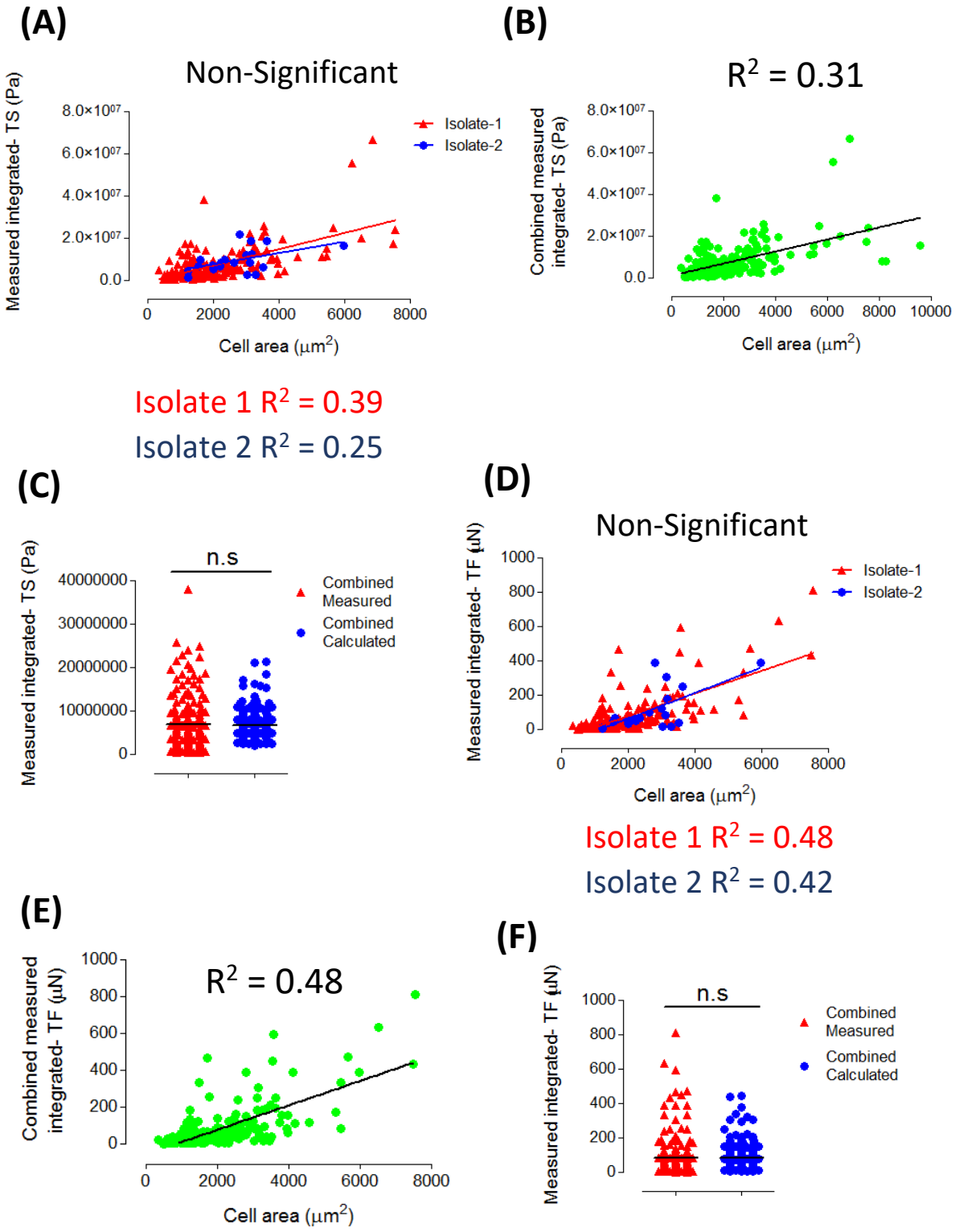

Figure 3.12: Refinement of VSMC integrated-TS/TF formula. (A) Graph shows distribution of integrated-TS magnitude plotted against cell area for both Isolate-1 and 2 of VSMCs and **(B)** combined distribution of this is shown. **(C)** Shows measured vs calculated integrated-TS of both isolates, using trend-line formula generated from **(B).** **(D)** Shows relationship between integrated-TF magnitude and cell area for both isolates and **(E)** combined distribution of this is shown. **(F)** Shows measured vs calculated integrated-TF of both isolates, using trend-line formula generated from **(E).** Data represent the measurement of over 100 VSMCs from 6 independent experiments. Statistical significance was determined using linear regression analysis (non-significant; p = >0.05) as well as a paired Student's t test (measured vs calculated) (non-significant; p = >0.05). TF: Traction force; TS: Traction stress; VSMC: Vascular smooth muscle cell.

3.4.7 Effect of matrix stiffness on VSMC focal adhesion organisation

The actin cytoskeleton is physically anchored to the cell membrane and the ECM via a network of proteins that constitute the focal adhesion complex (221). Vinculin, in particular, crosslinks the actin cytoskeleton to integrin receptors, allowing force transduction to the ECM (10). Focal adhesions are known mechanosensors and previously work has shown matrix rigidity can cause an increase in the size and expression of VSMC focal adhesion complexes (222, 223). To validate earlier findings, VSMCs were grown in serum and seeded on collagen-1 coated polyacrylamide hydrogels, with an average Young's modulus of 12kPa (healthy) and 72kPa (stiff). VSMC focal adhesions were stained with anti-vinculin prior to immunofluorescence microscopy. In agreement with earlier findings, VSMCs possessed significantly larger vinculin positive adhesions on the 72kPa hydrogel (0.8105±0.02098 μM) than on the 12kPa hydrogel (0.5431±0.01819 μM) (**Figure 3.13A** & **B**). In addition, there was a significant increase in the number of adhesions per cell between the 12kPa (44.38±4.031) and 72kPa (124.5±9.647) conditions **(Figure 3.13A** & **C**). Subsequent analysis revealed no differences in vinculin circularity and aspect ratio (**Figure 3.13D** & **E**).

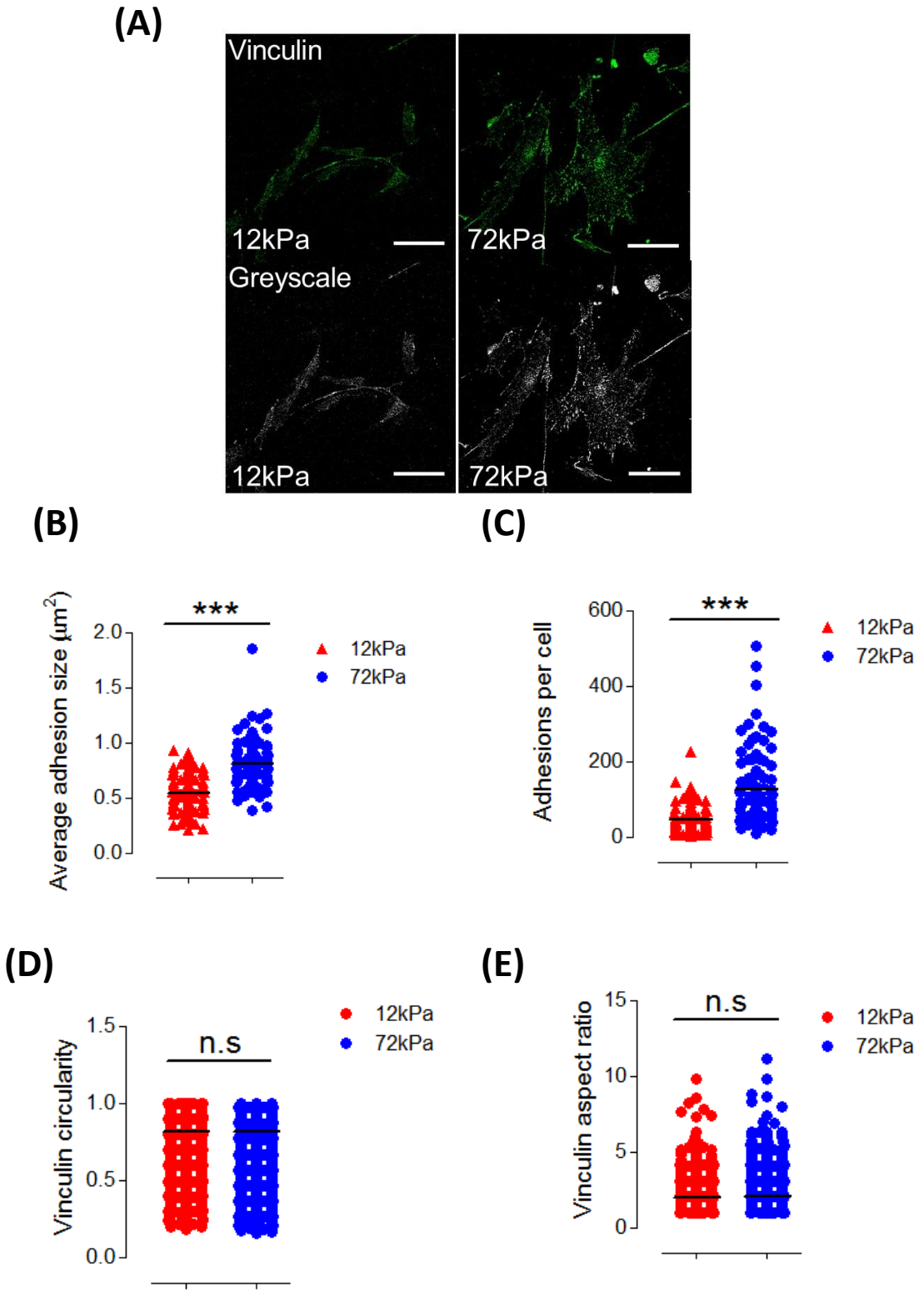

Figure 3.13: Size and number of vinculin-positive focal adhesion complexes augments on a stiffer matrix. (A) Confocal microscopy shows the vinculin organisation of VSMCs stained using anti-vinculin (green) and grey-scale images of vinculin (grey) are shown on 12kPa and 72kPa polyacrylamide hydrogels. Scale bar represents 100 μm. Image J software was used to measure the **(B)** the vinculin size, **(C)** the number of vinculin per cell, **(D)** circularity and **(E)** the aspect ratio. Data are based on the measurement of >100 VSMCs from 3 independent experiments. Statistical significance was determined using a paired Student's t test (12 vs 72) (non-significant; p = >0.05, *** p = <0.0001). VSMC: Vascular smooth muscle cell.

Next, we wanted to investigate adhesion size and number and its relationship with VSMC spreading. Results show that VSMC spreading present moderate/strong correlation with the number of adhesions present (12 kPa R^2 = 0.49 and 72 kPa R^2 = 0.76) (**Figure 3.14A**) but not with the size of those adhesion complexes (12 kPa R^2 = 0.015 and 72 kPa R^2 = 0.014) (**Figure 3.14B**). Importantly, adhesion number revealed a significant difference between 12 kPa and 72 kPa trend-line gradients, confirming this relationship is enhanced by matrix stiffness. This confirms that as VSMC spreading augments on the stiffer matrix, the recruitment rate of adhesion molecules is also enhanced.

(A)

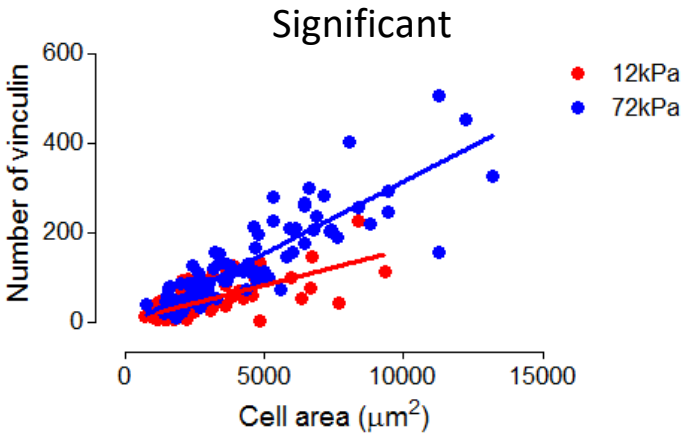

12kPa R^2 = 0.49

72kPa R^2 = 0.76

(B)

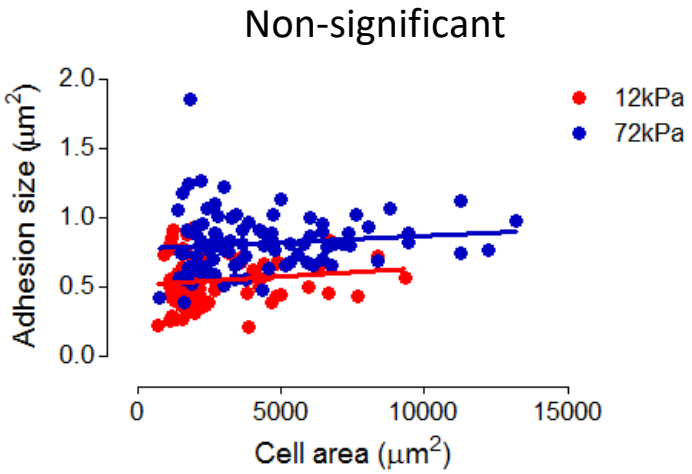

12kPa R^2 = 0.015

72kPa R^2 = 0.014

Figure 3.14: Vinculin number and size show differential relationships to VSMC spreading in response to matrix stiffness. Graphs shows **(A)** number of vinculin (*** p = <0.0001) and **(B)** vinculin area (non-significant; p = >0.05) plotted against VSMC area on 12 kPa and 72 kPa polyacrylamide hydrogels. Data are based on the measurement of >100 VSMCs from 3 independent experiments. Statistical significance was determined using linear regression analysis. VSMC: Vascular smooth muscle cell.

After, we wanted to investigate whether there was a correlation between focal adhesion number and integrated-TS. To investigate this, we used Equation 3A to calculate

the integrated-TS from the fixed cell area data of **Figure 3.14**, and this reaffirmed that enhanced matrix rigidity augments calculated integrated-TS magnitude (**Figure 3.15A**). Similar to **Figure 3.14A**, the relationship between the number of vinculin positive focal adhesions and calculated integrated-TS magnitude showed significantly different trend-line gradients depending on the stiffness of the matrix that cells were cultured on (12 kPa R^2 = 0.49 and 72 kPa R^2 = 0.76), confirming this association is enhanced by a stiffer matrix (**Figure 3.15B**). We then sought to find out whether higher integrated-TS magnitude in larger VSMCs was driven by increased adhesion number. Surprisingly, analysis revealed the average traction stress per adhesion had significantly decreased on the 72 kPa hydrogel (**Figure 3.15C**). Despite the fact that the VSMCs grown on 72 kPa hydrogels possessed an increased number of adhesions/μm^2 (**Figure 3.15D**), they displayed a significantly lower TS/μm^2 than VSMCs grown on 12 kPa hydrogels (**Figure 3.15E**).

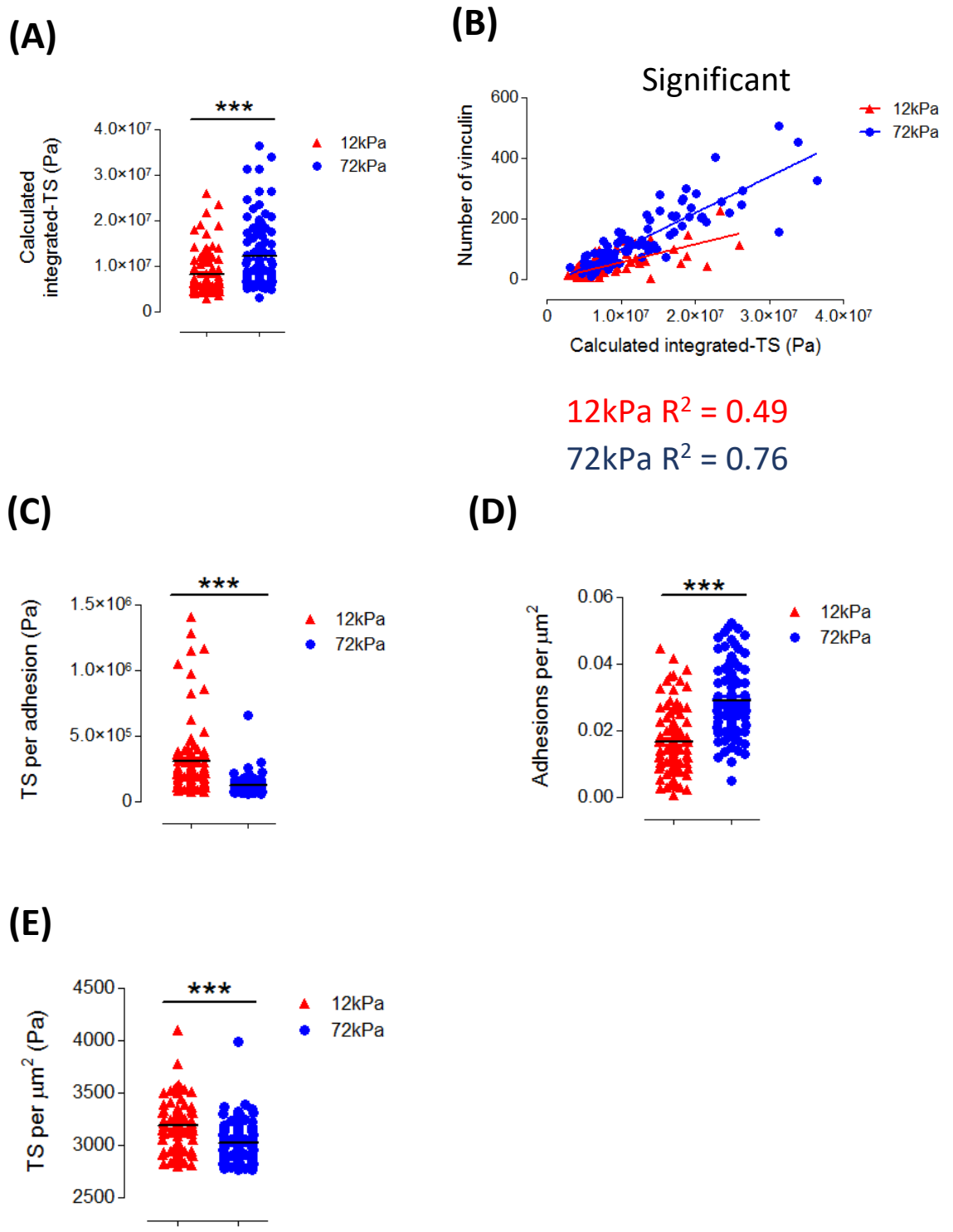

Figure 3.15: Calculated integrated-TS formula shows stiffness-dependent differences in traction stress transmission. Graphs shows **(A)** calculated integrated-TS and **(B)** number of vinculin plotted against calculated integrated-TS on 12 kPa and 72 kPa polyacrylamide hydrogels. **(C)** Shows traction stress per adhesion, **(D)** adhesions per µm^2 and **(E)** traction stress per µm^2. Data are based on the measurement of >100 VSMCs from 3 independent experiments. Statistical significance was determined using linear regression analysis (*** p = <0.0001) and a paired Student's t test (12 vs 72) (*** p = <0.0001). TS: Traction stress; VSMC: Vascular smooth muscle cell.

Following from this, we investigated calculated integrated-TF using formula 3B. Matrix stiffness, as expected, was shown to significantly enhance calculated integrated-TF and its relationship with the number of vinculin positive focal adhesions (12 kPa R^2 = 0.49 and 72 kPa R^2 = 0.76) (**Figure 3.16A** & **B**). In line with **Figure 3.15C**, the average traction force per adhesion was higher on the 12 kPa hydrogel. However, unlike traction stress, the TF/μm^2 was shown to be significantly higher on the 72 kPa hydrogel (**Figure 3.16D**).

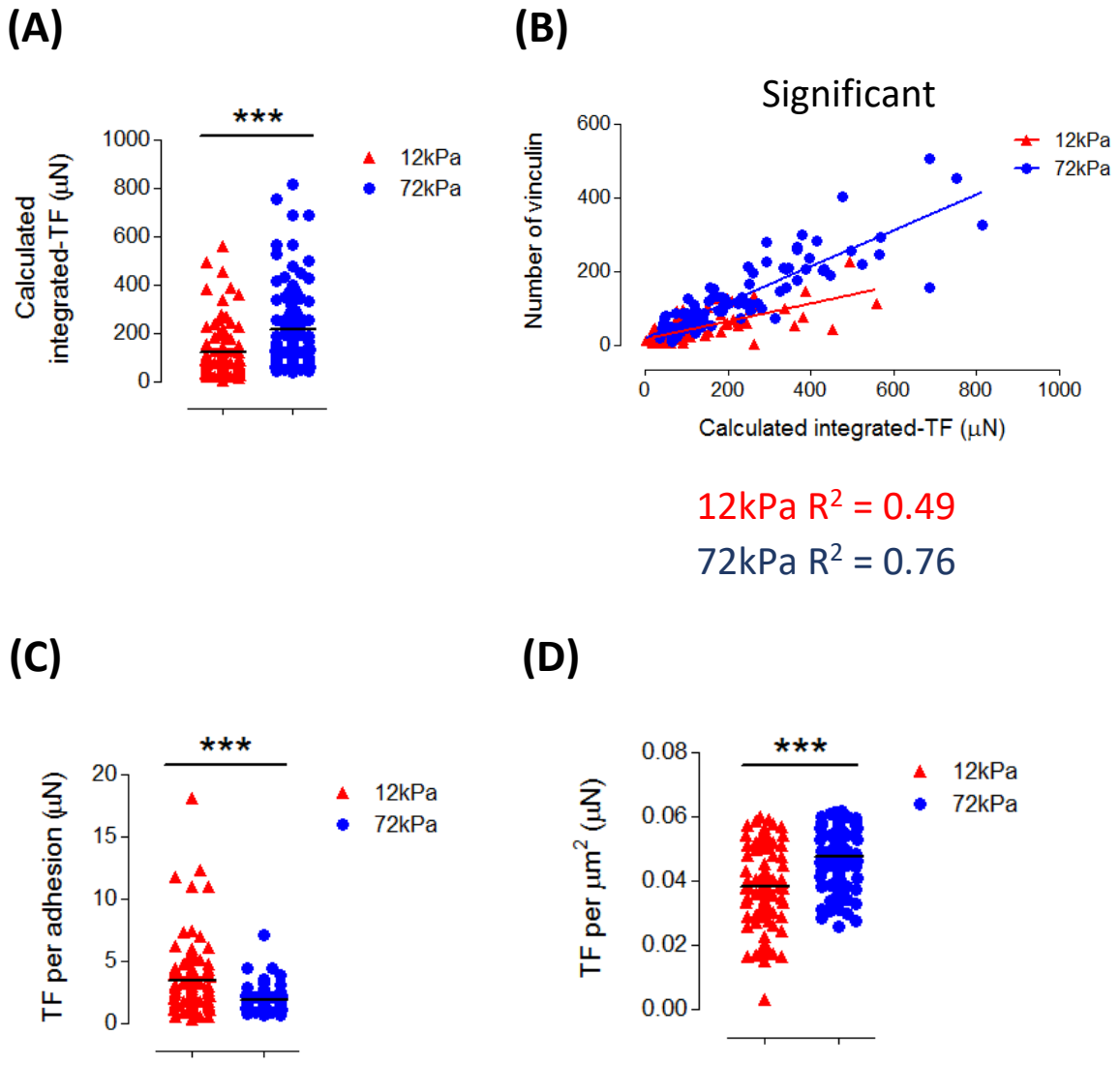

Figure 3.16: Calculated integrated-TF formula shows stiffness-dependent differences in traction force transmission. Graphs shows **(A)** calculated integrated-TF and **(B)** number of vinculin plotted against calculated integrated-TF on 12 kPa and 72 kPa polyacrylamide hydrogels. **(C)** Shows traction force per adhesion and **(D)** traction force per µm^2. Data are based on the measurement of >100 VSMCs from 3 independent experiments. Statistical significance was determined using linear regression analysis (*** p = <0.0001) and a paired Student's t test (12 vs 72) (*** p = <0.0001). TF: Traction force; VSMC: Vascular smooth muscle cell.

3.5 Discussion

It is well-documented that matrix stiffness can cause VSMCs to transition to a synthetic proliferative phenotype. However, the specific outcome of matrix stiffness on VSMC function has not been extensively reviewed. To further our current understanding, this chapter extends on previous findings by characterising the relationship between synthetic VSMC morphology, intracellular organisation and traction force as well as the impact of matrix stiffness upon it.

3.5.1 Characterising VSMC morphological changes associated with matrix stiffness

Cell morphology is an important characteristic in defining the phenotype of a cell and is crucial in performing vital cellular processes. VSMCs possess remarkable plasticity, and in events of vascular pathologies, will transition to a synthetic phenotype (224). Matrix stiffening is prevalent in CVD development, and in previous studies has been shown to induce fibroblast and endothelial cell spreading on protein-laminated polyacrylamide hydrogels. Stiffer matrices have also been shown to cause similar changes in mesenchymal stem cell morphology. Despite this, the influence of matrix stiffness on cell spreading is cell-type specific as neutrophils presented no change in response to augmentations in matrix rigidity (214, 225). In our work, we show that VSMC spreading is enhanced by matrix stiffness and this is in agreement with earlier research using VSMCs from atherosclerotic plaques (226). Prior work has shown that VSMCs isolated from older donors spread further when grown in culture compared to younger counterparts (217) and therefore we speculate matrix stiffness, a key event in ageing, to drive these changes.

The actin cytoskeleton usually performs a myriad of functions within the cell, with examples being contractility, motility and proliferation (227, 228). As the actin cytoskeleton has been shown to define cell structure and shape, the morphological changes associated with matrix stiffness are heavily reliant on it (229). Previously, the addition of green fluorescent protein (GFP)-actin has been shown to cause additional spread of smooth muscle cells under a defined tension (230). This gives speculation that actin filament density in smooth muscle may be augmented in response to matrix stiffness. Our data gives support to this as levels of filamentous actin were shown to significantly increase on stiffer matrices.

Formerly, this has been observed in fibroblast cells where F-actin density showed augmentations in response to enhanced matrix rigidity (231).

Filamentous actin align into bundles when exposed to mechanical tension in order to appropriately respond to changes in their external environment (232). In our study, we show that matrix stiffness can cause significant increases in F-actin alignment both at 24 and 72 hours. VSMCs potentially mechanosense the stiffer ECM and reorganise the cytoskeleton for greater traction force generation. This is validated by a previous study which show actin inhibitors can decrease actomyosin-induced VSMC stiffness caused by stiffer matrices (198). The actin cytoskeleton has been discussed to be immensely important, and as a result, any matrix stiffness-related changes to cytoskeletal structure may be crucial for the maintenance of normal cell function.

In some cases, the shape of the nucleus is altered by forces that act from the cytoplasm. The LINC complex, comprised of nesprin-family members and SUN-domain containing proteins, is involved in essential mechanotransduction. Giant nesprin-1/2 are localised on the outer nuclear membrane and associate with filamentous actin (120). The physical linkage allows transfer of mechanical forces spanning from adhesion receptors present on the cell membrane to the nuclear core (233). Prior research has revealed that mesenchymal stem cells demonstrate nuclear mechanosensitivity as they show increased spreading of nuclei on stiffer matrices (234). Our work supports this as VSMCs present significantly larger nuclei when exposed to increased matrix stiffness.

3.5.2 Regulation of VSMC actomyosin activity and traction force

Matrix rigidity has been shown to influence VSMC actomyosin activity however its regulation requires further clarification. Phosphorylation of the myosin light chain is a hallmark characteristic of actomyosin activity and it promotes myosin minifilament formation that travel along and pull the actin filament (235). Our studies show higher integrated-TS/TF magnitude due to matrix stiffness suggesting that actomyosin-generated force is increased. However, analysis of VSMC mean pMLC levels show a significant decrease on the rigid hydrogel whilst total pMLC levels show equal levels due to VSMC spreading. This contrasts former studies which highlight how decreasing the mechanical compliance of the ECM can augment pMLC levels (236). Additionally, our work shows matrix stiffness diminishes cell spreading/total pMLC relationship suggesting that VSMC may possess a compensatory mechanism to generate increased integration-TS/TF magnitude.

Matrix adhesions undergo dramatic remodelling in response to matrix stiffness and numerous reports have stated changes in number and size of adhesions within multiple cell types (237). Vinculin, in particular, has previously been shown to be upregulated twofold when increasing stiffness from 25 kPa to 135 kPa. This study demonstrated SMC spreading had no effect on focal adhesion size but it held a strong relationship to focal adhesion number on both soft and stiff substrates (238). Our work expanded on this showing VSMCs possess a strong cell spreading/adhesion number per cell relationship and this was enhanced further by a six-fold increase in matrix stiffness. We propose that matrix rigidity enables a protective mechanism that preserves increased force generation of the VSMCs whilst simultaneously protecting it from actomyosin-induced damage. Our data suggests VSMC use increased adhesion anchor points to enhance force transmission in order to maintain safe actomyosin levels. Unrestrained actomyosin activity can trigger DNA damage in other cell types and VSMCs can undergo premature ageing as a result of DNA damage (139-141). Therefore, this mechanism may serve to protect VSMC from ageing as a result of stiffness-induced actomyosin activity.

Our study is in agreement with previous work utilising embryonic aortic VSMCs, which show matrix rigidity significantly increases both VSMC traction force magnitude and spreading (142). Despite this, the study mentioned utilised hydrogels with stiffness between 10 kPa-25 kPa. AFM has shown that these rigidities fall within the average range of healthy adult aorta (142). Our work is the first to investigate this finding within mature adult VSMCs utilising a stiffness that is more representative of CVD rigidity. Earlier research has demonstrated matrix rigidity enhances the relationship between cell spreading/integrated traction forces in other cell types (219, 220). However, we have shown that this relationship is independent of matrix stiffness in two independent isolates of adult VSMCS. Using our data, we have generated a model to calculate integrated-TS/TF magnitude from fixed VSMC area. This model has proved capable of calculating traction stress/force without the need of performing technical TFM experiments, with no significant difference observed between measured and calculated integrated-TS/TF within smooth muscle cells.

Despite increased recruitment of adhesive units due to VSMC spreading, the integrated-TS/TF per adhesion presented a significant decline in response to matrix rigidity. Therefore, it is possible that adhesion number/μm^2 was significantly higher in order to enable greater integrated-TS/TF generation. However, traction force and traction stress per μm^2 showed differential responses in response to matrix stiffness. A possible explanation is the integrated-TF compiled from both isolate datasets presented a stronger relationship to VSMC spreading (**Figure 3.12E**) compared to integrated-TS (**Figure 3.12B**). As enhanced matrix stiffness induces increased VSMC spreading, this may have resulted in a larger

integrated-TF generation when normalised to the cell area. Additionally, the traction force calculation accounts for traction stress distribution, and hence the more widespread the distribution, the larger the resulting traction force. Cell adhesive strength is characterised by the amount of force required for cell detachment (239), and appropriate traction stress distribution is necessary to ensure VSMCs remain attached to their ECM. Potentially, traction stress distribution may become more concentrated in regions where focal adhesion populations are dense whilst its distribution could be more widespread in response to dispersed adhesion populations. As traction stress may be localised to a smaller specific region of the cell, it may not be accurate to assume equal distribution of the stress by normalising to the cell area. Integrated-TF/μm^2 takes this into account and therefore gives a more representable account of VSMC force distribution.

Despite these differences, VSMC spreading has been shown to ultimately increase both integrated-TS and TF. In spite of generating higher integrated-TS/TF, VSMCs ability to displace the surrounding ECM shows dramatic diminishment with matrix rigidity. In healthy aorta, VSMCs regularly maintain vascular tone via vessel constriction (208) and our data supports this showing efficient displacement at normal (12kPa) aortic stiffness. Deformation of the ECM occurs via enhanced actomyosin activity and this allows VSMCs to appropriately respond to their mechanical environment. However, our findings demonstrate that, despite causing enhanced VSMC actomyosin activity, VSMCs can no longer manipulate their microenvironment and hence are unable to significantly contribute to vascular tone due to matrix stiffness.

3.5.3 Chapter Three conclusions

This chapter clearly demonstrates that matrix stiffness causes alterations in synthetic VSMC morphology, intracellular organisation and traction force magnitude. Increased matrix stiffness induces increased VSMC spreading and integrated-TS/TF generation and this is due to a higher recruitment of adhesive units. Additionally, actomyosin activity and adhesion concentration present an inverse relationship. Matrix rigidity causes a decrease in mean pMLC levels whilst enhancing adhesive anchor points. Due to this, we speculate that VSMCs focus on efficient distribution of traction stress under matrix rigidity and increased filamentous actin density helps facilitate this. We hypothesise that these changes act as a compensatory mechanism that enable increased VSMC traction force generation on rigid ECMs without causing actomyosin-induced DNA damage.

Synthetic VSMCs were utilised within this chapter however we must consider contractile VSMC counterparts, which may possess greater ability of deforming the stiffer matrix. However, previous reports state vascular injury can stimulate smooth muscle cell proliferation (240, 241), and therefore VSMC traction force generation, phenotypic regulation and vessel compliance present an intricate relationship. Further research is required to better understand this relationship as aortic stiffness and VSMC phenotypic switching are prevalent events that lead to decreased aortic compliance within CVD. This chapter has shown key changes in synthetic VSMC morphology and contractile apparatus structure, and our model will allow further interrogation of these pathways to better understand synthetic VSMC force regulation within the diseased state.

3.5.4 Limitation and future work

3.5.4.1 VSMC isolates

The experiments conducted within this chapter were performed using two VSMC stocks. Due to time restraints and accessibility to VSMC stocks, the results obtained within the current study are limited. In the future, our model will be tested and validated using further stocks of isolate-2 VSMCs.

3.5.4.2 VSMC synthetic vs contractile phenotype

Throughout this chapter, our study utilised VSMCs within the synthetic phenotype. However, as mentioned before, VSMCs display remarkable plasticity and normally exist in the quiescent contractile phenotype. Phenotypic transitioning is accompanied by changes in the gene expression of key contractile protein markers (242). A key difference between the two phenotypes is that contractile VSMCs express both SM-myosin II and NM-myosin II, whereas synthetic VSMCs largely express the latter (45). Previous studies have shown SM-myosin II participates in fast phasic contraction whilst NM-myosin II has a role in slower tonic contraction. Due to this, NM-myosin II has shown decreased force exertion than its counterpart. (46, 243, 244). Changes in the relative contribution of both proteins in response to matrix rigidity requires further clarification and therefore our work remains limited in accounting for phenotypic alterations.

3.5.4.3 Traction force model

TFM is a time consuming and specialised technique and therefore our model serves to give an accurate prediction of smooth muscle cell traction force based on cell spreading data. Whilst cell spreading and traction force magnitude hold a strong relationship, there are other factors that also play a role in integrated-TF. The aorta presents increased collagen levels in CVD, and previous work has shown that very high collagen accumulation can instead cause a decline in cell spreading (245). Our study employs a stiffness 6-fold higher (72kPa) than normal healthy aorta (12kPa) and therefore we must consider the possibility of differential responses at higher rigidities. Additionally, ligand affinity and cell alignment also play a strong factor towards the kinetics and total levels of traction force (246, 247) and due to this, our model could be further refined to account for these elements.

3.5.4.4 2D vs 3D traction force

Our work has been performed on 2D polyacrylamide hydrogels however 2D systems have previously been shown to display cell bioactivities that deviate away from true *in vivo* responses. Many studies have shown that introducing a 3D environment can significantly alter cell proliferation, differentiation and the mechano-response (248-250). Importantly, it has been reported that out-of-plane traction stress can increase ten-fold when sensing substrate stiffness in 3D (251). Ultimately, all of this must be considered when studying

VSMC traction force and therefore future work will assess whether 3D-TFM shows similar compensatory mechanisms at those observed in 2D.

Chapter 4: The impact of matrix stiffness on smooth muscle cell contraction

4.1 Introduction

Thus far, the focus of the thesis has been to characterise the impact of matrix stiffness on synthetic VSMC morphology, intracellular organisation and traction force magnitude. We highlighted novel compensatory mechanisms that are introduced in response to increased traction force on rigid polyacrylamide hydrogels. Despite this, VSMCs were shown to be inefficient in displacing the stiffer matrix due to decreased compliance. Synthetic VSMCs were utilised within the previous chapter and therefore this chapter focuses on its contractile counterparts which may possess a greater capability of deforming stiffer matrices.

The primary function of VSMCs is to exert actomyosin-derived contractile forces with regulatory cues, such as mechanical stretch derived from pulsatile blood pressure, assisting the cells to maintain vascular tone (252, 253). VSMC contractile forces are initiated from an increase of intracellular calcium via external stimuli, causing rapid phase contractions (72). Within the contractile phenotype, SM-myosin II is located in tissue regions where fast phasic contractions occur. SM-myosin II is a marker protein of the quiescent VSMC phenotype and has been found to generate a higher contractile force than NM-myosin II, observed predominantly in the synthetic state (46, 243, 244).

This chapter expands on VSMC function by isolating the contractile activity of the VSMC via serum starvation. Serum starvation has previously been shown to cause a shift to the contractile phenotype and increase expression of key contractile marker proteins (254-257). Although serum starvation does not achieve complete restoration of the contractile phenotype, the expressional changes allow it alter cellular mechanical properties to become more akin to the differentiated state (254-257). Thus, making the system used suitable for assessing the mechanical and morphological properties of contractile VSMCs. Within this chapter, our polyacrylamide-based system was used to screen the effects of various contractility agonists/antagonists on quiescent VSMC morphology.

4.2 Aim of this chapter

This chapter will investigate the effect of numerous contractile agonists and antagonists on quiescent VSMC morphology to develop a new screening method for a novel contractility assay. Additionally, we will further our earlier study by exploring the role of matrix stiffness on VSMCs possessing mechanical properties more akin to the contractile phenotype.

4.3 Hypothesis

We hypothesise that our contractile assay will reveal more information on quiescent VSMC structural changes under matrix stiffness. Our assumption is that VSMCs seeded on the 72kPa polyacrylamide hydrogel will present altered contractile function and this will reveal new potential functional avenues to explore the underlying mechanism.

4.4 Results

4.4.1 Optimisation of microscopy imaging

To obtain suitable representative images of morphological studies, optimisation of microscopy imaging was performed on VSMCs that were seeded on 12 kPa polyacrylamide hydrogels and pre-treated with 0.1 μM Angiotensin II. F-actin staining was performed with rhodamine phalloidin on VSMCs prior to immunofluorescence microscopy. As shown, samples were imaged on both confocal and widefield microscopes (**Figure 4.1A & B**). The difference in quality is presented, revealing confocal images to be more appropriate for Image J software analysis. However, due to time constraints, some images shown were taken with a widefield microscope as these were deemed suitable for analysis. This is shown by **Figure 4.1C** which confirms the cell area to be comparable as they are shown to be within a similar range with both forms of microscopy.

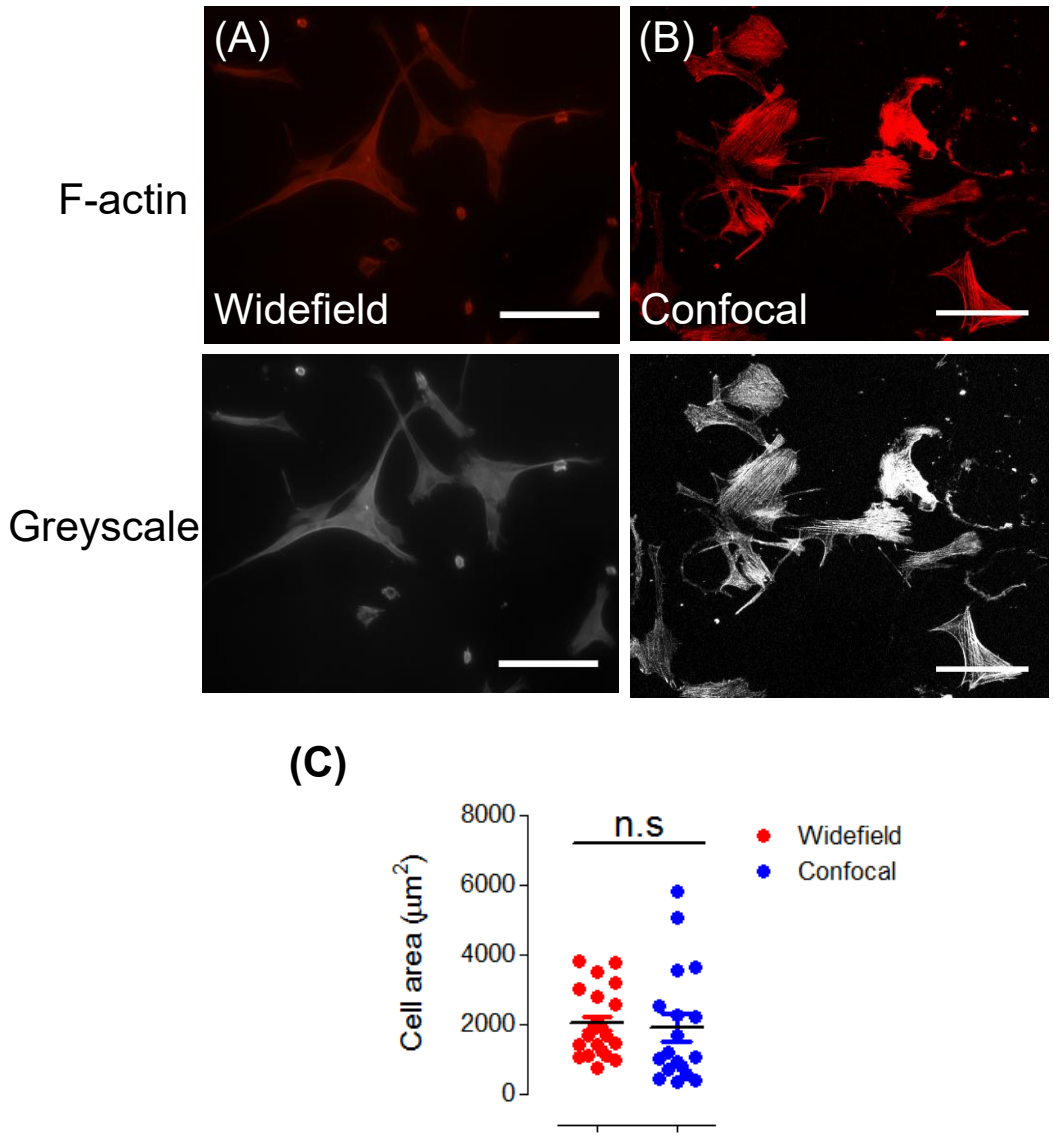

Figure 4.1: Optimisation of microscopy imaging. Representative immunofluorescence images of VSMC actin filaments treated with a low-dose (0.01 µM) of Angiotensin II. Images show VSMC actin filaments (F-actin) stained using rhodamine phalloidin (red) and grey-scale images of F-actin (grey) on 12 kPa polyacrylamide hydrogels. Images were captured using a **(A)** widefield microscope and a **(B)** confocal microscope. Scale bar represents 100 µm. Image J software was used to manually measure **(C)** the cell area of pre-treated VSMCs captured with widefield and confocal microscopes. Data are based on the measurement of >20 VSMCs from 2 independent experiments. Statistical significance was determined using a paired Student's *t* test on cell area (Widefield vs Confocal) (non-significant; p = >0.05). VSMC: Vascular smooth muscle cell.

4.4.2 Effect of contractile agonists on VSMC morphology

Angiotensin II has been established to have numerous roles within vascular smooth muscle, such as regulating vascular tone (258), hyperplasia (259), hypertrophy (260, 261)

and extracellular matrix production (262). Despite this, the mechanical and morphological properties induced by Angiotensin II require further characterisation. Previously, it's been shown that epithelial cells display a flattened and elongated structure when treated with Angiotensin II (263). We speculated that Angiotensin II treatment would cause a decrease in VSMC spreading due to augmented contractile function, and to validate this, VSMCs were grown in basal medium and seeded on collagen-1 coated polyacrylamide hydrogels, with an average Young's modulus of 12 kPa. Prior work involving VSMCs have utilised 1 μM concentrations of Angiotensin II (264). As a result, cells were treated with a serial dilution of Angiotensin II, ranging from 0.01 μM-100 μM, and prior to immunofluorescence microscopy, F-actin staining was performed with rhodamine phalloidin.

Using Image J software, it was revealed VSMCs possessed significantly lower cell areas when treated with 10 μM (1423±60.74 μm^2) and 100 μM (1238±48.86 μm^2) of Angiotensin II compared to lower-dose counterparts (**Figure 4.2A & B**). Further analysis revealed there to be no significant change on cell aspect ratio with increasing concentrations of Angiotensin II (**Figure 4.2A & C**).

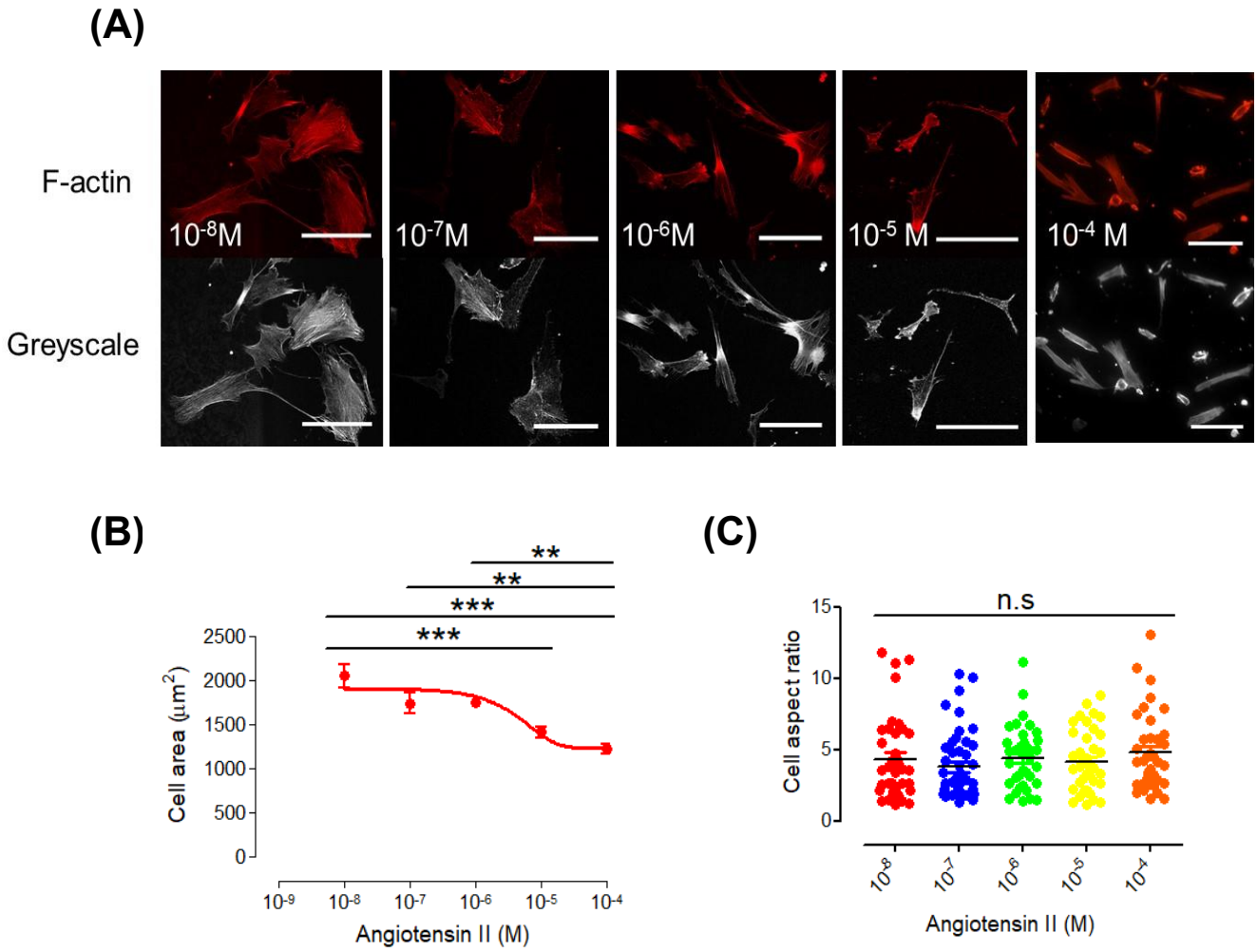

Figure 4.2: The impact of Angiotensin II treatment on VSMC morphology. **(A)** Representative immunofluorescence images of VSMC actin filaments treated with a serial dilution of Angiotensin II. Images show VSMC actin filaments (F-actin) stained using rhodamine phalloidin (red) and grey-scale images of F-actin (grey) on 12 kPa polyacrylamide hydrogels. Scale bar represents 100 µm. Image J software was used to manually measure the **(B)** cell area and **(C)** aspect ratio of the VSMCs. Data are based on the measurement of >150 VSMCs from 3 independent experiments. Statistical significance was determined using a one-way ANOVA to show differences in cell area (** p = <0.001, *** p = <0.0001) and cell aspect ratio (non-significant; p = >0.05), followed by a Bonferroni's multiple comparison test. VSMC: Vascular smooth muscle cell.

Additionally, prior research has shown that the nucleocytoplasmic ratio within specific cell types are confined within a narrow range (265). Based on this evidence, we next looked at nuclei spreading in response to Angiotensin II to investigate whether this holds true within VSMCs. VSMCs were once again grown in basal medium and seeded on collagen-1 coated polyacrylamide hydrogels, with an average Young's modulus of 12 kPa. Cells were stimulated with a serial dilution of Angiotensin II 30 minutes prior to fixation and VSMC nuclei were stained with DAPI in preparation for immunofluorescence microscopy. Much like VSMC

spreading, nuclear area showed a significant decrease in response to higher concentrations of angiotensin II (**Figure 4.3A & B**). Additionally, in agreement with previous findings, nucleocytoplasmic ratio shows no significant change with increasing doses of Angiotensin II (**Figure 4.3A & C**).

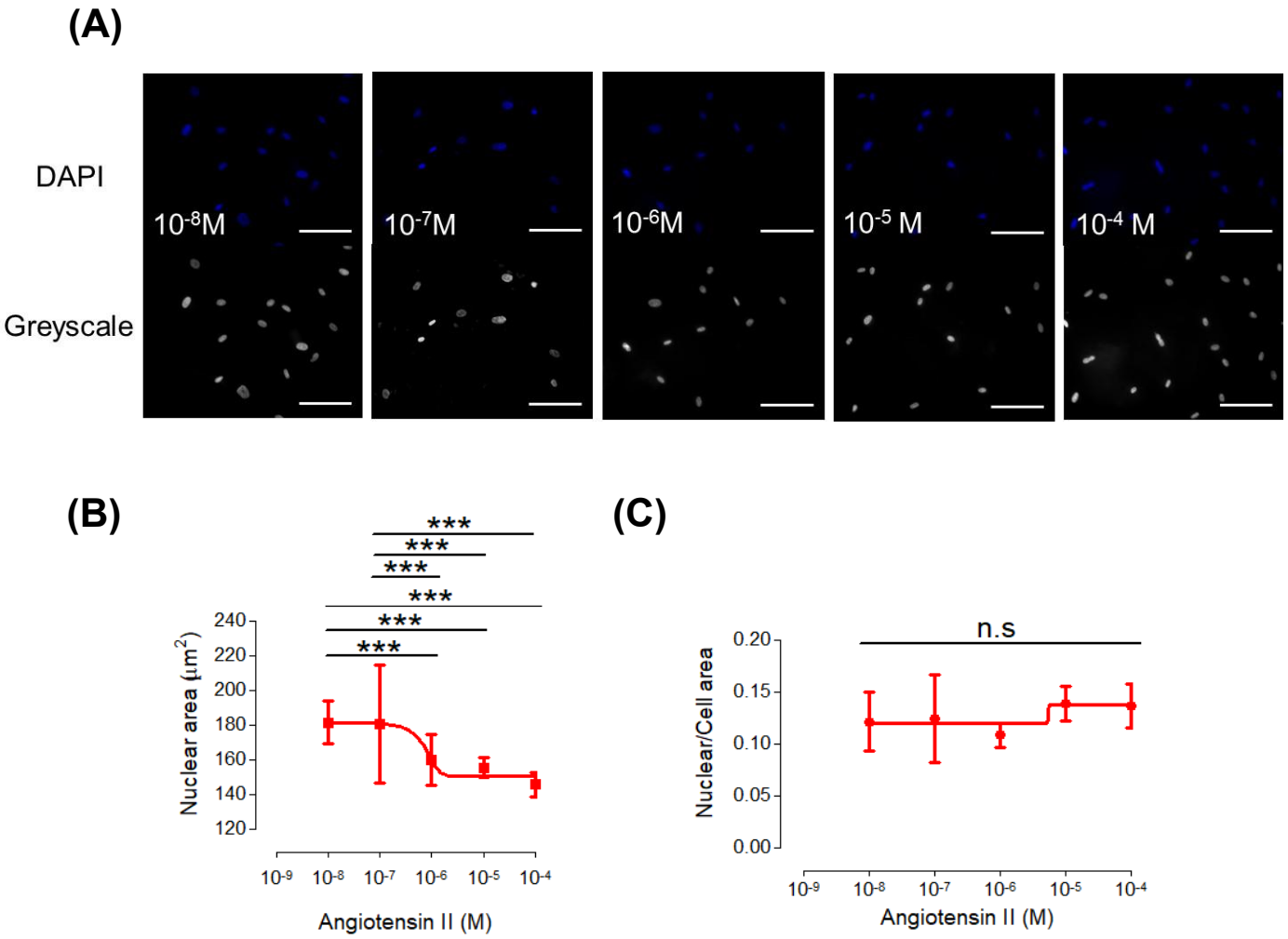

Figure 4.3: The impact of Angiotensin II treatment on VSMC nuclear morphology. **(A)** Representative immunofluorescence images of VSMC nuclei treated with a serial dilution of Angiotensin II. Images show VSMC nuclei stained using DAPI (blue) and grey-scale images of nuclei (grey) on 12 kPa polyacrylamide hydrogels. Scale bar represents 100 µm. Image J software was used to manually measure the **(B)** nuclear area and **(C)** shows the ratio between nuclear to cell area. Data are based on the measurement of >150 VSMCs from 3 independent experiments. Statistical significance was determined using a one-way ANOVA to show differences in nuclear area (*** p = <0.0001) and nuclear to cell area ratio (non-significant; p = >0.05), followed by a Bonferroni's multiple comparison test. VSMC: Vascular smooth muscle cell.

Next, we utilised Carbachol as a second contractile agonist to reaffirm our findings. Carbachol binds to muscarinic receptors within smooth muscle cells and increases intracellular calcium to cause contraction (266). Earlier studies involving VSMCs have

utilised a 100 µM dose of Carbachol to use as a positive control for contraction (267). Due to this, we hypothesised to see the same effect within VSMCs as observed with Angiotensin II. To be able to determine this, we repeated the above experimental procedure but treated with a serial dilution treatment of Carbachol this time. In preparation for immunofluorescence microscopy, VSMC actin filaments and nuclei were stained with rhodamine phalloidin and DAPI, respectively.

Our results corroborated with earlier findings, showing high doses of Carbachol ranging between 10 µM (1303±62.62 μm^2) to 100 µM (996.1±47.72 μm^2) can induce a significant reduction in cell area (**Figure 4.4A & B**), but no change to cell aspect ratio (**Figure 4.4A & C**).

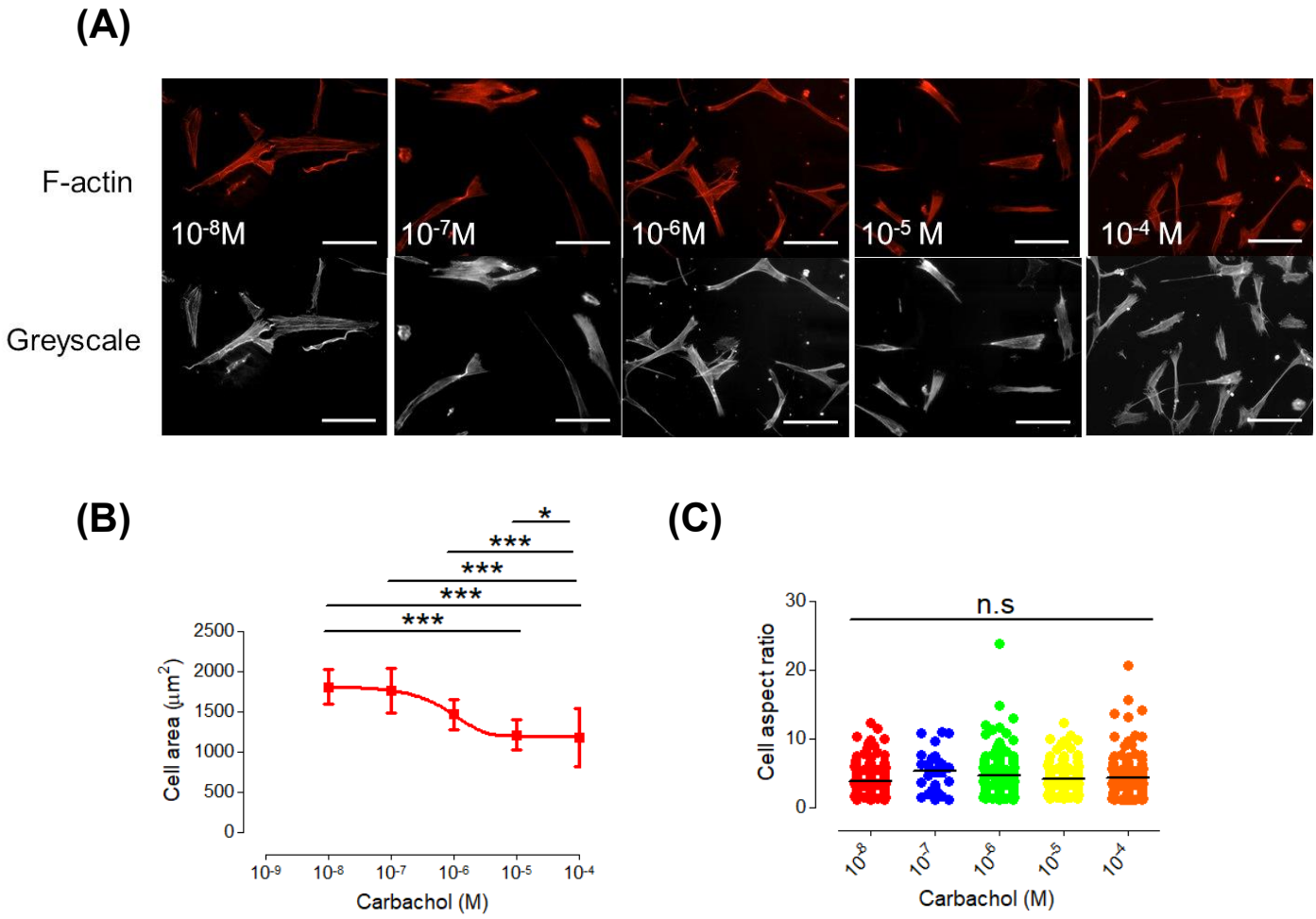

Figure 4.4: The impact of Carbachol treatment on VSMC morphology. **(A)** Representative immunofluorescence images of VSMC actin filaments treated with a serial dilution of Carbachol. Images show VSMC actin filaments (F-actin) stained using rhodamine phalloidin (red) and grey-scale images of F-actin (grey) on 12 kPa polyacrylamide hydrogels. Scale bar represents 100 µm. Image J software was used to manually measure the **(B)** cell area and **(C)** aspect ratio of the VSMCs. Data are based on the measurement of >150 VSMCs from 3 independent experiments. Statistical significance was determined using a one-way ANOVA to show differences in cell area (* p = <0.05, *** p = <0.0001) and cell aspect ratio (non-significant; p = >0.05), followed by a Bonferroni's multiple comparison test. VSMC: Vascular smooth muscle cell.

Additionally, nuclear size showed dramatic decreases as observed previously (**Figure 4.5A & B**). One difference revealed is that the nucleocytoplasmic ratio showed significant changes with high doses of Carbachol, showing that specific cell types can show variation depending on drug treatments (**Figure 4.5A & C**).

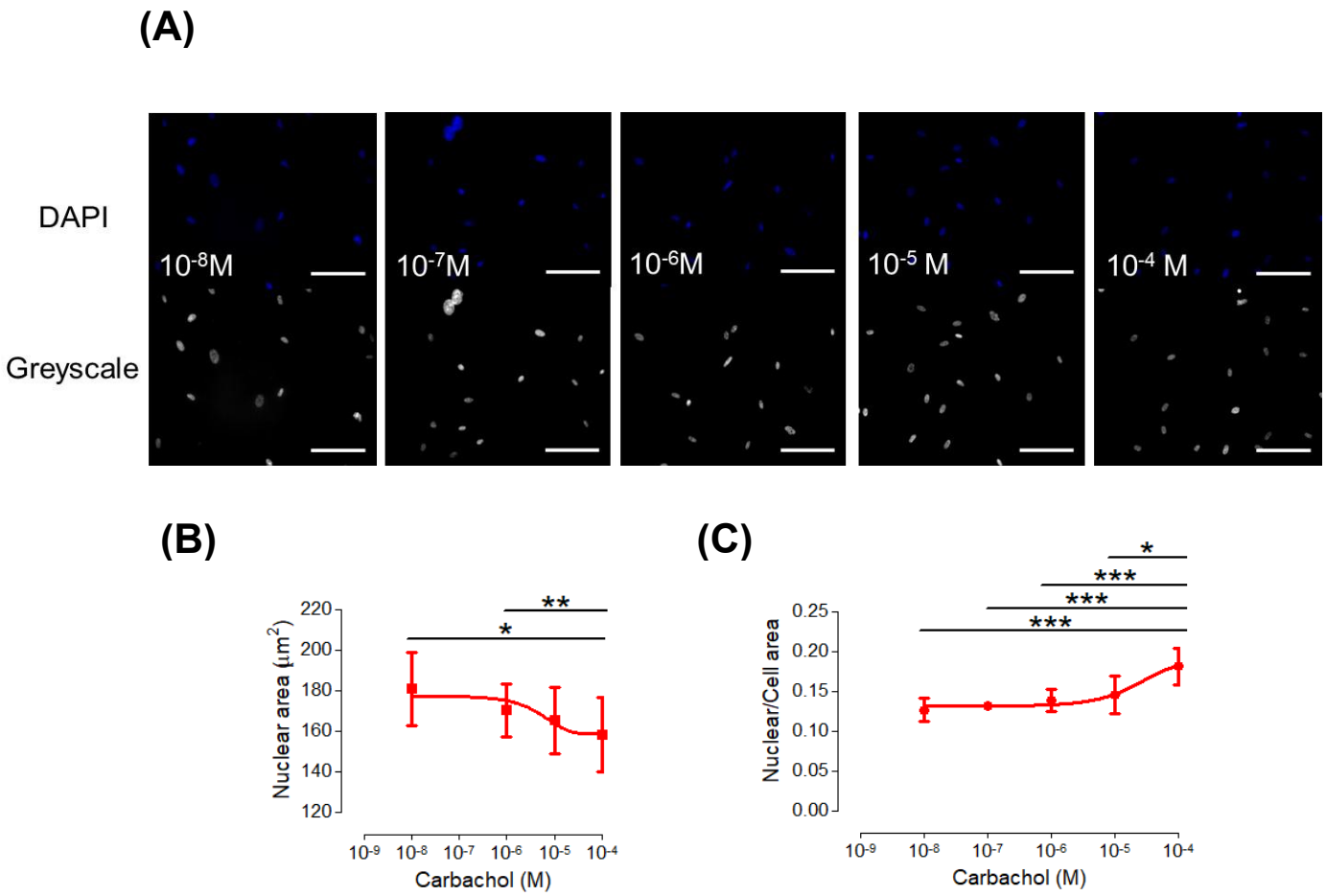

Figure 4.5: The impact of Carbachol treatment on VSMC nuclear morphology. **(A)** Representative immunofluorescence images of VSMC nuclei treated with a serial dilution of Carbachol. Images show VSMC nuclei stained using DAPI (blue) and grey-scale images of nuclei (grey) on 12 kPa polyacrylamide hydrogels. Scale bar represents 100 µm. Image J software was used to manually measure the **(B)** nuclear area and **(C)** shows the ratio between nuclear to cell area. Data are based on the measurement of >150 VSMCs from 3 independent experiments. Statistical significance was determined using a one-way ANOVA to show differences in nuclear area (* p = <0.05, ** p = <0.001) and nuclear to cell area ratio (* p = <0.05, *** p = <0.0001), followed by a Bonferroni's multiple comparison test. VSMC: Vascular smooth muscle cell.

Change in cell and nuclear area was compared between both agonists by overlaying graphs (**Figure 4.6A & B**), with no significant difference observed between them. The sigmoidal dose responses were subjected to a non-linear regression analysis and this gave corresponding EC50 values of both agonists (**Figure 4.6C**). Both Angiotensin II and

Carbachol yielded EC50 values of ~1 µM. As a result, our work shows that cell and nuclear area show a progressive decrease in response to increased doses of different contractile agonists, with identical EC50 values derives from both morphological parameters. Due to this, we observe that cell and nuclear area serve as a good guide to VSMC contractile function.

(A)

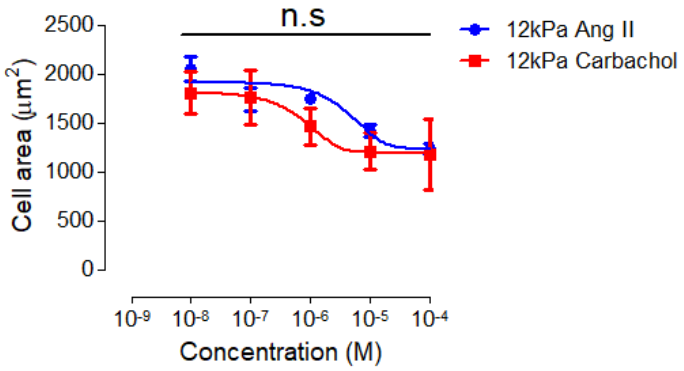

(B)

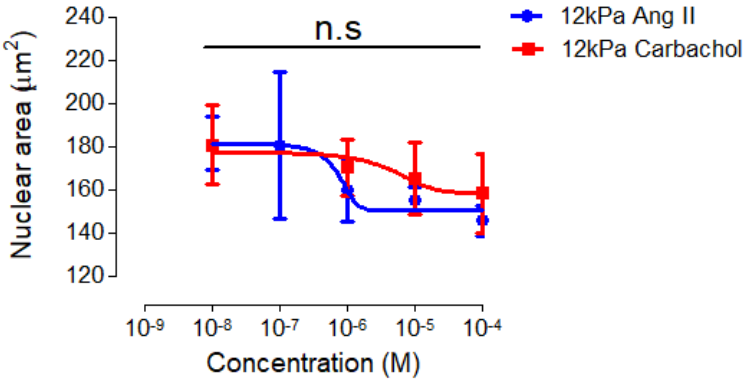

(C)

	EC50
Angiotensin II 12kPa	0.99µM
Carbachol 12kPa	1.00µM

Figure 4.6: Comparing the effect of contractile agonists on VSMC morphology. Graphs show overlay on the effect of Carbachol and Angiotensin II on VSMC **(A)** cell area and **(B)** nuclear area on 12 kPa polyacrylamide hydrogels. **(C)** Shows EC50 values of Angiotensin II and Carbachol derived from non-linear regression analysis. Data are based on the measurement of >150 VSMCs from 3 independent experiments. Statistical significance was determined using a two-way ANOVA to show differences in cell area (non-significant; p = >0.05) and nuclear area (non-significant; p = >0.05), followed by a Bonferroni's multiple comparison test. VSMC: Vascular smooth muscle cell.

4.4.3 Inhibition of receptor-mediated effects

Next, we wanted to confirm whether the changes induced by the contractile agonists were receptor-mediated. To be able to do this, we utilised Irbesartan and Atropine which are receptor-specific antagonists for Angiotensin II and Carbachol, respectively. Irbesartan binds to Angiotensin II type 1 (AT1) receptor with an IC_{50} value of 1.6 nM, and has previously been shown to efficiently block the binding of angiotensin II to the AT1 receptor within VSMCs (268, 269).

Due to this, VSMCs were seeded on 12 kPa polyacrylamide hydrogels, as previously stated, and treated with a serial dilution of Irbesartan, ranging between 23 pM-230 nM, after the addition of 10 μM of Angiotensin II. Similarly, filamentous actin and nuclei were stained with rhodamine phalloidin and DAPI, respectively. Image J software revealed that the reduction in VSMC area induced by Angiotensin II stimulation is receptor-mediated as increasing doses of Irbesartan gradually restored VSMC morphology. Analysis showed that doses as low as 2.3 nM (1582±104.6 μm^2) can significantly increase VSMC area, thus showing Irbesartan is efficient in antagonising the effects discussed (**Figure 4.7**).

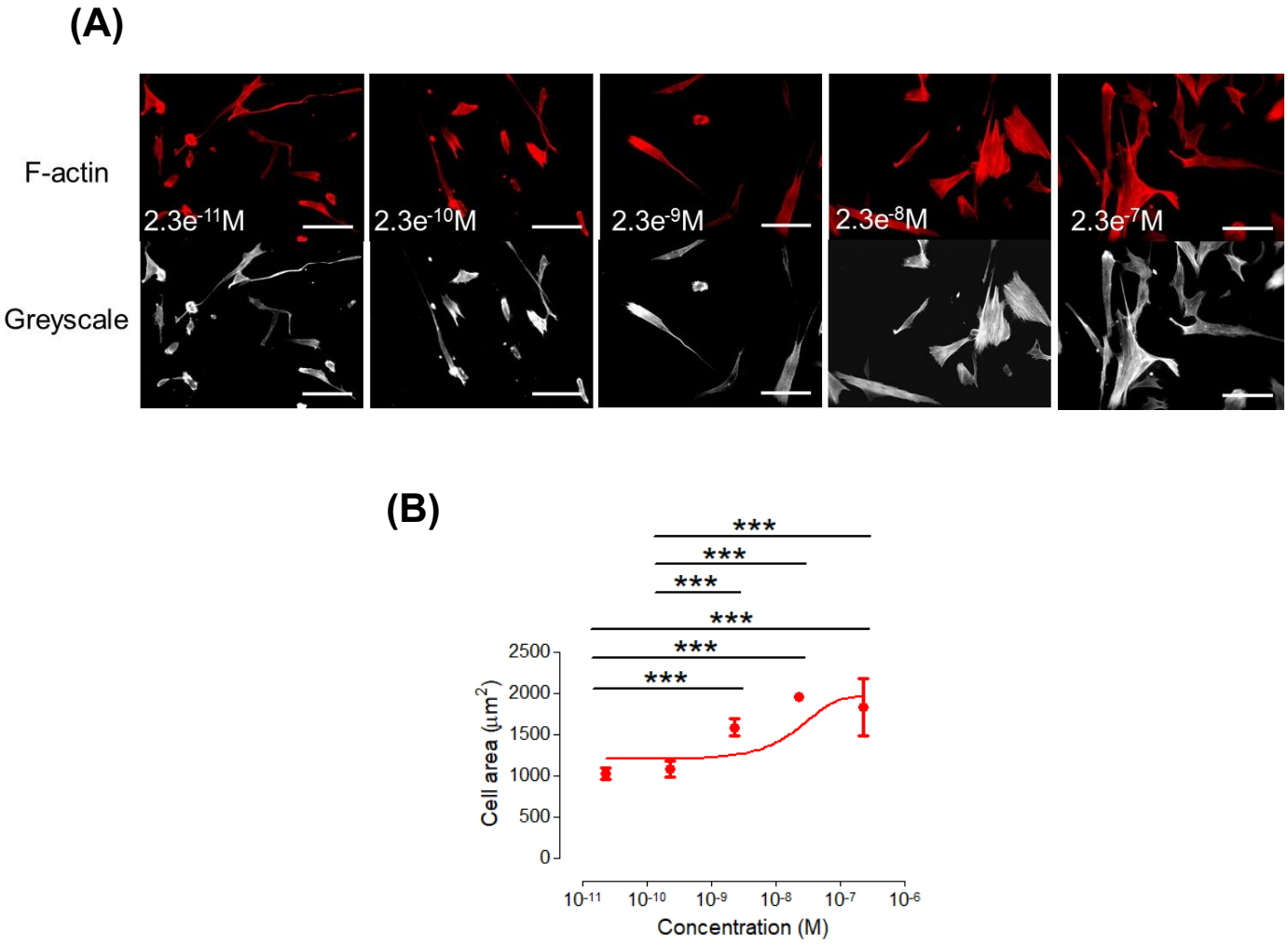

Figure 4.7: The impact of Irbesartan treatment on VSMC morphology. **(A)** Representative immunofluorescence images of VSMC actin filaments treated with a serial dilution of Irbesartan. Images show VSMC actin filaments (F-actin) stained using rhodamine phalloidin (red) and grey-scale images of F-actin (grey) on 12 kPa polyacrylamide hydrogels. Scale bar represents 100 µm. Image J software was used to manually measure the **(B)** cell area of the VSMCs. Data are based on the measurement of >150 VSMCs from 3 independent experiments. Statistical significance was determined using a one-way ANOVA to show differences in cell area (*** p = <0.0001), followed by a Bonferroni's multiple comparison test. VSMC: Vascular smooth muscle cell.

Likewise, nuclear area of VSMCs treated with Angiotensin II showed significant augmentations when utilising higher doses of Irbesartan (**Figure 4.8A & B**). Next, the cell and nuclear data was compiled and the relationship between both factors was investigated. It was discovered, via linear regression analysis, that the association between nuclear to cell area change was relatively weak (**Figure 4.8C**) and therefore there may be other differential factors that contribute to changes in morphology.

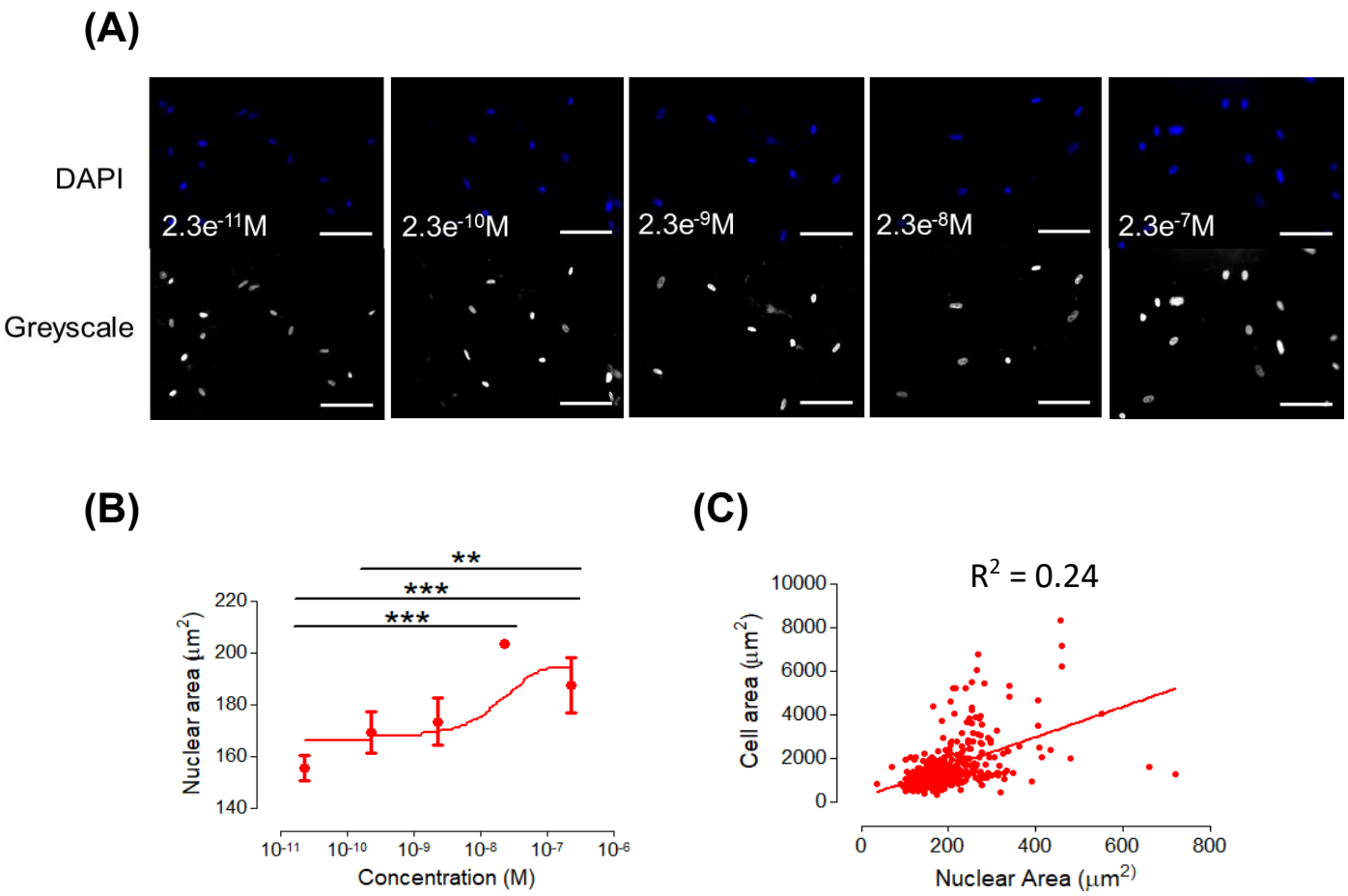

Figure 4.8: The impact of Irbesartan treatment on VSMC nuclear morphology. **(A)** Representative immunofluorescence images of VSMC nuclei treated with a serial dilution of Irbesartan. Images show VSMC nuclei stained using DAPI (blue) and grey-scale images of nuclei (grey) on 12 kPa polyacrylamide hydrogels. Scale bar represents 100 μm. Image J software was used to manually measure the **(B)** nuclear area of the VSMCs and **(C)** shows its relationship to cell area. Data are based on the measurement of >150 VSMCs from 3 independent experiments. Statistical significance was determined using a one-way ANOVA to show differences in nuclear area (** p = <0.001, *** p = <0.0001), followed by a Bonferroni's multiple comparison test. Additionally, statistical significance was also determined using linear regression analysis. VSMC: Vascular smooth muscle cell.

Following this, Atropine was utilised to see if Carbachol-mediated effects could also be inhibited. Atropine is a competitive antagonist that binds at acetylcholine-muscarinic receptors within smooth muscle, with an IC_{50} value of 8.5 nM (270, 271). To confirm this, we replicated our earlier experimental set up with Irbesartan, however this time with a serial dilution Atropine ranging between 36 pM-360 nM. Staining of the VSMCs was performed in the same way as previously described prior to immunofluorescence microscopy. Data analysis gave support to existing findings, revealing only a 38 nM dose of Atropine is required to significantly increase cell (2547±274 μm^2) and nuclear (118.4±8.097 μm^2) area

(**Figure 4.9 & 4.10**). Due to this, our work shows that the actomyosin-mediated morphological changes induced by contractile agonists can be regulated at the receptor level.

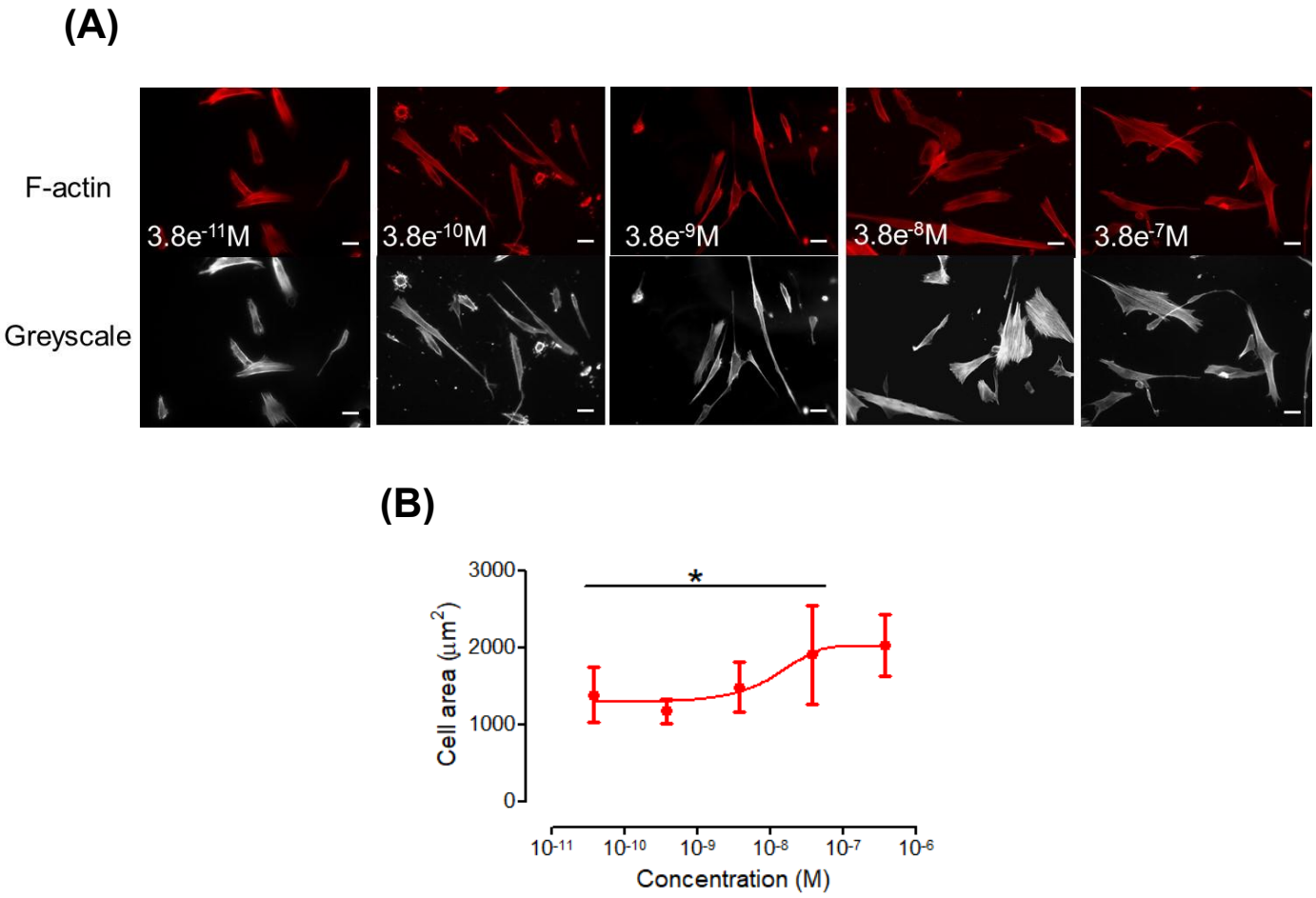

Figure 4.9: The impact of Atropine treatment on VSMC morphology. **(A)** Representative immunofluorescence images of VSMC actin filaments treated with a serial dilution of Atropine. Images show VSMC actin filaments (F-actin) stained using rhodamine phalloidin (red) and grey-scale images of F-actin (grey) on 12 kPa polyacrylamide hydrogels. Scale bar represents 100 µm. Image J software was used to manually measure the **(B)** cell area of the VSMCs. Data are based on the measurement of >50 VSMCs from 3 independent experiments. Statistical significance was determined using a one-way ANOVA to show differences in cell area (* p = <0.05), followed by a Bonferroni's multiple comparison test. VSMC: Vascular smooth muscle cell.

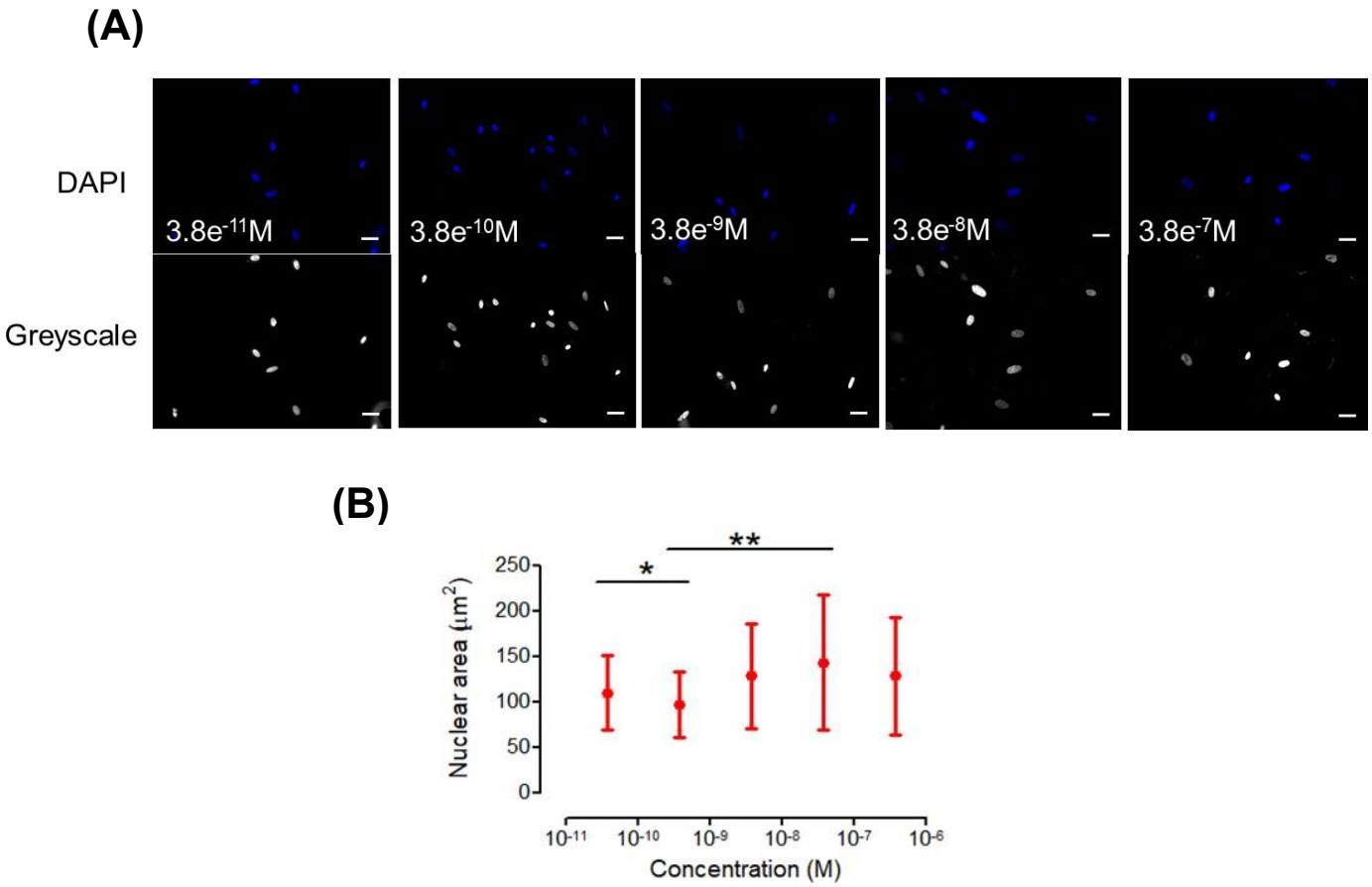

Figure 4.10: The impact of Atropine treatment on VSMC nuclear morphology. **(A)** Representative immunofluorescence images of VSMC nuclei treated with a serial dilution of Atropine. Images show VSMC nuclei stained using DAPI (blue) and grey-scale images of nuclei (grey) on 12 kPa polyacrylamide hydrogels. Scale bar represents 100 µm. Image J software was used to manually measure the **(B)** nuclear area of the VSMCs. Data are based on the measurement of >150 VSMCs from 3 independent experiments. Statistical significance was determined using a one-way ANOVA to show differences in nuclear area (* p = <0.05, ** p = <0.001), followed by a Bonferroni's multiple comparison test. VSMC: Vascular smooth muscle cell.

4.4.4 Inhibition of agonist-mediated effects on VSMC morphology

The work conducted within this chapter so far shows that contractile agonists can cause similar morphological changes within VSMCs on a compliant matrix. However, further work is required to elucidate the mechanism driving this, and in particular, to confirm if these changes occur via stimulated actomyosin activity. This chapter expands on this by utilising a variety of actomyosin inhibitors to see if the observed morphological response can be inhibited.

VSMC tonic contractions maintain vascular tone in the absence of external stimuli and they are regulated by the calcium-independent pathway (80). One of the key molecular

components of this pathway is the serine/threonine kinase ROCK (86). ROCK displays a myriad of functions within VSMCs, with its core action in regulating contractile activity. It does this primarily through the inhibition of myosin light chain phosphatase (80, 86). Earlier work has utilised 5 μM of Y-27632, a ROCK-specific inhibitor, to investigate the role of VSMC actomyosin activity (207). We hypothesised that inhibiting ROCK kinase would restore morphological characteristics of VSMCs prior to contraction.

To be able to investigate this, VSMCs were grown in basal media and seeded on collagen-1 coated polyacrylamide hydrogels, with an average Young's modulus of 12 kPa. VSMCs were pre-treated with 10 μM of Angiotensin II and this was followed with the addition of a 5 μM of Y-27632. Prior to microscopy imaging, filamentous actin and nuclei of VSMCs were stained with rhodamine phalloidin and lamin A/C, respectively. Using Image J software, it was shown VSMCs presented significantly larger cell and nuclear areas when co-treated with Y-27632 as opposed to Angiotensin II alone (**Figure 4.11**). This revealed that abolishment of actomyosin activity via ROCK inhibition restored the morphological changes previously induced by Angiotensin II.

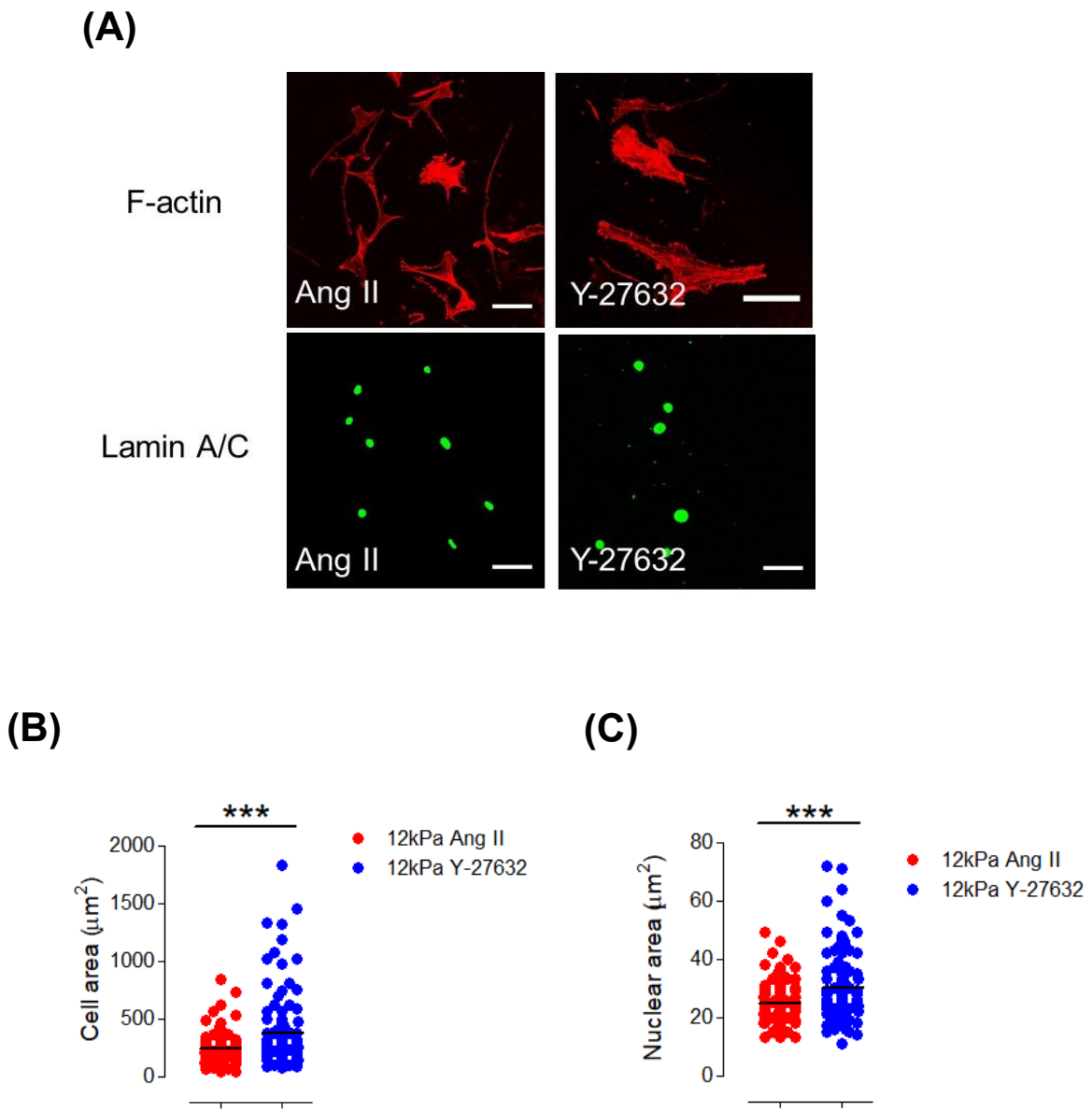

Figure 4.11: The effect of a ROCK inhibitor on VSMC morphology. **(A)** Representative immunofluorescence images of VSMC actin filaments and nuclei treated with Y-27632. Images show VSMC actin filaments (F-actin) stained using rhodamine phalloidin (red) and nuclei stained using lamin A/C (green) on 12 kPa polyacrylamide hydrogels. Scale bar represents 100 µm. Image J software was used to manually measure the **(B)** cell area and **(C)** nuclear area of the VSMCs. Data are based on the measurement of >150 VSMCs from 3 independent experiments. Statistical significance was determined using a paired Student's *t* test on cell area and nuclear area (Ang II vs Y-27632) (*** p = <0.0001). Ang II: Angiotensin II; ROCK: Rho-associated protein kinase; VSMC: Vascular smooth muscle cell.

To consolidate this, we utilised the NM-myosin II inhibitor Blebbistatin and Atorvastatin inhibitor to build upon our findings. Blebbistatin binds to the myosin head which interferes with phosphate release, and has previously been utilised at 40 µM to inhibit VSMC

actomyosin activity (207, 272). Contrastingly, Atorvastatin prevents the formation of isoprenoid intermediates which are essential for the activation of small GTP-binding proteins such as Rho (273). Like Blebbistatin, Atorvastatin has been utilised within earlier VSMC studies, with concentrations ~1 µM (274). As a result, both compounds work effectively to inhibit VSMC contractility.

Due to this, we set up identical experimental conditions to **Figure 4.11**, however this time with 40 µM of Blebbistatin or 0.5 µM of Atorvastatin. Similarly, we stained VSMC actin filaments and nuclei with rhodamine phalloidin and lamin A/C, respectively. Analysis of resulting microscopy images show these results fall in agreement with previous findings, presenting significant increases in both VSMC and nuclear area in response to both treatments (**Figure 4.12 & 4.13A-C)**. As expected, this confirmed that VSMC morphological changes induced via contractile agonists are actomyosin-dependent.

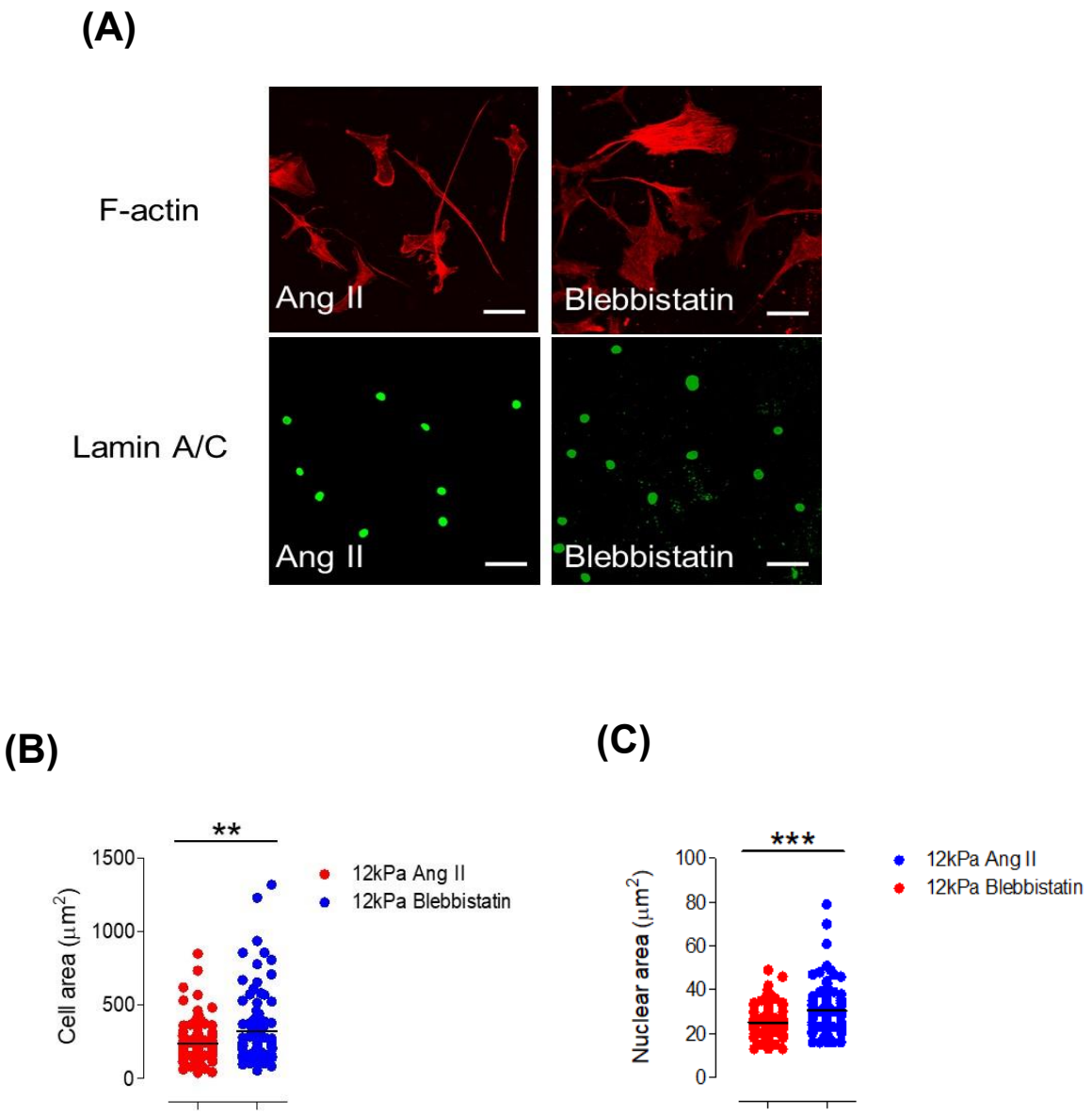

Figure 4.12: The effect of a Myosin II inhibitor on VSMC morphology. **(A)** Representative immunofluorescence images of VSMC actin filaments and nuclei treated with Blebbistatin. Images show VSMC actin filaments (F-actin) stained using rhodamine phalloidin (red) and nuclei stained using lamin A/C (green) on 12 kPa polyacrylamide hydrogels. Scale bar represents 100 μm. Image J software was used to manually measure the **(B)** cell area and **(C)** nuclear area of the VSMCs. Data are based on the measurement of >150 VSMCs from 3 independent experiments. Statistical significance was determined using a paired Student's *t* test on cell area and nuclear area (Ang II vs Blebbistatin) (** p = <0.001, *** p = <0.0001). Ang II: Angiotensin II; VSMC: Vascular smooth muscle cell.

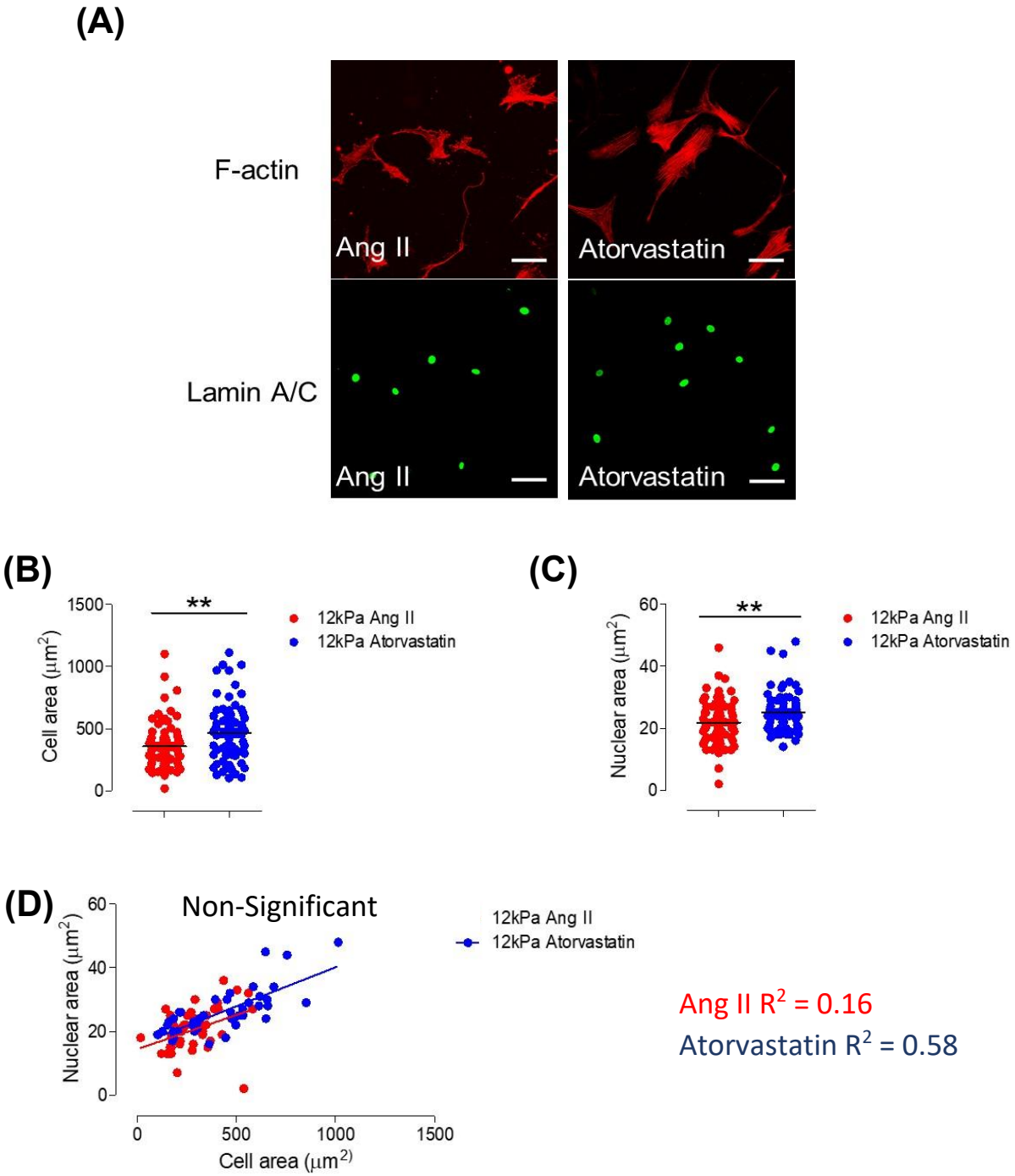

Figure 4.13: The effect of Atorvastatin on VSMC morphology. **(A)** Representative immunofluorescence images of VSMC actin filaments and nuclei treated with Atorvastatin. Images show VSMC actin filaments (F-actin) stained using rhodamine phalloidin (red) and nuclei stained using lamin A/C (green) on 12 kPa polyacrylamide hydrogels. Scale bar represents 100 μm. Image J software was used to manually measure the **(B)** cell area and **(C)** nuclear area of the VSMCs and **(D)** shows the relationship between both. Data are based on the measurement of >150 VSMCs from 3 independent experiments. Statistical significance was determined using a paired Student's *t* test on cell and nuclear area (Ang II vs Atorvastatin) (** p = <0.001). Additionally, a linear regression analysis was used to determine statistical significance for the cell and nuclear area relationship (non-significant; p = >0.05). Ang II: Angiotensin II; VSMC: Vascular smooth muscle cell.

Following this, the relationship between VSMC area and nuclear area was investigated via linear regression analysis (**Figure 4.13D**). This relationship was subjected to Angiotensin II treatment alone and with Atorvastatin. Despite presenting a moderate relationship for the nucleocytoplasmic ratio, Atorvastatin presented no significant difference to Angiotensin II.

4.4.5 Effect of matrix stiffness on contractile quiescent VSMCs

The above data describes how contractile stimulation of quiescent VSMCs causes morphological changes on pliable polyacrylamide hydrogels. Next, we examined the effect of matrix stiffness on quiescent VSMCs. VSMCs typically undergo a change in mechanical environment during cardiovascular disease development, in which aortic stiffness becomes a predicative biomarker (14-16). Due to this, we utilised our novel assay to examine the relationship between quiescent contractile activity, decreased compliance and change in VSMC morphology more closely.

To begin with, we looked at the effect of Angiotensin II and matrix stiffness on quiescent VSMCs. To do this, VSMCs were cultured in basal medium and seeded on collagen-1 coated polyacrylamide hydrogels, with an average Young's modulus of 72 kPa. Cells were treated with a serial dilution of Angiotensin II, and F-actin was stained with rhodamine phalloidin prior to microscopy imaging. Image J analysis revealed that, similarly to 12 kPa, concentrations of 10 uM (1965±100.1 μm^2) and 100uM (2137±134.0 μm^2) were found to evoke significant changes compared to their lower dose counterparts. However, in this case, it was found that stronger stimulation of VSMC contractile activity within a rigid environment rather increased cell spreading (**Figure 4.14A & B**). Following this, we wanted to compare the effects of Angiotensin II on quiescent VSMC morphology between the physiological and rigid environments. To do this, we generated an overlay of the 12 kPa and 72 kPa response. Performing a two-way ANOVA, it was shown that VSMC area presented significance between both rigidities for doses of 0.01 µM, 0.1 µM, 10 µM and 100 µM (**Figure4.14C**).

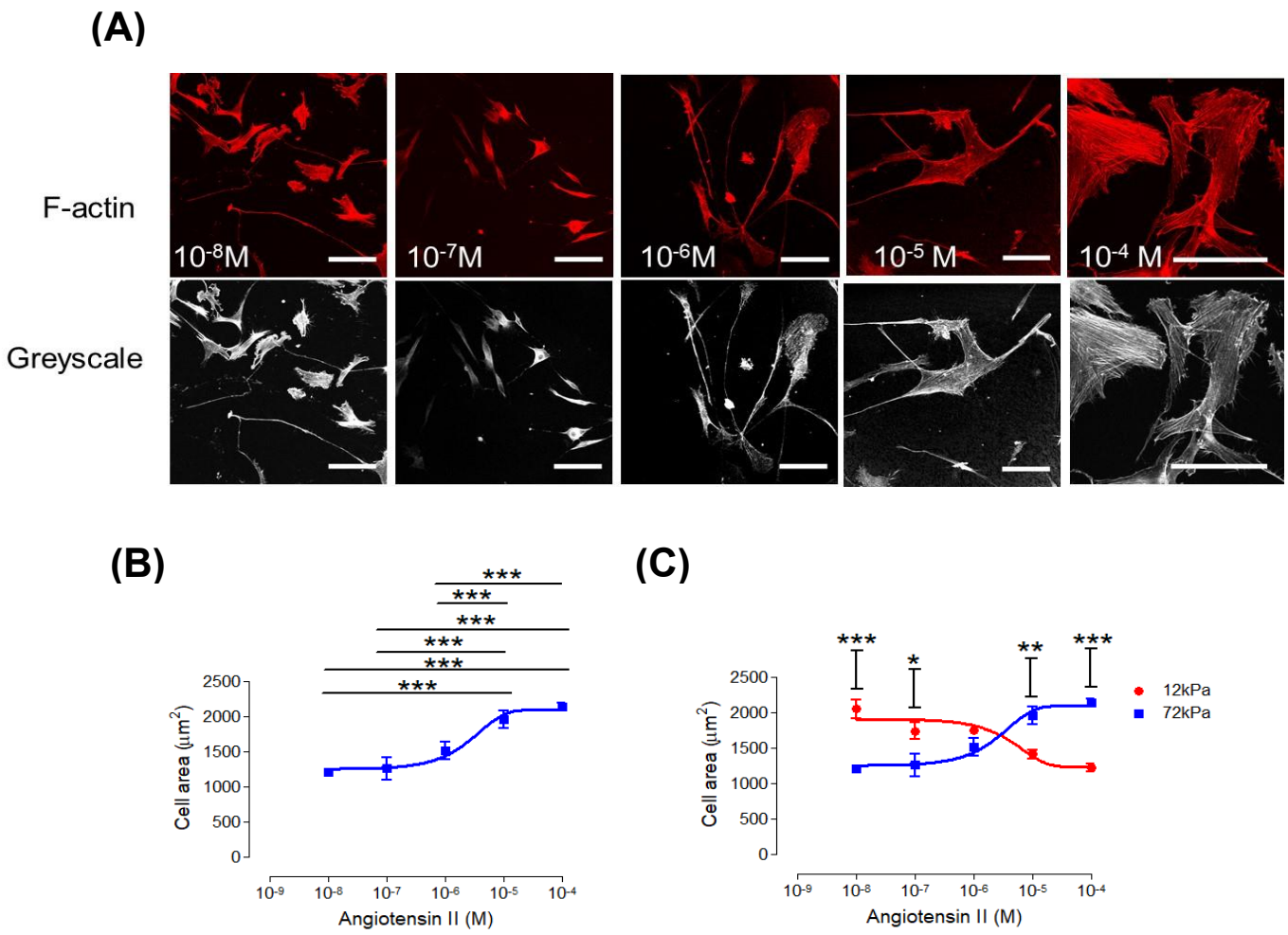

Figure 4.14: The impact of Angiotensin II treatment and matrix stiffness on VSMC morphology. **(A)** Representative immunofluorescence images of VSMC actin filaments treated with a serial dilution of Angiotensin II. Images show VSMC actin filaments (F-actin) stained using rhodamine phalloidin (red) and grey-scale images of F-actin (grey) on 72 kPa polyacrylamide hydrogels. Scale bar represents 100 µm. Image J software was used to manually measure the **(B)** cell area and **(C)** shows an overlay of 12 kPa and 72 kPa cell area change. Data are based on the measurement of >150 VSMCs from 3 independent experiments. Statistical significance was determined using a one-way ANOVA to show differences in cell area (*** p = <0.0001). Additionally, a two-way ANOVA was utilised to show differences between 12 kPa and 72 kPa cell area changes (* p = <0.05, ** p = <0.001, *** p = <0.0001) Both tests were followed by a Bonferroni's multiple comparison test. VSMC: Vascular smooth muscle cell.

Next, we looked at VSMC nuclei via DAPI staining and results presented a similar pattern, with higher doses causing a significant augmentation in area (**Figure 4.15A & B**). When comparing nuclear area change between 12 kPa and 72 kPa, two-way ANOVA revealed significance at 100 µM (**Figure 4.15C**).

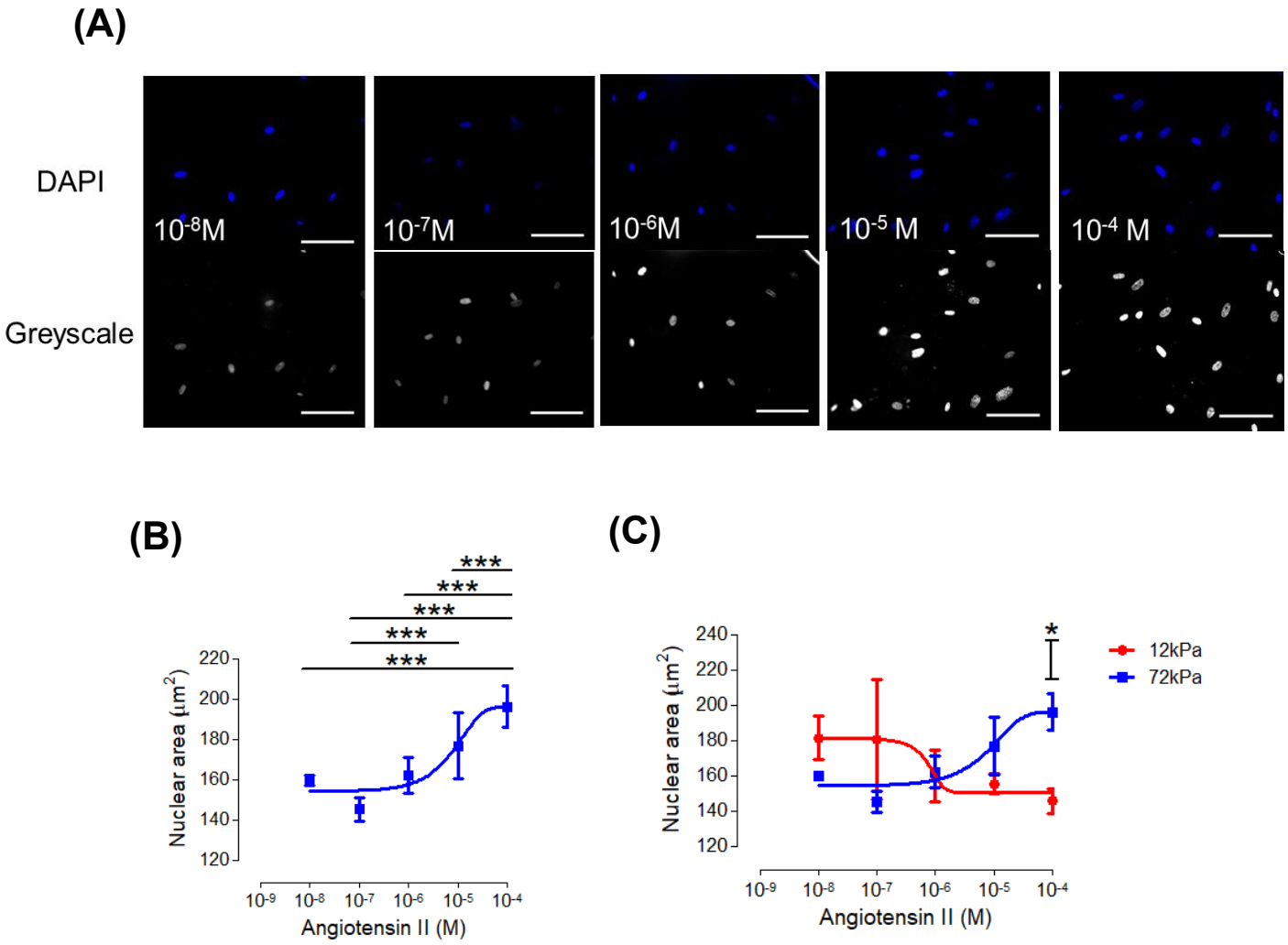

Figure 4.15: The impact of Angiotensin II treatment and matrix stiffness on VSMC nuclear morphology. **(A)** Representative immunofluorescence images of VSMC nuclei treated with a serial dilution of Angiotensin II. Images show VSMC nuclei stained using DAPI (blue) and grey-scale images of nuclei (grey) on 72 kPa polyacrylamide hydrogels. Scale bar represents 100 µm. Image J software was used to manually measure the **(B)** nuclear area and **(C)** shows an overlay of 12 kPa and 72 kPa nuclear area change. Data are based on the measurement of >150 VSMCs from 3 independent experiments. Statistical significance was determined using a one-way ANOVA to show differences in nuclear area (*** p = <0.0001). Additionally, a two-way ANOVA was utilised to show differences between 12 kPa and 72 kPa nuclear area changes (* p = <0.05). Both tests were followed by a Bonferroni's multiple comparison test. VSMC: Vascular smooth muscle cell.

After, we wanted to see if the nucleocytoplasmic ratio showed any significant changes in response to Angiotensin II within the rigid environment. Our results show both 10 µM (0.1224±0.007) and 100µM (0.1260±0.007) addition of Angiotensin II significantly decreases this ratio, suggesting VSMC area shows greater spreading than its nuclei in response to stiffness (**Figure 4.16A**). When comparing the nucleocytoplasmic ratio changes from both

physiological and pathological stiffness, there was no significant difference detected (**Figure 4.16B**).

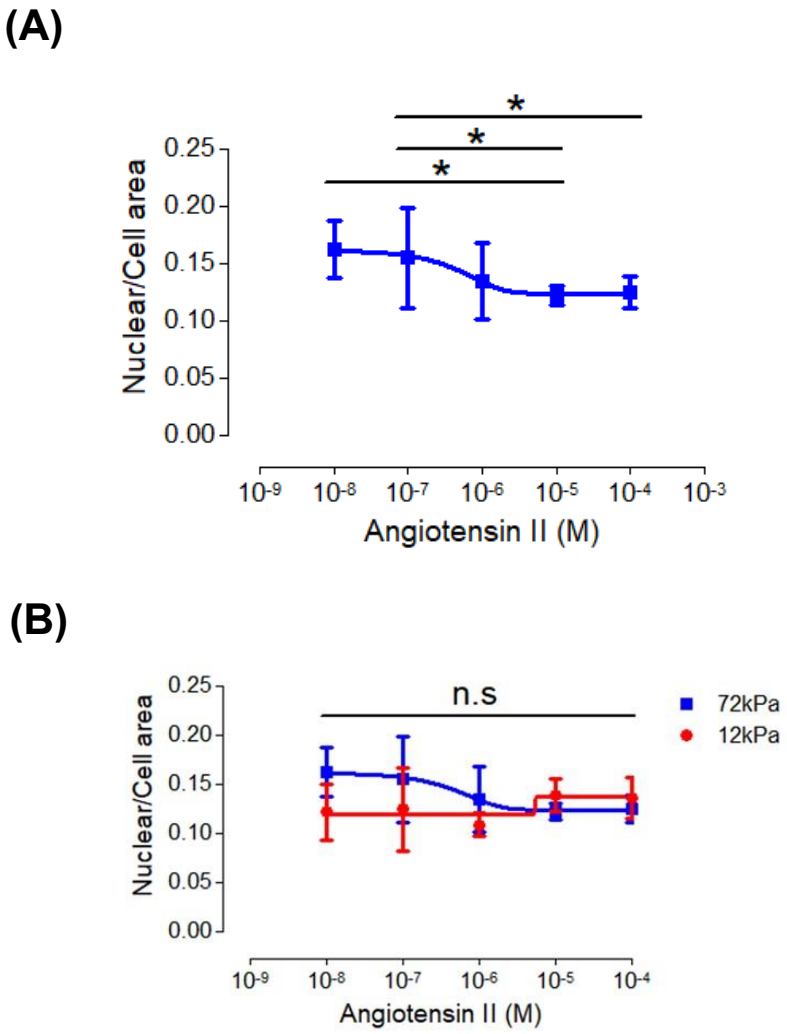

Figure 4.16: Comparing the effect of matrix stiffness on VSMC nuclear area to cell area ratio using Angiotensin II. **(A)** shows the ratio between nuclear to cell area of VSMCs seeded on 72 kPa polyacrylamide hydrogels in response to a serial dilution treatment of Angiotensin II. **(B)** shows an overlay which compares this ratio between VSMCs seeded on 12 kPa and 72 kPa polyacrylamide hydrogels. Data are based on the measurement of >150 VSMCs from 3 independent experiments. Statistical significance was determined using a one-way ANOVA to show differences in VSMC nuclear to cell area ratio on 72 kPa hydrogels (* p = <0.05). Additionally, a two-way ANOVA was utilised to show differences between 12 kPa and 72 kPa nuclear to cell area ratios (non-significant; p = >0.05). Both tests were followed by a Bonferroni's multiple comparison test. VSMC: Vascular smooth muscle cell.

To consolidate this, we utilised Carbachol once more as a secondary agonist. Like Angiotensin II, 10 uM (2121±149.7 μm^2) and 100 uM (2042±141.5 μm^2) of Carbachol caused

significant augmentations in VSMC area (**Figure 4.17A & B**) when seeded on the rigid environment. However, in this case, when comparing the physiological and pathological response via a two-way ANOVA, there was no significant difference detected, despite similar trend patterns to the initial agonist (**Figure 4.17C**).

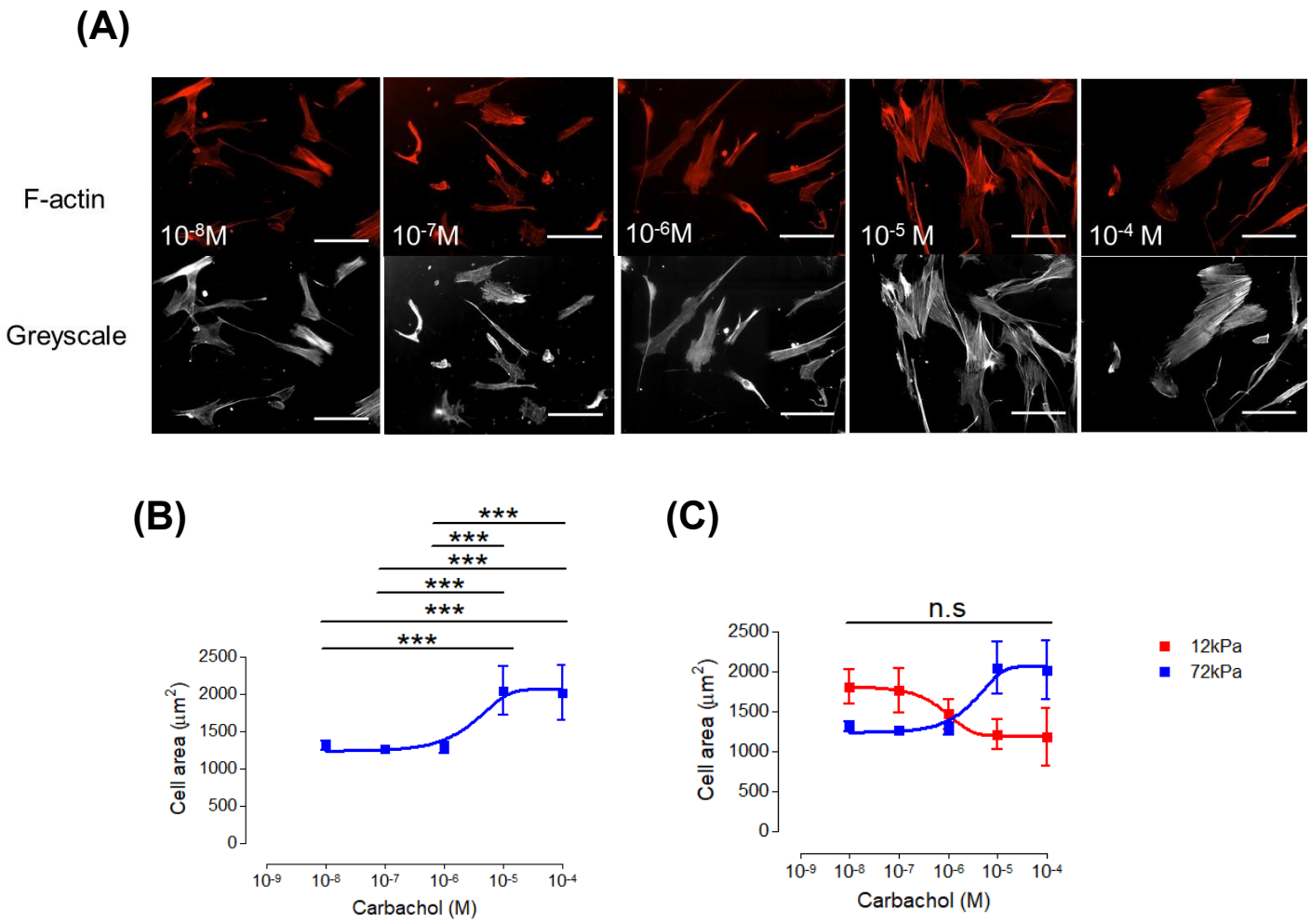

Figure 4.17: The impact of Carbachol treatment and matrix stiffness on VSMC morphology. **(A)** Representative immunofluorescence images of VSMC actin filaments treated with a serial dilution of Carbachol. Images show VSMC actin filaments (F-actin) stained using rhodamine phalloidin (red) and grey-scale images of F-actin (grey) on 72 kPa polyacrylamide hydrogels. Scale bar represents 100 µm. Image J software was used to manually measure the **(B)** cell area and **(C)** shows an overlay of 12 kPa and 72 kPa cell area change. Data are based on the measurement of >150 VSMCs from 3 independent experiments. Statistical significance was determined using a one-way ANOVA to show differences in cell area (*** p = <0.0001). Additionally, a two-way ANOVA was utilised to show differences between 12 kPa and 72 kPa cell area changes (non-significant; p = >0.05). Both tests were followed by a Bonferroni's multiple comparison test. VSMC: Vascular smooth muscle cell.

Additionally, nuclear spread showed comparable changes in response to matrix stiffness, with significant area augmentations presented from higher Carbachol stimulation

(**Figure 4.18A & B**). Like VSMC area, no significant changes of the nuclei were shown via Carbachol treatment when comparing the 12 kPa and 72 kPa response (**Figure 4.18C**).

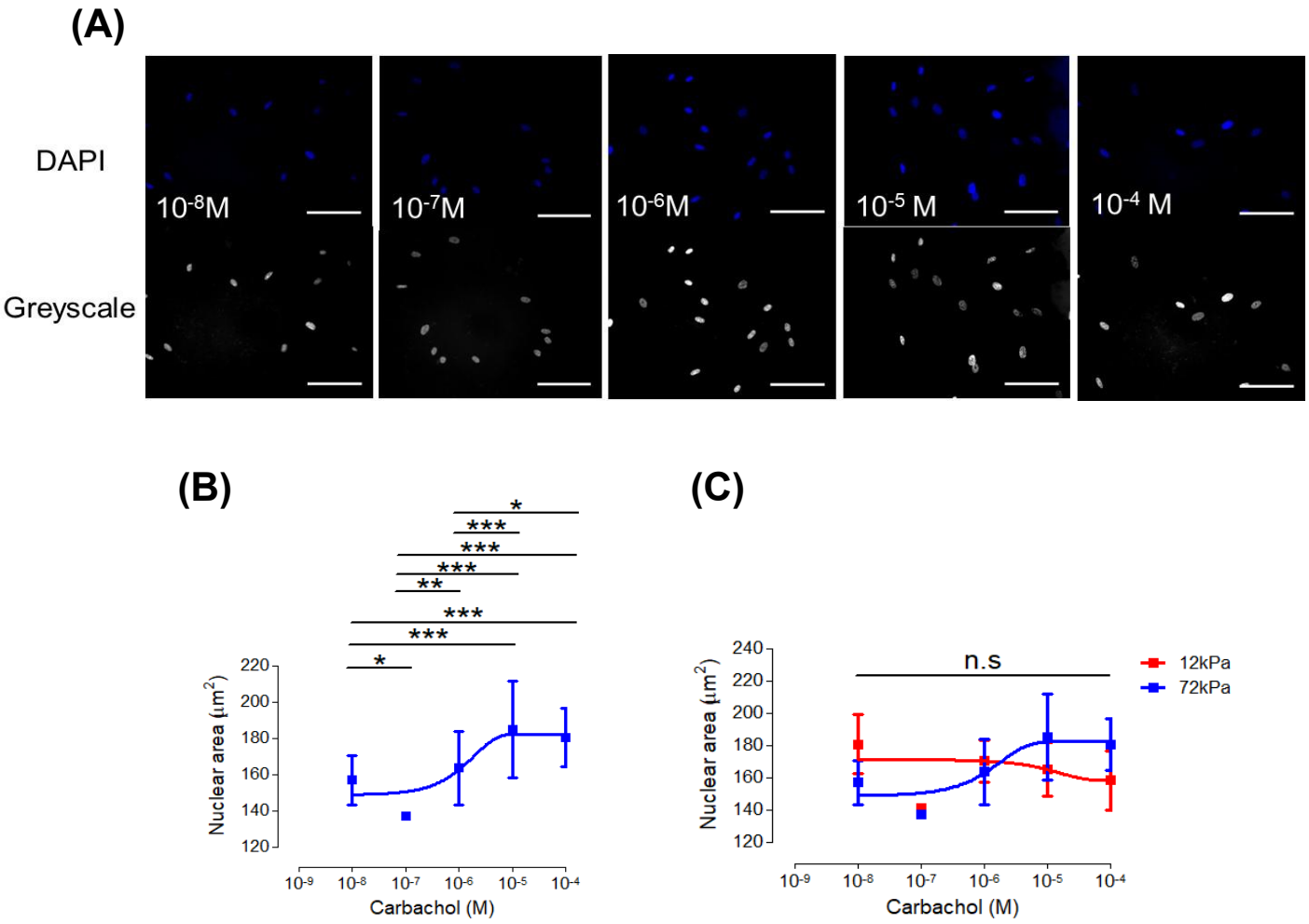

Figure 4.18: The impact of Carbachol treatment and matrix stiffness on VSMC nuclear morphology. **(A)** Representative immunofluorescence images of VSMC nuclei treated with a serial dilution of Carbachol. Images show VSMC nuclei stained using DAPI (blue) and grey-scale images of nuclei (grey) on 72 kPa polyacrylamide hydrogels. Scale bar represents 100 µm. Image J software was used to manually measure the **(B)** nuclear area and **(C)** shows an overlay of 12 kPa and 72 kPa nuclear area change. Data are based on the measurement of >150 VSMCs from 3 independent experiments. Statistical significance was determined using a one-way ANOVA to show differences in nuclear area (* p = <0.05, ** p = <0.001, *** p = <0.0001). Additionally, a two-way ANOVA was utilised to show differences between 12 kPa and 72 kPa nuclear area changes (non-significant; p = >0.05). Both tests were followed by a Bonferroni's multiple comparison test. VSMC: Vascular smooth muscle cell.

Similar to the physiological environment, the nucleocytoplasmic ratio revealed a significant change in response to high concentrations to Carbachol. However, in the case of

stiffness, the nuclear/cell area ratio showed a decrease. The varied response between both rigidities was reaffirmed via two-way ANOVA analysis, revealing a significant change at 100 uM (**Figure 4.19**). From this, it becomes apparent that matrix compliance can differentially regulate agonist-induced morphological changes within VSMCs.

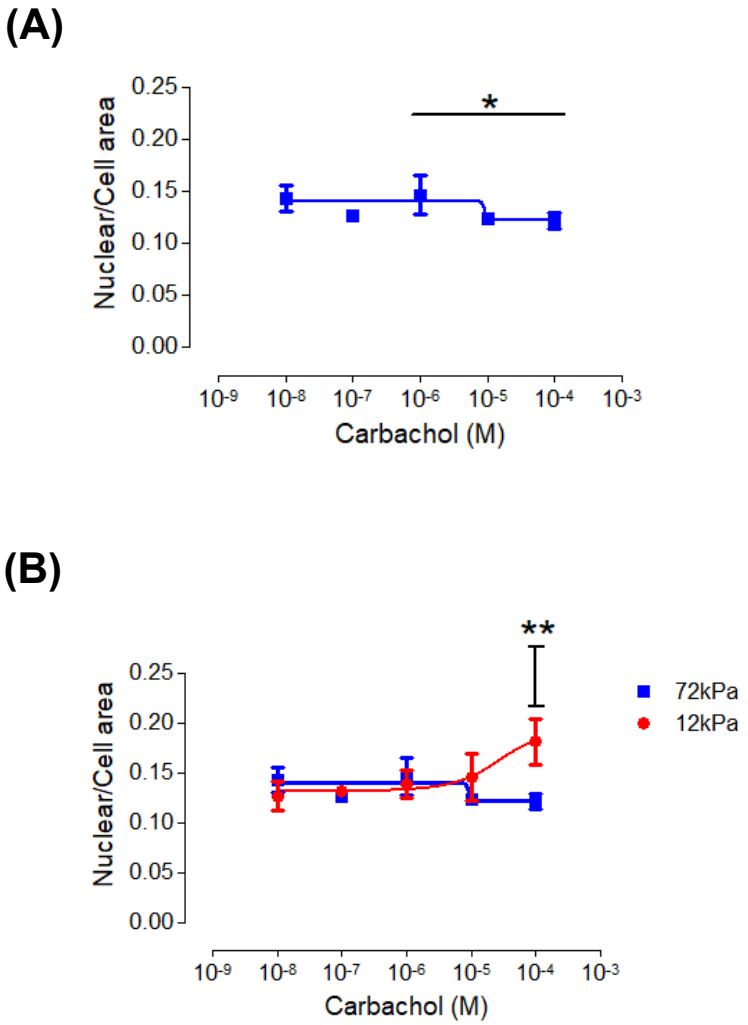

Figure 4.19: Comparing the effect of matrix stiffness on VSMC nuclear area to cell area ratio using Carbachol. **(A)** Shows the ratio between nuclear to cell area of VSMCs seeded on 72 kPa polyacrylamide hydrogels in response to a serial dilution treatment of Carbachol. **(B)** Shows an overlay which compares this ratio between VSMCs seeded on 12 kPa and 72 kPa polyacrylamide hydrogels. Data are based on the measurement of >150 VSMCs from 3 independent experiments. Statistical significance was determined using a one-way ANOVA to show differences in VSMC nuclear to cell area ratio on 72 kPa hydrogels (* p = <0.05). Additionally, a two-way ANOVA was utilised to show differences between 12 kPa and 72 kPa nuclear to cell area ratios (** p = <0.001). Both tests were followed by a Bonferroni's multiple comparison test. VSMC: Vascular smooth muscle cell.

Earlier, we showed how our novel contractile assay could successfully extract the EC50 values of different contractile agonists. Therefore, we wanted to investigate whether this function of our assay was possible within a range of rigidities. To do this, we compared the cell and nuclear area change between both agonists on a 72 kPa polyacrylamide hydrogel (**Figure 4.20A & B**). A non-linear regression analysis was performed on the sigmoidal dose curves and the trends positively revealed the corresponding EC50 values of our agonists (**Figure 4.20C**). Data showed that agonists maintained the same EC50 values as observed within the physiological environment, displaying values close or equal to 1 uM.

(A)

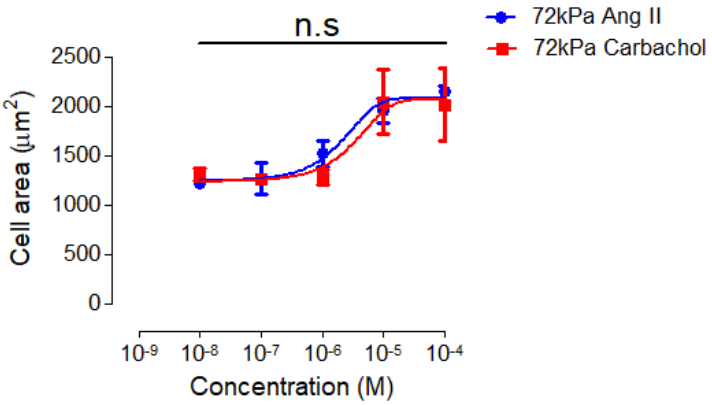

(B)

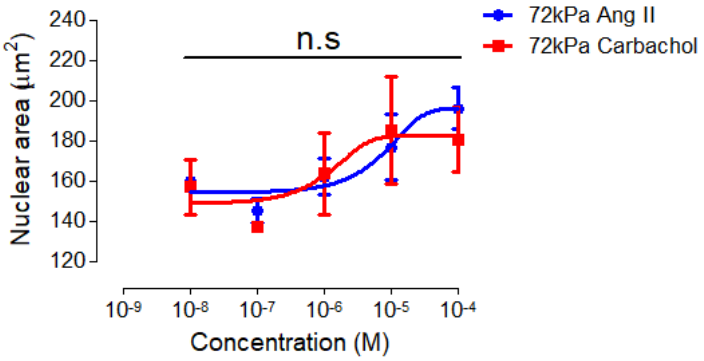

(C)

	EC50
Angiotensin II 72kPa	1.00µM
Carbachol 72kPa	0.99µM

Figure 4.20: Comparing the effect of contractile agonists on VSMC morphology within a stiffer environment. Graphs show overlay on the effect of Carbachol and Angiotensin II on VSMC **(A)** cell area and **(B)** nuclear area on 72 kPa polyacrylamide hydrogels. **(C)** shows EC50 values of Angiotensin II and Carbachol derived from non-linear regression analysis. Data are based on the measurement of >150 VSMCs from 3 independent experiments. Statistical significance was determined using a two-way ANOVA to show differences in cell area (non-significant; p = >0.05) and nuclear area (non-significant; p = >0.05), followed by a Bonferroni's multiple comparison test. VSMC: Vascular smooth muscle cell.

4.4.6 Inhibition of aberrant VSMC spreading

So far, it has been shown that contractile stimulation on a rigid matrix promotes cytoplasmic and nuclear spreading of VSMCs. Earlier work has shown that matrix stiffening also causes elevated levels of pMLC and Rho/ROCK activity in a variety of different cell types (275-277). To begin with, we wanted to confirm whether these effects, much like the physiological environment, were receptor-mediated. In order to investigate whether it possesses a role in inhibiting aberrant VSMC function, we utilised Irbesartan once more. Image J software revealed higher doses of Irbesartan significantly reduced VSMC area, preventing abnormal spreading (**Figure 4.21A & B**). When comparing its effect with VSMCs on a physiological environment, a two-way ANOVA analysis revealed significance between both responses at 2.3 nM (**Figure 4.21C**). Additionally, a 1 nM dose was established to be the IC50 value between both rigidities via non-linear regression analysis (**Figure 4.21D**).

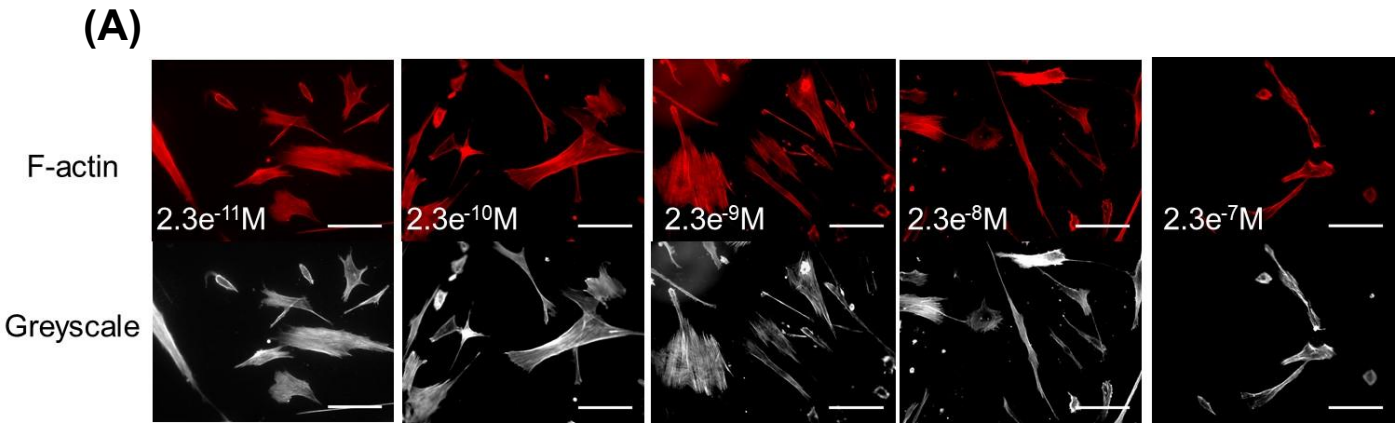

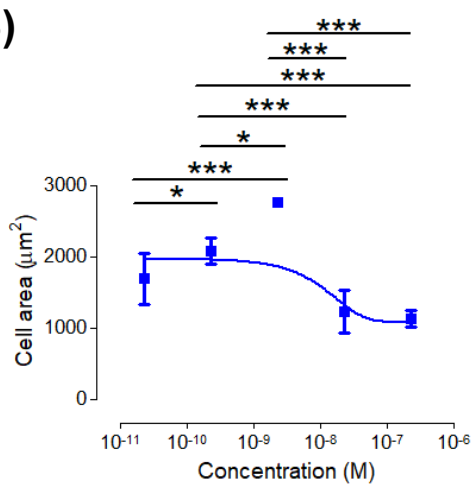

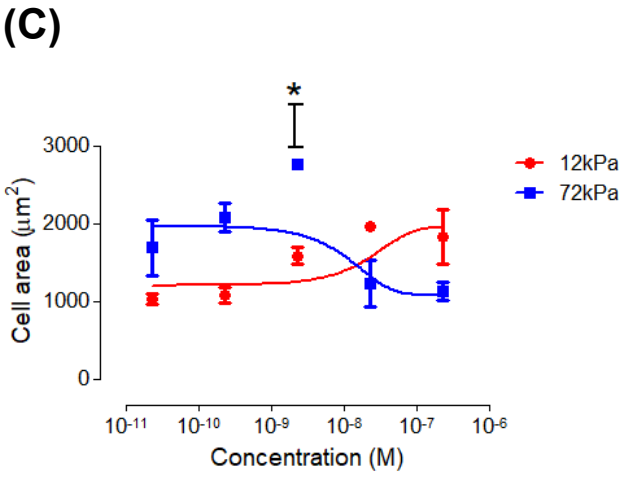

(D)

	IC50
Irbesartan 12kPa	1.00nM
Irbesartan 72kPa	1.00nM

Figure 4.21: The impact of Irbesartan treatment on VSMC morphology within a stiffer environment. **(A)** Representative immunofluorescence images of VSMC actin filaments treated with a serial dilution of Irbesartan. Images show VSMC actin filaments (F-actin) stained using rhodamine phalloidin (red) and grey-scale images of F-actin (grey) on 72 kPa polyacrylamide hydrogels. Scale bar represents 100 µm. Image J software was used to manually measure the **(B)** cell area of the VSMCs and **(C)** shows an overlay of 12 kPa and 72 kPa cell area change. **(D)** Shows EC50 values of Irbesartan in normal (12 kPa) and rigid (72 kPa) physiology derived from non-linear regression analysis. Data are based on the measurement of >150 VSMCs from 3 independent experiments. Statistical significance was determined using a one-way ANOVA to show differences in cell area (* p = <0.05, *** p = <0.0001). Additionally, a two-way ANOVA was utilised to show differences between 12 kPa and 72 kPa cell area changes (* p = <0.05). Both tests were followed by a Bonferroni's multiple comparison test. VSMC: Vascular smooth muscle cell.

An identical trend in size reduction was further shown when observing the nuclear response of VSMCs treated with Irbesartan (**Figure 4.22A & B**), although no significant difference was detected when comparing both rigidities (**Figure 4.22C**).

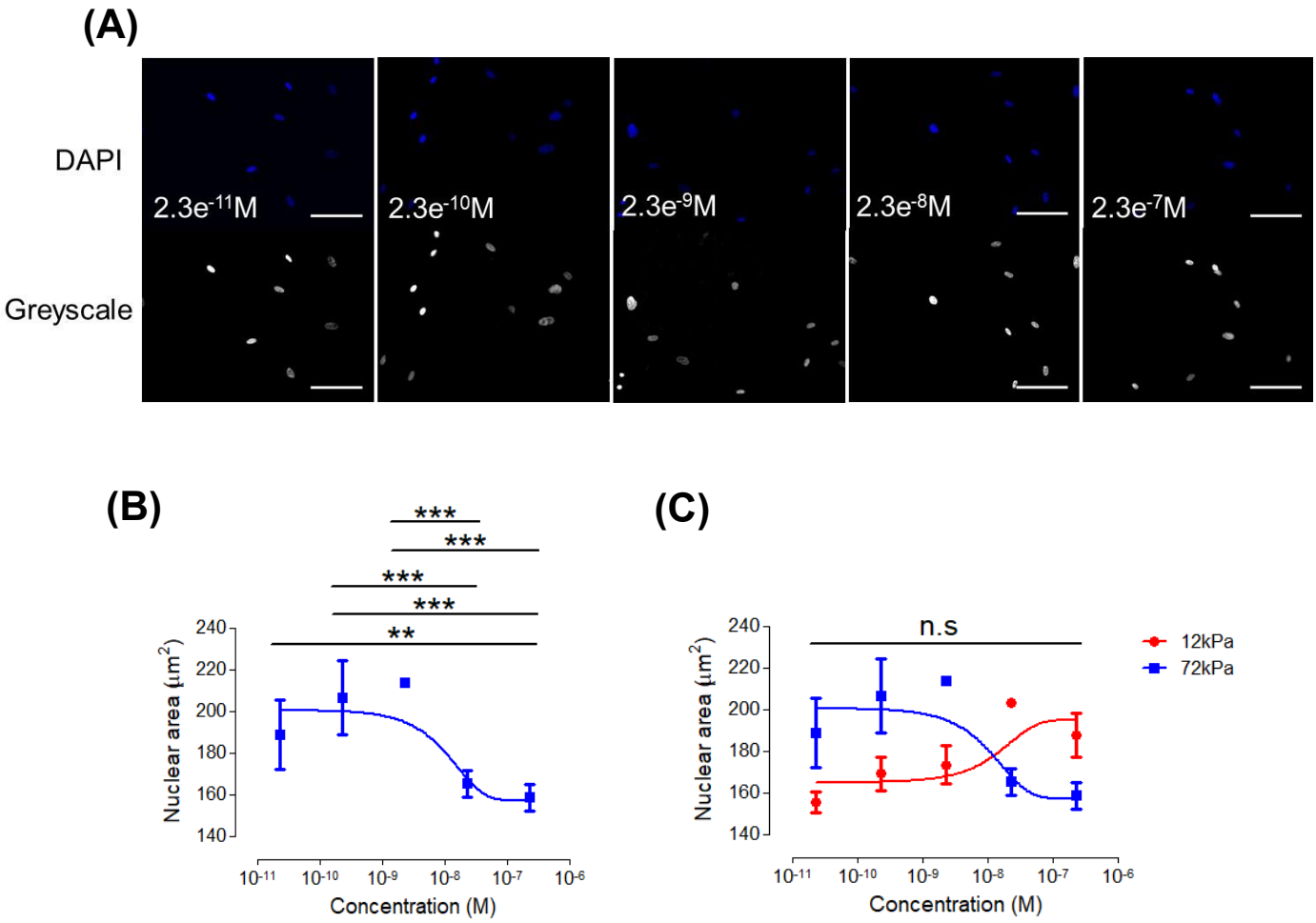

Figure 4.22: The impact of Irbesartan treatment on VSMC nuclear morphology within a stiffer environment. **(A)** Representative immunofluorescence images of VSMC nuclei treated with a serial dilution of Irbesartan. Images show VSMC nuclei stained using DAPI (blue) and grey-scale images of nuclei (grey) on 72 kPa polyacrylamide hydrogels. Scale bar represents 100 µm. Image J software was used to manually measure the **(B)** nuclear area of the VSMCs and **(C)** shows an overlay of 12 kPa and 72 kPa nuclear area change. Data are based on the measurement of >150 VSMCs from 3 independent experiments. Statistical significance was determined using a one-way ANOVA to show differences in nuclear area (** p = <0.001, *** p = <0.0001). Additionally, a two-way ANOVA was utilised to show differences between 12 kPa and 72 kPa cell area changes (non-significant; p = >0.05). Both tests were followed by a Bonferroni's multiple comparison test. VSMC: Vascular smooth muscle cell.

To supplement this, Atropine was utilised in a serial-dilution manner within the rigid environment and imaging/analysis was performed, as previously described. Results showed that a 360 nM dose of Atropine can restore VSMC morphology due to a significant reduction

(**Figure 4.23A & B**). Comparison with the physiological environment presents an inverted trend, however no significant difference was detected (**Figure 4.23C**). Much like Irbesartan, a non-linear regression analysis revealed IC50 values of Atropine to be approximately 1 nM in both the healthy and stiffer environment (**Figure 4.23D**).

(A)

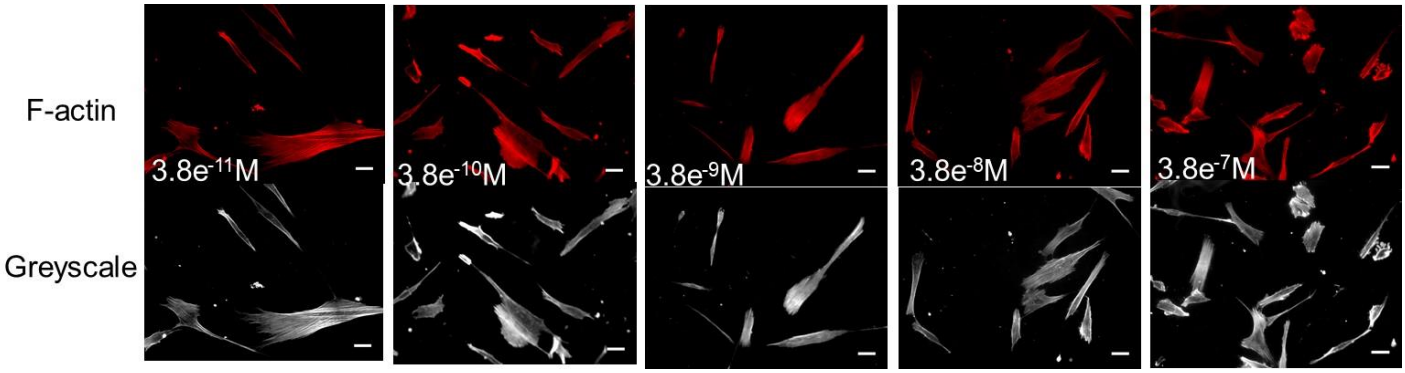

(B)

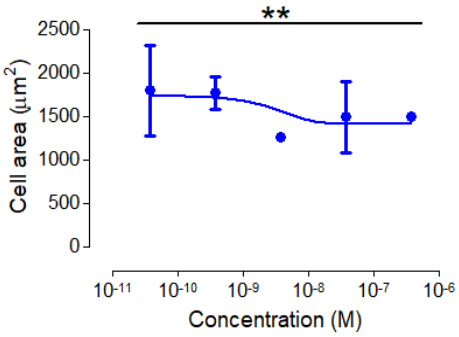

(C

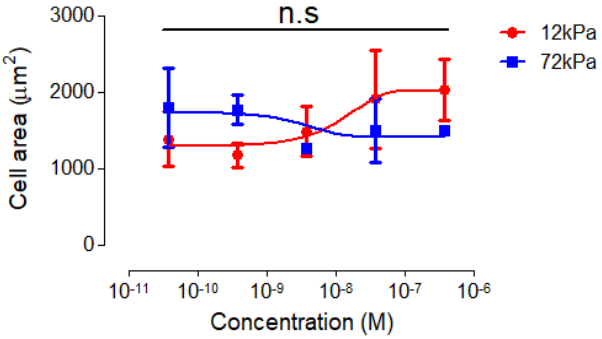

(D)

	IC50
Atropine 12kPa	1.00nM
Atropine 72kPa	1.00nM

Figure 4.23: The impact of Atropine treatment on VSMC morphology within a stiffer environment. **(A)** Representative immunofluorescence images of VSMC actin filaments treated with a serial dilution of Atropine. Images show VSMC actin filaments (F-actin) stained using rhodamine phalloidin (red) and grey-scale images of F-actin (grey) on 72 kPa polyacrylamide hydrogels. Scale bar represents 100 µm. Image J software was used to manually measure the **(B)** cell area of the VSMCs and **(C)** shows an overlay of 12 kPa and 72 kPa cell area change. **(D)** Shows EC50 values of Atropine in normal (12 kPa) and rigid (72 kPa) physiology derived from non-linear regression analysis. Data are based on the measurement of >150 VSMCs from 3 independent experiments. Statistical significance was determined using a one-way ANOVA to show differences in cell area (** p = <0.001). Additionally, a two-way ANOVA was utilised to show differences between 12 kPa and 72 kPa cell area changes (non-significant; p = >0.05). Both tests were followed by a Bonferroni's multiple comparison test. VSMC: Vascular smooth muscle cell.

Despite this, Atropine treatment was found to further stimulate nuclear spreading in response to matrix stiffness (**Figure 4.24A & B**), showing a very similar trend to prior results observed on the 12 kPa polyacrylamide hydrogel (**Figure 4.24C**).

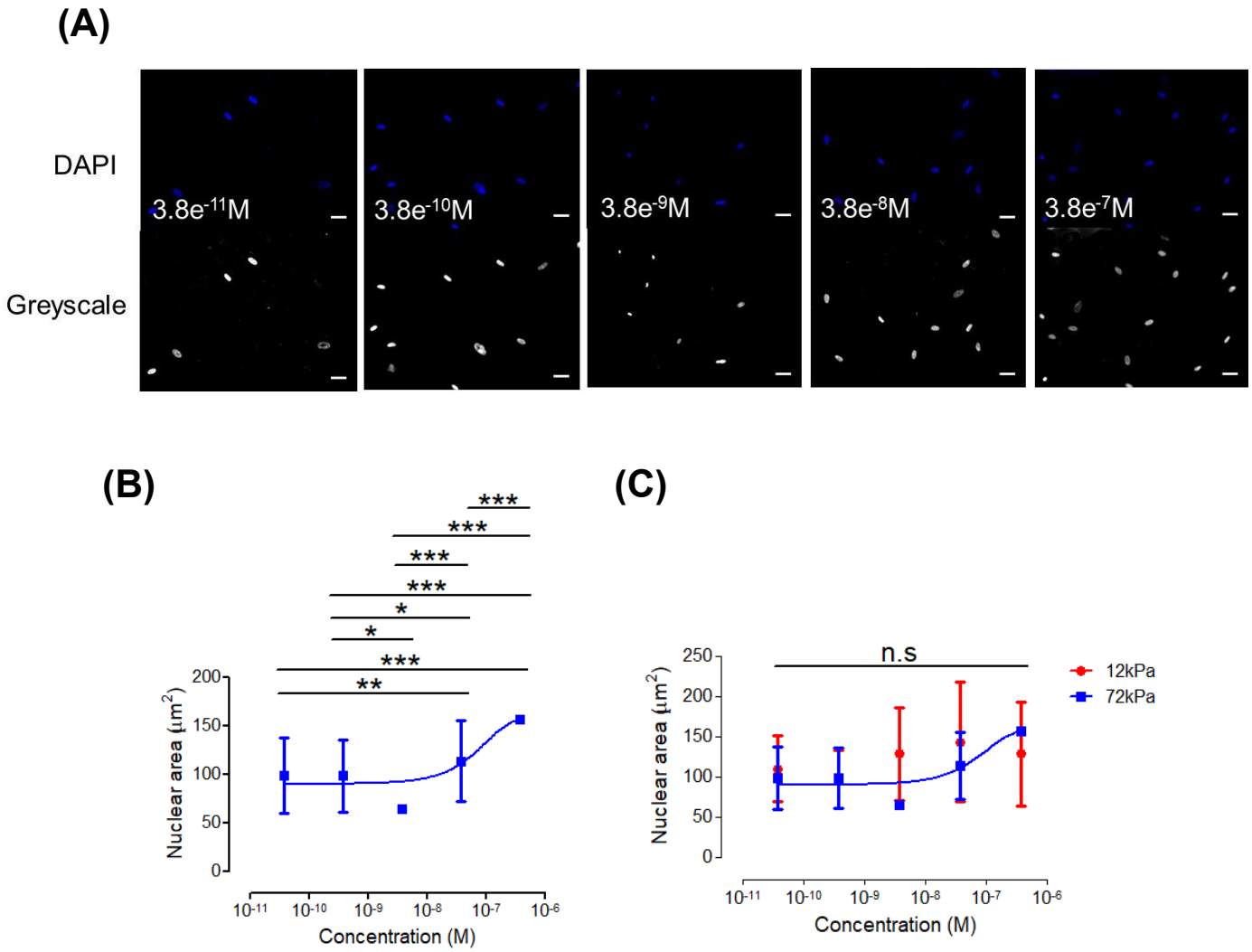

Figure 4.24: The impact of Atropine treatment on VSMC nuclear morphology within a stiffer environment. **(A)** Representative immunofluorescence images of VSMC nuclei treated with a serial dilution of Atropine. Images show VSMC nuclei stained using DAPI (blue) and grey-scale images of nuclei (grey) on 72 kPa polyacrylamide hydrogels. Scale bar represents 100 µm. Image J software was used to manually measure the **(B)** nuclear area of the VSMCs and **(C)** shows an overlay of 12 kPa and 72 kPa nuclear area change. Data are based on the measurement of >150 VSMCs from 3 independent experiments. Statistical significance was determined using a one-way ANOVA to show differences in nuclear area (* p = <0.05, ** p = <0.001 *** p = <0.0001). Additionally, a two-way ANOVA was utilised to show differences between 12 kPa and 72 kPa nuclear area changes (non-significant; p = >0.05). Both tests were followed by a Bonferroni's multiple comparison test. VSMC: Vascular smooth muscle cell.

Despite this, it currently remains unknown whether these morphological changes share the same actomyosin-dependent processes as shown within the physiological environment. We investigated this further, by utilising prior actomyosin inhibitors, in order to elucidate the mechanisms underlying the differential response within the stiffer environment. Initially, we looked at the effect of Rho/ROCK within the rigid environment via the ROCK inhibitor Y-27632. VSMCs were cultured in basal media, as described previously, and seeded on collagen-1 coated polyacrylamide hydrogels, with an average Young's modulus of 72 kPa. Drug treatments were performed identically to earlier Y-27632 work. Staining of VSMC filamentous actin and nuclei were done with rhodamine phalloidin and lamin A/C, respectively. Our results confirm that increase in VSMC spreading is mediated via the Rho-ROCK pathway as treatment caused a significant decrease in cytoplasmic spreading (**Figure 4.25A & B**). However, in this case, VSMC nuclei showed a further increase in area with Y-27632 treatment (**Figure 4.25A & C**), revealing discrepancies in cell and nuclear response. This is consistent with earlier observations of Atropine treatment (**Figure 4.24**), giving indication that the nuclear morphological response may be regulated via differential signalling pathways to cytoplasmic area.

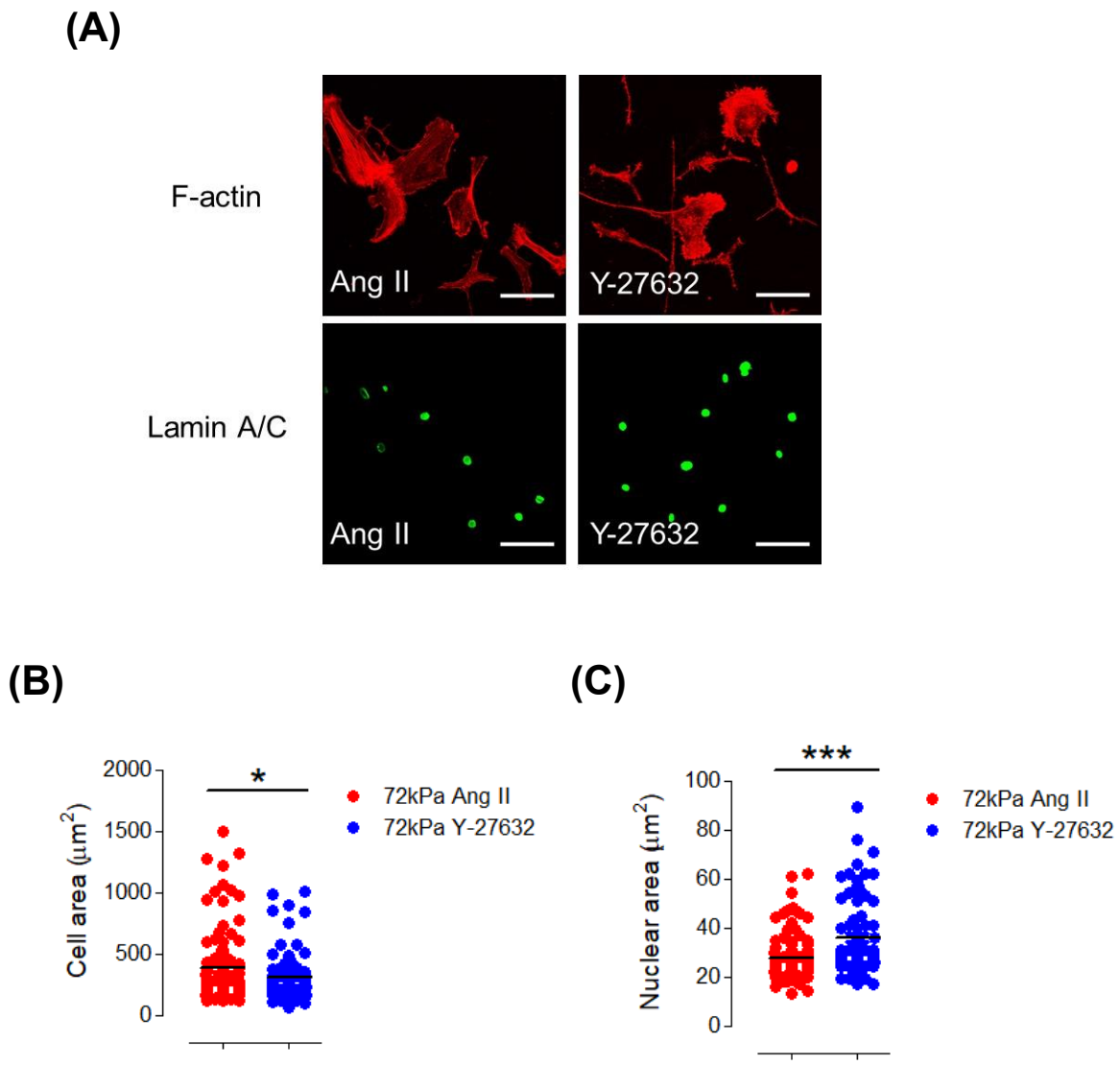

Figure 4.25: The effect of a ROCK inhibitor on the morphology of VSMCs pre-treated with Angiotensin II within a stiffer environment. **(A)** Representative immunofluorescence images of VSMC actin filaments and nuclei treated with Y-27632. Images show VSMC actin filaments (F-actin) stained using rhodamine phalloidin (red) and nuclei stained using lamin A/C (green) on 72 kPa polyacrylamide hydrogels. Scale bar represents 100 µm. Image J software was used to manually measure the **(B)** cell area and **(C)** nuclear area of the VSMCs. Data are based on the measurement of ~150 VSMCs from 3 independent experiments. Statistical significance was determined using a paired Student's *t* test on cell area and nuclear area (Ang II vs Y-27632) (* p = <0.05, *** p = <0.0001). Ang II: Angiotensin II; ROCK: Rho-associated protein kinase; VSMC: Vascular smooth muscle cell.

To investigate this further, we utilised both Blebbistatin and Atorvastatin once more. Experiments for both compounds were set up identically to before, however cell seeding was

performed on collagen-1 coated 72 kPa hydrogels. Image J analysis revealed that Blebbistatin caused successful inhibition of both cell and nuclear spreading (**Figure 4.26**).

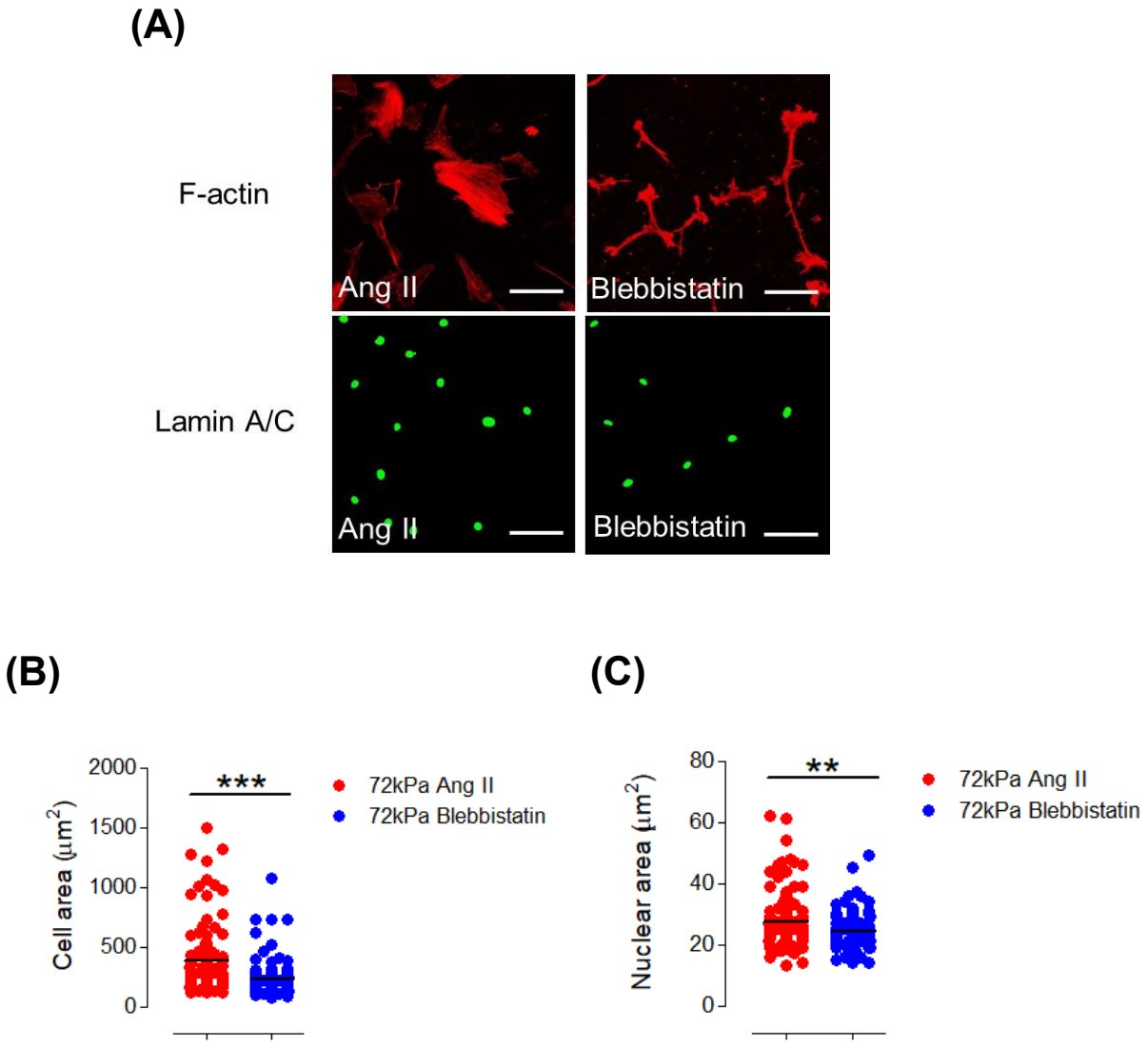

Figure 4.26: The effect of a Myosin II inhibitor on VSMC morphology within a stiffer environment. **(A)** Representative immunofluorescence images of VSMC actin filaments and nuclei treated with Blebbistatin. Images show VSMC actin filaments (F-actin) stained using rhodamine phalloidin (red) and nuclei stained using lamin A/C (green) on 72 kPa polyacrylamide hydrogels. Scale bar represents 100 µm. Image J software was used to manually measure the **(B)** cell area and **(C)** nuclear area of the VSMCs. Data are based on the measurement of >150 VSMCs from 3 independent experiments. Statistical significance was determined using a paired Student's *t* test on cell area and nuclear area (Ang II vs Blebbistatin) (** p = <0.001, *** p = <0.0001). Ang II: Angiotensin II; VSMC: Vascular smooth muscle cell.

Additionally, Atorvastatin treatment presented similar trends, however no significance was shown for cell or nuclear area compared to Angiotensin alone (**Figure 4.27A-C**). Linear

regression analysis revealed that the relationship between cytoplasmic and nuclear area within VSMCs showed similar trends between Atorvastatin and Angiotensin II treatments, with weak correlations presented for both (**Figure 4.27D**). These studies show that there may be excluding factors, outside of actomyosin activity, that may further contribute to VSMC spreading in response to matrix stiffness.

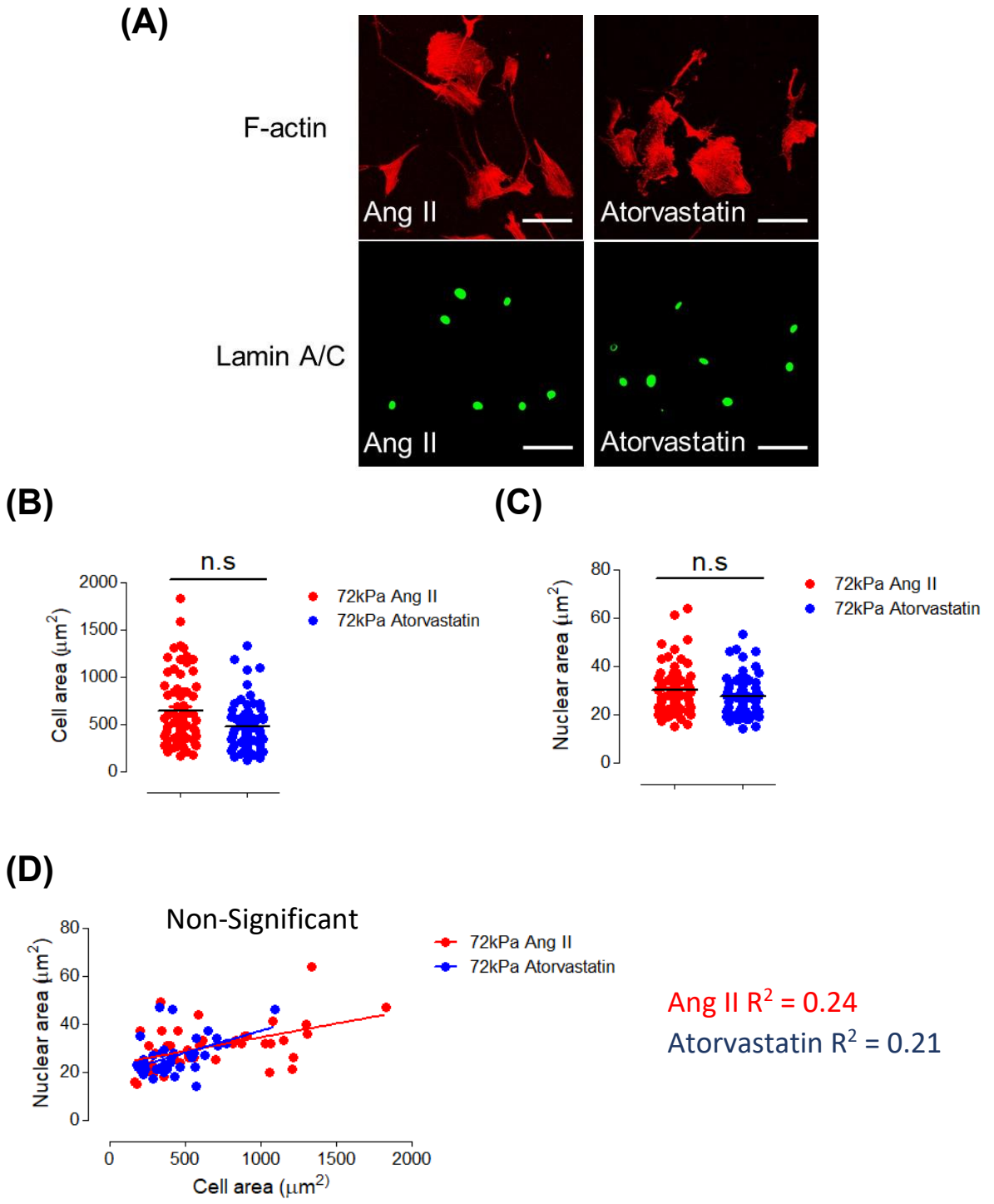

Figure 4.27: The effect of Atorvastatin on VSMC morphology within a stiffer environment. **(A)** Representative immunofluorescence images of VSMC actin filaments and nuclei treated with Atorvastatin. Images show VSMC actin filaments (F-actin) stained using rhodamine phalloidin (red) and nuclei stained using lamin A/C (green) on 72 kPa polyacrylamide hydrogels. Scale bar represents 100 µm. Image J software was used to manually measure the **(B)** cell area and **(C)** nuclear area of the VSMCs and **(D)** shows the relationship between both. Data are based on the measurement of ~100 VSMCs from 3 independent experiments. Statistical significance was determined using a paired Student's *t* test on cell and nuclear area (Ang II vs Atorvastatin) (non-significant; p = >0.05). Additionally, a linear regression analysis was used to determine statistical significance for the cell and nuclear area relationship (non-significant; p = >0.05). Ang II: Angiotensin II; VSMC: Vascular smooth muscle cell.

Throughout this chapter, we utilised various actomyosin inhibitors and revealed differential effects in cell and nuclear area of pre-constricted VSMCs in response to a change in substrate rigidity, and a summary of this is presented in **Table 4.1**.

Table 4.1: Summarising the effects of actomyosin inhibitors on cell and nuclear area for VSMCs pre-treated with 10 μM of Angiotensin II.

Area change			
	Y-27632	**Blebbistatin**	**Atorvastatin**
12 kPa Cell area	Increase	Increase	Increase
12 kPa Nuclear area	Increase	Increase	Increase
72 kPa Cell area	Decrease	Decrease	No change
72 kPa Nuclear area	Increase	Decrease	No change

4.4.7 Effects of aberrant contractility on VSMC epigenetics

As mentioned before, VSMCs have shown to transition from a contractile to a synthetic phenotype during CVD and this is particularly apparent in atherosclerotic lesions (166). The transition involves a regulatory change in the expression of key marker proteins and this is facilitated by histone modifications which can alter chromatin packaging (37). Due to this reason, we wanted to observe if there were any discrepancies in the epigenetic modifications, in particular with H3K9 acetylation levels of VSMCs when stimulated to contract at different rigidities.

To do this, VSMCs were grown in basal medium and seeded on collagen-1 coated polyacrylamide hydrogels, with an average Young's modulus of 12 kPa and 72 kPa. Cells were then treated with a serial dilution of Angiotensin II and processed for immunofluorescence as described previously. Prior to microscopy imaging, VSMC filamentous actin, nuclei and H3K9 were stained with rhodamine phalloidin, DAPI and anti-H3K9 acetylation, respectively. Image J analysis revealed that both mean and total H3K9 acetylation intensity showed a steady reduction on a compliant matrix (**Figure 4.28**), indicating a controlled decrease in gene expression.

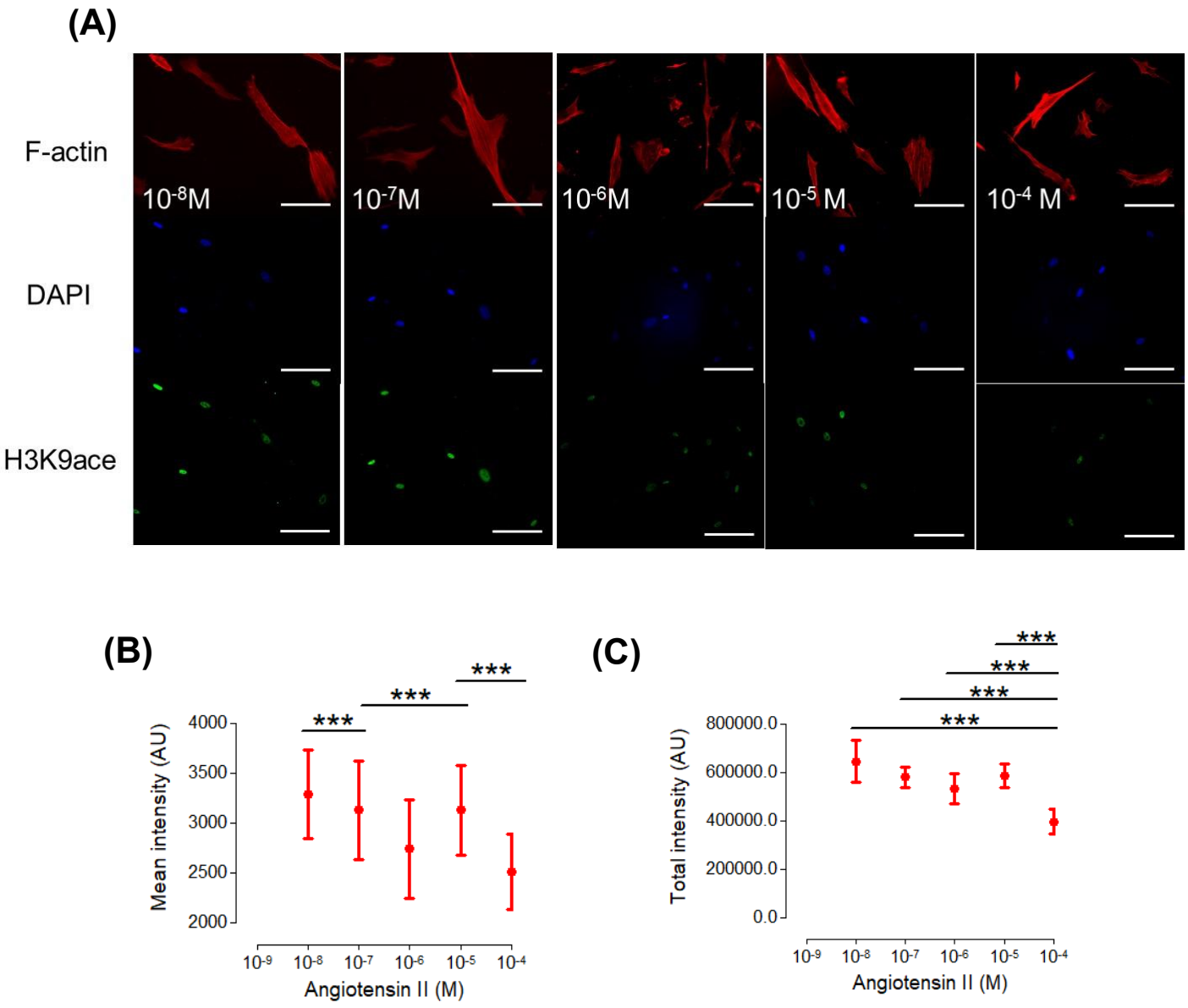

Figure 4.28: The effect of Angiotensin II on VSMC histone acetylation. **(A)** Representative immunofluorescence images of VSMC actin filaments, nuclei and H3K9 acetylation levels when treated with serial dilution of Angiotensin II. Images show VSMC actin filaments (F-actin) stained using rhodamine phalloidin (red), nuclei stained using DAPI (blue) and H3K9 stained using anti-H3K9ace (green) on 12 kPa polyacrylamide hydrogels. Scale bar represents 100 μm. Image J software was used to manually measure the **(B)** mean intensity and **(C)** total intensity of the VSMCs. Data are based on the measurement of >150 VSMCs from 3 independent experiments. Statistical significance was determined using a one-way ANOVA to show differences in mean intensity (*** p = <0.0001) and total intensity (*** p = <0.0001), followed by a Bonferroni's multiple comparison test. H3K9ace: Histone 3 Lysine-9 acetylation; VSMC: Vascular smooth muscle cell.

Contrastingly, Angiotensin II failed to generate any trend in H3K9 acetylation levels within the rigid matrix (**Figure 4.29**).

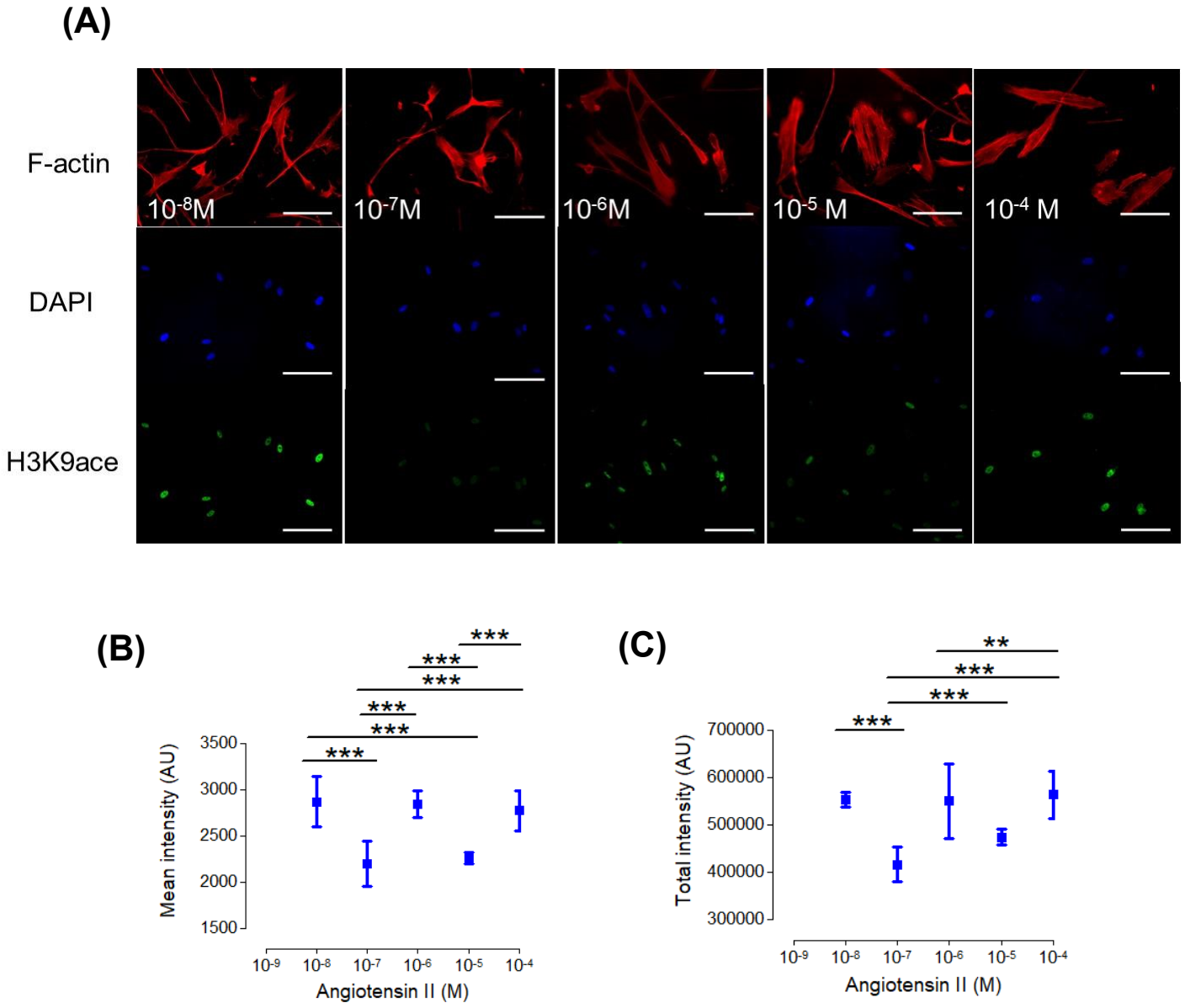

Figure 4.29: The effect of Angiotensin II and matrix stiffness on VSMC histone acetylation. **(A)** Representative immunofluorescence images of VSMC actin filaments, nuclei and H3K9 acetylation levels when treated with serial dilution of Angiotensin II. Images show VSMC actin filaments (F-actin) stained using rhodamine phalloidin (red), nuclei stained using DAPI (blue) and H3K9 stained using anti-H3K9ace (green) on 72 kPa polyacrylamide hydrogels. Scale bar represents 100 µm. Image J software was used to manually measure the **(B)** mean intensity and **(C)** total intensity of the VSMCs. Data are based on the measurement of >150 VSMCs from 3 independent experiments. Statistical significance was determined using a one-way ANOVA to show differences in mean intensity (*** p = <0.0001) and total intensity (** p = <0.001, *** p = <0.0001), followed by a Bonferroni's multiple comparison test. H3K9ace: Histone 3 Lysine-9 acetylation; VSMC: Vascular smooth muscle cell.

Despite trend variances between both environments, no significant difference in mean or total H3K9 acetylation levels was observed (**Figure 4.30**).

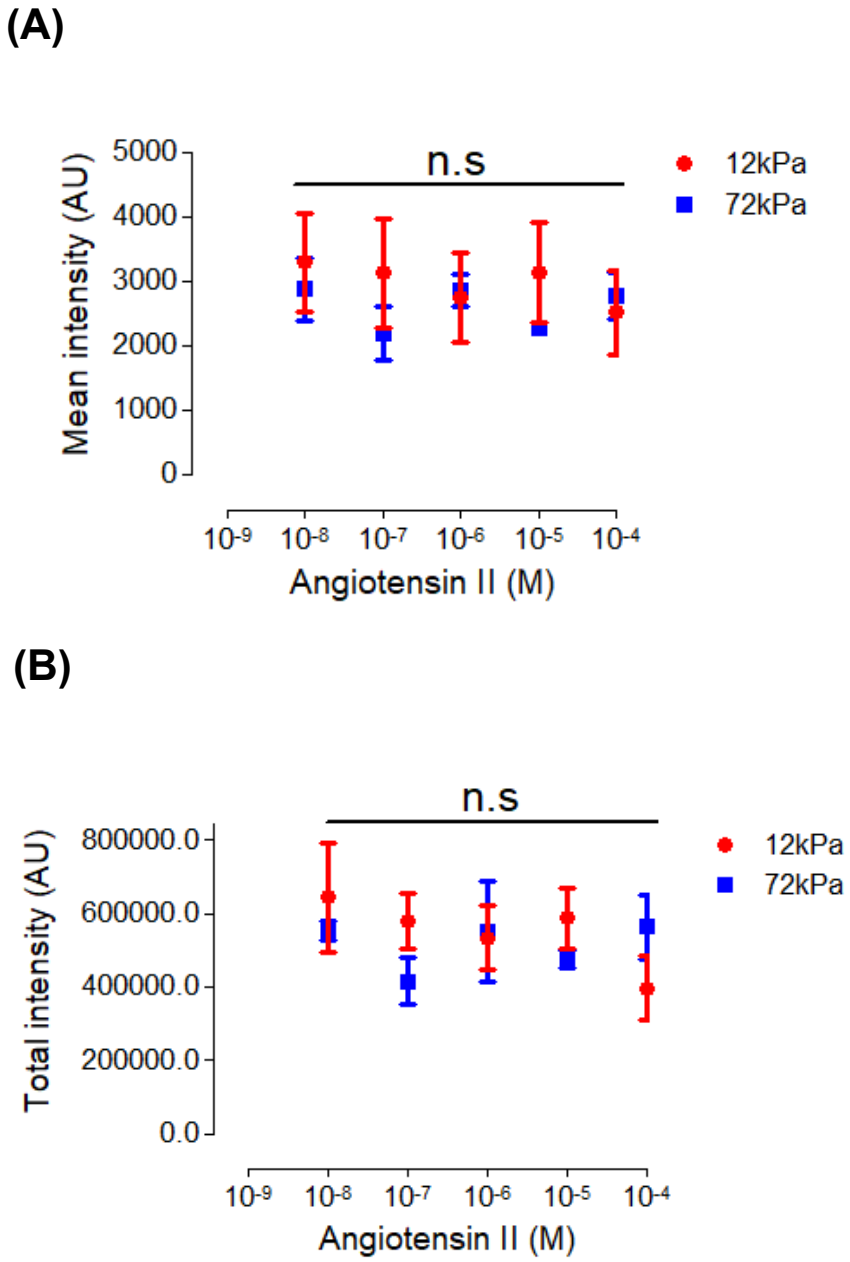

Figure 4.30: Comparing the effect of matrix stiffness on VSMC histone acetylation levels. Graphs show overlay of the effect of normal (12 kPa) and stiff (72 kPa) polyacrylamide hydrogels on **(A)** mean intensity and **(B)** total intensity of the VSMCs. Data are based on the measurement of >150 VSMCs from 3 independent experiments. Statistical significance was determined using a two-way ANOVA to show differences in mean intensity (non-significant; p = >0.05) and total intensity (non-significant; p = >0.05), followed by a Bonferroni's multiple comparison test. VSMC: Vascular smooth muscle cell.

4.5 Discussion

This chapter explored the relationship between quiescent VSMC morphology, actomyosin activity and matrix stiffness. By creating a novel contractile assay, we were able to determine the efficacy of various agonists and antagonists on VSMCs. We investigated whether the morphological changes were actomyosin-dependent between both rigidities and established different regulatory levels of these responses. This work provides strength to earlier morphological studies described in chapter three. As a result, we can reveal that VSMC morphology presents a differential response due to matrix stiffness as well as giving insight into new potential functional avenues that may explain this.

4.5.1 Effect of contractility on VSMC morphology amongst different rigidities

Within healthy adult blood vessels, VSMCs typically exist in a quiescent contractile state. This phenotype is characterised by dense contractile fibres, possessing a high expression of phenotype-specific proteins. The function of the VSMCs revolves around maintaining vascular tone via controlled contraction and relaxation in order to ensure efficient blood circulation (166, 278-280). Contractile stimulation is often utilised for necessary maintenance of a variety of cell types. Earlier work has shown that neuronal cells present healthy reconstitution from Angiotensin II treatment within *in vitro* cerebral ischemia models, as well as an outgrowth of neurites in control samples (281, 282). In our work, we reveal contraction of VSMCs via progressive cell area reduction in response to agonist treatments on a compliant matrix. These findings are supported by prior research which show that Carbachol can further enhance the contractile activity of VSMCs pre-treated with calcium and also cause smooth muscle-like interstitial cells to have near a 50% reduction in cell length (283, 284). Thus, our work supports the notion that VSMCs facilitate vessel constriction in healthy physiology via external contractile stimuli.

Under pathological conditions, however, VSMCs no longer regulate vascular tone efficiently which lead to consequences in the arterial structure such as intimal thickening and atherosclerotic plaque formation (130). These structural aberrations commonly occur with older age resulting in stiffer arterial walls, which are both larger and thicker in diameter (285). Earlier work shows that the rigidity of the substrate can directly augment contractility and spreading of endothelial cells (219). Despite this, the study mentioned utilised substrates with rigidities between 1-10 kPa. These fall within the stiffness of healthy aorta and therefore

further investigation was required to assess whether this may hold true in VSMCs within a more representative diseased state. By employing substrates with rigidities illustrative of stiffer arterial constructs, we show VSMCs present increased spreading in response to contractile stimulation.

Earlier work had shown that a high concentration of Atropine, which inhibits calcium release, can efficiently prevent contraction of smooth muscle strips (286). Our findings are in agreement showing that the VSMC morphological changes induced by contractile agonists can be prevented via actomyosin inhibitors. Within CVD conditions, VSMCs typically increase synthesis of extracellular matrix proteins, in particular collagen type I, III and V (287). The AT1 receptor antagonist, Irbesartan, has previously been shown to have a positive therapeutic role in spontaneously hypertensive rats (SHR) via the blocking of collagen synthesis within VSMCs (288). Our studies further support this by presenting Irbesartan and atropine as efficient compounds that inhibit the aberrant VSMC structural changes that occur in response to matrix stiffness. Thus, revealing the dysregulated signalling, which leads to structural and functional changes of VSMCs, can be regulated at the receptor level.

We had previously shown in chapter three that VSMCs cannot efficiently displace the stiffer matrix despite exerting more traction force. Our work in this chapter gives a better understanding towards its consequences and as a result, we speculate that the tension held at the cell membrane may open SACs, causing VSMC spreading via increased cytosolic volume. SACs have previously been identified within smooth muscle cells and earlier studies have shown they allow significant calcium concentrations through to the cytosol of the cell (177, 289, 290). Potentially, this could augment VSMC contractile forces and cell spreading, as observed, however more work is required to confirm this.

4.5.2 VSMC nuclear morphology and epigenetic changes

Given the high rigidity of the nucleus, changes in nuclear morphology would require great forces, most likely originating from the LINC complex. As mentioned in chapter three, the LINC complex allows essential mechanotransduction to occur which facilitates important nuclear responses caused by extracellular cues (233). Within both rigidities, our work reveals that nuclear area of quiescent VSMCs show similar responses to the cytoplasm in response to agonist stimulation. This is supported by previous studies which reveal nuclei of other cell types closely mimic cellular spreading patterns on a large variety of matrices (291).

Previously, it's been shown that culturing cells on stiff substrates can cause nuclear rupture whilst compliant matrices preserve healthy morphology (133). If ruptured, the nuclei will allow passage of cytoplasmic factors into the nuclear space (292). This leakage may facilitate nuclear spreading as observed with our work of VSMCs on rigid hydrogels. Despite this, nuclear pore disruption has only been presented in cells with lamin-A defects (133). Reduced lamin A/C level has previously been reported to cause loss of cellular stiffness and importantly, this reduction in tension can be mimicked with LINC complex disruption (293-295). Therefore, it is possible that the LINC complex may face mechanical overload within the stiffer environment which could cause aberrant changes to nuclear structure. Contrastingly, prior research has shown that increased myosin II contractility induced from stiffness can augment mesenchymal lamin A/C levels, indicating these responses may be cell-type specific (128). Our work shows significant changes in nuclear/cell area within the rigid matrix as well as limited restoration of nuclear morphology with various inhibitors. This indicates that matrix stiffness may disrupt the mechanical link between the VSMC cytoplasm and nuclei leading to differential responses.

Additionally, the vasculature commonly undergoes arterial stiffness within CVD and stiffer tissues become enriched in collagen levels, presenting smaller matrix pores as a result (128, 129). Under these conditions, VSMCs typically migrate to the tunica intima via the small pores and the mechanical pressure faced may cause changes in epigenetic regulation and genomic stability (130). A previous study consolidates this showing compressive forces can cause decreased actomyosin activity as well as histone deacetylation within fibroblast cells, ultimately leading to a reduction in transcriptional activity (169). Within VSMCs, these epigenetic changes are also present and an example of such modifications are H3K4 dimethylation and H3K9 acetylation. Such epigenetic changes are commonly found near the CArG elements of important VSMC differentiation marker genes such as SM α-actin (165). Our study showed a progressive decrease in VSMC transcriptional activity in response to Angiotensin II within the physiological environment. This is supported by prior work which show Angiotensin II directly regulate expressional changes of important VSMC proteins via acetylation of H3K9/14 residues (168). However, when increasing the rigidity of the substrate, no correlation in H3K9 acetylation levels were found indicating that gene regulation may become dysregulated within matrix stiffness. Further work is now required to extend our understanding on whether this may be a driving force in DNA damage accumulation within VSMCs.

4.5.3 Development and advantages of the novel contractile assay

Currently, there are a range of techniques used to analyse the contractility of various cell types. TFM has proven itself as the gold standard providing accurate traction force/stress data along with important morphological information (296, 297). Despite this, TFM is a very time consuming and specialised protocol, hence not accessible in every lab. Another popular method is the collagen plug assay. This method, however, is constrained to relatively large cell sample sizes, with high gel consumptions along with ambiguous post-contraction gel borders (298-301). Measuring tissue deformations, such as collagen gel deformation is a suitable alternative though it is limited due to the inability to compare across different systems and its difficulty in altering matrix rigidity (302). Additionally, the electric-cell-substrate impedance sensing (ECIS) method, previously used with smooth muscle cells, presents similar limitations with adjusting the substrate stiffness (303).

In our work, we investigated the effect of different rigidities on VSMC morphology. Our research fabricated polyacrylamide hydrogels with materials readily available in almost any cell biology lab. The system allows easy adjustment of matrix rigidity and is capable of assessing the effects of specific drugs across a wide variety of systems. It is not exclusive to large cell samples and can utilise smaller sets in cases of limited primary cell lines. Our method allowed us to be able to assess the different effects of multiple agonists/antagonists. By doing so, we were able to obtain important morphological responses of our cells revealing new mechanistic insights as well as extract important pharmacological properties of the compounds used. Importantly, our study established both cell and nuclear area as effective readouts for VSMC contractility. Whilst cell area is a more robust and common reporter of contractile function, it is more time consuming in its analysis in comparison to nuclear morphology, as described in section 2.6.1.1. We propose nuclear area as a more efficient readout for VSMC contractility as our findings show no significant difference in the response of both to different contractile agonists within a range of rigidities, and reveal identical EC50 values derived from the two morphological parameters. Therefore, within this chapter, we present a novel contractile assay which may provide new advantages to previous methods.

4.5.4 Chapter Four conclusions

This chapter demonstrates the difference in VSMC morphology between the physiological and pathological environment in response to contractile stimulants. Matrix stiffness causes a gradual spreading of the VSMC cytoplasm and nuclei and this process was found to be actomyosin-dependent. We hypothesise that SACs may be opened in response to cell tension and this may drive VSMC spreading and contractility. Additionally, there is indication that the nuclear response is decoupled from the cytoplasm due to mechanical pressure and this may cause a dysregulation of gene expression patterns within the stiffer environment. We speculate that high osmotic pressure may lead to nuclear damage or rupture resulting in potential DNA damage and thus give reason as to why nuclear morphology could be not fully restored by specific inhibitor treatments.

Our assay has given insight into possible mechanisms that facilitate differential responses within VSMC morphology, however further work is required to better understand the link between unrestrained actomyosin activity, aortic compliance and gene regulation. These are crucial factors that contribute to CVD and therefore clarity of this relationship is essential. This chapter has presented key structural changes that occur within VSMCs and further interrogation of these pathways may identify new therapeutic interventions for future treatments.

4.5.5 Limitations and future work

4.5.5.1 Co-culture system

The experiments performed within this chapter investigated the VSMC contractile pathway in response to its mechanical environment. However, in real physiology, there are a variety of soluble factors which play an important role in its regulation. For instance, nitric oxide (NO) serves as a protective molecule within the vascular system and is pre-dominantly produced by endothelial NO synthase (eNOS) (304). It works via the protein kinase G (PKG) pathway to cause relaxation within smooth muscle cells (305). As the tunica media neighbours the tunica intima along the arterial wall (10), a co-culture system of VSMCs and endothelial would replicate a sub-maximal contractile response more representative of the *in vivo* environment. Due to time constraints, we were unable to do this, however, our *in vitro* system can be further refined for future work in order to better determine the role of matrix stiffness within VSMCs.

4.5.5.2 The role of VSMC SACs within matrix stiffness

Our work utilised various actomyosin and receptor-specific inhibitors in order to characterise different levels of regulation within VSMC morphology. However, our knowledge remains limited as we have yet to investigate whether there is an aberrant function of SACs in response to matrix stiffness. As previously discussed, SAC expression has been shown within smooth muscle cells, and its opening can significantly increase intracellular calcium concentrations (177, 289, 290). Despite this, further clarity is required to know which channels are specifically present within VSMCs, and if so, whether they show an increase in expression on higher rigidities. Thus, future work must consider the possible effects SACs may have on VSMC morphology, actomyosin activity and nuclear integrity.

4.5.5.3 Regulation of VSMC epigenetics

Due to time constraints, the epigenetic work within this chapter remains restricted as our experiments only utilised one marker, H3K9 acetylation, to give indication of how gene regulation may change within the stiffer environment. There are a variety of epigenetic markers which have previously presented changes within VSMCs (165, 168),and these will have to be considered in the future to consolidate our findings.

4.5.5.4 Contractility assay

Whilst our novel assay presents advantages over previous methods, it is limited in a few ways. To begin with, our system is low throughput compared to existing assays due to longer methods of analysis. Additionally, it does not present the gel/matrix displacement caused via contractility, as shown by alternative experiments such as TFM and the collagen plug assay (306, 307). Due to this, it cannot calculate individual contractile forces or the collective force exerted. Ultimately, these factors will have to be considered when studying VSMC contractility in the future and forthcoming work will investigate new ways to refine our assay.

Chapter 5: The role of VSMC stretch activated channels in matrix stiffness contractile response

5.1 Introduction

The work within the previous chapter placed focus on the effect of matrix rigidity on quiescent VSMC morphology, via the use of contractile agonists. We highlighted how VSMCs present an aberrant spreading when stimulated to contract under matrix stiffness. This corroborates with previous findings which highlight multiple other cell types adhere and spread better on rigid substrates (308). CVD has been shown to occur with developing arterial stiffness and thickening (309). There are a multitude of factors that can contribute to this, one being VSMC hypertrophy via an increase in cytoplasmic volume (310, 311). Hypertrophic changes can be driven by changes in cell volume, and therefore it is important to investigate whether this may have a role in the dysregulated spreading discussed. However, prior work conflicts with this as it has been shown that mammalian cell types, including airway smooth muscle cells, rather present a reduction in cell volume when cultured on stiff substrates (312).

Despite this, cell volume is an underestimated parameter that plays a crucial role within cellular mechanical properties (313, 314), cell growth (315), and importantly gene expression (316). Prior work has shown that changes in cytosolic volume could cause nuclear deformation which would impede chromatin condensation (317, 318) Importantly, VSMCs display high plasticity and transition to the synthetic phenotype during CVD development, and this is accompanied by gene expressional changes of key contractile protein markers (242). As a result, it becomes necessary to consider volume when observing the structural and functional changes that occur during disease progression.

Previous research has also shown the expression of SACs within smooth muscle cells (290), and these may play a role in the potential hypertrophic response observed. Opening of these channels may allow ions and solutes to enter the cell, causing an increase in cytosolic volume and intracellular calcium levels (177, 289). Further work is required to see if this holds true within quiescent VSMCS, and if so, to investigate the implications this may cause. Within this chapter, we look at the relationship between VSMC volume, SACs and DNA regulation to better understand how matrix stiffness may drive the pathological changes observed within CVD.

5.2 Aim of this chapter

This chapter will investigate whether quiescent VSMC and nuclear volume is altered by changes in actomyosin activity and whether this holds a positive correlation to cell/nuclear spreading. Along with this, we will explore the structural and functional roles of SACs within VSMCs. By gaining an understanding of how these aberrant morphological changes may be caused, we hope to see whether this alters VSMC DNA regulation and gene expression patterns.

5.3 Hypothesis

We have shown that matrix stiffness causes changes in the cytosolic and nuclear area of VSMCs. We hypothesise that VSMC volume will also be altered and that these changes will be driven by SACs activation. Traction force generation may become altered under these conditions, and if so, this may cause aberrant modifications to the nuclear structure and DNA integrity of the VSMCs.

5.4 Results

5.4.1 Effect of Angiotensin II on VSMC volume

As mentioned before, Angiotensin II holds numerous roles within the vasculature, in particular within VSMCs. Despite this, further studies are required to fully characterise the mechanical and morphological properties produced by the contractile agonist. Several studies have shown that mechanical forces have an effect on cell volume, with substrate stiffness inducing a decrease in volume due to water efflux (314, 319). Other supporting work has shown that cell volume is directly correlated to substrate stiffness and mechanical loading (313, 320), and therefore we investigated the effect of Angiotensin II on quiescent VSMC volume cultured on ECMs representative of both physiological and pathological stiffness. To do this, VSMCs were cultured in basal medium and seeded on collagen-1 coated polyacrylamide hydrogels, with an average Young's modulus of 12 kPa and 72 kPa. Cells were treated with 10 μM of angiotensin II, followed by F-actin staining prior to immunofluorescence microscopy.

Analysis revealed that VSMCs show a significantly larger cell volume when grown on a stiffer polyacrylamide hydrogel compared to its physiological counterpart (**Figure 5.1A & B**). Further analysis investigated the cell area to volume relationship and subjected it to linear regression analysis, which presented a moderate correlation on the physiological substrate but a weaker trend on the 72 kPa polyacrylamide hydrogel (**Figure 5.1C**). Despite this, there was no significant difference found between both trend lines and further work may be required to increase the end numbers.

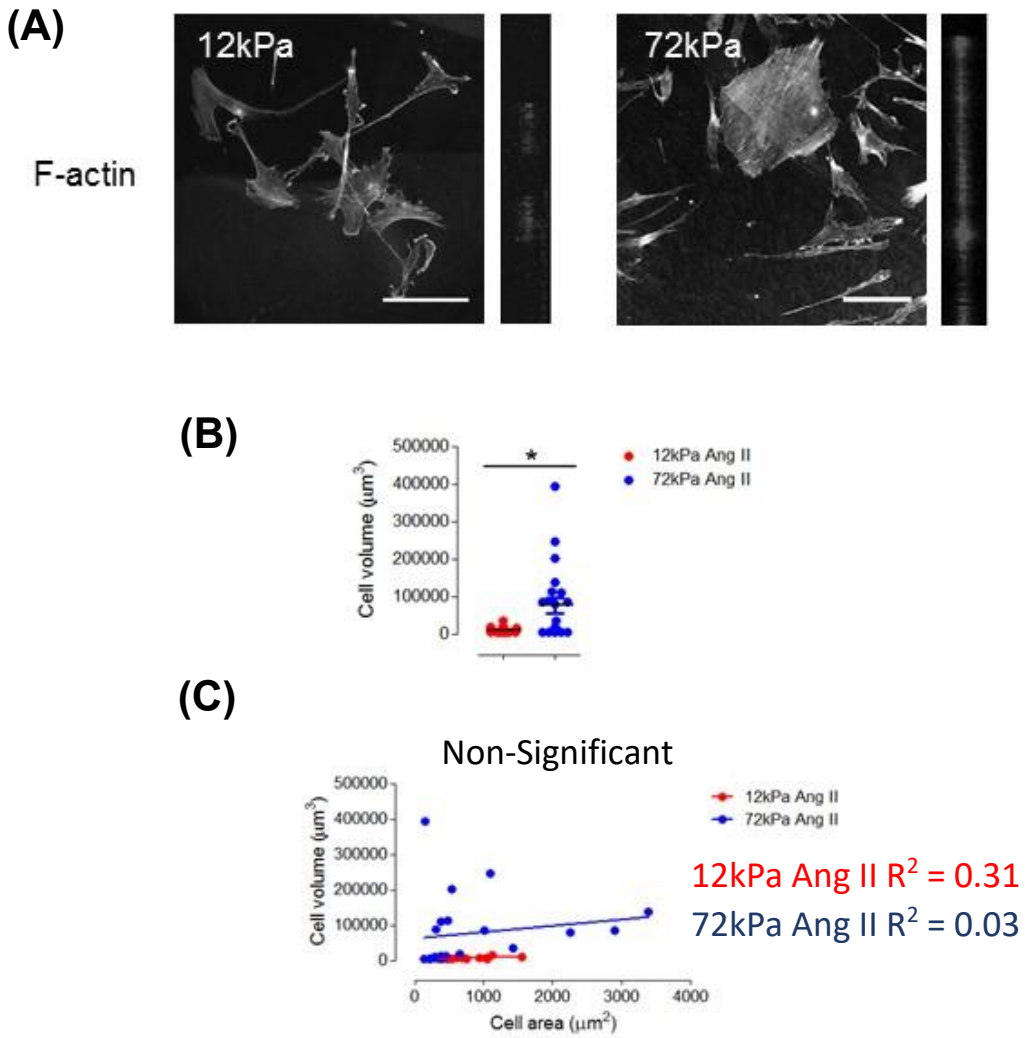

Figure 5.1: The impact of matrix stiffness on the volume of VSMCs constricted with Angiotensin II. **(A)** Representative immunofluorescence images of VSMC actin filaments treated with 10 µM of Angiotensin II. Images show VSMC actin filaments (F-actin) stained using rhodamine phalloidin, with grey-scale images presented on 12 kPa and 72 kPa polyacrylamide hydrogels. Scale bar represents 100 µm. Volocity software was used to manually measure **(B)** cell volume. Image J software was used to plot **(C)** VSMC area against volume on 12 kPa and 72 kPa polyacrylamide hydrogels. Data are based on the measurement of ~20 VSMCs from 2 independent experiments. Statistical significance was determined using a paired Student's *t* test on cell volume (12 kPa Ang II vs 72 kPa Ang II) (**p* = <0.05). Additionally, a linear regression analysis was used to determine statistical significance for the cell area and volume relationship (non-significant; *p* = >0.05). Ang II: Angiotensin II; VSMC: Vascular smooth muscle cell.

Next, we expanded upon these findings by performing a time course experiment to observe whether there was a progressive change induced in cell area and volume via

contractile stimulation. To do this, we set up identical experimental conditions, as described previously, however modified Angiotensin II treatment times to range between 0-30 minutes. Results obtained using Image J software presented contrasting responses between both rigidities. The physiological substrate produced a significant progressive increase in cell area within 5 minutes followed by a progressive decrease whilst the rigid matrix caused increased VSMC spreading within 10 minutes (**Figure 5.2A-C**). Volume, displayed the same trend observed on both the 12 kPa and 72 kPa polyacrylamide hydrogels (**Figure 5.2A & D-E**). As a result, we can observe a rapid morphological response of the VSMCs in response to Angiotensin II stimulation under both rigidities.

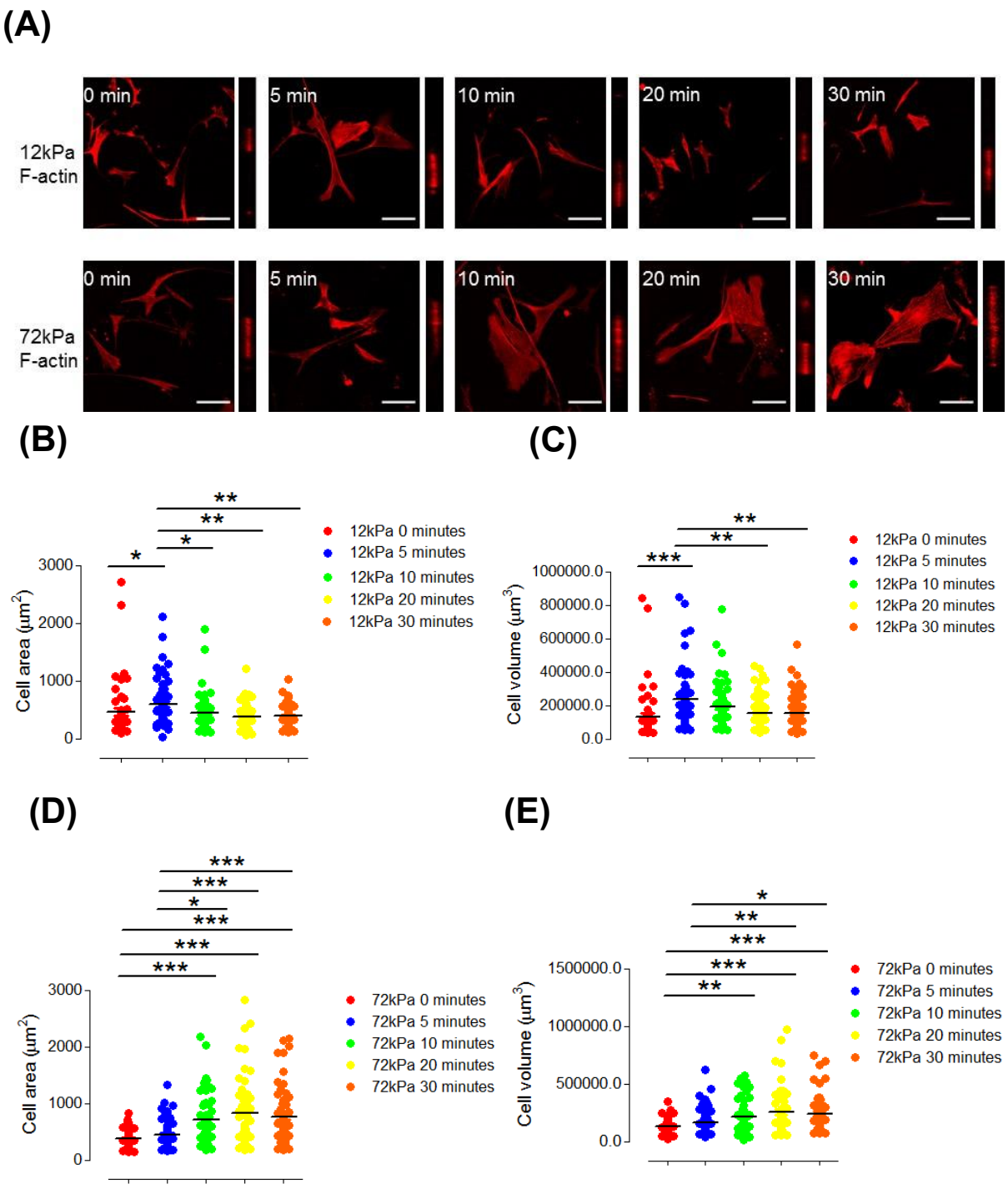

Figure 5.2: Time course experiment showing the effects of Angiotensin II treatment on VSMC area and volume. **(A)** Representative immunofluorescence images of VSMC actin filaments within different time points after treatment with 10 µM of Angiotensin II. Images show VSMC actin filaments (F-actin) stained using rhodamine phalloidin (red) presented on 12 kPa and 72 kPa polyacrylamide hydrogels. Scale bar represents 100 µm. Image J software was used to manually measure cell area on **(B)** 12 kPa and **(C)** 72 kPa polyacrylamide hydrogels. Volocity software was also used to measure cell volume on **(D)** 12 kPa and **(E)** 72 kPa rigidities. Data are based on the measurement of ~100 VSMCs from 3 independent experiments. Statistical significance was determined using a one-way ANOVA to show differences in cell area and cell volume (* p = <0.05, ** p = <0.001, *** p = <0.0001), followed by a Bonferroni's multiple comparison test. VSMC: Vascular smooth muscle cell.

To supplement this, linear regression analysis was performed on the cell area to volume relationship of each time point and results indicated a moderate to strong relationship in this case (**Figure 5.3**). Despite this, when comparing each timepoint, there was found to be significant differences in the trendlines, indicating the cell area-volume relationship is time-dependent.

(A)

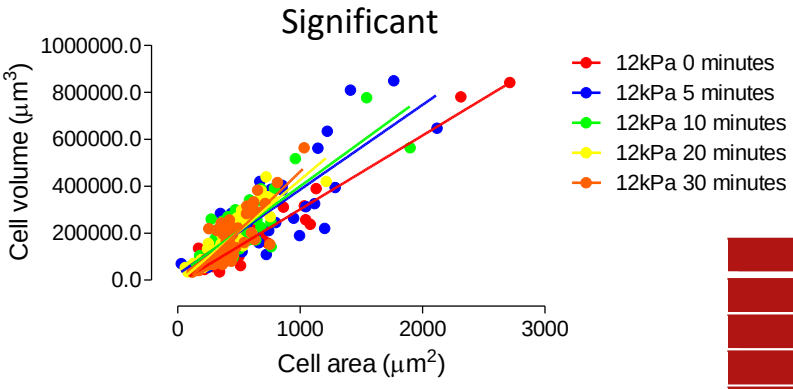

	R^2
0 min	0.95
5 min	0.70
10 min	0.71
20 min	0.77
30 min	0.71

(B)

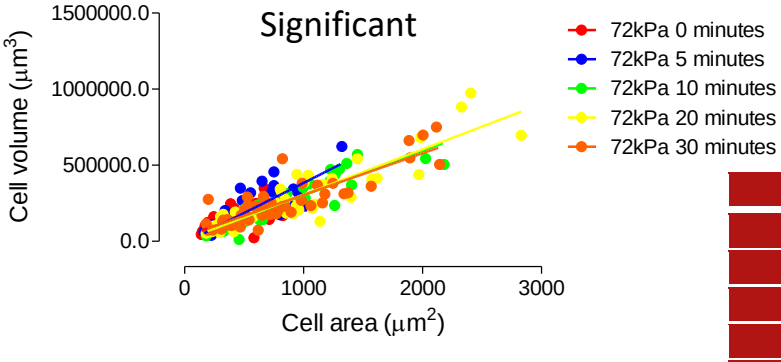

	R^2
0 min	0.45
5 min	0.72
10 min	0.85
20 min	0.83
30 min	0.77

Figure 5.3: Angiotensin II time course experiment showing the relationship between VSMC area and volume on different rigidities. Graphs show VSMC area plotted against VSMC volume on both **(A)** 12 kPa (*** p = <0.0001) and **(B)** 72 kPa (*** p = <0.0001) polyacrylamide hydrogels, with corresponding tables presenting R^2 values of each time point. Data are based on the measurement of ~100 VSMCs from 3 independent experiments. Statistical significance between the VSMC area and volume relationship of each timepoint was determined using linear regression analysis. VSMC: Vascular smooth muscle cell.

5.4.2 Inhibition of actomyosin activity and it's role on VSMC volume

Our work so far shows that an increase in VSMC volume is induced when stimulated to contract on a rigid matrix. We show that this effect is time-dependent and can occur as early as 5 minutes after stimulation. However, we required further insight into what regulates this hypertrophic change and therefore we utilised the actomyosin inhibitors previously discussed in chapter four. The ROCK pathway primarily works to inhibit MLCP which increases the basal level of pMLC for contraction, however more work is required to know whether this contributes to cytosolic/nuclear volume (321). Earlier research showed the ROCK kinase signalling pathway was shown to modulate endothelial cell volume via the gating regulation of volume regulated anion channels (VRACs) (322). Due to this, we hypothesised that inhibition of this pathway could ameliorate the morphological changes shown in VSMCs.

To investigate this, we utilised the ROCK inhibitor Y-27632. VSMCs were cultured as described previously on collagen-1 coated polyacrylamide hydrogels, with an average Young's modulus of 12 kPa and 72 kPa. VSMCs were pre-treated with 10 µM of Angiotensin II for 30 minutes, followed by treatment with 5 µM of Y-27632. Cells were fixed, and then stained with rhodamine phalloidin and anti-lamin A/C to image VSMC filamentous actin and nuclei, respectively. Volocity software revealed that within the physiological environment, inhibition of the ROCK pathway caused a significant increase in VSMC cytosolic volume compared to Angiotensin II alone (**Figure 5.4A & B**). When comparing the cell area to volume relationship, Angiotensin II alone presented a moderate trend whilst utilisation of the ROCK inhibitor significantly enhanced the relationship (**Figure 5.4C**).

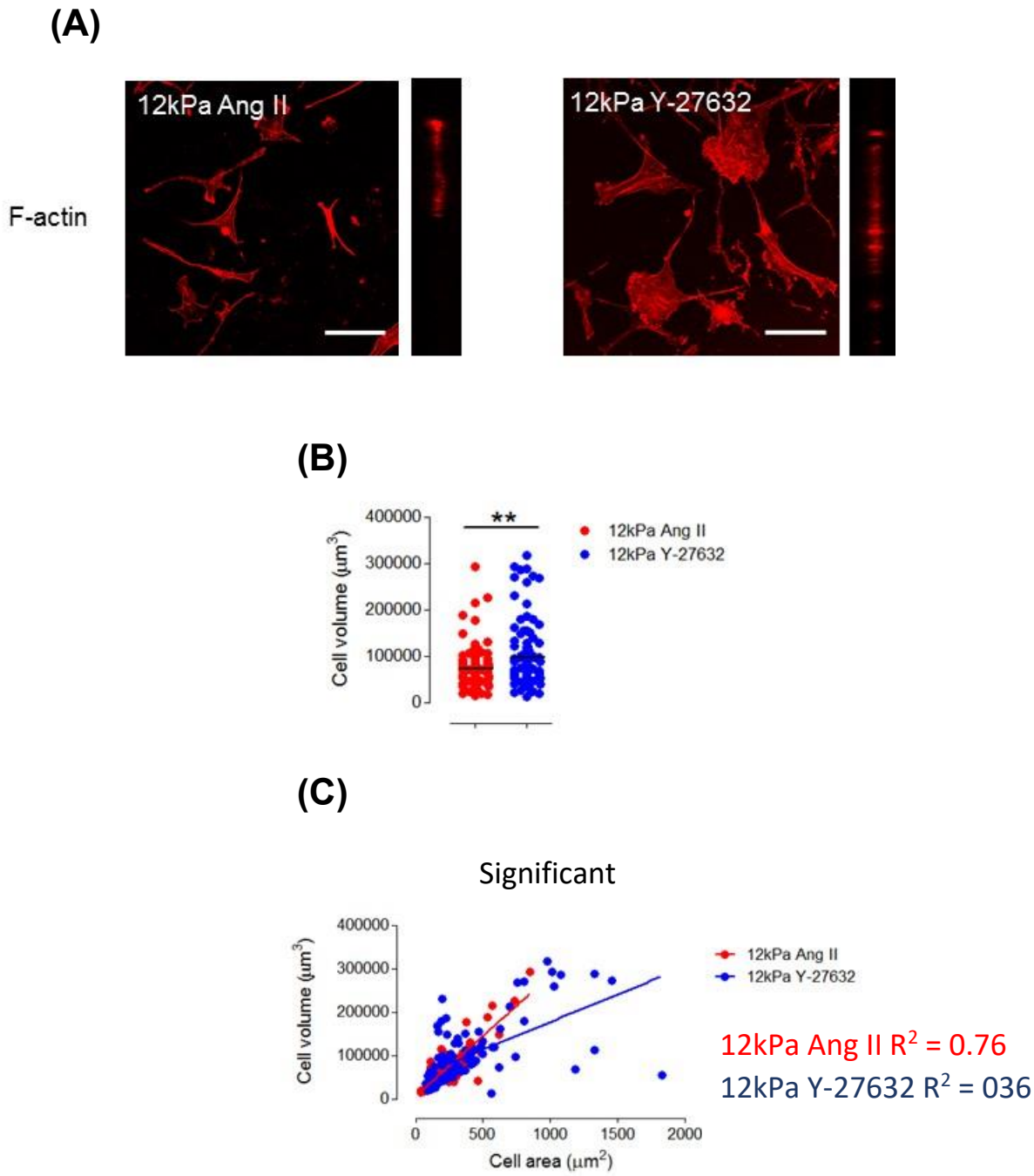

Figure 5.4: The impact of a ROCK inhibitor on VSMC volume. **(A)** Representative immunofluorescence images of VSMC actin filaments treated with Y-27632. Images show VSMC actin filaments (F-actin) stained using rhodamine phalloidin (red) on 12 kPa polyacrylamide hydrogels. Scale bar represents 100 µm. Volocity software was used to manually measure **(B)** cell volume. Image J software was used to plot **(C)** VSMC area against volume on cells treated with Angiotensin II alone and with Y-27632. Data are based on the measurement of >150 VSMCs from 3 independent experiments. Statistical significance was determined using a paired Student's *t* test on cell volume (12 kPa Ang II vs 12 kPa Y-27632) (** p = <0.001). A linear regression analysis was also performed to determine statistical significance for the cell area and volume relationship (*** p = <0.0001). Ang II: Angiotensin II; ROCK: Rho-associated protein kinase; VSMC: Vascular smooth muscle cell.

Conversely, nuclear volume showed opposing results as treatment with Y-27632 induced a significant reduction (**Figure 5.5A & B**). Like before, it was found that ROCK inhibition significantly enhanced the nuclear area to volume relationship (**Figure 5.5C**).

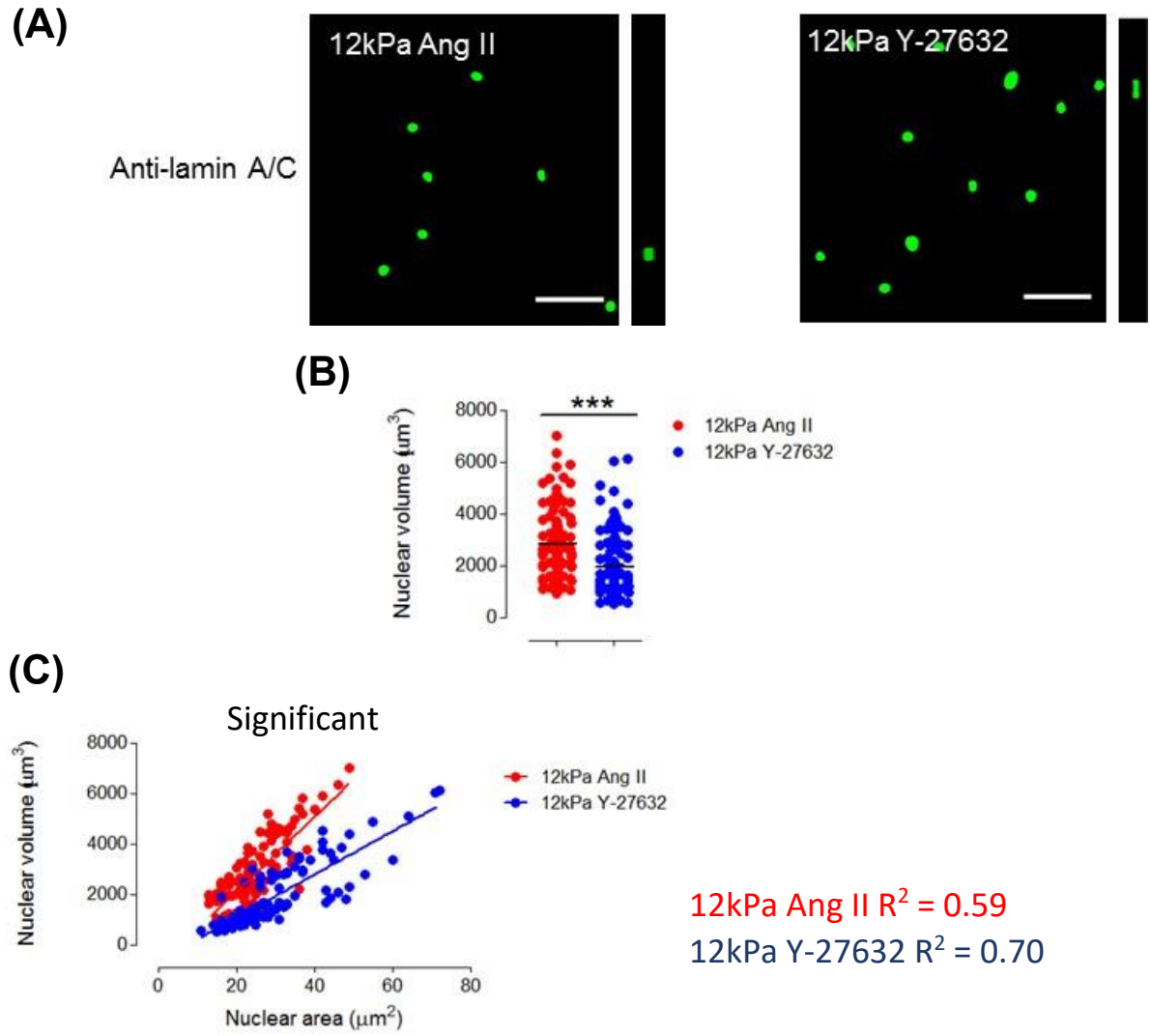

Figure 5.5: The impact of a ROCK inhibitor on VSMC nuclear volume. **(A)** Representative immunofluorescence images of VSMC nuclei treated with Y-27632. Images show VSMC nuclei stained using anti-lamin A/C (green) on 12 kPa polyacrylamide hydrogels. Scale bar represents 100 µm. Volocity software was used to manually measure **(B)** nuclear volume. Image J software was used to plot **(C)** VSMC nuclear area against volume on cells treated with Angiotensin II alone and with Y-27632. Data are based on the measurement of >150 VSMCs from 3 independent experiments. Statistical significance was determined using a paired Student's *t* test on nuclear volume (12 kPa Ang II vs 12 kPa Y-27632) (*** p = <0.0001). A linear regression analysis was also performed to determine statistical significance for the nuclear area and volume relationship (*** p = <0.0001). Ang II: Angiotensin II; ROCK: Rho-associated protein kinase; VSMC: Vascular smooth muscle cell.

In contrast, VSMCs on 72 kPa hydrogels displayed no difference in cytosolic volume via Y-27632 treatment (**Figure 5.6A & B**). Additionally, the cell area to volume relationship did not significantly alter between treatment groups, with both presenting strong trends (**Figure 5.6C**).

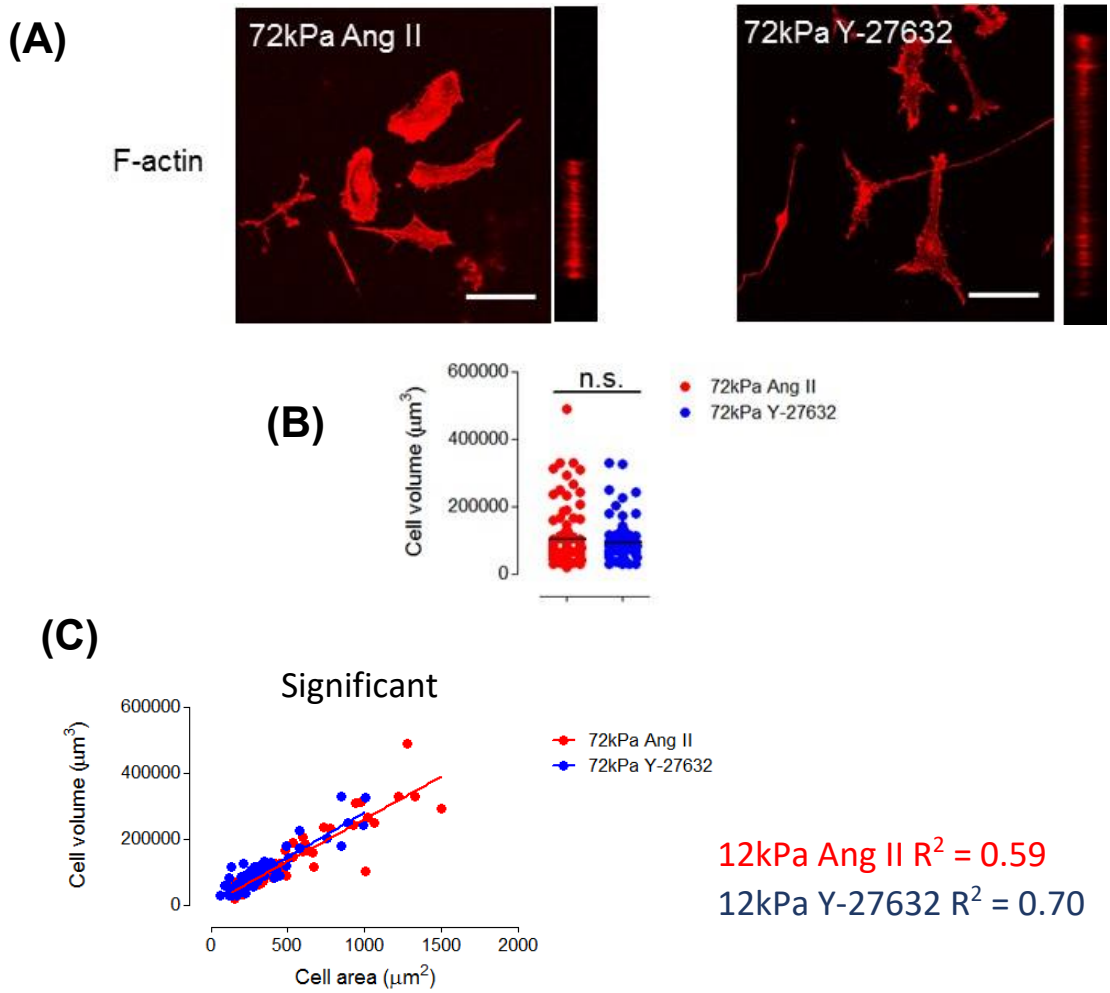

Figure 5.6: The impact of a ROCK inhibitor and matrix stiffness on VSMC volume. **(A)** Representative immunofluorescence images of VSMC actin filaments treated with Y-27632 within a stiffer matrix. Images show VSMC actin filaments (F-actin) stained using rhodamine phalloidin (red) on 72 kPa polyacrylamide hydrogels. Scale bar represents 100 µm. Volocity software was used to manually measure **(B)** cell volume. Image J software was used to plot **(C)** VSMC area against volume on cells treated with Angiotensin II alone and with Y-27632. Data are based on the measurement of >150 VSMCs from 3 independent experiments. Statistical significance was determined using a paired Student's *t* test on cell volume (72 kPa Ang II vs 72 kPa Y-27632) (non-significant; p = >0.05). A linear regression analysis was also performed to determine statistical significance for the cell area and volume relationship (*** p = <0.0001). Ang II: Angiotensin II; ROCK: Rho-associated protein kinase; VSMC: Vascular smooth muscle cell.

Nuclear volume, however, presented contrasting results on the 72kPa hydrogel with a significant increase shown when the ROCK-mediated pathway was inhibited (**Figure 5.7A & B**). In this case, Y-27632 treatment was shown to significantly enhance the nuclear area to volume relationship (**Figure 5.7C**). This may be due to Y-27632 increasing nuclear volume, causing a subsequent increase in nuclear area enhancing the relationship as a result. This conflicts findings for the cell area to volume relationship (**Figure 5.6C**), which could be on account of Y-27632 treatment inducing no change in cell volume.

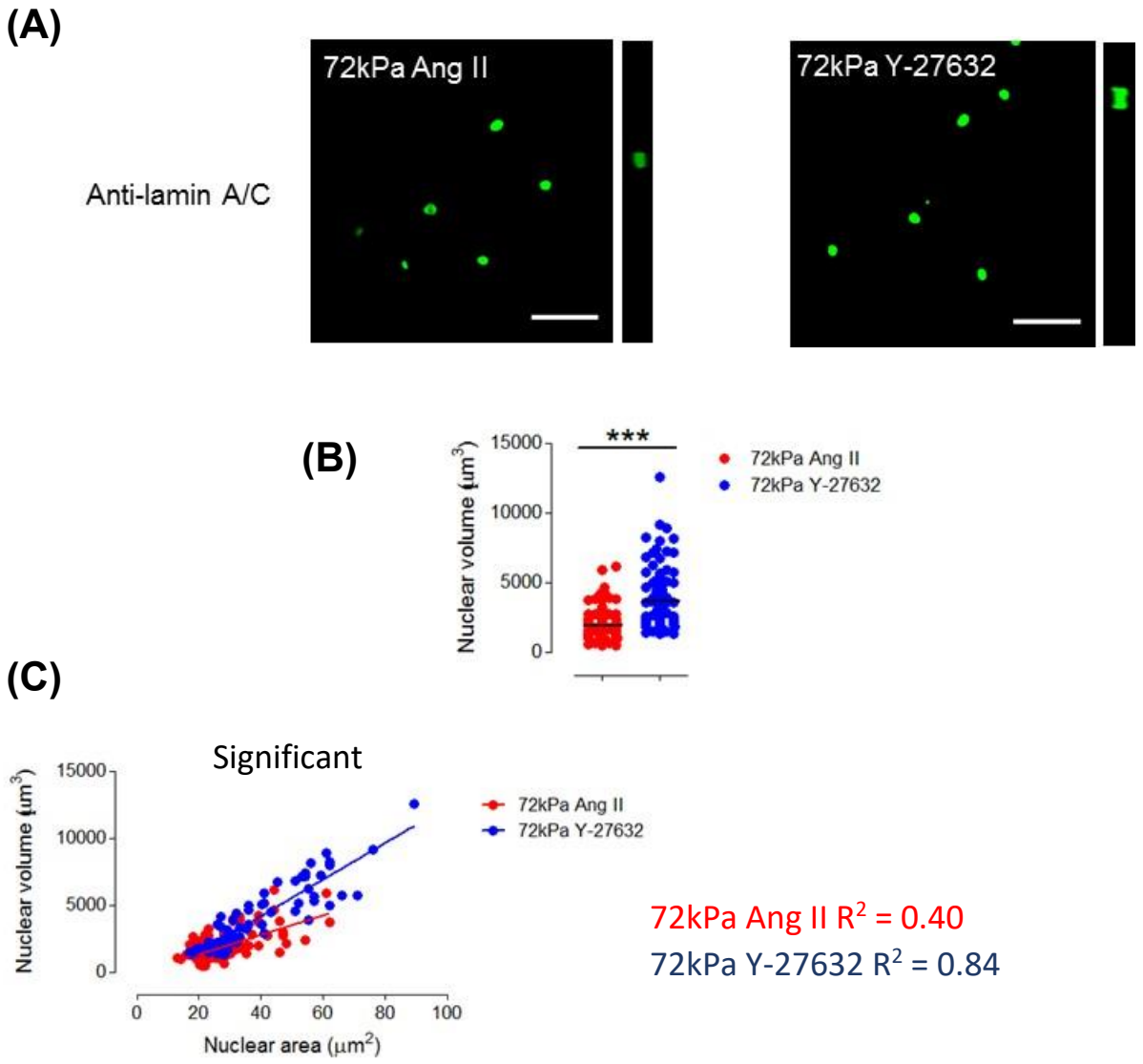

Figure 5.7: The impact of a ROCK inhibitor and matrix stiffness on VSMC nuclear volume. **(A)** Representative immunofluorescence images of VSMC nuclei treated with Y-27632 within a stiffer matrix. Images show VSMC nuclei stained using anti-lamin A/C (green) on 72 kPa polyacrylamide hydrogels. Scale bar represents 100 µm. Volocity software was used to manually measure **(B)** nuclear volume. Image J software was used to plot **(C)** VSMC nuclear area against volume on cells treated with Angiotensin II alone and with Y-27632. Data are based on the measurement of >150 VSMCs from 3 independent experiments. Statistical significance was determined using a paired Student's *t* test on nuclear volume (72 kPa Ang II vs 72 kPa Y-27632) (*** p = <0.0001). A linear regression analysis was also used to determine statistical significance for the nuclear area and volume relationship (*** p = <0.0001). Ang II: Angiotensin II; ROCK: Rho-associated protein kinase; VSMC: Vascular smooth muscle cell.

From the results above, it is shown the ROCK inhibition does not significantly alter the VSMC volume. However, its effects do significantly increase nuclear volume which may cause additional mechanical pressure. These results may be due to the fact that ROCK mediates numerous cellular processes via the actin cytoskeleton, and as a result, we next utilised Blebbistatin as this is a specific inhibitor of myosin II (81, 272). Previous studies have found that inhibition of myosin-II contraction caused a reduction in nuclear volume within mesenchymal stem cells (323). As a result, we cultured and stained our VSMCs as mentioned before, however this time treated with 40 µM of Blebbistatin.

Our results here show that, much like Y-27632, Blebbistatin treatment induces a larger cytosolic volume in VSMCs grown on 12 kPa polyacrylamide hydrogels (**Figure 5.8A & B**). The cell area to volume relationship presented no significant difference to the control (**Figure 5.8C**).

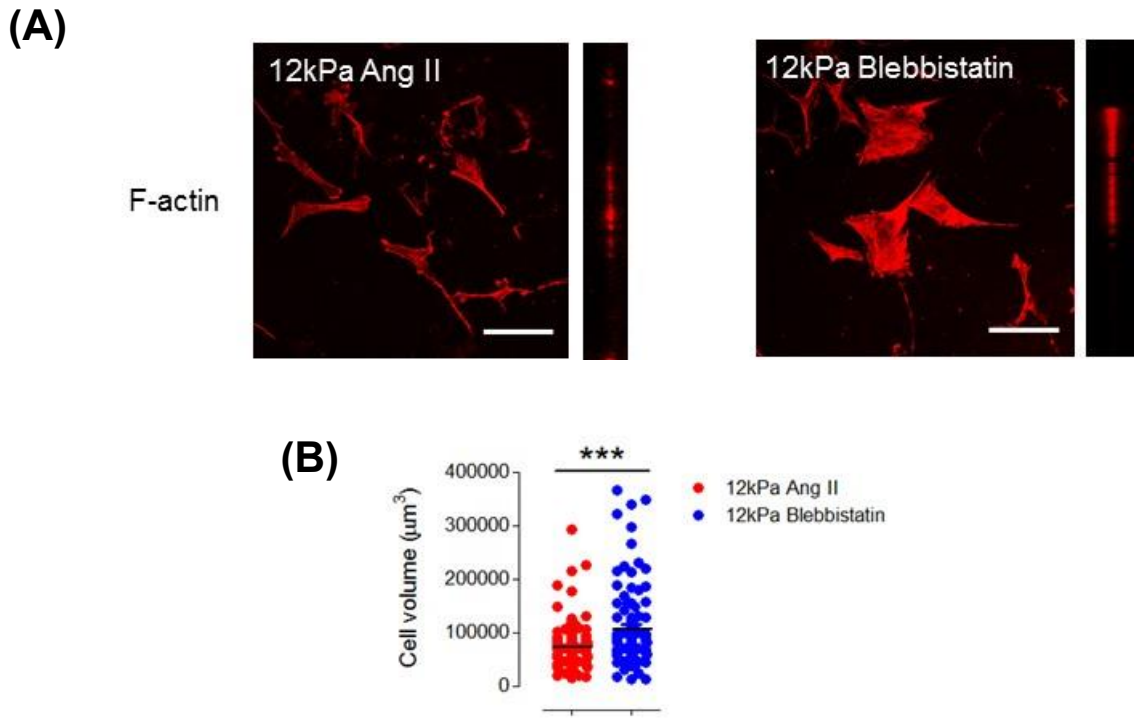

Figure 5.8: The impact of a Myosin II inhibitor on VSMC volume. **(A)** Representative immunofluorescence images of VSMC actin filaments treated with Blebbistatin. Images show VSMC actin filaments (F-actin) stained using rhodamine phalloidin (red) on 12 kPa polyacrylamide hydrogels. Scale bar represents 100 µm. Volocity software was used to manually measure **(B)** cell volume. Image J software was used to plot **(C)** VSMC area against volume on cells treated with Angiotensin II alone and with Blebbistatin. Data are based on the measurement of >150 VSMCs from 3 independent experiments. Statistical significance was determined using a paired Student's *t* test on cell volume (12 kPa Ang II vs 12 kPa Blebbistatin) (*** p = <0.0001). A linear regression analysis was also performed to determine statistical significance for the cell area and volume relationship (non-significant; p = >0.05). Ang II: Angiotensin II; VSMC: Vascular smooth muscle cell.

Contrastingly, no change in nuclear volume was observed (**Figure 5.9A & B**). Much like the cell area to volume trends, the nuclear area/volume relationship presented no significant difference between both treatment groups (**Figure 5.9C**).

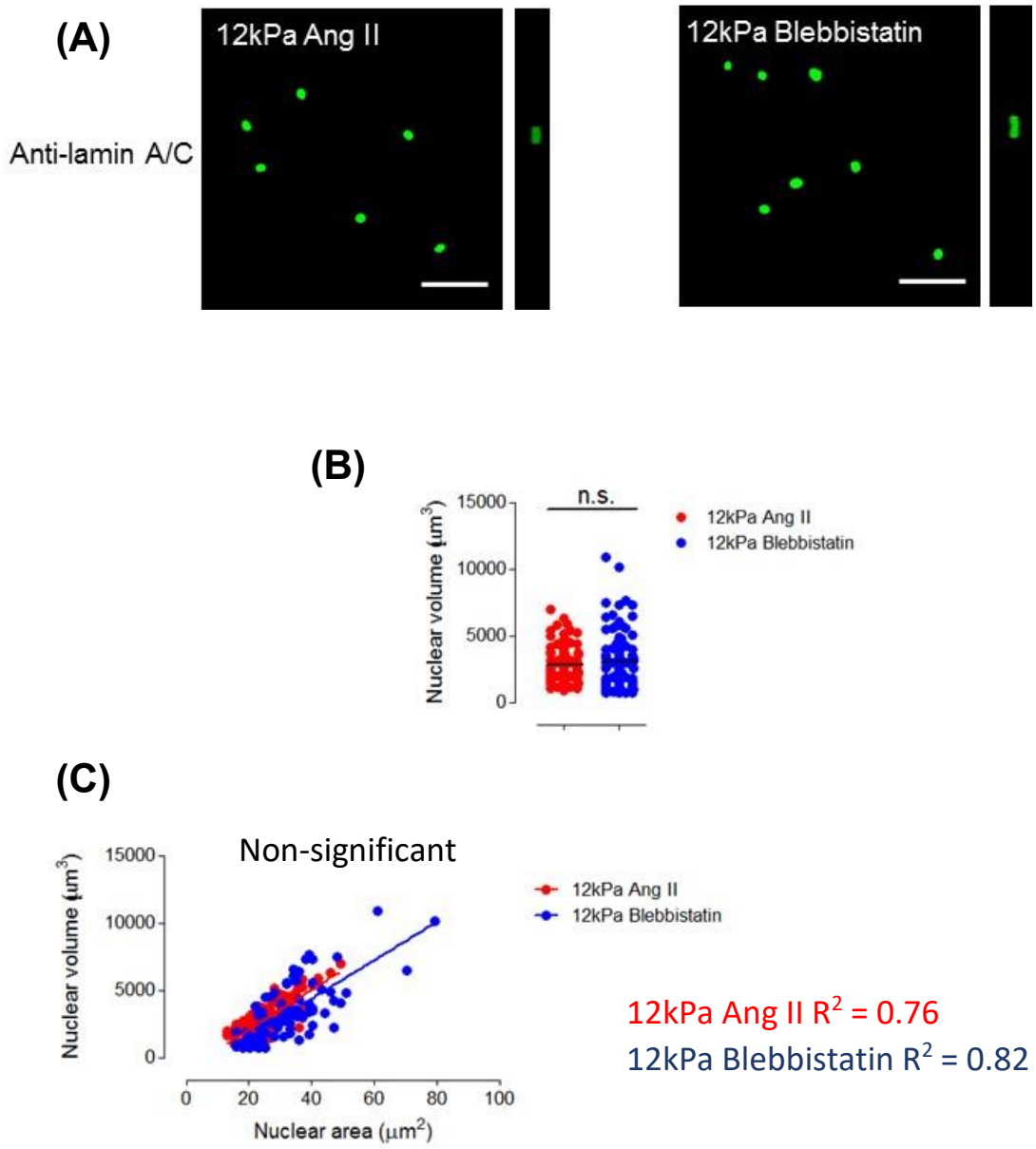

Figure 5.9: The impact of a Myosin II inhibitor on VSMC nuclear volume. **(A)** Representative immunofluorescence images of VSMC nuclei treated with Blebbistatin. Images show VSMC nuclei stained using anti-lamin A/C (green) on 12 kPa polyacrylamide hydrogels. Scale bar represents 100 µm. Volocity software was used to manually measure **(B)** nuclear volume. Image J software was used to plot **(C)** VSMC nuclear area against volume on cells treated with Angiotensin II alone and with Blebbistatin. Data are based on the measurement of >150 VSMCs from 3 independent experiments. Statistical significance was determined using a paired Student's *t* test on nuclear volume (12 kPa Ang II vs 12 kPa Blebbistatin) (non-significant; p = >0.05). A linear regression analysis was also performed to determine statistical significance for the nuclear area and volume relationship (non-significant; p = >0.05). Ang II: Angiotensin II; VSMC: Vascular smooth muscle.

When cultured on a rigid substrate, Blebbistatin evokes a similar decrease in VSMC volume compared to Y-27632 treatment (**Figure 5.10A & B**). Both Angiotensin II alone and Blebbistatin treated VSMCs present a strong relationship in their area to volume trends (**Figure 5.10C**).

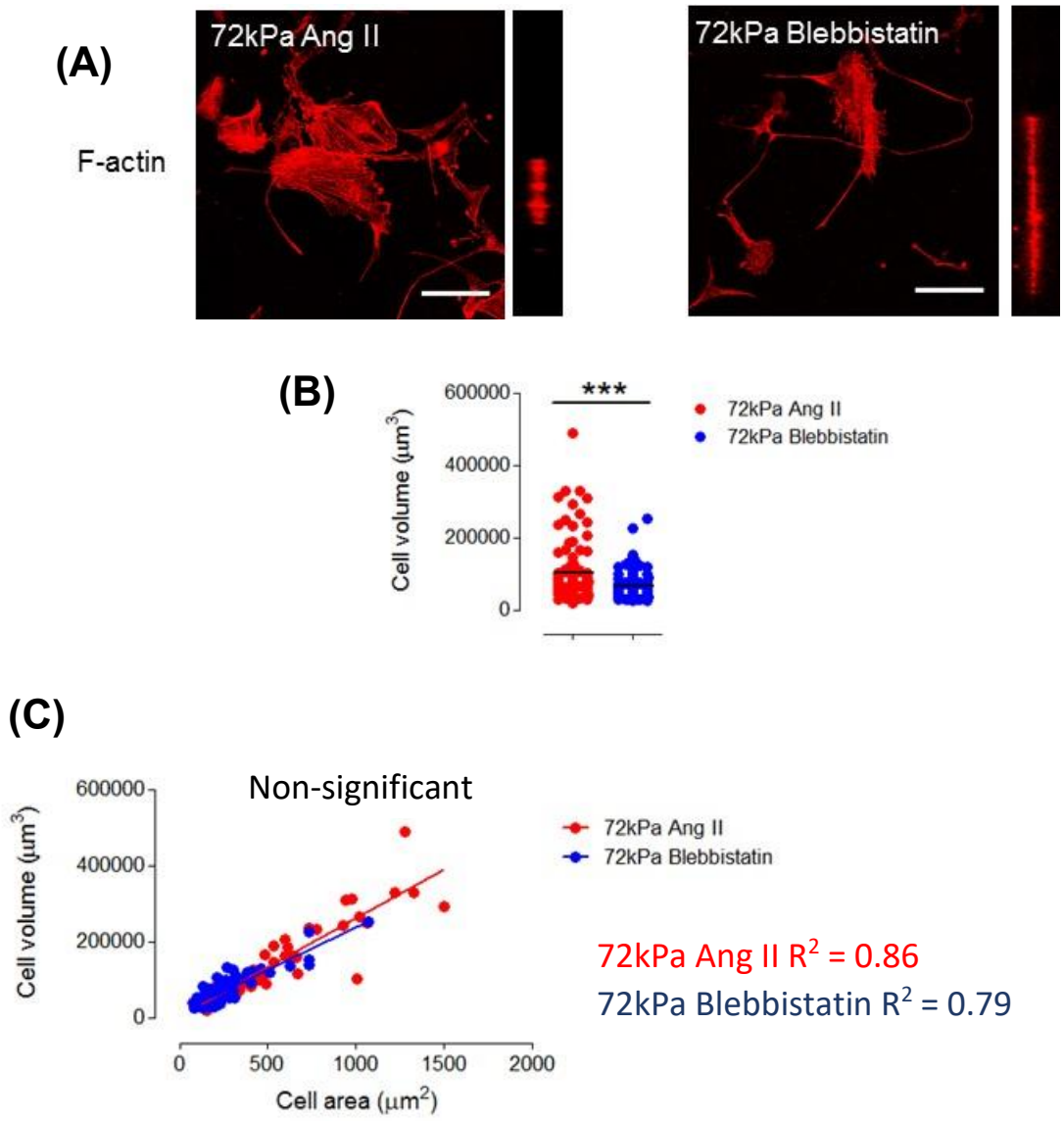

Figure 5.10: The impact of a Myosin II inhibitor and matrix stiffness on VSMC volume. **(A)** Representative immunofluorescence images of VSMC actin filaments treated with Blebbistatin within a stiffer matrix. Images show VSMC actin filaments (F-actin) stained using rhodamine phalloidin (red) on 72 kPa polyacrylamide hydrogels. Scale bar represents 100 µm. Volocity software was used to manually measure **(B)** cell volume. Image J software was used to plot **(C)** VSMC area against volume on cells treated with Angiotensin II alone and with Blebbistatin. Data are based on the measurement of >150 VSMCs from 3 independent experiments. Statistical significance was determined using a paired Student's *t* test on cell volume (72 kPa Ang II vs 72 kPa Blebbistatin) (*** p = <0.0001). Additionally, a linear regression analysis was performed to determine statistical significance for the cell area and volume relationship (non-significant; p = >0.05). Ang II: Angiotensin II; VSMC: Vascular smooth muscle.

Next, we observed the nuclear volume. Volocity analysis revealed no significant difference in the nuclear volume, with weak correlations shown in the area to volume relationships of the nuclei (**Figure 5.11**).

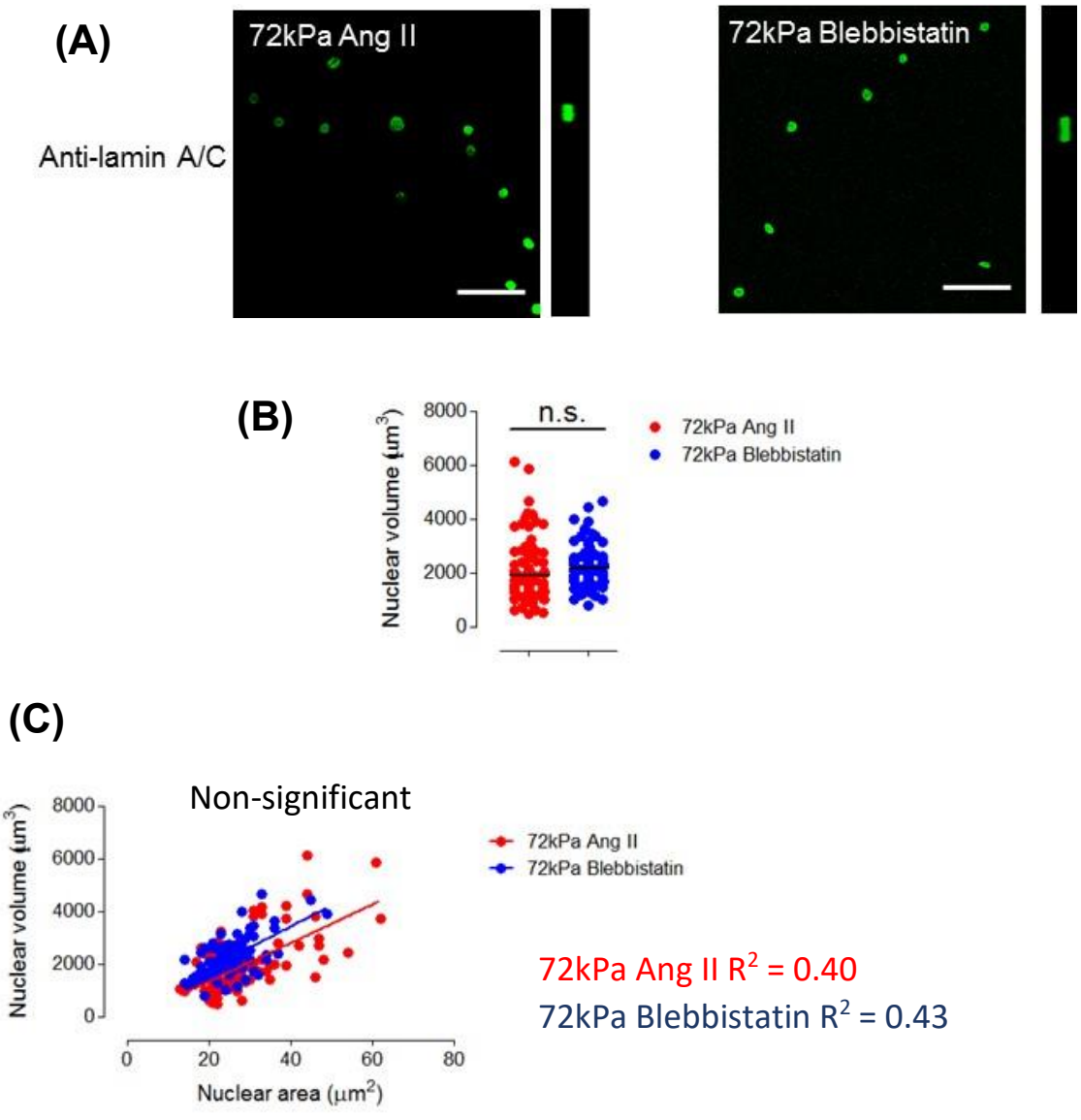

Figure 5.11: The impact of a Myosin II inhibitor and matrix stiffness on VSMC nuclear volume. **(A)** Representative immunofluorescence images of VSMC nuclei treated with Blebbistatin within a stiffer matrix. Images show VSMC nuclei stained using anti-lamin A/C (green) on 72 kPa polyacrylamide hydrogels. Scale bar represents 100 µm. Volocity software was used to manually measure **(B)** nuclear volume. Image J software was used to plot **(C)** VSMC nuclear area against volume on cells treated with Angiotensin II alone and with Blebbistatin. Data are based on the measurement of >150 VSMCs from 3 independent experiments. Statistical significance was determined using a paired Student's *t* test on nuclear volume (72 kPa Ang II vs 72 kPa Blebbistatin) (non-significant; p = >0.05). A linear regression analysis was also performed to determine statistical significance for the nuclear area and volume relationship (non-significant; p = >0.05). Ang II: Angiotensin II; VSMC: Vascular smooth muscle.

To consolidate our findings, we utilised another inhibitor of the Rho/ROCK pathway. Experimental conditions were kept the same but this time with 0.5 µM of Atorvastatin. Interestingly, Atorvastatin treatment showed no significant difference in either VSMC/nuclear volume, with little to no correlation in area to volume trends when seeded on a compliant matrix (**Figure 5.12 & 13**).

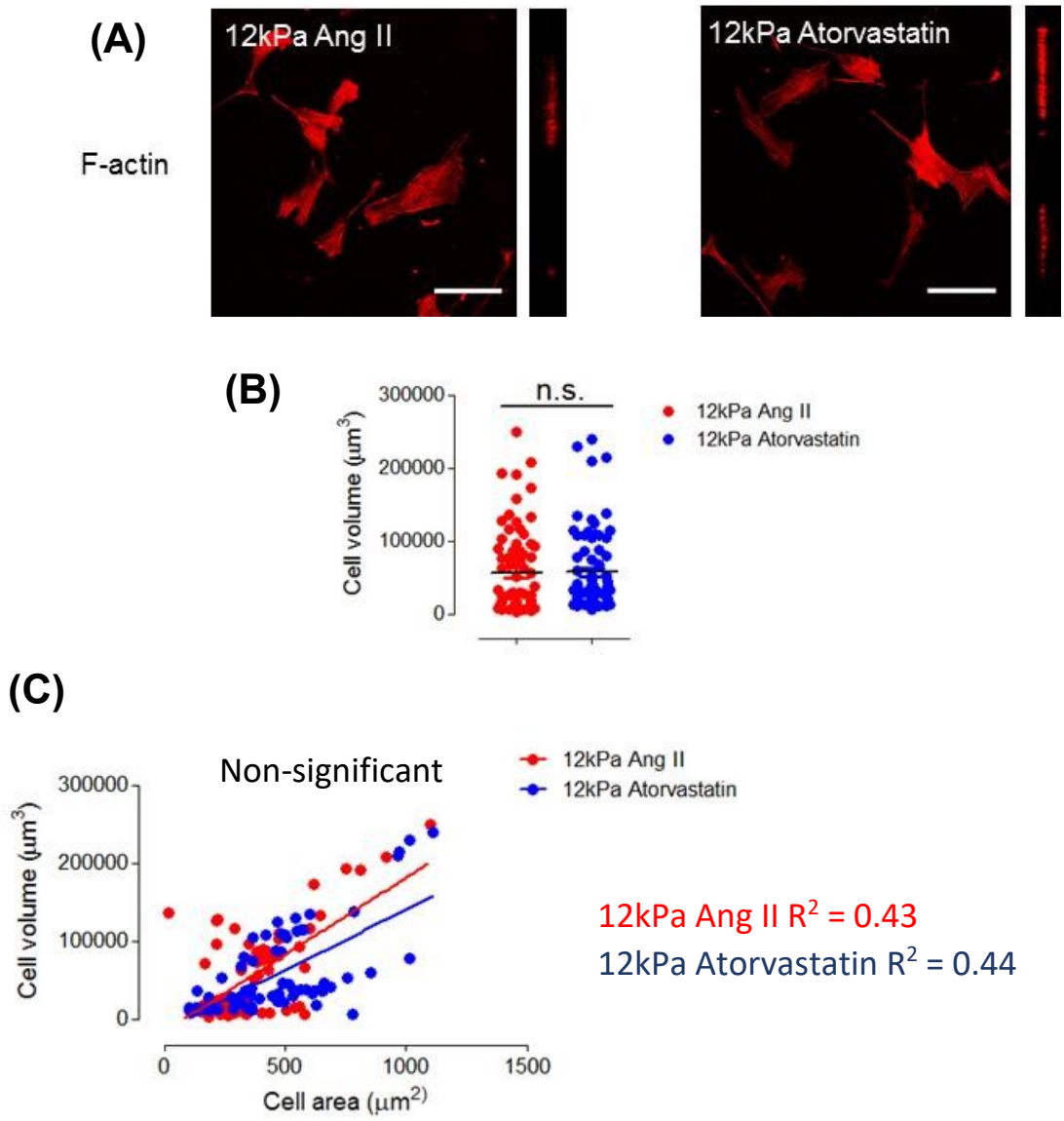

Figure 5.12: The impact of Atorvastatin on VSMC volume. **(A)** Representative immunofluorescence images of VSMC actin filaments treated with Atorvastatin. Images show VSMC actin filaments (F-actin) stained using rhodamine phalloidin (red) on 12 kPa polyacrylamide hydrogels. Scale bar represents 100 µm. Volocity software was used to manually measure **(B)** cell volume. Image J software was used to plot **(C)** VSMC area against volume on cells treated with Angiotensin II alone and with Atorvastatin. Data are based on the measurement of ~100 VSMCs from 3 independent experiments. Statistical significance was determined using a paired Student's *t* test on cell volume (12 kPa Ang II vs 12 kPa Atorvastatin) (non-significant; p = >0.05). A linear regression analysis was also performed to determine statistical significance for the cell area and volume relationship (non-significant; p = >0.05). Ang II: Angiotensin II; VSMC: Vascular smooth muscle.

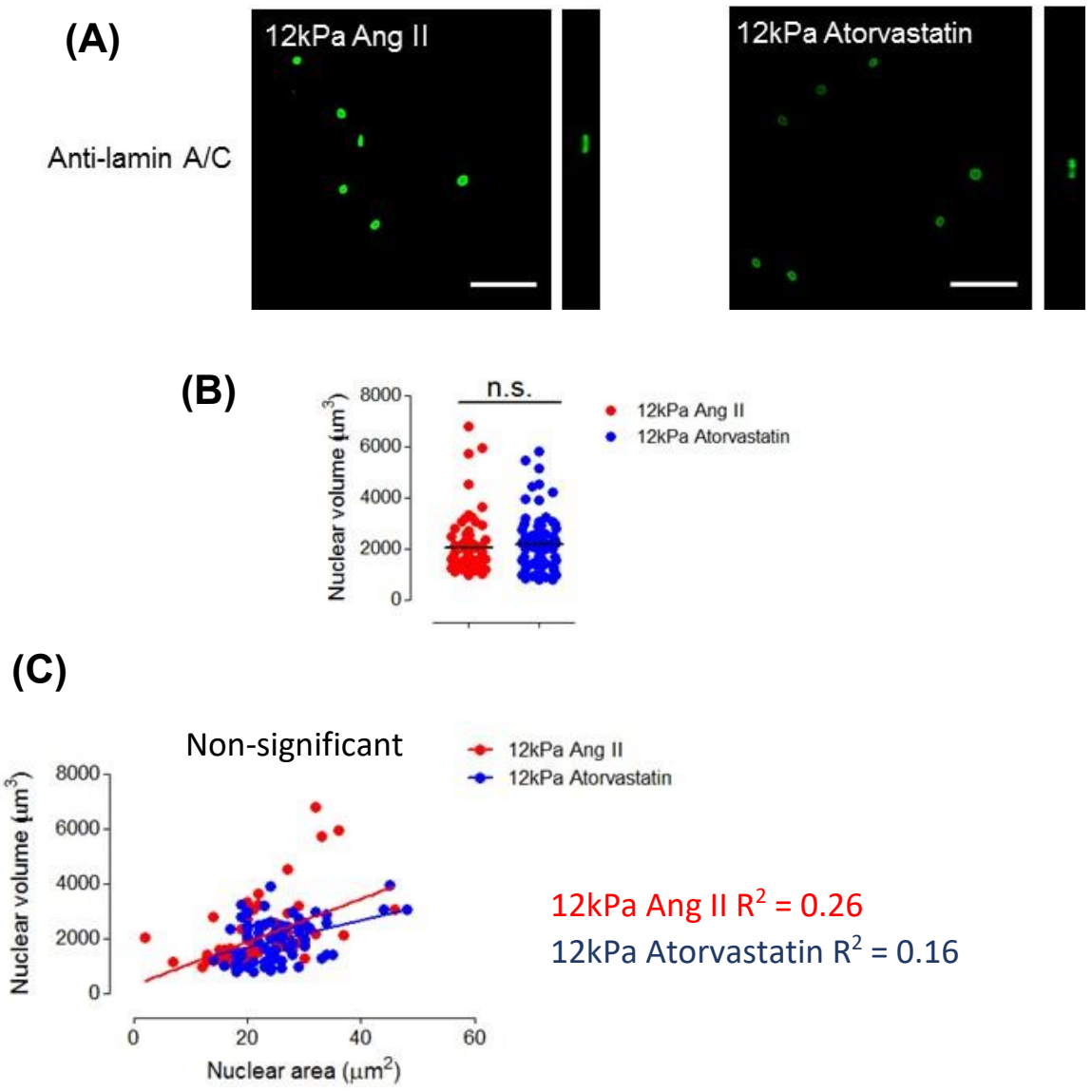

Figure 5.13: The impact of Atorvastatin on VSMC nuclear volume. **(A)** Representative immunofluorescence images of VSMC nuclei treated with Atorvastatin. Images show VSMC nuclei stained using anti-lamin A/C (green) on 12 kPa polyacrylamide hydrogels. Scale bar represents 100 µm. Volocity software was used to manually measure **(B)** nuclear volume. Image J software was used to plot **(C)** VSMC nuclear area against volume on cells treated with Angiotensin II alone and with Atorvastatin. Data are based on the measurement of ~100 VSMCs from 3 independent experiments. Statistical significance was determined using a paired Student's *t* test on nuclear volume (12 kPa Ang II vs 12 kPa Atorvastatin) (non-significant; p = >0.05). A linear regression analysis was also performed to determine statistical significance for the nuclear area and volume relationship (non-significant; p = >0.05). Ang II: Angiotensin II; VSMC: Vascular smooth muscle.

However, unlike the 12 kPa hydrogel, the Atorvastatin inhibitor was shown to significant decrease cell volume when VSMCs were seeded on a rigid substrate (**Figure 5.14A & B**). This suggests that the Rho/ROCK pathway may in fact contribute to changes in cytosolic volume on the 72 kPa hydrogel. Additionally, Atorvastatin treatment was found to significantly diminish the cell area to volume relationship (**Figure 5.14C**), and this may be due to the reduction in cytosolic volume previously induced.

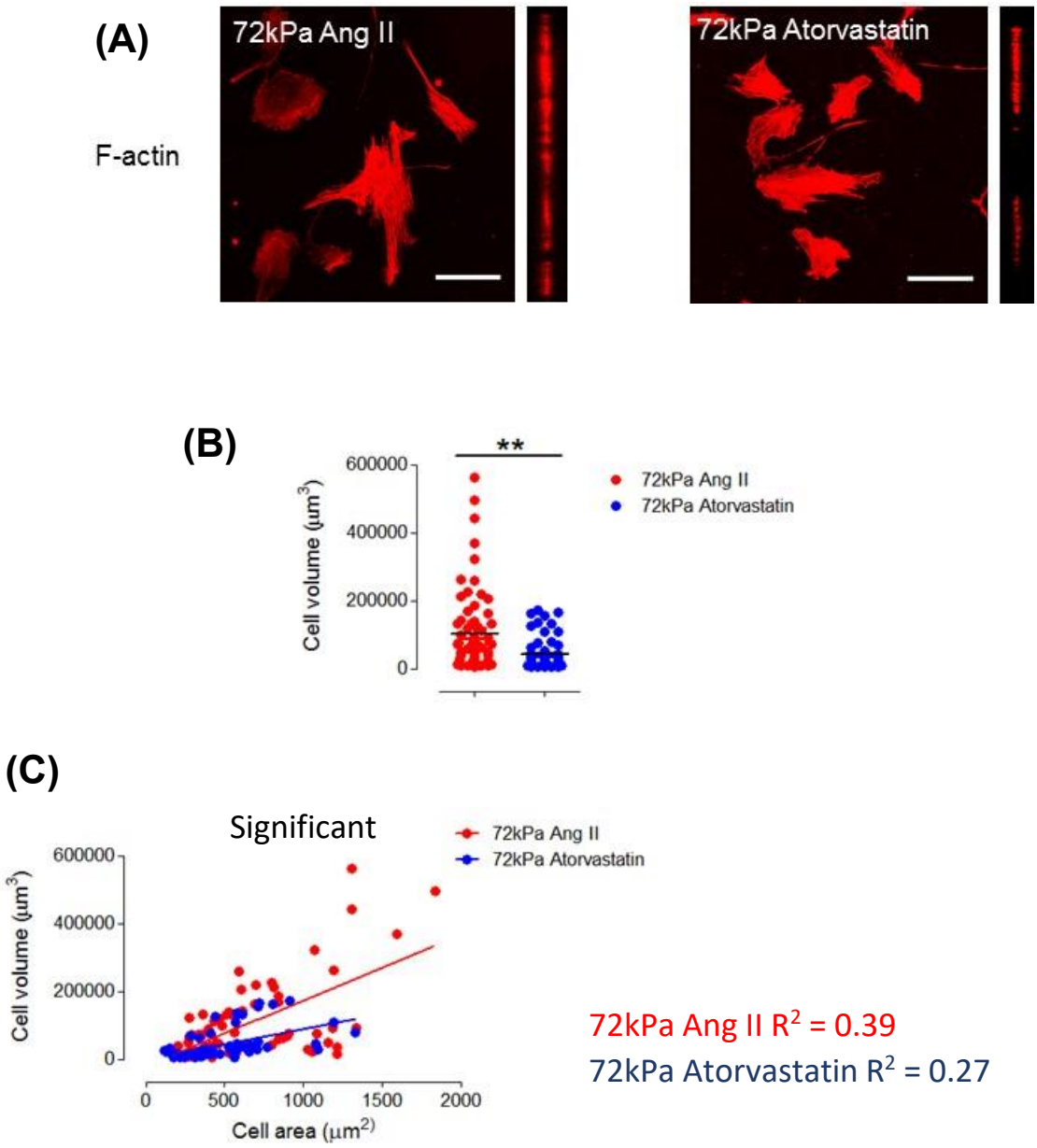

Figure 5.14: The impact of Atorvastatin and matrix stiffness on VSMC volume. **(A)** Representative immunofluorescence images of VSMC actin filaments treated with Atorvastatin within a stiffer matrix. Images show VSMC actin filaments (F-actin) stained using rhodamine phalloidin (red) on 72 kPa polyacrylamide hydrogels. Scale bar represents 100 µm. Volocity software was used to manually measure **(B)** cell volume. Image J software was used to plot **(C)** VSMC area against volume on cells treated with Angiotensin II alone and with Atorvastatin. Data are based on the measurement of ~100 VSMCs from 3 independent experiments. Statistical significance was determined using a paired Student's *t* test on cell volume (72 kPa Ang II vs 72 kPa Atorvastatin) (** p = <0.001). Additionally, a linear regression analysis was performed to determine statistical significance for the cell area and volume relationship (*** p = <0.0001). Ang II: Angiotensin II; VSMC: Vascular smooth muscle.

Alongside this, despite not being a specific inhibitor for myosin II, Atorvastatin presents similar responses to Blebbistatin treatment evoking no significant change in the nuclear volume (**Figure 5.15A & B**). Area to volume trends were shown to have similar correlations to what was observed on the 12 kPa polyacrylamide hydrogel for Atorvastatin treated VSMCs (**Figure 5.15C**).

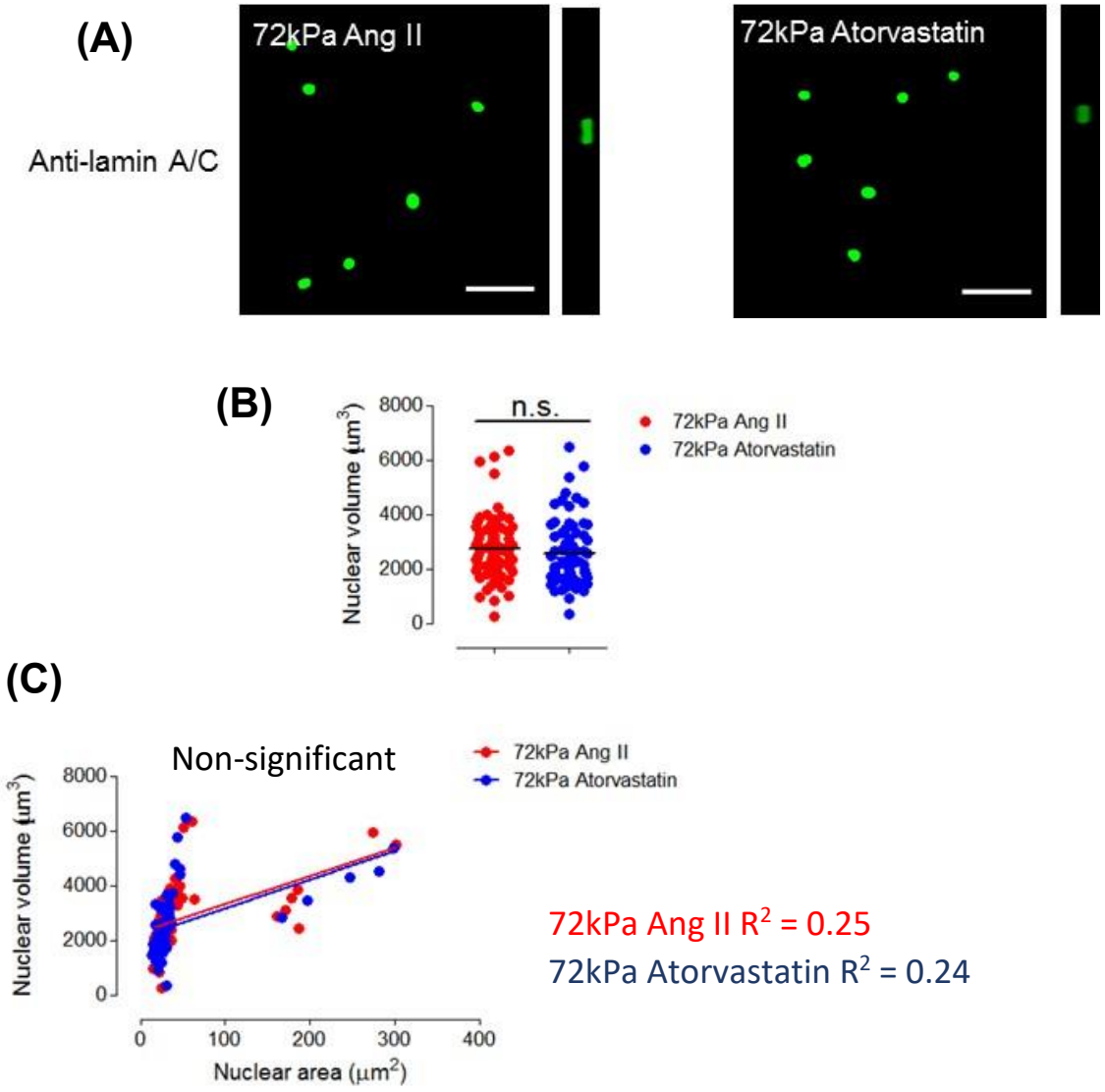

Figure 5.15: The impact of Atorvastatin and matrix stiffness on VSMC nuclear volume. **(A)** Representative immunofluorescence images of VSMC nuclei treated with Atorvastatin within a stiffer matrix. Images show VSMC nuclei stained using anti-lamin A/C (green) on 72 kPa polyacrylamide hydrogels. Scale bar represents 100 µm. Volocity software was used to manually measure **(B)** nuclear volume. Image J software was used to plot **(C)** VSMC nuclear area against volume on cells treated with Angiotensin II alone and with Atorvastatin. Data are based on the measurement of ~100 VSMCs from 3 independent experiments. Statistical significance was determined using a paired Student's *t* test on nuclear volume (72 kPa Ang II vs 72 kPa Atorvastatin) (non-significant; p = >0.05). A linear regression analysis was also performed to determine statistical significance for the nuclear area and volume relationship (non-significant; p = >0.05). Ang II: Angiotensin II; VSMC: Vascular smooth muscle.

To conclude, we observe that the actomyosin inhibitors utilised within this project can induce differential effects in both cell and nuclear volume for VSMCs pre-treated with Angiotensin II, and a table summarising these changes is shown below (**Table 5.1**).

Table 5.1: Summarising the effects of actomyosin inhibitors on cell and nuclear volume for VSMCs pre-treated with 10 μM of Angiotensin II.

Volume change			
	Y-27632	**Blebbistatin**	**Atorvastatin**
12 kPa Cell volume	Increase	Increase	No change
12 kPa Nuclear volume	Decrease	No change	No change
72 kPa Cell volume	No change	Decrease	Decrease
72 kPa Nuclear volume	Increase	No change	No change

5.4.3 Role of stretch activation channels in matrix stiffness

In this chapter, we have demonstrated that VSMC hypertrophy is mediated via actomyosin activity. However, we needed to clarify the mechanisms driving this altered response. In conditions of aortic stiffness, pulse pressure is unable to expand the arterial wall, and as a result, increased blood pressure is generated (17). Earlier studies have shown the SACs possess a greater probability of opening with increased pressure (324, 325), and we hypothesise this may contribute to the cell swelling phenomena observed.

To investigate this, we utilised the SAC blocker GsMTx-4. VSMCs were grown in basal medium to induce quiescence, and then cultured on collagen-1 coated polyacrylamide hydrogels, with an average Young's modulus of 12 kPa and 72 kPa. Previous work has utilised GsMTx-4 with doses around 250 nM (326). As a result, VSMCS were pre-treated with a serial dilution of GsMTx-4, with concentrations ranging between 0.05 nM-500 nM, for 30 minutes which was followed with 10μM of Angiotensin II stimulation for an additional 30 minutes. Prior to immunofluorescence microscopy, VSMC filamentous actin and nuclei were stained with rhodamine phalloidin and DAPI, respectively. When looking at cell area, our results show that the SAC blocker has no significant effect within the physiological environment. However, we show that VSMC area was significantly decreased by a 500 nM dose on 72 kPa hydrogels (**Figure 5.16**).

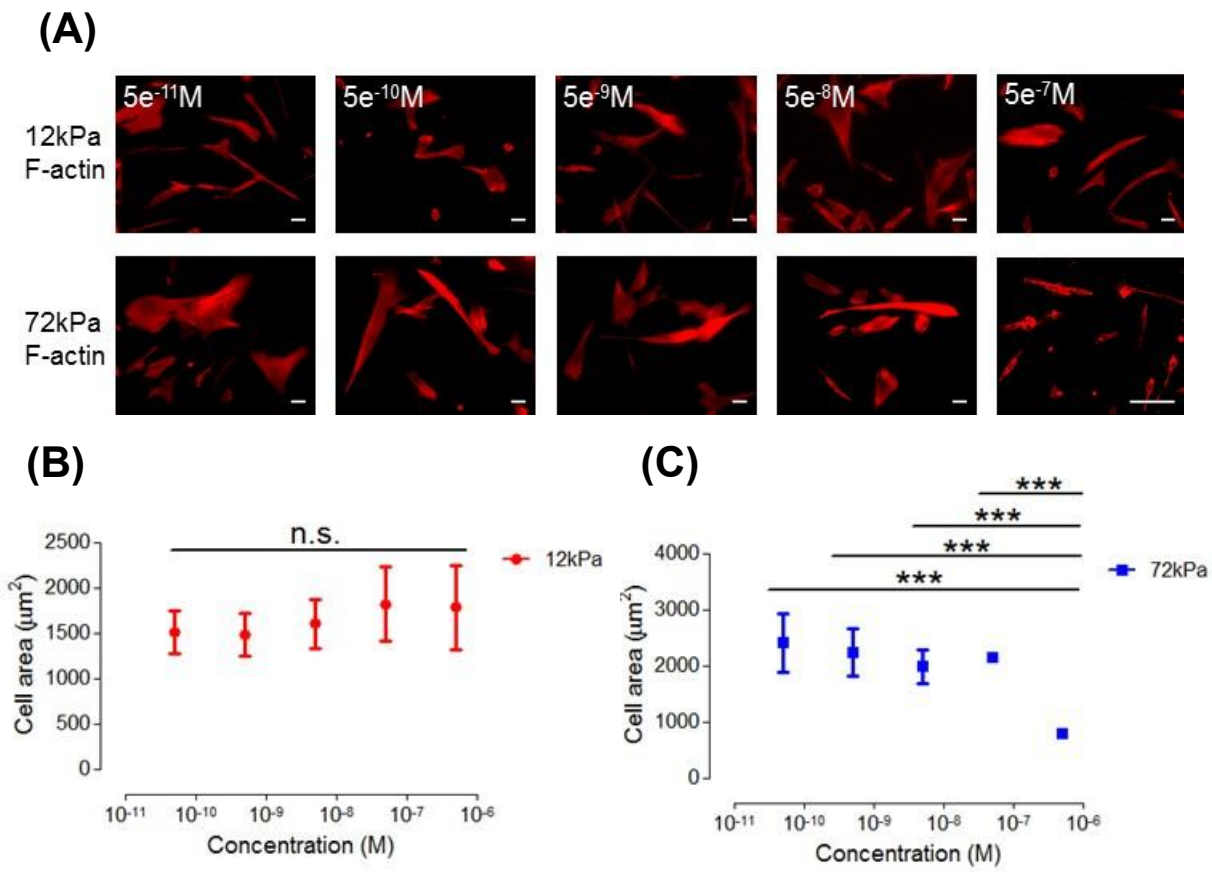

Figure 5.16: The impact of mechanical-gated ion channel blocker on VSMC morphology. **(A)** Representative immunofluorescence images of VSMC actin filaments pre-treated with a serial dilution of GsMTx-4, followed by 10 µM of Angiotensin II stimulation. Images show VSMC actin filaments (F-actin) stained using rhodamine phalloidin (red) on both 12 kPa and 72 kPa polyacrylamide hydrogels. Scale bar represents 100 µm. Image J software was used to manually measure the cell area of the VSMCs on **(B)** 12 kPa and **(C)** 72 kPa polyacrylamide hydrogels. Data are based on the measurement of >150 VSMCs from 3 independent experiments. Statistical significance was determined using a one-way ANOVA to show differences in cell area on 12 kPa (non-significant; p = >0.05) and 72 kPa (*** p = <0.0001) matrices, followed by a Bonferroni's multiple comparison test. VSMC: Vascular smooth muscle cells.

When observing nuclear morphology, we found this was in agreement with our previous findings (**Figure 5.17A & C**), showing a 500 nM dose of GsMTx-4 can significantly reduce nuclear area on the 72 kPa hydrogel. In contrast to cell area (**Figure 5.16A & B**), we find a 50 nM dose of GsMTx-4 can induce a significant increase in nuclear area (**Figure 5.17A & B**). This gives indication that SACs may play an active role within VSMCs when seeded on both 12 kPa and 72 kPa hydrogels.

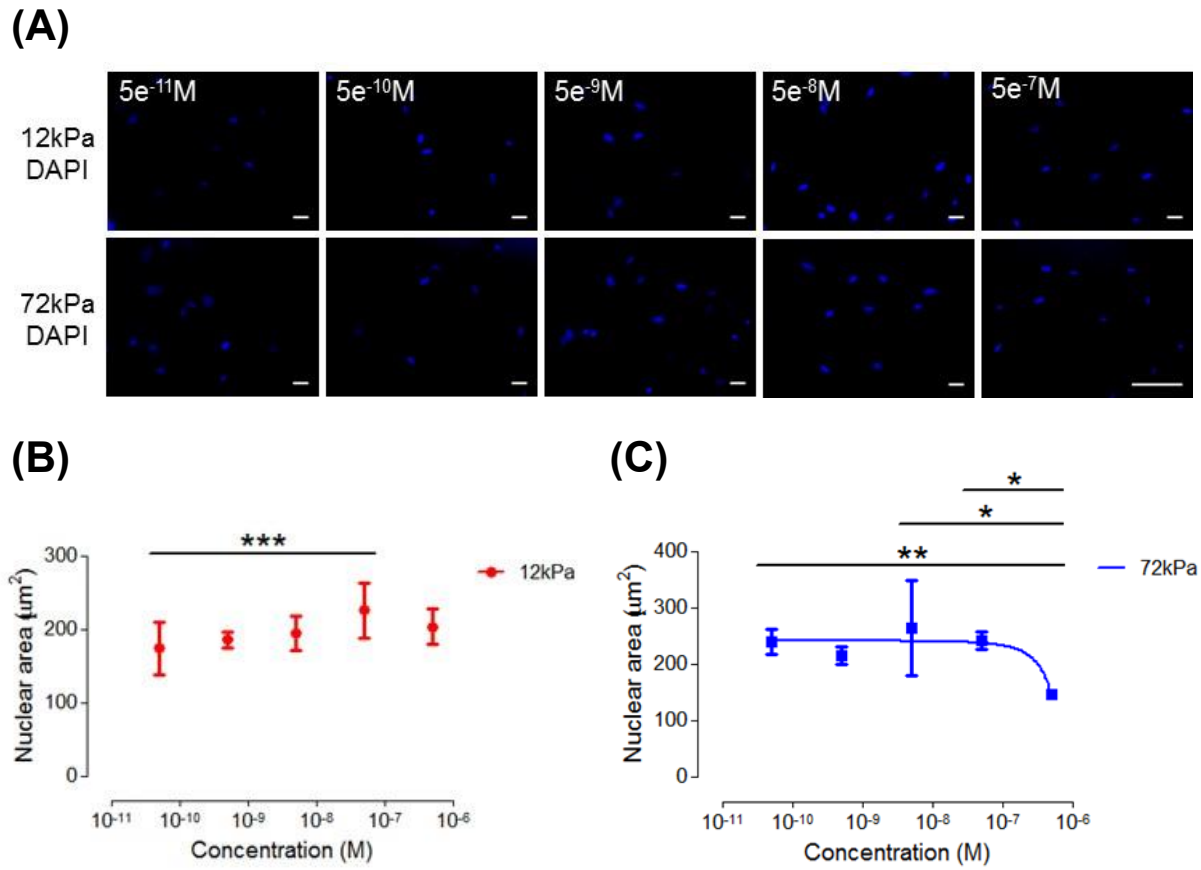

Figure 5.17: The impact of mechanical-gated ion channel blocker on VSMC nuclear morphology. **(A)** Representative immunofluorescence images of VSMC nuclei pre-treated with a serial dilution of GsMTx-4, followed by 10 µM of Angiotensin II stimulation. Images show VSMC nuclei stained using DAPI (blue) on both 12 kPa and 72 kPa polyacrylamide hydrogels. Scale bar represents 100 µm. Image J software was used to manually measure the nuclear area of the VSMCs on **(B)** 12 kPa and **(C)** 72 kPa polyacrylamide hydrogels. Data are based on the measurement of >150 VSMCs from 3 independent experiments. Statistical significance was determined using a one-way ANOVA to show differences in nuclear area on 12 kPa (*** p = <0.0001) and 72 kPa (* p = <0.05, ** p = <0.001) matrices, followed by a Bonferroni's multiple comparison test. VSMC: Vascular smooth muscle cell.

Next, we looked at the TRPC channels. TRPC channels have previously been shown to be expressed in variety of mammalian cell types, including VSMCs, and GsMTx-4 has been used to implicate these channels within muscle pathology in prior research (327, 328). Previous work has shown GsMTx-4 to successfully inhibit TRPC1, TRPC6 and Piezo1 (329, 330). As a result, we hypothesised that the TRPC channels may be a potential candidate for the matrix stiffness-driven response observed, and so we utilised a TRPC6 blocker SAR-7334 to investigate this. Prior studies have utilised SAR-7334 at low nanomolar concentrations ranging between 1-1000 nM to treat epithelial cells (331). Due to this, our experiments were set up as previous described with the GsMTx-4 serial dilution, however

concentrations utilised in this case ranged between 0.1 nM-10 µM. The results obtained showed that there was no difference in cell area with increasing concentrations of SAR-7334 for both rigidities (**Figure 5.18**).

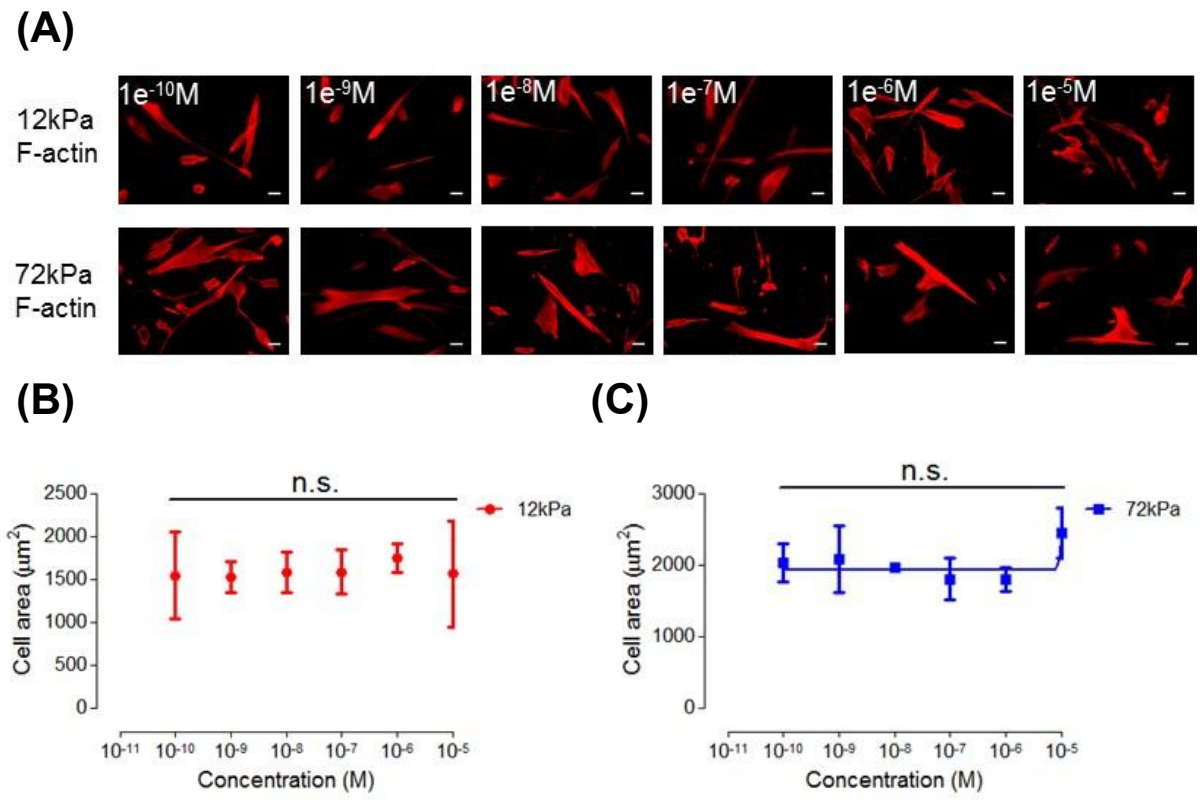

Figure 5.18: The impact of a TRPC6 channel blocker on VSMC morphology. **(A)** Representative immunofluorescence images of VSMC actin filaments pre-treated with a serial dilution of SAR-7334, followed by 10 µM of Angiotensin II stimulation. Images show VSMC actin filaments (F-actin) stained using rhodamine phalloidin (red) on both 12 kPa and 72 kPa polyacrylamide hydrogels. Scale bar represents 100 µm. Image J software was used to manually measure the cell area of the VSMCs on **(B)** 12 kPa and **(C)** 72 kPa polyacrylamide hydrogels. Data are based on the measurement of >150 VSMCs from 3 independent experiments. Statistical significance was determined using a one-way ANOVA to show differences in cell area on 12 kPa (non-significant; p = >0.05) and 72 kPa (non-significant; p = >0.05) matrices, followed by a Bonferroni's multiple comparison test. TRPC6: Transient receptor canonical 6; VSMC: Vascular smooth muscle cell.

When looking at nuclear morphology, we do see a significant decrease on the compliant matrix induced by higher concentrations, however no established effect was observed on the rigid hydrogel (**Figure 5.19**). This suggests that TRPC6 function may be

active within the physiological environment, however, it becomes unlikely that, on the 72kPa hydrogel, TRPC6 mediates the effects we see inhibited by GsMTx-4.

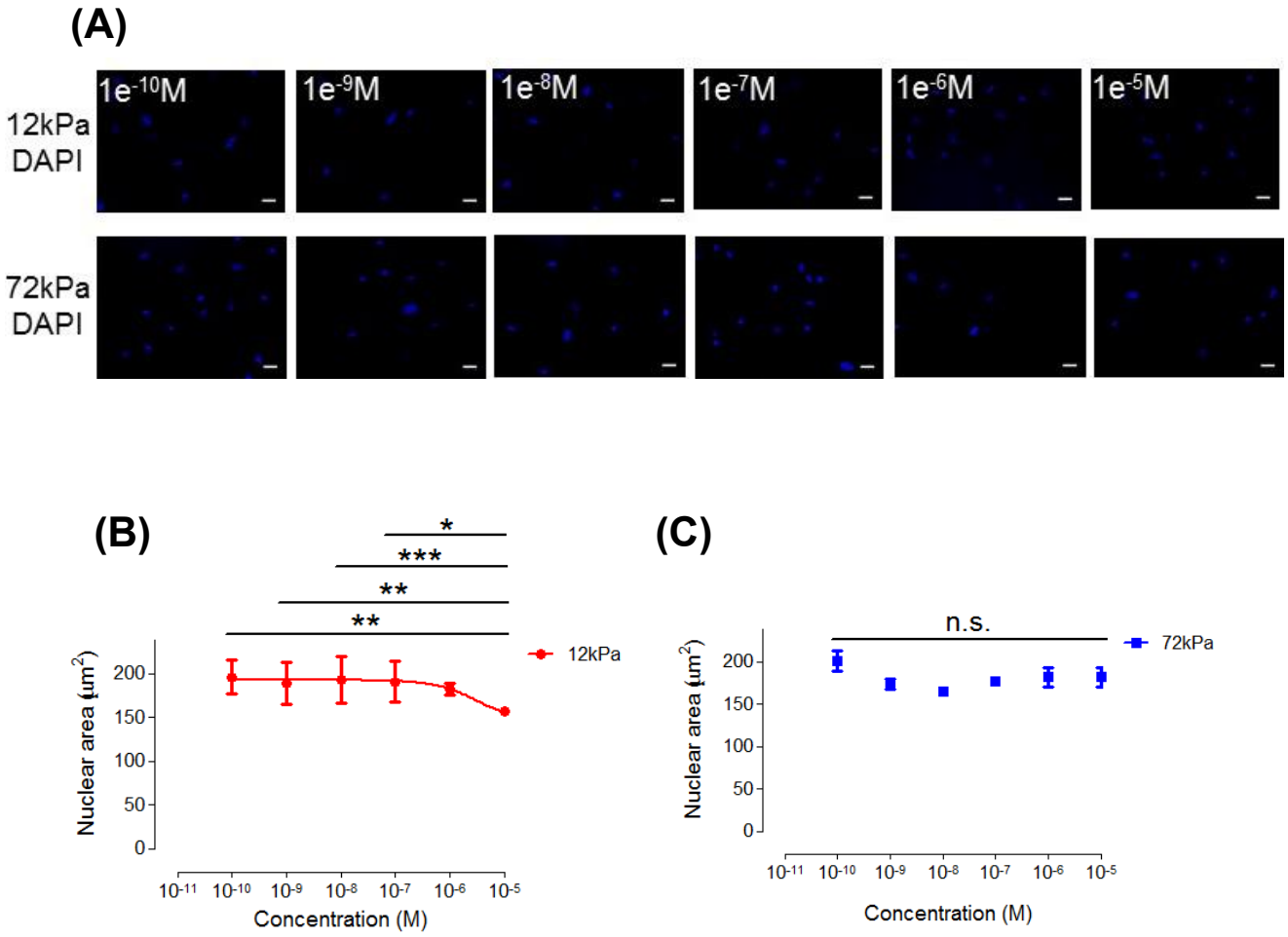

Figure 5.19: The impact of a TRPC6 channel blocker on VSMC nuclear morphology. **(A)** Representative immunofluorescence images of VSMC pre-treated with a serial dilution of SAR-7334, followed by 10 µM of Angiotensin II stimulation. Images show VSMC nuclei stained using DAPI (blue) on both 12 kPa and 72 kPa polyacrylamide hydrogels. Scale bar represents 100 µm. Image J software was used to manually measure the nuclear area of the VSMCs on **(B)** 12 kPa and **(C)** 72 kPa polyacrylamide hydrogels. Data are based on the measurement of >150 VSMCs from 3 independent experiments. Statistical significance was determined using a one-way ANOVA to show differences in nuclear area on 12 kPa (* p = <0.05, ** p = <0.001, *** p = <0.0001) and 72 kPa (non-significant; p = >0.05) matrices, followed by a Bonferroni's multiple comparison test. TRPC6: Transient receptor canonical 6; VSMC: Vascular smooth muscle cell.

From this, we can see that GsMTx-4 induced inhibition of the aberrant VSMC morphology observed on a rigid matrix, and this was not mirrored via the SAR-7334 blocker. Next, we wanted to observe whether we could attenuate the increase in VSMC volume when using GsMTx-4. To do this, VSMCs were grown and cultured, as previously described with

the SAC blocker, however treatments were performed with only 500 nM doses of GsMTx-4. VSMC filamentous actin and nuclei were stained with rhodamine phalloidin and anti-lamin A/C, respectively. Our results were in agreement with our previous findings, showing the cell area/volume is significantly higher on the rigid matrix (**Figure 5.20**). Additionally, we showed that the GsMTx-4 treatment evoked a significant reduction in VSMC area/volume when seeded on the 72 kPa polyacrylamide hydrogel, and these levels were comparable with those observed on the physiological stiffness. When looking at the effects of GsMTx-4 on VSMCs seeded on the 12 kPa hydrogel, we see no apparent change in cell area or volume (**Figure 5.20**).

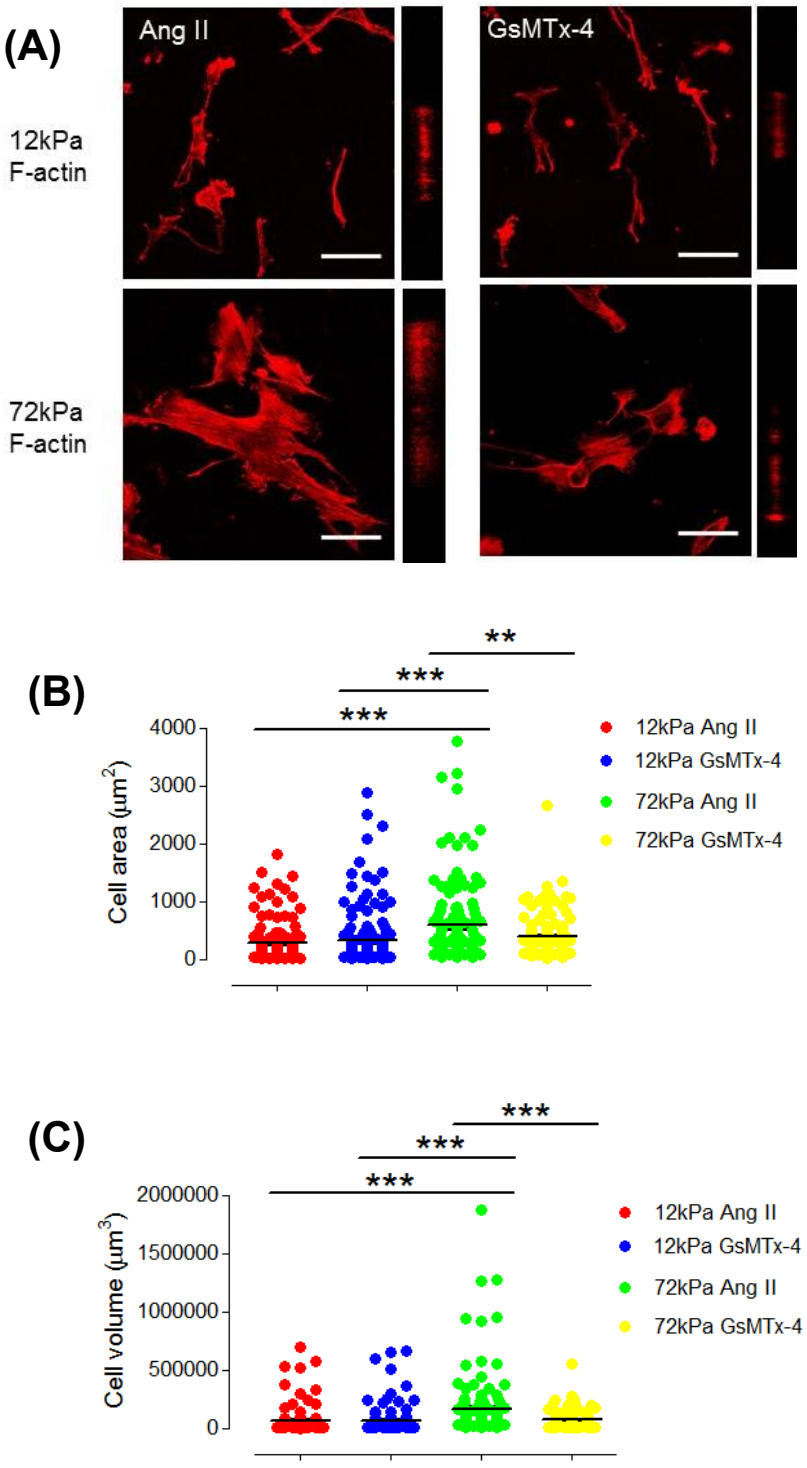

Figure 5.20: The impact of a mechanical-gated ion channel inhibitor on VSMC morphology. **(A)** Representative immunofluorescence images of VSMC actin filaments treated with GsMTx-4. Images show VSMC actin filaments (F-actin) stained using rhodamine phalloidin (red) on 12 kPa and 72 kPa polyacrylamide hydrogels. Scale bar represents 100 μm. Image J software was used to manually measure **(B)** cell area and Volocity software was used to measure **(C)** cell volume. Data are based on the measurement of ~150 VSMCs from 4 independent experiments. Statistical significance was determined using a one-way ANOVA to show differences in cell area and cell volume (** p = <0.001, *** p = <0.0001), followed by a Bonferroni's multiple comparison test. Ang II: Angiotensin II; VSMC: Vascular smooth muscle cell.

Likewise, with nuclear morphology, we observed identical trends on both the 12 kPa and 72 kPa hydrogels, revealing no change on the physiological substrate and a reduction in area/volume on the rigid matrix with GsMTx-4 treatment (**Figure 5.21**).

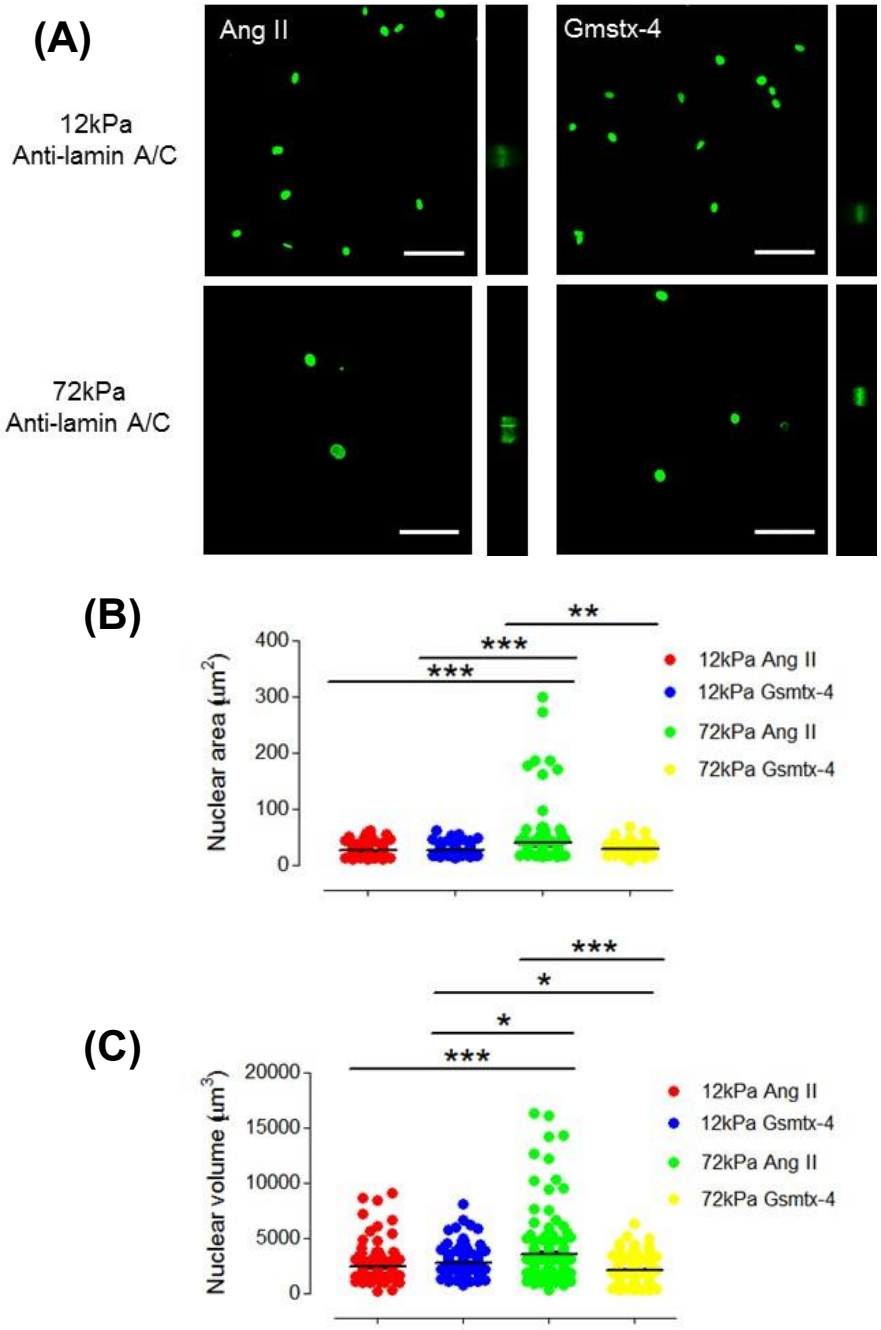

Figure 5.21: The impact of a mechanical-gated ion channel inhibitor on VSMC nuclear morphology. **(A)** Representative immunofluorescence images of VSMC nuclei treated with GsMTx-4. Images show VSMC nuclei stained using anti-lamin A/C (green) on 12 kPa and 72 kPa polyacrylamide hydrogels. Scale bar represents 100 μm. Image J software was used to manually measure **(B)** nuclear area and Volocity software was used to measure **(C)** nuclear volume. Data are based on the measurement of ~150 VSMCs from 4 independent experiments. Statistical significance was determined using a one-way ANOVA to show differences in nuclear area (** p = <0.001, *** p = <0.0001) and nuclear volume (* p = <0.05, *** p = <0.0001), followed by a Bonferroni's multiple comparison test. Ang II: Angiotensin II; VSMC: Vascular smooth muscle cell.

Interestingly, when comparing area to volume relationships, it was found that the GsMTx-4 blocker enhanced the correlation for the cell area to volume whilst diminishing it for the nuclei on the 12 kPa hydrogel. This is in contrast to the 72 kPa conditions, which revealed GsMTx-4 to abolish both weak/moderate correlations observed within the stiffer environment (**Figure 5.22**). These results give support that SACs may contribute to the VSMC hypertrophic response observed within matrix stiffness.

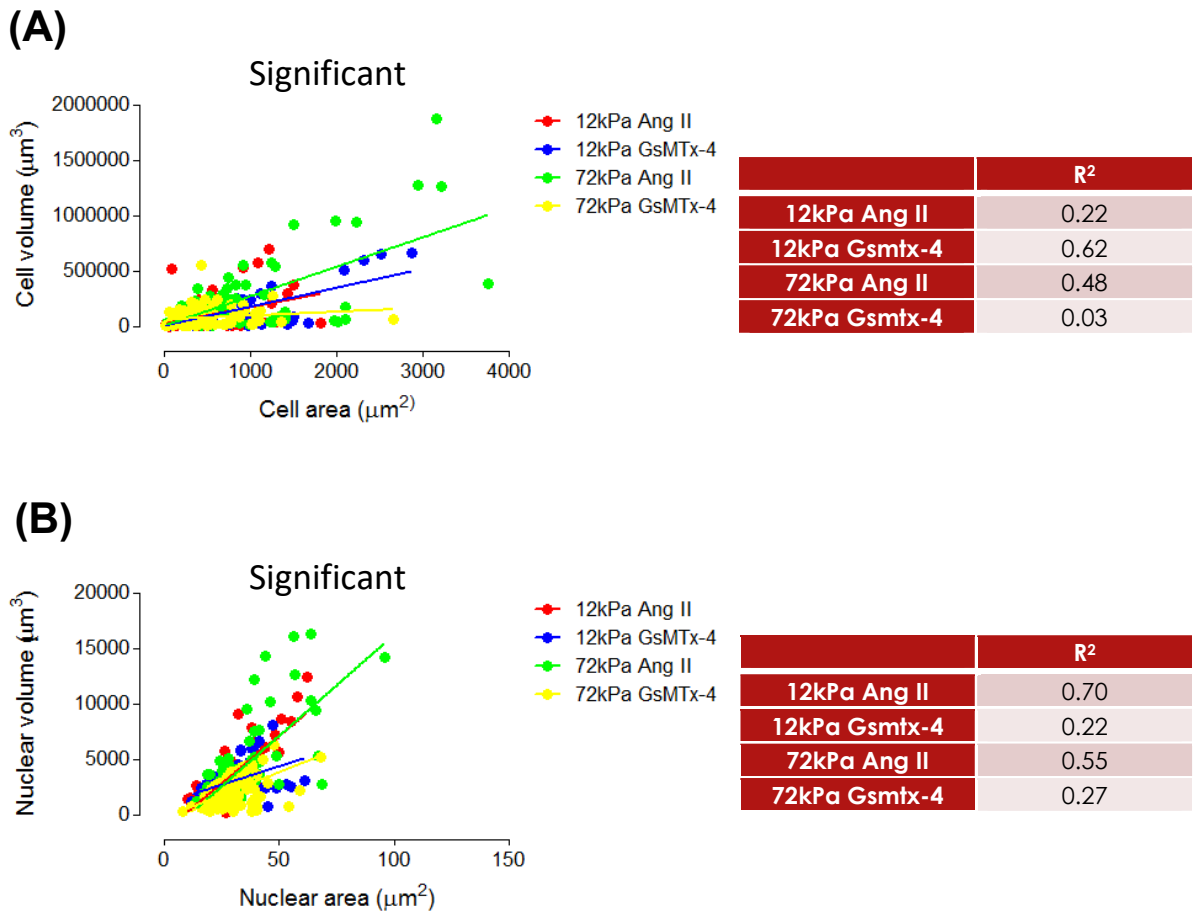

	R^2
12kPa Ang II	0.22
12kPa Gsmtx-4	0.62
72kPa Ang II	0.48
72kPa Gsmtx-4	0.03

	R^2
12kPa Ang II	0.70
12kPa Gsmtx-4	0.22
72kPa Ang II	0.55
72kPa Gsmtx-4	0.27

Figure 5.22: The relationship between cell/nuclear area and volume in VSMCs using a mechanical-gated ion channel inhibitor. Graphs show area plotted against volume for both **(A)** cell and **(B)** nuclear morphology, with corresponding tables presenting R^2 values of each treatment condition. Data are based on the measurement of ~150 VSMCs from 4 independent experiments. Statistical significance between the area and volume relationship of each treatment condition was determined using linear regression analysis (*** p = <0.0001).

5.4.4 Effect of stretch activated channels in quiescent VSMC traction force

So far, we have shown that there is a hypertrophic effect within VSMCs when seeded on a rigid matrix and this is attenuated via abolishment of actomyosin activity and inhibition of SAC opening. As a result, we believe these morphological changes may cause alterations in normal VSMC function. In chapter three, we investigated the effect of matrix stiffness on synthetic VSMC traction force generation. However, as mentioned before, VSMCs typically exist in the quiescent VSMC contractile state within the arterial wall and they work to regulate vessel tone (252). Because of this, we next looked at how matrix stiffness influences quiescent VSMC traction force generation and investigated whether SACs may be implicated within it. To do this, we performed TFM with VSMCs grown on collagen-1 coated polyacrylamide hydrogels, with an average Young's modulus of 12 kPa and 72 kPa. 10 µM of Angiotensin II was added to the VSMCs 30 minutes prior to cell lysis, and bead displacement were then captured.

The results obtained showed that quiescent VSMCs were less capable of displacing the fluorescent beads embedded within the 72 kPa polyacrylamide hydrogel in comparison to the 12 kPa (**Figure 5.23A & B)**. However, when looking at the maximum traction stress, we see a larger generation by the VSMCs when seeded on the rigid hydrogel (**Figure 5.23C**). This is mirrored by the integrated traction stress (**Figure 5.23D**) and force (**Figure 5.23E**) indicating VSMCs respond to the stiffer 72 kPa hydrogel by generating stronger actomyosin-derived forces.

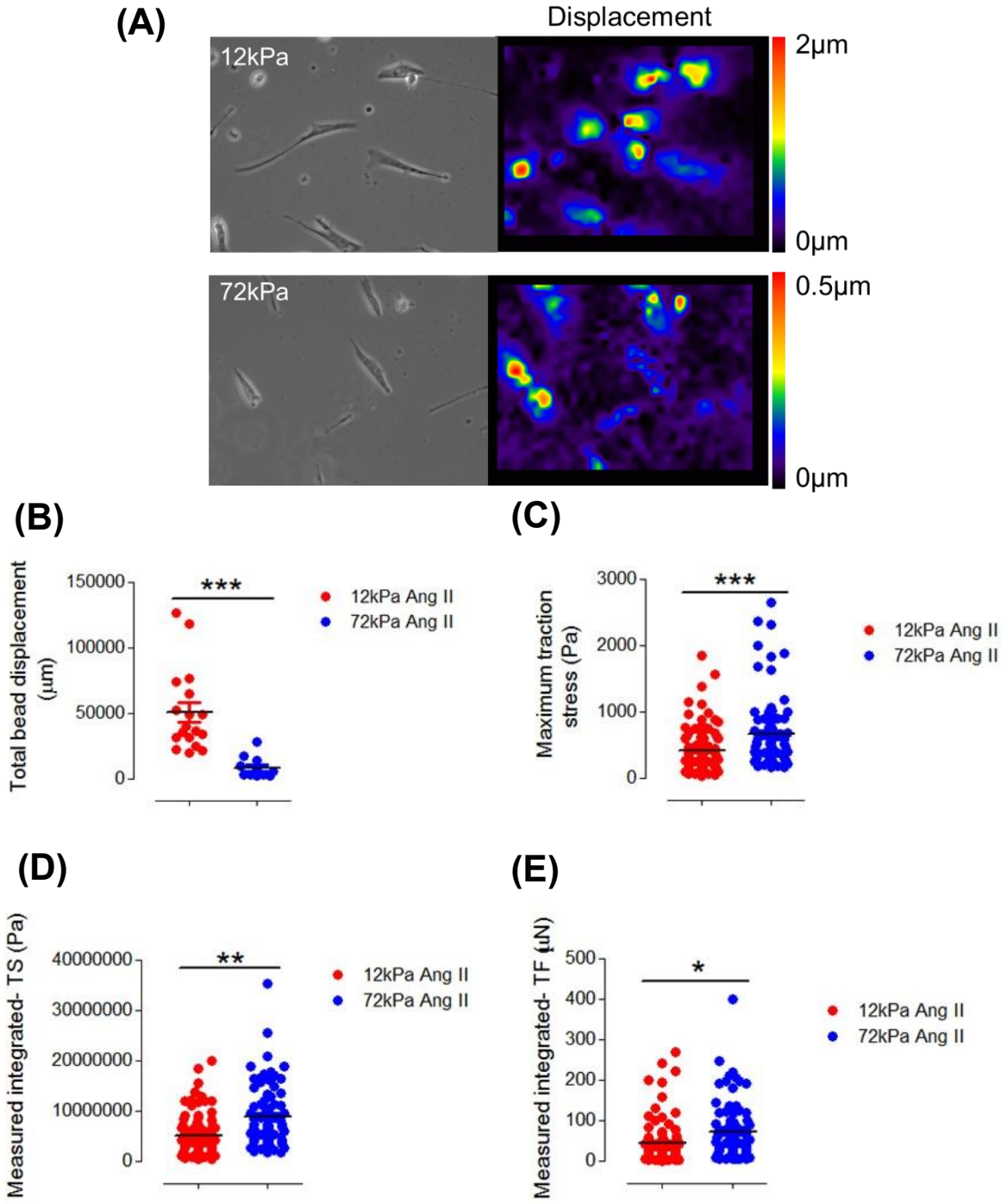

Figure 5.23: Matrix rigidity influences quiescent VSMC traction force. (A) Representative bead displacements maps of quiescent VSMCs grown on 12 kPa and 72 kPa polyacrylamide hydrogels. Graphs show **(B)** integrated bead displacements, **(C)** maximum-TS magnitude, **(D)** integrated-TS magnitude and **(E)** integrated-TF magnitude generated for quiescent VSMCs grown on 12 kPa and 72 kPa polyacrylamide hydrogels. Image J software was used to measure the bead displacements and traction stress generation of the VSMCs. Traction stress/force data represent the measurement of ~100 VSMCs from 7 independent experiments. Statistical significance was determined using a paired Student's *t* test (12 kPa vs 72 kPa) (* p = <0.05, ** p = <0.001, *** p = <0.0001). Ang II: Angiotensin II; TF: Traction force; TS: Traction stress; VSMC: Vascular smooth muscle cell.

Next, we wanted to expand on our previous experiment by investigating whether there was a time-dependent effect on cellular traction stress/force generation. We hypothesised that traction force generation may be an early response to Angiotensin II stimulation, and to investigate this, we stimulated our quiescent VSMC with Angiotensin II on 12 kPa polyacrylamide hydrogels and captured live phase/bead displacement images for 20 minutes, with 4-minute intervals. Our results show that, similar to earlier time-lapse experiments performed (**Figure 5.2A & B**), VSMCs present a progressive decrease in cell area, giving indication of successful contraction (**Figure 5.24A & B**). However, when looking at maximum and integrated traction stress/force, we notice that they show a dramatic increase within 8 minutes of stimulation, although not significant, before plateauing (**Figure 5.24C-E**). From this, we can infer that quiescent VSMC traction force generation is much more rapid than the morphological changes observed when the cells begin to exert force.

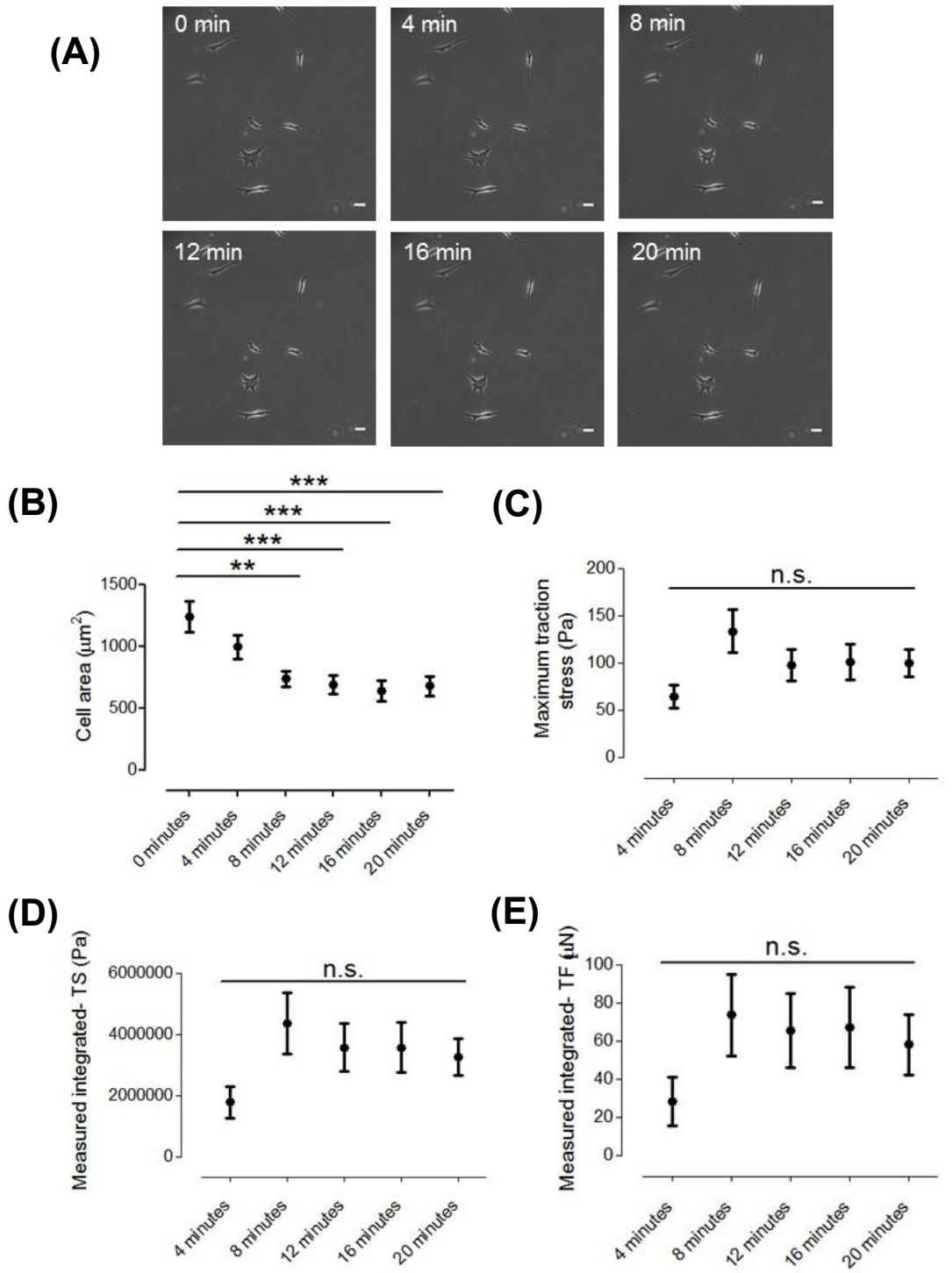

Figure 5.24: The time-dependent effect of Angiotensin II on quiescent VSMC area and traction force generation. (A) Representative phase images of VSMCs grown on 12 kPa polyacrylamide hydrogels following Angiotensin II stimulation. Graphs show **(B)** VSMC area, **(C)** maximum-TS magnitude, **(D)** integrated-TS magnitude and **(E)** integrated-TF magnitude generated within each time point. Image J software was used to measure the bead displacements and traction stress generation of the VSMCs. Data represent the measurement of ~30 VSMCs from 2 independent experiments. Statistical significance was determined using a one-way ANOVA to show differences in cell area (** p = <0.001, *** p = <0.0001), maximum-TS magnitude (non-significant; p = >0.05), integrated-TS magnitude (non-significant; p = >0.05) and integrated-TF magnitude (non-significant; p = >0.05), followed by a Bonferroni's multiple comparison test. TF: Traction force; TS: Traction stress; VSMC: Vascular smooth muscle cell.

Previous work has shown that cell hypertrophy induced via hypotonic swelling causes an increase in intracellular calcium (176). Due to this, we speculated that the higher traction force generation observed on the 72 kPa polyacrylamide hydrogel is being driven by SAC-induced calcium entry. In support of this, augmentations in calcium levels were shown to be abolished in the absence of extracellular calcium or via the use of the GsMTx-4 blocker (176). Due to this, we now looked at how SACs affected quiescent VSMC traction force generation within the stiffer environment. To do this, we performed TFM using quiescent VSMCs grown on collagen-1 coated polyacrylamide hydrogels with previous rigidities mentioned. 500 nM of GsMTx-4 was used to pre-treat the VSMCs for 30 minutes, and stimulation with 10µM of Angiotensin followed after for a further 30 minutes. Fluorescent bead images were captured before and after cell lysis to monitor bead displacements.

Our results fall in agreement with earlier findings, showing quiescent VSMCs showed significantly lower displacements within the stiffer environment for both treatment conditions (**Figure 5.25A & B**). Interestingly, the use of GsMTx-4 was shown to significantly attenuate the matrix stiffness-induced traction force generation back to physiological levels (**Figure 5.25C-E**). Additionally, much like cell and nuclear morphology (**Figure 5.21 & 5.22**), pre-treatment with GsMTx-4 has no effect on quiescent traction force generation with VSMCs seeded on the 12 kPa hydrogel (**Figure 5.25C-E**). From this, it becomes apparent that SACs contribute towards quiescent VSMC traction force generation within matrix stiffness.

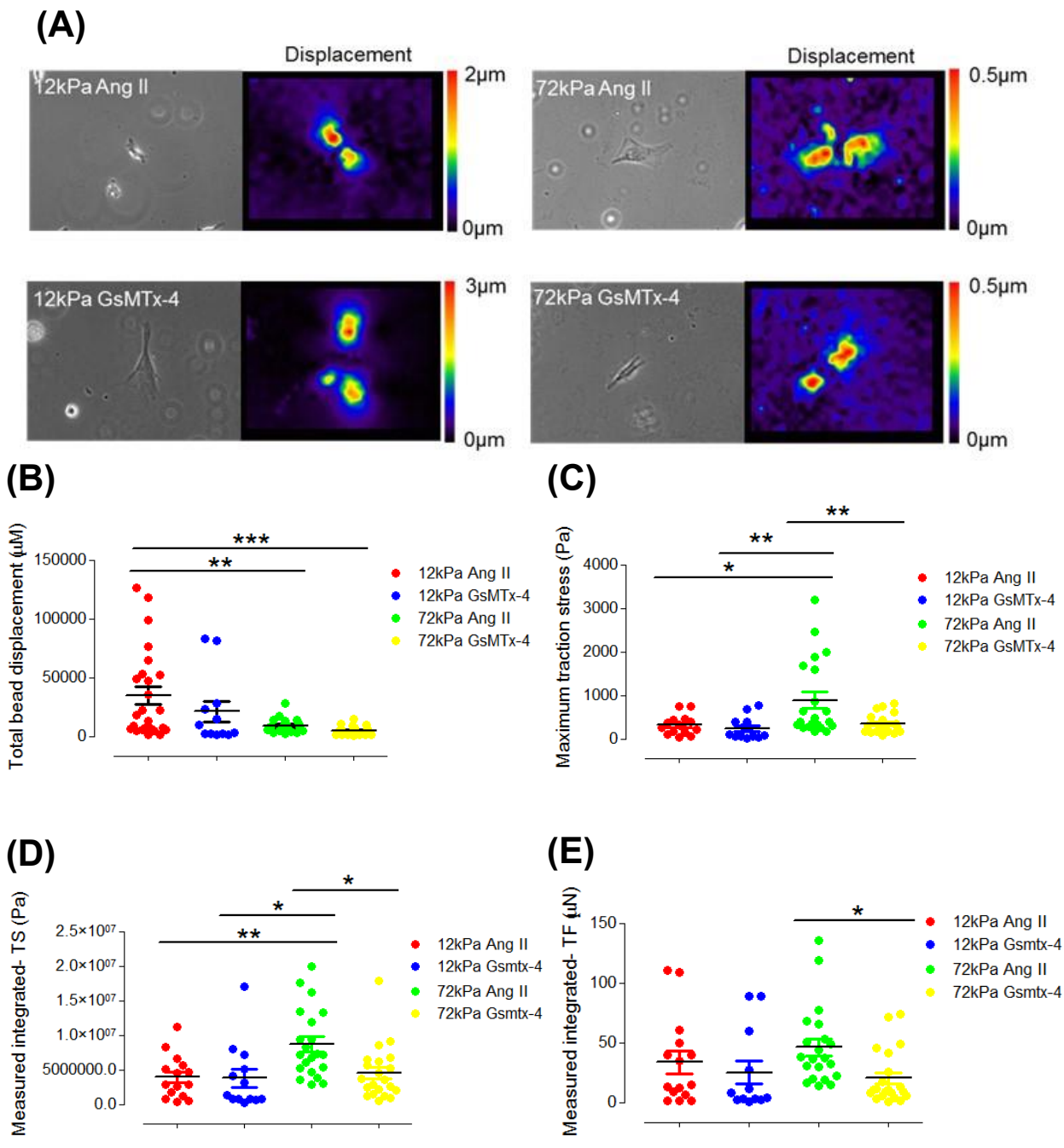

Figure 5.25: Mechanical gated channels influence quiescent VSMC traction force under matrix stiffness. (A) Representative bead displacements maps of quiescent VSMCs grown on 12 kPa and 72 kPa polyacrylamide hydrogels, treated with Angiotensin II alone and following GsMTx-4 pre-treatment. Graphs show **(B)** integrated bead displacements, **(C)** maximum-TS magnitude, **(D)** integrated-TS magnitude and **(E)** integrated-TF magnitude generated for quiescent VSMCs grown on 12 kPa and 72 kPa polyacrylamide hydrogels. Image J software was used to measure the bead displacements and traction stress generation of the VSMCs. Traction stress/force data represent the measurement of ~30 VSMCs from 3 independent experiments. Statistical significance was determined using a one-way ANOVA to show differences in integrated bead displacements (** p = <0.001, *** p = <0.0001), maximum-TS magnitude (* p = <0.05, ** p = <0.001), integrated-TS magnitude (* p = <0.05, ** p = <0.001) and integrated-TF magnitude (* p = <0.05), followed by a Bonferroni's multiple comparison test. Ang II: Angiotensin II; TF: Traction force; TS: Traction stress; VSMC: Vascular smooth muscle cell.

Following this, we wanted to confirm whether the increase in quiescent VSMC traction force generation observed within the 72 kPa environment was mediated via an increased influx of extracellular calcium, and so we repeated the experiment with calcium-free media. VSMCs were grown as previously described in basal media, and then stimulated with 10 µM of Angiotensin II prior to cell lysis. Our results here corroborate with our current hypothesis. Bead displacements once again show a significant reduction on the rigid hydrogel (**Figure 5.26A & B**), and the absence of extracellular calcium reduced traction stress/force levels down to that displayed by VSMCs at physiological stiffness (**Figure 5.26C-E**). Much like GsMTx-4, the absence of extracellular calcium had no effect on quiescent VSMC traction force generation when VSMCs were seeded on the 12 kPa hydrogel (**Figure 5.26C-E**). In summation, our work suggests that SACs mediate the observed increase in matrix stiffness-induced traction force generation via increased intracellular calcium, and this may potentially cause a hypertrophic effect within the quiescent VSMCs.

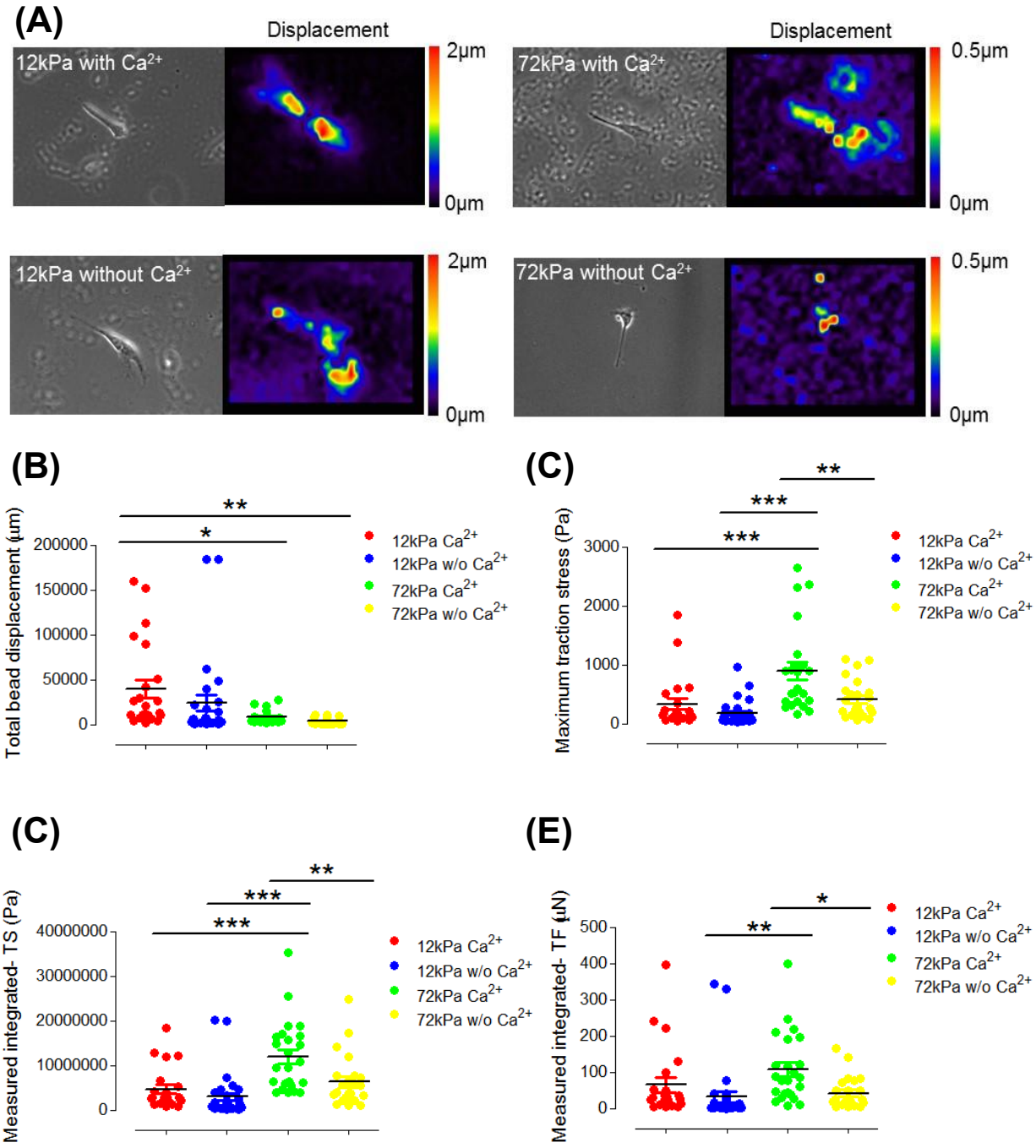

Figure 5.26: Inhibition of extracellular calcium entry influences quiescent VSMC traction force under matrix stiffness. (A) Representative bead displacements maps of quiescent VSMCs grown on 12 kPa and 72 kPa polyacrylamide hydrogels, treated with Angiotensin II in media with and without calcium. Graphs show **(B)** integrated bead displacements, **(C)** maximum-TS magnitude, **(D)** integrated-TS magnitude and **(E)** integrated-TF magnitude generated for quiescent VSMCs grown on 12 kPa and 72 kPa polyacrylamide hydrogels. Image J software was used to measure the bead displacements and traction stress generation of the VSMCs. Traction stress/force data represent the measurement of ~30 VSMCs from 3 independent experiments. Statistical significance was determined using a one-way ANOVA to show differences in integrated bead displacements (* p = <0.05, ** p = <0.001), maximum-TS magnitude (** p = <0.001, *** p = <0.0001), integrated-TS magnitude (** p = <0.001, *** p = <0.0001) and integrated-TF magnitude (* p = <0.05, ** p = <0.001), followed by a Bonferroni's multiple comparison test. TF: Traction force; TS: Traction stress; VSMC: Vascular smooth muscle cell.

5.4.5 Matrix stiffness and DNA damage within quiescent VSMCs

Arterial stiffness within CVD present tissues with enriched collagen levels, and these result in smaller matrix pores (128, 129). During this, VSMCs begin to migrate via these pores to reach the tunica intima (130). We show that VSMCs undergo a hypertrophic effect within the rigid ECM, and therefore predict movement via these apertures will result in high mechanical pressure. When mechanical load becomes unmanageable, it can cause nuclear rupture, and this has been shown to augment DNA damage (332). A common marker used to assess DNA damage are γH2AX foci. They are induced via the phosphorylation of the Serine 139 residue within mammals in order to mediate early repair response for DNA double strand breaks (333). Previously, it has been shown that overexpression of non-muscle myosin II can cause increased actomyosin-induced DNA damage, measured via γH2AX foci levels (134). We speculate that increased intracellular calcium levels, mediated via SAC opening, may cause the same effect within quiescent VSMCs.

To investigate this, we utilised the SAC blocker GsMTx-4 once more. VSMCs were seeded on collagen-coated polyacrylamide hydrogels, with previous rigidities mentioned, then cultured in basal media to induce quiescence. VSMCs were initially pre-treated with 500 nM of GsMTx-4 for 30 minutes, followed by 10 μM of Angiotensin II stimulation for a further 30 minutes. Cells were then fixed, and stained with anti-lamin A/C and anti-γH2AX to image VSMC nuclei and potential DNA damage foci, respectively. Our results show that the γH2AX foci observed in VSMCs with angiotensin treatment alone showed significantly larger spread foci within the stiffer environment compared to any other condition (**Figure 5.27A & B**). Additionally, Angiotensin II treatment was also found to significantly increase the number of γH2AX foci per nuclei when rigidity was introduced (**Figure 5.27A & C**). Interestingly, utilising a SAC blocker was found to induce a significant reduction in the size and number of the γH2AX foci observed within the rigid ECM (**Figure 5.27**).

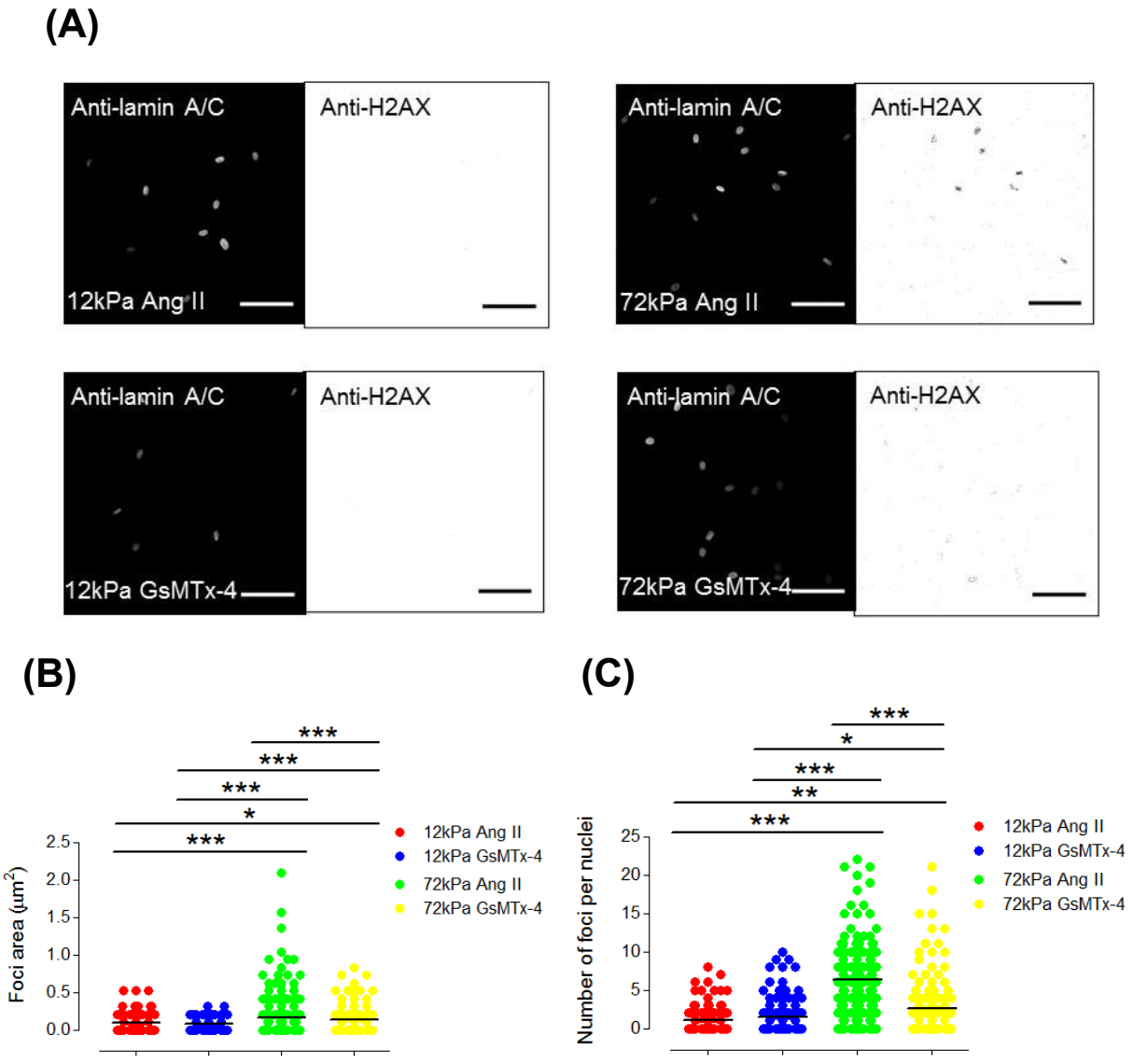

Figure 5.27 Mechanical gated channels influence γH2AX foci formation of quiescent VSMCs under matrix stiffness. (A) Representative immunofluorescence images of nuclei and γH2AX foci from VSMCs stimulated with Angiotensin II alone and following pre-treatment with GsMTx-4. Images show VSMC nuclei stained using anti-lamin A/C (grey-scale) and anti-H2AX on 12 kPa and 72 kPa polyacrylamide hydrogels. Scale bar represents 100 μm. Image J software was used to measure **(B)** foci area and **(C)** number of foci per nuclei. Data are based on the measurement of ~150 VSMCs from 3 independent experiments. Statistical significance was determined using a one-way ANOVA to show differences in foci area (* p = <0.05, *** p = <0.0001) and number of foci per nuclei (* p = <0.05, ** p = <0.001, *** p = <0.0001), followed by a Bonferroni's multiple comparison test. Ang II: Angiotensin II; VSMC: Vascular smooth muscle cell.

From this, we can see that the aberrant effects of VSMCs extend to DNA damage within matrix stiffness and that SACs may pose as a potential therapeutic target for it. To supplement this, we next looked at the p53-binding protein 1 (53BP1). 53BP1 has been characterised as a DNA damage response (DDR) factor. Within cases of DNA damage, it is recruited to the site of damage where it forms ionising radiation (IR)-induced foci that can be visualised via microscopy (334). In agreement with our previous findings, we found that the number of nuclei with/without 53BP1 foci per image was significantly higher on the 72 kPa polyacrylamide hydrogel, when treated with Angiotensin II alone. Like before, we observed that GsMTx-4 treatment causes a significant reduction in the number of nuclei with/without 53BP1 foci per image within the stiffer environment (**Figure 5.28**). Our previous experiment demonstrated that utilising a SAC blocker can cause a reduction in DNA damage and therefore these results corroborate with our narrative that less 53BP1 repair factors were required due to this.

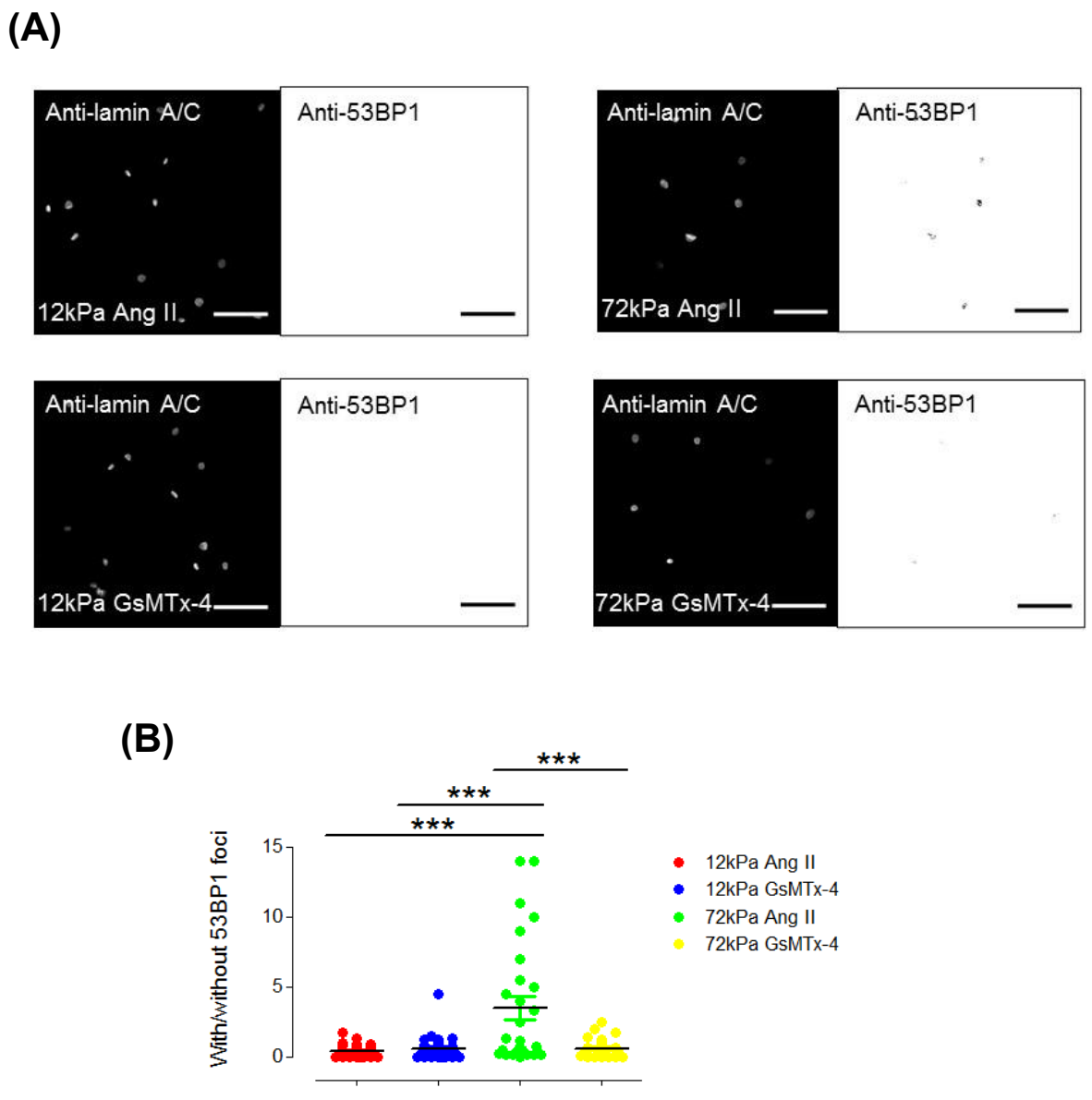

Figure 5.28 Mechanical gated channels influence 53BP1 foci formation of quiescent VSMCs under matrix stiffness. (A) Representative immunofluorescence images of nuclei and 53BP1 foci from VSMCs stimulated with Angiotensin II alone and following GsMTx-4 pre-treatment. Images show VSMC nuclei stained using anti-lamin A/C (grey-scale) and anti-53BP1 on 12 kPa and 72 kPa polyacrylamide hydrogels. Scale bar represents 100 μm. Image J software was used to measure number of nuclei **(B)** with/without 53BP1 foci per image. Data are based on the measurement of ~35 VSMCs from 6 independent experiments. Statistical significance was determined using a one-way ANOVA to show differences in nuclei with/without 53BP1 foci (*** p = <0.0001), followed by a Bonferroni's multiple comparison test. Ang II: Angiotensin II; VSMC: Vascular smooth muscle cell.

Next, we wanted to see if the DNA damage observed via the γH2AX foci was actomyosin-mediated. Prior research has shown that cells that were seeded on a rigid ECM,

or where non-muscle myosin II was overexpressed, typically had a mislocalisation of repair factors and increased DNA damage. Importantly, it was shown that Blebbistatin inhibition of myosin II prevented these changes, suggesting that actomyosin plays a crucial role in DNA damage regulation (134). To investigate this further, we utilised Atorvastatin to see if it could replicate the positive effects that were induced by GsMTx-4. To do this, we replicated previous experimental settings for the γH2AX study, however treated the VSMCs with 500 nM of Atorvastatin following Angiotensin II stimulation. In this case, our results showed no significant difference between the size of the γH2AX foci when treating with Atorvastatin (**Figure 5.29A & B**). Importantly, we reveal that Atorvastatin caused no significant reduction to the number of γH2AX on the 72 kPa polyacrylamide hydrogel, with both conditions presenting more γH2AX foci than their physiological counterparts (**Figure 5.29A & C**). From this, we can suggest that, within VSMCs, regulation of actomyosin activity does not seem to possess a therapeutic role for DNA damage regulation.

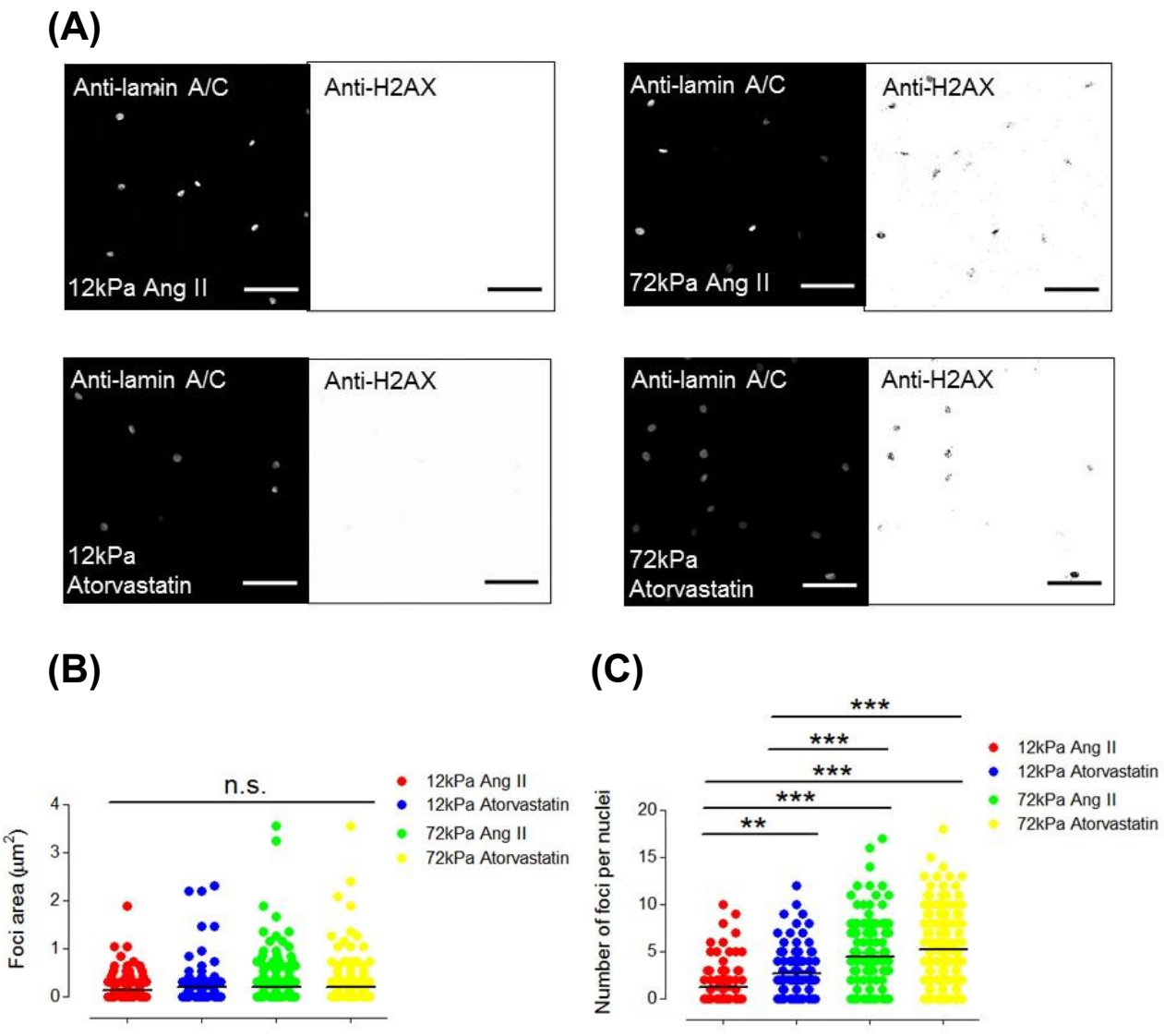

Figure 5.29 Atorvastatin presents no effect on inhibiting γH2AX foci formation of quiescent VSMCs under matrix stiffness. (A) Representative immunofluorescence images of nuclei and γH2AX foci from VSMCs treated Angiotensin treatment alone and with Atorvastatin. Images show VSMC nuclei stained using anti-lamin A/C (grey-scale) and anti-H2AX on 12 kPa and 72 kPa polyacrylamide hydrogels. Scale bar represents 100 μm. Image J software was used to measure **(B)** foci area and **(C)** number of foci per nuclei. Data are based on the measurement of ~150 VSMCs from 3 independent experiments. Statistical significance was determined using a one-way ANOVA to show differences in foci area (non-significant; p = >0.05) and number of foci per nuclei (** p = <0.001, *** p = <0.0001), followed by a Bonferroni's multiple comparison test. Ang II: Angiotensin II; VSMC: Vascular smooth muscle cell.

5.4.6 Role of Piezo1 in stiffness-induced aberrant VSMC function

GsMTx-4 works by inhibiting SAC opening, and has been shown to attenuate morphological and functional changes of VSMCs under matrix stiffness, as well as prevent DNA damage accumulation. Earlier, we considered TRPC6 channels as a potential candidate for pre-dominantly driving these changes, as GsMTx-4 has previous implicated TRPC channels within muscle pathology (327, 328). However, we found that it had no influence on VSMC morphology when seeded on a rigid ECM. Due to this, we considered other candidates. As mentioned before, prior research had shown that GsMTx-4 successfully acts at TRPC1, TRPC6 and Piezo1 channels within different cell types (329, 330). Similar to the TRPC channels, Piezo1 is a mechanosensitive channel, and its electrophysiological properties are akin to typical cationic mechanosensitive currents (177, 335). Research has shown GsMTx-4 being efficient at abolishing Piezo1 whole cell currents within HEK293 cells (330). As a result, we investigated to see whether any of these channels may potentially hold a role.

To begin with, we wanted to see if we could observe any gene expression of these channels within VSMCs when seeded on either a compliant or rigid matrix. To do this, we cultured our quiescent VSMCs on collagen-1 coated polyacrylamide hydrogels, with an average Young's modulus of 12 kPa and 72 kPa. Cells were lysed with TRIzol to obtain RNA, which was converted to cDNA via reverse transcriptase. To ensure we selected an appropriate housekeeping gene, we initially tested *ATP5B* via a real time qPCR run. Our results show that the CT value of multiple 12 kPa/72 kPa samples were within close proximity, deeming ATP5B as a suitable housekeeping gene within VSMCs (**Figure 5.30A**). We next tested the expression of two other housekeeping genes, *B2M* and *18S*, which were normalised to ATP5B. Expression of each showed no significant difference between the physiological and pathological stiffness (**Figure 5.30B & C**).

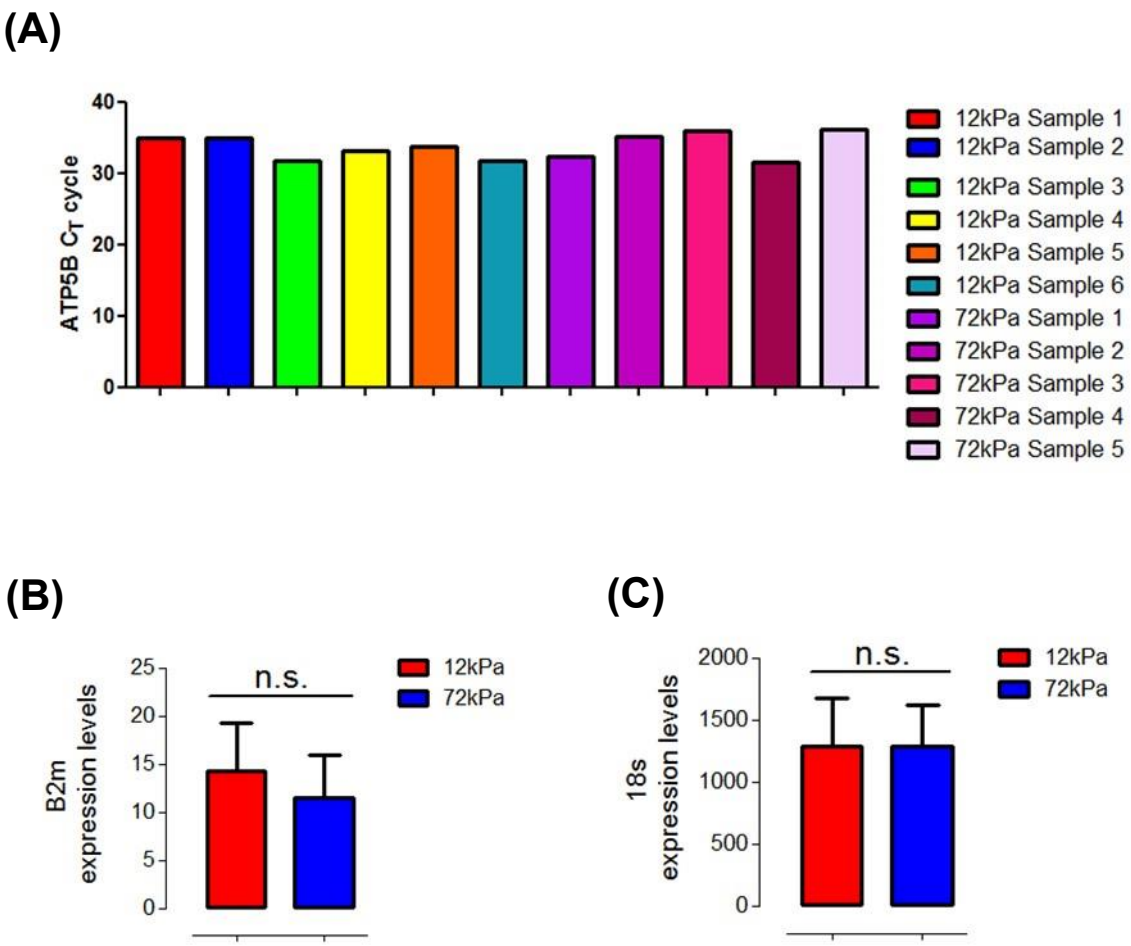

Figure 5.30 Trialling ATP5B housekeeping gene for qPCR experimentation. Graphs show **(A)** ATPB5 C_T values between multiple RNA samples that were extracted from VSMCs grown on 12 kPa and 72 kPa polyacrylamide hydrogels. qPCR analysis revealed similar expression of housekeeping genes for **(B)** B2M and **(C)** 18S within VSMCs when normalised to ATP5B expression. Data are based on the measurement of ~5 samples from 2 independent experiments and statistical significance was determined using a paired Student's *t* test (12 kPa vs 72 kPa) (non-significant; p = >0.05). qPCR: Quantitative polymerase chain reaction; VSMC: Vascular smooth muscle cell.

Following this, we looked at *TRPC1*, *TRPC6* and *PIEZO1* gene expression, and found no expression of the TRPC channels within VSMCs, as shown by **Table 5.2**.

Table 5.2: CT values of housekeeping gene ATP5BP and stretch-activated channel genes within quiescent vascular smooth muscle cells grown on 12 kPa and 72 kPa polyacrylamide hydrogels.

	ATP5B	**PIEZO1**	**TRPC3**	**TRPC6**
12 kPa				
Sample 1	30.19	35.37	Undetected	Undetected
Sample 2	31.85	34.99	Undetected	Undetected
Sample 3	30.93	36.39	Undetected	Undetected
Sample 4	31.57	35.86	Undetected	Undetected
72 kPa				
Sample 1	37.16	37.06	Undetected	Undetected
Sample 2	30.80	36.40	Undetected	Undetected
Sample 3	31.47	37.08	Undetected	Undetected
Sample 4	31.41	36.34	Undetected	Undetected

There was, however, low expression of Piezo1 on the compliant matrix, with a dramatic increase shown on the 72 kPa polyacrylamide hydrogel **(Figure 5.31A**). This gave indication that *PIEZO1* may contribute to our previous observations. However, to test this, we targeted Piezo1 using an siRNA-mediated approach. To confirm depletion, we performed western blotting. All siRNA and western blot experiments were performed by Dr Robert Johnson within the Warren lab. VSMCs were cultured in basal media to induce quiescence and seeded on plastic coverslips. Three Piezo1-specific siRNAs were utilised to deplete expression and protein lysates were then obtained. Our results show that both siRNA 5 and siRNA 7 cause depletion of Piezo1 protein expression, with the former being most efficient (**Figure 5.31B & C**).

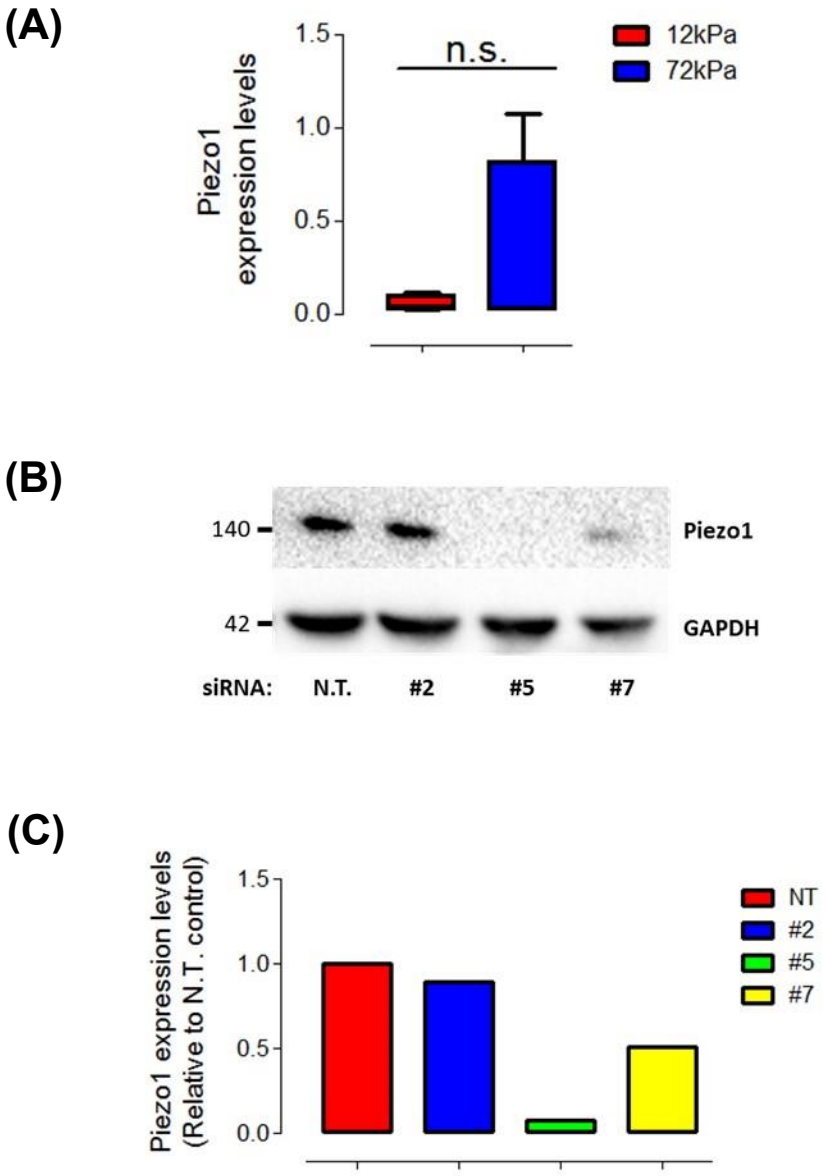

Figure 5.31 siRNA-mediated knock-out of Piezo1 from VSMCs. qPCR analysis revealed **(A)** expression levels of Piezo1 when increasing matrix rigidity for VSMCs. Western blot analysis of VSMCs grown on plastic shows **(B)** representative images of Piezo1 protein expression levels following treatment with Piezo1-specific siRNAs. GAPDH (negative control) indicated equal protein loading (25 µL of each protein lysate was loaded). Graph **(C)** quantifies the protein expression level of Piezo1 following the siRNA treatments. Western blot data is from 1 independent experiment. qPCR data are based on the measurement of ~4 samples from 2 independent experiments and statistical significance for this was determined using a paired Student's *t* test (12 kPa vs 72 kPa) (non-significant; p = >0.05). N.T: Non-targeted; qPCR: Quantitative polymerase chain reaction; VSMC: Vascular smooth muscle cell.

We previously showed that utilising the SAC blocker GsMTx-4 significantly reduced the number of γH2AX foci observed in Angiotensin II-stimulated VSMCs seeded on the 72 kPa hydrogel. We hypothesised that these effects may be mediated through Piezo1, and as a result, we utilised the siRNA5 and siRNA7 Piezo1-knock out VSMCs to be able to determine this. To do this, we set up experiments much like before (**Figure 5.27**), however in this case, we only stimulated our Piezo1-knock out VSMCs with 10 μM of Angiotensin II for 30 minutes. Cells were then fixed and stained with anti-lamin A/C and anti-γH2AX to image VSMC nuclei and potential DNA damage foci, respectively. The findings presented within **Figure 5.32 & 5.33** were performed and obtained by Dr Robert Johnson within the Warren lab. Our results here show a higher number of γH2AX foci within the rigid matrix in comparison to the physiological substrate for the control non-targeted VSMCs (**Figure 5.32**). Interestingly, utilising the Piezo1-specific siRNA5 or siRNA7 was found to induce a significant reduction in the number of γH2AX foci on the 72 kPa hydrogel. Additionally, both siRNA knockouts were found to have no effect on the 12 kPa gel indicating a stiffness-specific role for Piezo1 (**Figure 5.32**).

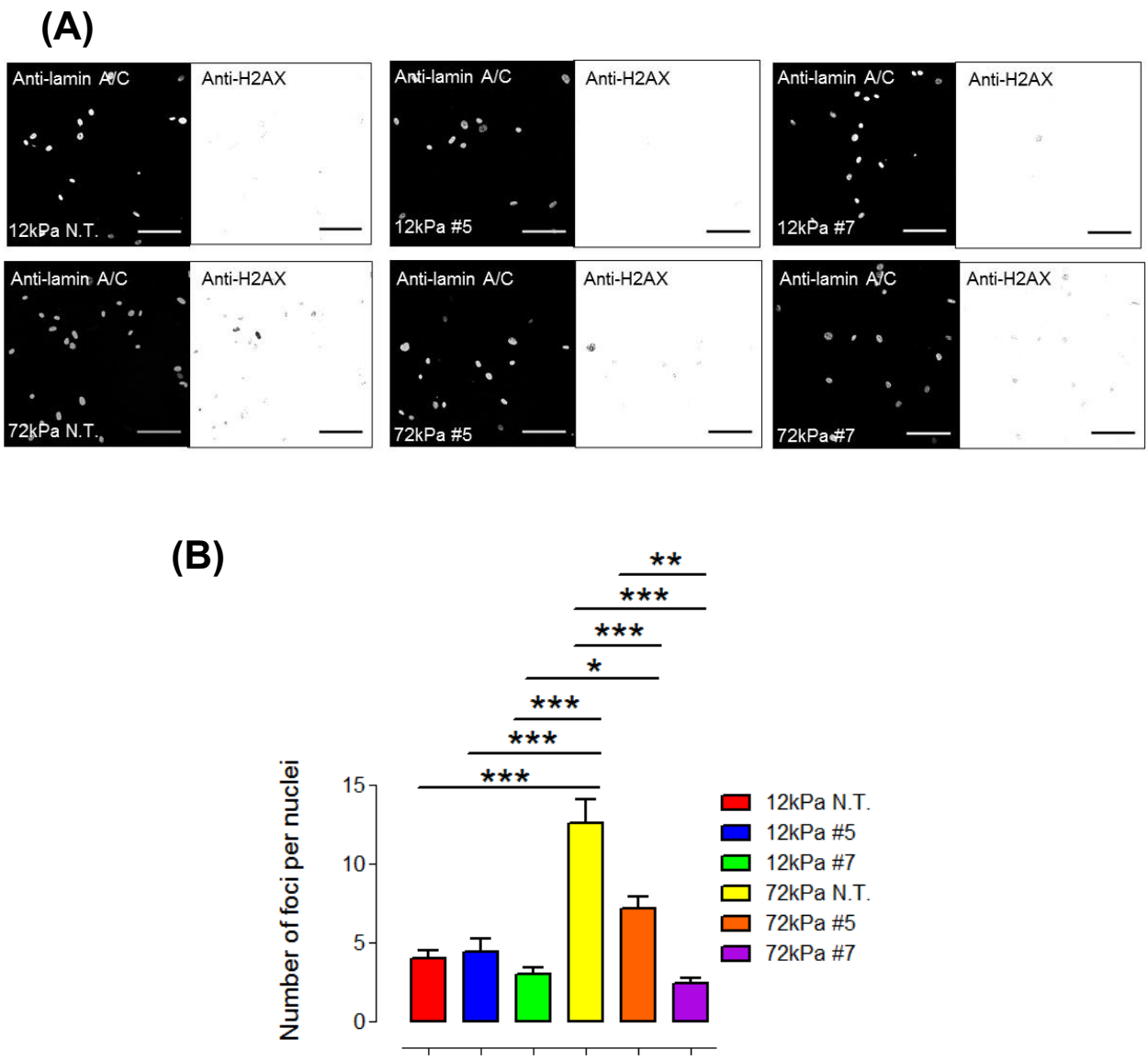

Figure 5.32 Piezo1 influences γH2AX foci formation of quiescent VSMCs under matrix stiffness. (A) Representative immunofluorescence images of nuclei and γH2AX foci from Piezo1-knockout VSMCs stimulated with Angiotensin II. Images show VSMC nuclei stained using anti-lamin A/C (grey-scale) and anti-H2AX on 12 kPa and 72 kPa polyacrylamide hydrogels. Scale bar represents 100 µm. Image J software was used to measure **(B)** number of foci per nuclei. Data are based on the measurement of ~250 VSMCs from 3 independent experiments. Statistical significance was determined using a one-way ANOVA to show differences in number of foci per nuclei (* p = <0.05, ** p = <0.001, *** p = <0.0001), followed by a Bonferroni's multiple comparison test. N.T: Non-targeted; VSMC: Vascular smooth muscle cell.

Next, we looked at the 53BP1 marker. This marker was also previously shown to augment on the 72 kPa hydrogel, with GsMTx-4 treatment causing a significant reduction back down to physiological levels. In agreement with our previous findings (**Figure 5.28**), we see that the use of siRNA 7 Piezo1 knockout VSMCs significantly decreased the number of nuclei with/without 53BP1 foci per image on the 72 kPa hydrogel, with no difference shown on the 12 kPa substrate (**Figure 5.33**). This indicates that aberrant opening of Piezo1 is likely mediating the DNA damage observed within VSMCs seeded the rigid hydrogel, and its knockdown/inhibition can successfully abolish the accumulation of key DNA damage markers.

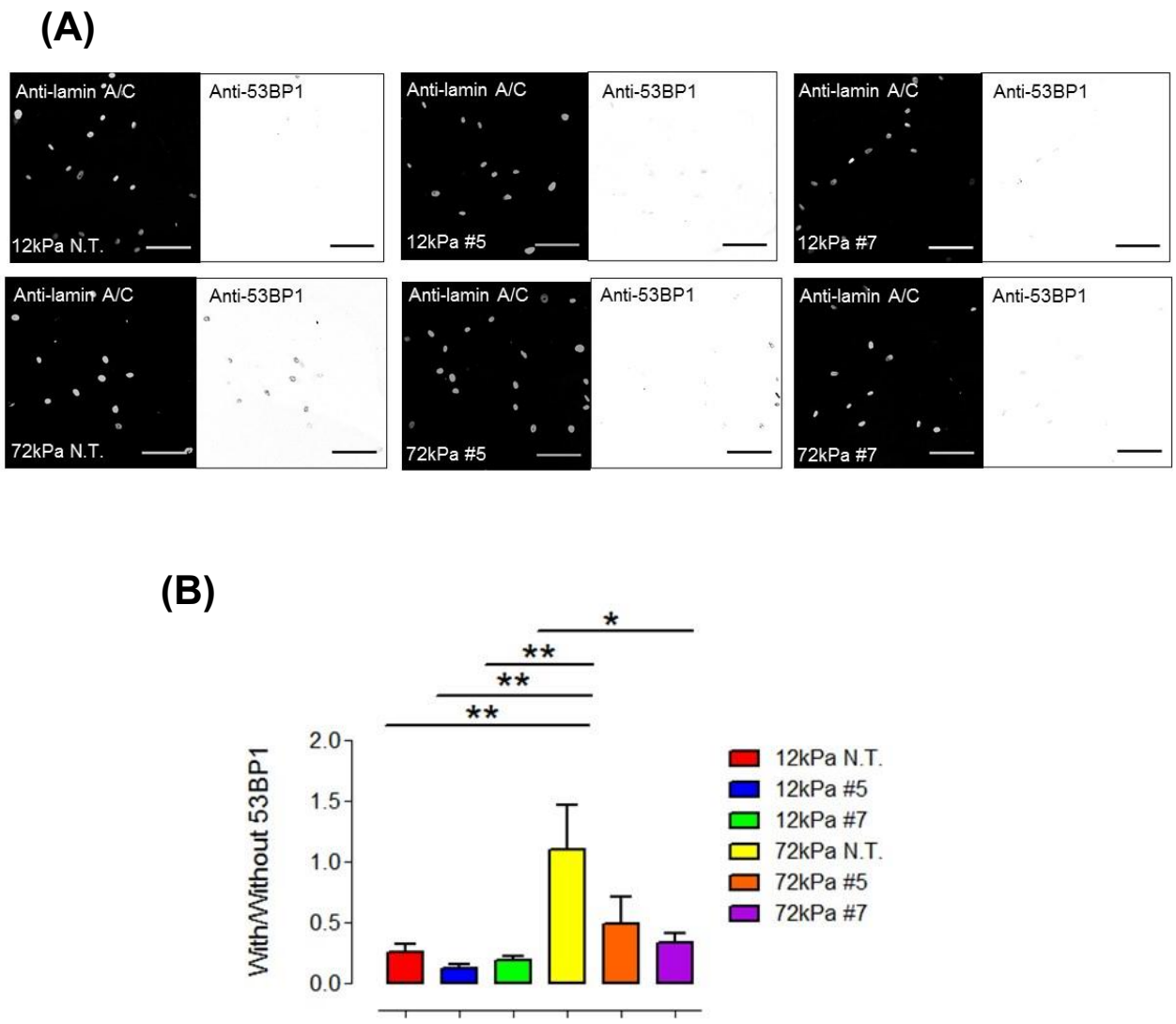

Figure 5.33 Piezo1 influences 53BP1 foci formation of quiescent VSMCs under matrix stiffness. (A) Representative immunofluorescence images of nuclei and 53BP1 foci from Piezo1-knockout VSMCs stimulated with Angiotensin II. Images show VSMC nuclei stained using anti-lamin A/C (grey-scale) and anti-53BP1 on 12 kPa and 72 kPa polyacrylamide hydrogels. Scale bar represents 100 µm. Image J software was used to measure number of nuclei **(B)** with/without 53BP1 foci per image. Data are based on the measurement of ~15 VSMCs from 3 independent experiments. Statistical significance was determined using a one-way ANOVA to show differences in nuclei with/without 53BP1 foci (* p = <0.05, ** p = <0.001), followed by a Bonferroni's multiple comparison test. N.T: Non-targeted; VSMC: Vascular smooth muscle cell.

5.5 Discussion

This chapter explored the relationship between quiescent VSMC volume, matrix stiffness-induced SAC activity and DNA damage. By looking at the effects of SAC blockers, we were able to better understand how matrix stiffness induces morphological changes, and highlight how these channels may regulate them. We were also able to observe how SAC channels regulate multiple processes within VSMCs, and link our study to previous observations. The work conducted within this chapter provides further understanding to the morphological studies performed in chapter four. Due to this, we can now offer new mechanistic insights towards the differential responses observed within quiescent VSMCs in response to matrix stiffness, as well as present novel therapeutic targets that could be exploited in the future.

5.5.1 Effect of matrix stiffness on VSMC volume

CVD development is caused by a variety of common risk factors such as hypertension and rise in cholesterol, and its progression involves essential structural and functional alterations that occur within the vascular wall (4). Previous research has shown that there is an unregulated thickening of the vessel wall during hypertension and this was caused by a significant increase in smooth muscle cell mass (336-339). However, there was speculation as to whether this was due to hypertrophy or hyperplasia of the cells (340, 341). Earlier studies have confirmed an increase in the number of smooth muscle cells via [^{3}H]thymidine labelling (342-346), however other researchers have contradicted these findings suggesting this was due a hypertrophic-induced change in chromosomal structure (347, 348). One finding given by Owen et al gives support to this claim as it found the average smooth muscle size was larger within SHR, and this hypertrophic change was coupled with a modification in nuclear ploidy (349).

VSMC hypertrophy has been shown to cause increased non-compliance of vessels within aged and hypertensive populations. It occurs alongside altered ECM deposition and phenotypic switching, and can cause systolic hypertension as well hypertrophy of the left ventricle (350). Angiotensin II has previously shown higher levels within various hypotensive models, and sustained activation of the angiotensin II type 1 receptor (ATR1) has induced increased vascular resistance via remodelling of the vascular wall (351-353). Our results give support to this, showing a progressive increase in cell volume with longer Angiotensin II

stimulations within the mechanically-resistant environment. This in agreement with earlier reports stating Angiotensin can cause VSMC hypertrophy, with augmentations in cell size and protein synthesis (260, 354).

The effects evoked by Angiotensin II-induced hypertrophy can be abolished by targeting key components of actomyosin pathway. Prior work has shown that ROCK inhibition, via Y-27632 treatment, can slow down pathological hypertrophy induced by Angiotensin II stimulation within mice and rats (355). Other studies offer support to this as they have shown that ROCK1$^{-/-}$ mice exhibited a reduction of hypertrophic markers (356). Our results corroborate with these findings as they show the stiffness-induced increase in cytoplasmic mass can be efficiently reduced within VSMCs via actomyosin inhibition. This gives strength to earlier studies that indicate key contractile components hold a crucial role towards the hypertrophic response of other cell types (357).

5.5.2 Role of SACs within quiescent VSMC traction force

Given the significant increase of VSMC volume observed within matrix stiffness, we speculated hypertrophy, mediated via an influx ion and solutes, to originate from SAC opening. As mentioned in chapter four, VSMCs were unable to efficiently displace the extracellular matrix when seeded on a rigid hydrogel, and we hypothesised that the tension held at the membrane may open the channels. Our results show that inhibition of SACs via GsMTx-4 treatment revert VSMC volume back to physiological levels, and therefore identify a new potential regulatory component within VSMC hypertrophy.

Within normal physiology, SACs serve as a mechanical sensor for myogenic responses (178). However, during pathological stiffening, quiescent VSMCs were revealed to exert increased traction force, and we show via GsMTx-4, that this is due to SAC activity. Earlier studies show calcium permeability to be low at physiological concentrations, and therefore it was suggested calcium entry via SACs may not be adequate for contraction (358). As a result, it has been proposed that it may instead be sufficient to induce depolarisation of the membrane to open voltage gated calcium channels (VGCCs) (359, 360). However, others researchers have disputed this, presenting findings that show significant calcium entry can be mediated via SACs alone (177). Our study confirms calcium to be an essential component in SAC activity, by demonstrating that in the absence of extracellular calcium, VSMC traction force is restored back to a healthy range. Further research is now required to determine whether VGCCs assist in traction force generation of quiescent VSMCs within the stiffer environment or whether this is via SAC activity alone.

5.5.3 Mechanical pressure-induced VSMC DNA damage

As mentioned before, CVD can evoke structural changes within the vascular wall, such as an enrichment of collagen that results in smaller pores (128, 129). Alongside this, quiescent VSMCs were shown to exert increased traction force in response to stiffer ECMs, and this possibly facilitates entry via these narrow passages. However, within this study, we have revealed SACs to induce VSMC hypertrophy in the absence of physiological compliance, and therefore speculate this may cause aberrant mechanical pressure.

Previously, we discussed how the LINC complex transmits mechanical stimuli from the cell cytoskeleton/ECM to the nuclei in order to ensure structural integrity (233). However, prior studies have shown that within a pathological setting, incidence of nuclear rupture and DNA damage is increased when seeded on a rigid matrix (133, 134, 361). Our work shows inhibition of SAC opening can reduce recruitment of important DNA-damage response factors, such as 53BP1, indicating positive therapeutic effects. Despite this, earlier research has shown overexpression of myosin II can result in mislocalisation of KU80, an essential protein in the non-homologous end joining (NHEJ) pathway, via nuclear rupture (134, 362, 363). Therefore, it is possible that unregulated contractility observed within the 72kPa polyacrylamide hydrogel may result in disruption of VSMC nuclear integrity. Despite this, we strengthen our earlier assumption that GsMTx-4 exhibits positive therapeutic effects by showing a significant reduction in γH2AX foci when abolishing SAC activity.

Although we have shown evidence that SACs may contribute to DNA damage within the stiffer environment, the mechanism behind it requires further clarification. It is possible that the DNA impairment could be caused via volume-induced hydrostatic pressure and/or unconstrained actomyosin activity. Previously, it has been shown that Blebbistatin treatment can decrease DNA damage within cancer cells that either possess overexpressed non-muscle myosin II or deficient lamin A (134). Our work, however, shows that actomyosin inhibition, via Atorvastatin treatment, does not reduce γH2AX foci levels within the rigid environment. Therefore, we speculate that DNA damage regulation within matrix stiffness is cell-type specific. Our work further supports this as it shows GsMTx-4 treatment can restore nuclear volume back to physiological levels, whilst actomyosin inhibitors show no significant change. As a result, this gives indication that nuclear and cell hypertrophy can be decoupled within VSMCs due to different regulatory components.

5.5.4 New potential therapeutic targets in CVD

Currently, there are a wide range of therapies available within CVD, with drug delivery positioned as the major treatment modality. One group of medications currently prescribed are antiplatelets (364). Within CVD development, platelet activation usually occurs during interaction with atherosclerotic plaques, resulting in atherothrombosis. Antiplatelets work to intervene the clot formation by binding to platelet cells and inhibiting their function (365). This form of medication has been proven effective; however, it targets a late stage of CVD where vascular remodelling has already occurred. Our research focuses on the early pathological stages that occur within VSMCs, the primary cell type within the aortic wall, in order to identify potential therapeutic targets that can be exploited much earlier.

Other treatments include beta blockers and angiotensin-converting enzyme (ACE) inhibitors, which indirectly attenuate progression of arterial stiffness (31, 364). These drugs abolish cell signalling pathways that lead to increased contractility, and therefore target VSMCs, highlighting its fundamental role in CVD development. More recent research has revealed new novel components that may mediate VSMC dysregulation within disease progression. One example is microtubule acetylation which is shown to reciprocally coordinate with cell contractility within fibroblast cells (70). Within our study, we reveal that SACs directly influence quiescent VSMC morphology and contractility within the stiffer environment. Aortic stiffness is typically accompanied by altered expression of key contractile protein markers within VSMCs (366). One SAC in particular, identified as Piezo1, was revealed as a potential target as it showed augmented expression on the 72kPa hydrogel. Earlier work has implicated Piezo1 as a critical component in arterial remodelling within hypertension, influencing both vessel diameter and thickness (189). We show knockdown of Piezo1 can attenuate DNA damage accumulation within VSMCs seeded on a rigid substrate. This strengthens the hypothesis that Piezo1 may induce aberrant effects within VSMCs in response to matrix stiffness, which could drive remodelling of the arterial wall. As a result, this study proposes a new molecular component that can potentially be targeted to treat/prevent early stages of CVD development.

5.5.5 Chapter Five conclusions

When discussing our results in chapter four, we speculated that potential SAC opening may cause DNA damage, via high osmotic pressure. Within this study, we confirm this, showing the utilisation of SAC blockers reduces volume and γH2AX foci levels back to a physiological range. Our results reveal actomyosin inhibition to have minimal effect on DNA damage, indicating this response is pre-dominantly driven by volume-induced hydrostatic pressure. Despite this, recent data has shown that inhibition of microtubule N-acetyltransferases, which indirectly regulate actomyosin activity, to attenuate nuclear impairment within VSMCs (151). Therefore, further interrogation of the link between actomyosin activity, microtubule acetylation, and DNA damage regulation is now required as it may provide new insights for future research.

In summation, this chapter demonstrates how quiescent VSMCs undergo hypertrophy in response to matrix stiffness. Our study shows this response is regulated partly by actomyosin activity, but also via SAC opening. SACs, within the stiffer environment, were shown to elicit a whole host of responses, such as morphological changes, increased contractility and dysregulated DNA damage. Importantly, we identify a novel therapeutic target, shown as Peizo1, that presents increased gene expression as a result of matrix rigidity. We reveal, via siRNA-mediated methods, that inhibition of this channel can attenuate DNA damage accumulation within VSMCs seeded on a rigid matrix, thus highlighting a new role for SACs within aberrant VSMC function.

5.5.6 Limitations and future work

5.5.6.1 Role of VGCCs within matrix stiffness

Our work highlights calcium to be essential for increased quiescent VSMC traction force generation within the stiffer environment. We show that SAC inhibition can abolish the force generated back down to physiological levels, via limited calcium entry. However, it currently remains unknown whether SACs are capable of independently increasing the actomyosin activity of the VSMCs, or whether VGCCs facilitate this via SAC-mediated depolarisation of the cell. Previous studies have indicated VGCC assistance due to low calcium permeability for SACs, however alternative work has shown significant entry via SACs to be possible (177, 359, 360). Therefore, further work is required to elucidate the mechanism within VSMCs to better understand the involvement of each component.

5.5.6.2 Mislocalisation of DNA damage response factors

Within this chapter, we speculate that DNA-damage was caused via increased hydrostatic pressure from SAC-induced hypertrophy. A marker that was utilised within this study was the 53BP1 protein, where its ionising radiation-induced foci was considered a positive sign for DNA damage. We concluded that the decrease in 53BP1 recruitment, via SAC treatment, indicated a reduction in DNA impairment. However, previous studies have shown that increased contractility can cause a mislocalisation of nuclear factors due to rupture of the nuclei (134, 362, 363). Due to this, further assessment of VSMC nuclear structure and rupture incidence under matrix stiffness will increase the clarity of our work.

5.5.6.3 The role of microtubules in VSMC dysregulation

We highlighted how actomyosin activity of quiescent VSMCs can become dysregulated within a rigid setting. Typically, this has been shown to cause dysregulation of VSMCs leading to remodelling of the vascular wall (10). Our study utilised actomyosin inhibitors as a regulatory component of this pathway to better understand its mechanism. However, more recently, it has been shown that an inverse relationship exists between microtubule acetylation and cell contractility in other cell types (70). Within VSMCs, Remodelin, an inhibitor of a key microtubule N-acetyltransferase, was also found to reduce DNA damage (151). Therefore, our work within this chapter remains limited as it does not account for how microtubule acetylation contributes to VSMC function within matrix stiffness.

Chapter 6: The role of NAT10 in actomyosin-induced dysregulation within VSMCs

6.1 Introduction

Our work so far shows that SACs play an important role within quiescent VSMC function in response to matrix stiffness. We show that that the aberrant opening of these channels can cause hypertrophy and increased contractility, via an influx of ions and solutes. This in agreement with prior studies which confirmed significant calcium entry via SACs, and described cell hypertrophy to be a common morphological response during CVD (177, 310, 311). We speculated that the increased actomyosin-induced tension held at the membrane may be sufficient to open the SACs on the rigid matrix.

Microtubules serve as another filamentous component within VSMCs. Microtubules are essential cytoskeletal structures, which serve to regulate numerous functions such as cell shape, transport and motility. Its function is regulated by a variety of factors such as interaction with microtubule associated proteins (MAPs) or modification of acetylation levels via NAT10 (51, 367). Recent data has suggested that they serve a role within actin cytoskeleton regulation and microtubules are essential for normal VSMC contractile function. Microtubules are stabilised by alpha-tubulin acetylation, however, the role of acetylation in VSMC contraction and the impact of matrix stiffness remain unknown. Within this chapter, we look at the link between NAT10 activity, VSMC hypertrophy and DNA damage to better understand how these filaments may contribute to the pathological changes observed.

6.2 Aim of this chapter

This chapter will investigate whether microtubule acetylation has any effect on quiescent VSMC volume by targeting one of its key regulators NAT10, and if so, whether this could also be mirrored within nuclear morphology. We will explore whether NAT10 regulation can induce any protective effects on the nucleus by investigating if its inhibition can attenuate the DNA damage accumulation within the stiffer environment. By gaining an understanding of how these aberrant changes may be interlinked with microtubule function, we hope to identify a new component that can be targeted for future research.

6.3 Hypothesis

We hypothesise that inhibiting NAT10 will protect the VSMC from hypertrophy on stiff hydrogels. We speculate that these changes will reduce the DNA damage accumulation that occurs when stimulated to contract on the 72kPa polyacrylamide hydrogel.

6.4 Results

6.4.1 Effect of NAT10 inhibition on VSMC volume

Recently, cellular contractility and microtubule acetylation have been shown to exist in a mechanical balance within fibroblast cells. Increased acetylation levels resulted in lower traction force (70). We speculate that modifying the acetylation levels of VSMC microtubules may influence the aberrant actomyosin activity seen in response to matrix stiffness. Previously, a key enzyme identified as NAT10 has been reported to have regulate microtubule function via tubulin acetylation (146). The microtubule structure consists of α/β-tubulins, and NAT10 inhibition has been shown to induce network reorganisation within the cytoskeletal polymer (150). Additionally, it has been shown that treatment with 1 μM of Remodelin, a NAT10 inhibitor, can extend the lifespan of aged VSMCs *in vitro* (151). As a result, we now investigated the effects of NAT10 inhibition on VSMC volume. To do this, serum starvation was performed on our VSMCs to induce quiescence, and they were then seeded on collagen-1 coated polyacrylamide hydrogels, with an average Young's modulus of 12 kPa and 72 kPa. Cells were pre-treated with 1 μM of Remodelin and then stimulated with 10 μM of Angiotensin II for 30 minutes each. F-actin was then stained with rhodamine phalloidin prior to confocal microscopy.

Interestingly, our results revealed that inhibition of NAT10 resulted in an increase in cell spreading and volume within the compliant matrix (**Figure 6.1A-C**). We speculate that increased cell volume (**Figure 6.1C**) may enhance cell area causing the relationship to be closer to 1. When looking at the correlation between area and volume however, we found no significant difference between both treatment groups, indicating Remodelin inhibition to have no effect towards it (**Figure 6.1D**). Despite this, the trend does show an enhancement from a weak to a moderate correlation via Remodelin treatment, and therefore more end numbers may be required to establish the difference.

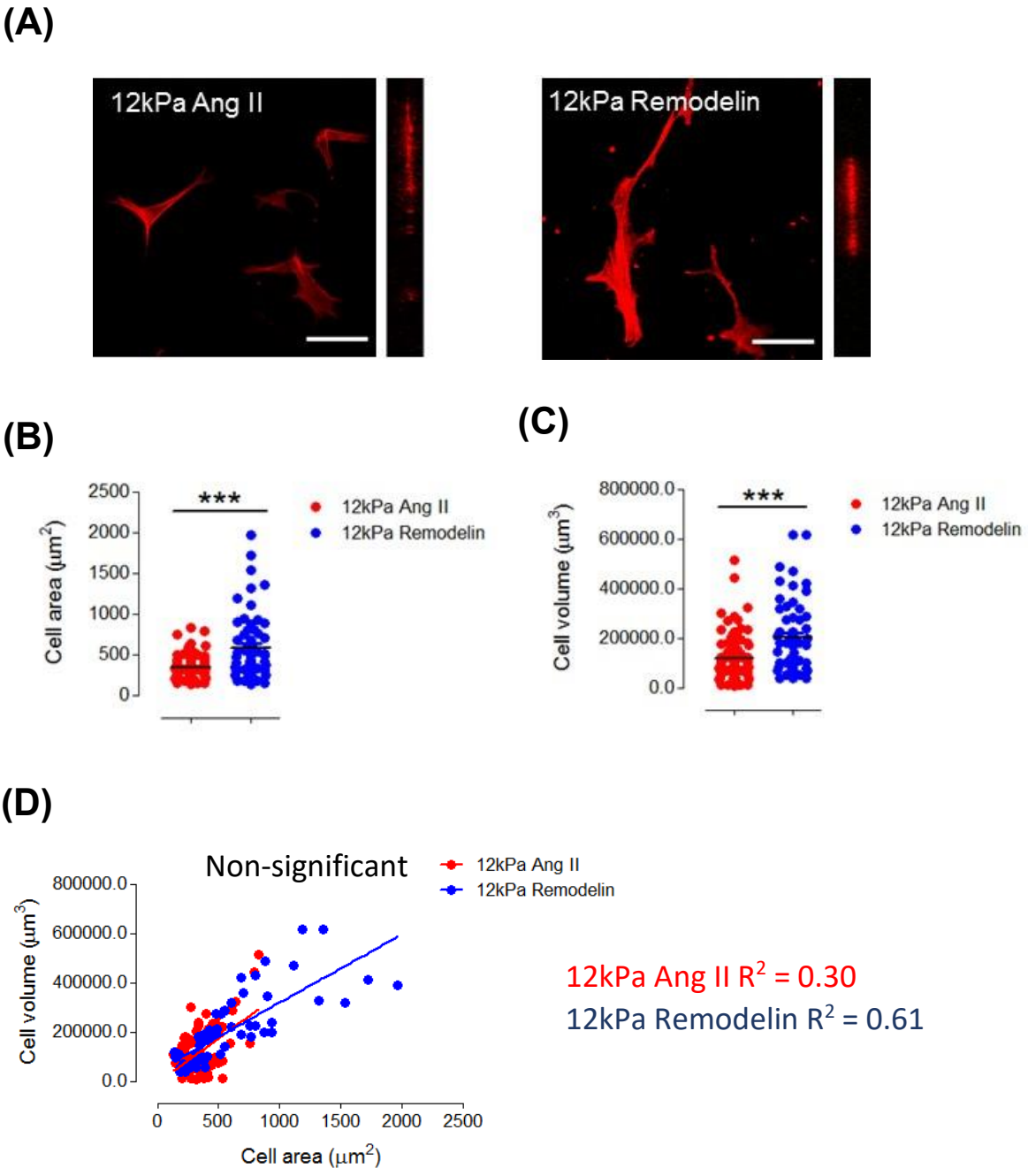

Figure 6.1: The impact of a NAT10 inhibitor on VSMC volume. **(A)** Representative immunofluorescence images of VSMC actin filaments with Angiotensin II alone and following pre-treatment with Remodelin. Images show VSMC actin filaments (F-actin) stained using rhodamine phalloidin (red) on 12 kPa polyacrylamide hydrogels. Scale bar represents 100 µm. Image J software and Volocity software were used to manually measure **(B)** cell area and **(C)** cell volume, respectively. Image J software was also used to plot **(D)** VSMC area against volume on cells treated with Angiotensin II alone and with Remodelin. Data are based on the measurement of ~100 VSMCs from 3 independent experiments. Statistical significance was determined using a paired Student's *t* test on cell area and volume (12 kPa Ang II vs 12 kPa Remodelin) (*** p = <0.0001). A linear regression analysis was also performed to determine statistical significance for the cell area and volume relationship (non-significant; p = >0.05). Ang II: Angiotensin II; NAT10: N-Acetyltransferase 10; VSMC: Vascular smooth muscle cell.

VSMCs seeded on a stiff matrix displayed decreased cell area and volume in response to Remodelin treatment (**Figure 6.2A-C**). This indicates an attenuation in the hypertrophy of the VSMCs with decreased microtubule acetylation. When observing the cell area to volume relationship, we see a moderate correlation established with Angiotensin II treatment alone due to the hypertrophic changes induced on the 72 kPa hydrogel. In this case, we reveal Remodelin treatment to maintain the relationship between the two morphological factors, with no difference found between both treatments. (**Figure 6.2D**).

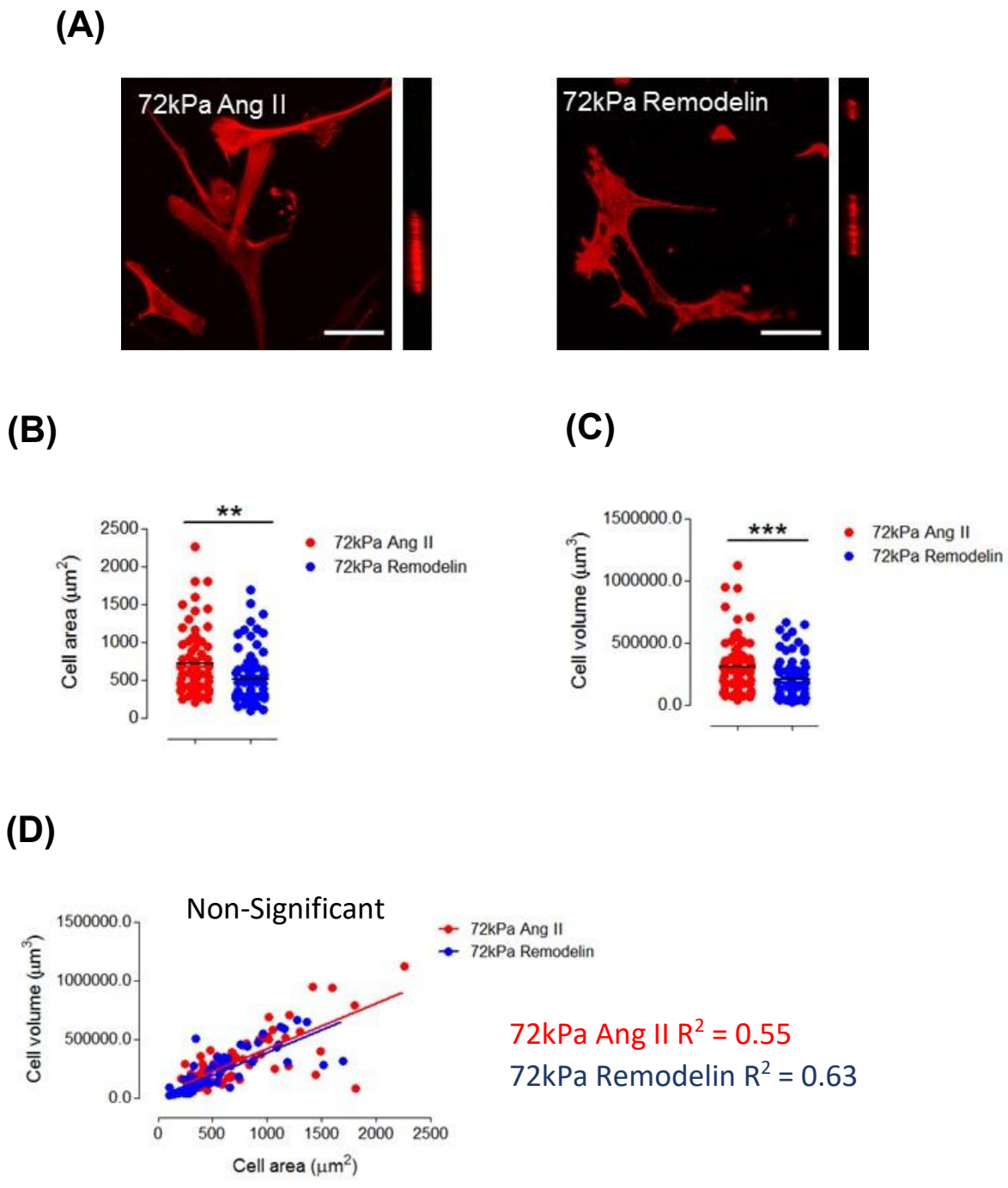

Figure 6.2: The impact of a NAT10 inhibitor and matrix stiffness on VSMC volume. **(A)** Representative immunofluorescence images of VSMC actin filaments treated with Angiotensin II alone and following pre-treatment with Remodelin within a stiffer matrix. Images show VSMC actin filaments (F-actin) stained using rhodamine phalloidin (red) on 72 kPa polyacrylamide hydrogels. Scale bar represents 100 µm. Image J and Volocity software were used to manually measure **(B)** cell area and **(C)** cell volume, respectively. Image J software was also used to plot **(D)** VSMC area against volume on cells treated with Angiotensin II alone and with Remodelin. Data are based on the measurement of ~100 VSMCs from 3 independent experiments. Statistical significance was determined using a paired Student's *t* test on cell area and volume (72 kPa Ang II vs 72 kPa Remodelin) (** p = <0.001, *** p = <0.0001). A linear regression analysis was also performed to determine statistical significance for the cell area and volume relationship (non-significant; p = >0.05). Ang II: Angiotensin II; NAT10: N-Acetyltransferase 10; VSMC: Vascular smooth muscle cell.

6.4.2 Effect of NAT10 inhibition on nuclear morphology

Next, we wanted to investigate the effects of Remodelin on nuclear morphology. As previously discussed, the nuclei of VSMCs display a hypertrophic effect on the stiff hydrogels when stimulated with Angiotensin II. Earlier studies have shown that NAT10 depletion can restore healthy nuclear morphology in lamin A knockdown fibroblast cells. Additionally, Hutchinson-Gilford progeria syndrome (HGPS) fibroblast cells present a significant reduction in the prevalence of nuclear abnormalities with Remodelin treatment (150). Based on our previous findings, we hypothesise that Remodelin treatment will reduce nuclear volume within the pathological environment. To investigate this, we repeated our previous experiment set up, however this time stained our nuclei with anti-lamin A/C prior to microscopy.

Like with cell morphology, the nuclear area presents a significant increase with Remodelin treatment on hydrogels of physiological stiffness (**Figure 6.3A & B**). However, in this case, there was no apparent change in nuclear volume (**Figure 6.3A & C**). In agreement with the cell data, the nuclear area-volume shows no significant change between both treatment groups (**Figure 6.3D**).

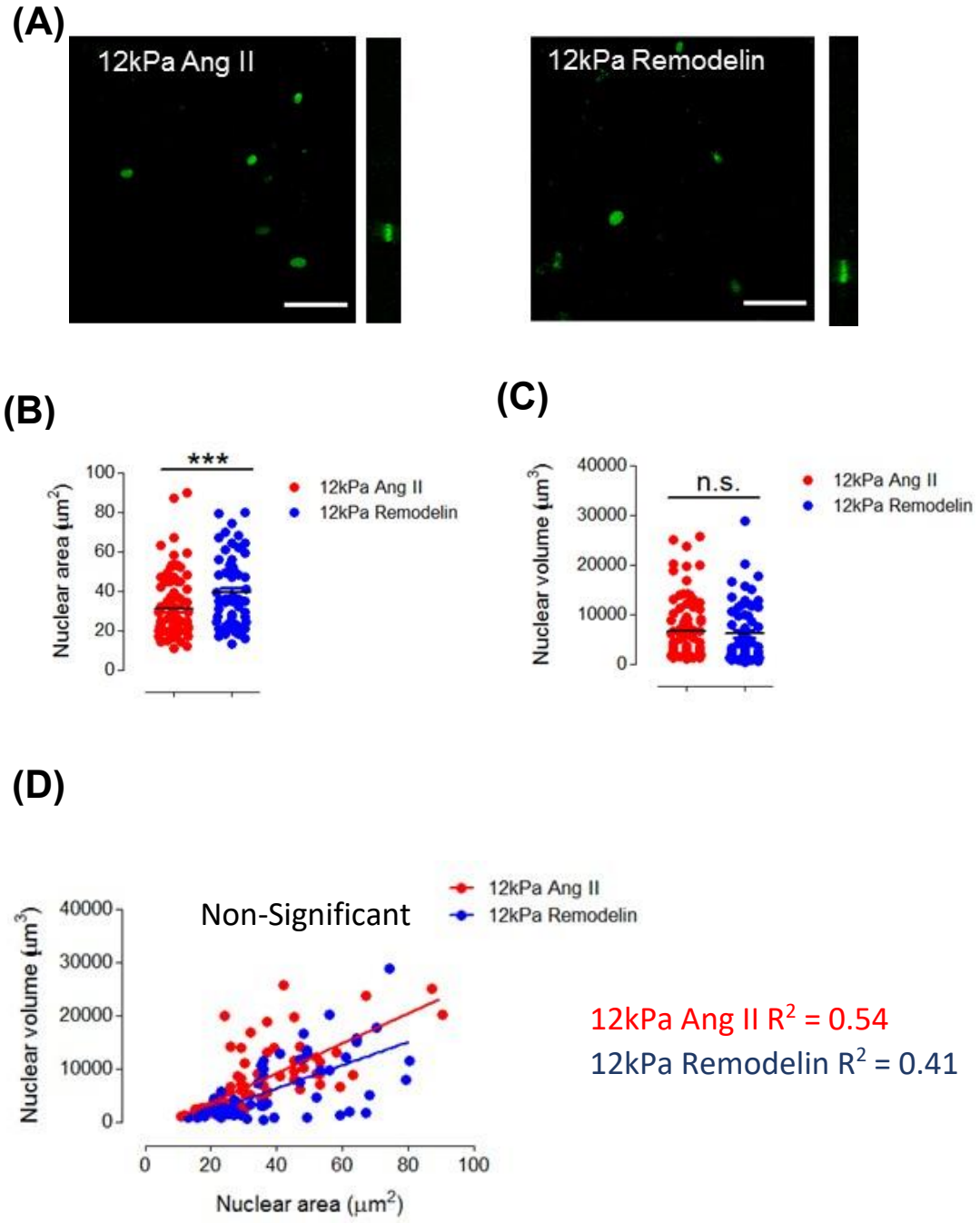

Figure 6.3: The impact of a NAT10 inhibitor on VSMC nuclear volume. **(A)** Representative immunofluorescence images of VSMC nuclei treated with Angiotensin II alone and following pre-treatment with Remodelin. Images show VSMC nuclei stained using anti-lamin A/C (green) on 12 kPa polyacrylamide hydrogels. Scale bar represents 100 µm. Image J and Volocity software were used to manually measure **(B)** nuclear area and **(C)** nuclear volume, respectively. Image J software was also used to plot **(D)** VSMC nuclear area against volume on cells treated with Angiotensin II alone and with Remodelin. Data are based on the measurement of ~100 VSMCs from 3 independent experiments. Statistical significance was determined using a paired Student's *t* test on nuclear area and volume (12 kPa Ang II vs 12 kPa Remodelin) (non-significant; p = >0.05, *** p = <0.0001). A linear regression analysis was also performed to determine statistical significance for the nuclear area and volume relationship (non-significant; p = >0.05). Ang II: Angiotensin II; NAT10: N-Acetyltransferase 10; VSMC: Vascular smooth muscle cell.

When introducing matrix rigidity, we observed a corresponding decrease in nuclear area, and importantly, nuclear volume (**Figure 6.4A-C**). This confirms that an inhibition of NAT10 is successful in attenuating VSMC nuclear hypertrophy on stiff hydrogels. The area to volume correlation, within these conditions, once again followed previous observations revealing no significant difference between both treatment groups (**Figure 6.4D**).

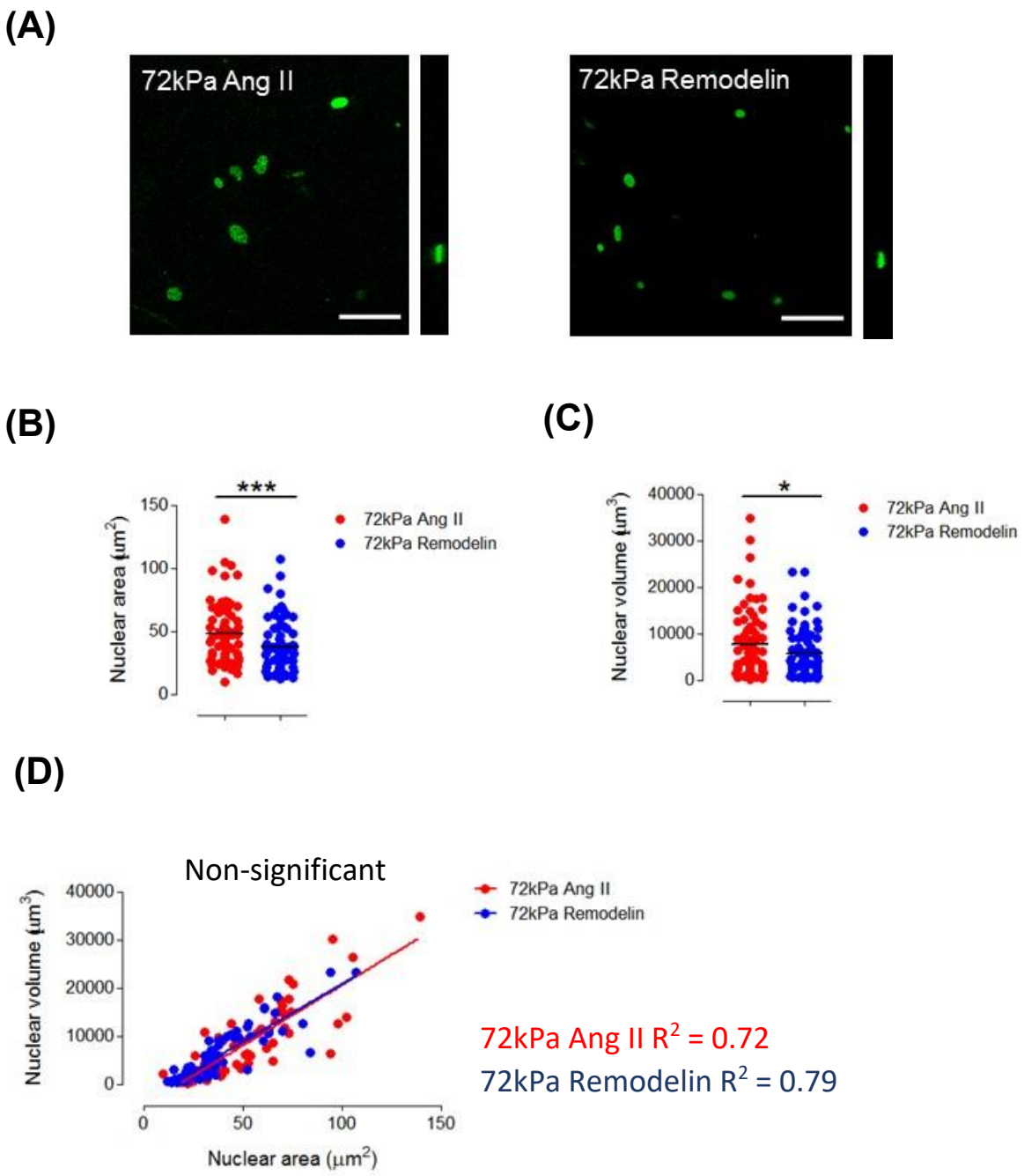

Figure 6.4: The impact of a NAT10 inhibitor and matrix stiffness on VSMC nuclear volume. **(A)** Representative immunofluorescence images of VSMC nuclei treated with Angiotensin II alone and following pre-treatment with Remodelin within a stiffer matrix. Images show VSMC nuclei stained using anti-lamin A/C (green) on 72 kPa polyacrylamide hydrogels. Scale bar represents 100 µm. Image J and Volocity software were used to manually measure **(B)** nuclear area and **(C)** volume. Image J software was also used to plot **(D)** VSMC nuclear area against volume on cells treated with Angiotensin II alone and with Remodelin. Data are based on the measurement of ~100 VSMCs from 3 independent experiments. Statistical significance was determined using a paired Student's *t* test on nuclear area and volume (72 kPa Ang II vs 72 kPa Remodelin) (* p = <0.05, *** p = <0.0001). A linear regression analysis was also used to determine statistical significance for the nuclear area and volume relationship (non-significant; p = >0.05). Ang II: Angiotensin II; NAT10: N-Acetyltransferase 10; VSMC: Vascular smooth muscle cell.

6.4.3 NAT10 activity and DNA damage within VSMCs

Within our previous chapter, we speculated that DNA damage accumulation within the stiffer environment was due to increased mechanical pressure from nuclear hypertrophy. It has been shown that modification of acetylation levels can induce changes in microtubule anchorage, and we speculate this may prevent additional pressure from being placed on the nucleus (150). Previously, it has been revealed that within aged VSMCs, Remodelin treatment can significantly decrease the levels of γH2AX (151). Our results show Remodelin treatment induce a significant reduction in nuclear volume, and therefore we hypothesise that inhibition of NAT10 may alleviate matrix stiffness-induced DNA damage.

To investigate this, quiescent VSMCs were stimulated with Angiotensin II alone or following pre-treatment with Remodelin. Prior to microscopy, VSMC nuclei and potential DNA damage foci were stained with anti-lamin A/C and anti-γH2AX, respectively. The findings presented within **Figure 6.5** were performed and obtained by Dr Robert Johnson within the Warren lab. Our results show that the size and number of γH2AX foci are significantly larger when VSMCs are treated with Angiotensin II on stiff hydrogels. Remodelin treatment, however, reduced the number of γH2AX foci present in nuclei of VSMCs on stiff hydrogels. This confirms our hypothesis that NAT10 inhibition can partially rescue DNA damage accumulation within VSMCs.

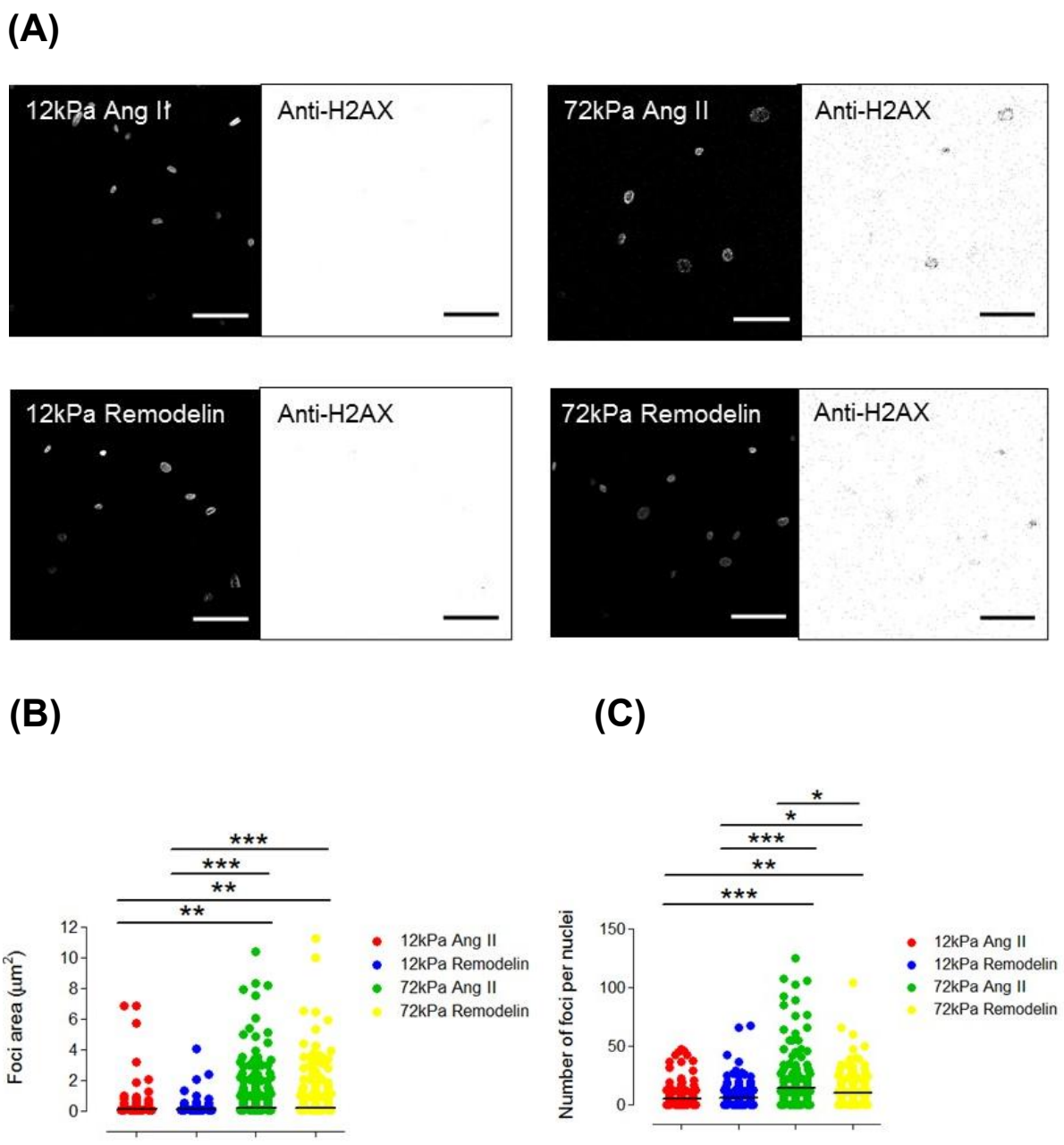

Figure 6.5 Inhibition of NAT10 influences γH2AX foci formation of quiescent VSMCs under matrix stiffness. (A) Representative immunofluorescence images of nuclei and γH2AX foci from VSMCs treated with Angiotensin II alone and following pre-treatment with Remodelin. Images show VSMC nuclei stained using anti-lamin A/C (grey-scale) and anti-H2AX on 12 kPa and 72 kPa polyacrylamide hydrogels. Scale bar represents 100 μm. Image J software was used to measure **(B)** foci area and **(C)** number of foci per nuclei. Data are based on the measurement of ~150 VSMCs from 3 independent experiments. Statistical significance was determined using a one-way ANOVA to show differences in foci area (** p = <0.001, *** p = <0.0001) and number of foci per nuclei (* p = <0.05, ** p = <0.001, *** p = <0.0001), followed by a Bonferroni's multiple comparison test. Ang II: Angiotensin II; NAT10: N-Acetyltransferase 10; VSMC: Vascular smooth muscle cell.

6.5 Discussion

This chapter investigated the relationship between NAT10, matrix stiffness-induced VSMC hypertrophy and DNA damage. By looking at the effects of Remodelin, a NAT10 inhibitor, we were able to better understand the balance between NAT10 activity and actomyosin-induced changes within matrix stiffness. As a result, the work performed within this chapter explores a different target within quiescent VSMCs, and potentially identifies an additional regulatory component of aberrant VSMC function within the pathological environment.

6.5.1 Balance between actomyosin and NAT10 activity

Within CVD, VSMCs typically abandon their role of regulating vascular tone and begin migrating towards the tunica intima. During this, there is a constant turnover of adhesion structures to allow disassembly of these complexes at the rear end, along with nascent formation at the front (69). Focal adhesion disassembly is regulated via microtubule function, which either induces endocytosis of integrin molecules or degradation of other components via proteolysis (54, 368-371). An additional method of detachment is via sheer force from the actin cytoskeleton (55). As a result, the two cytoskeletal structures may coordinate their function to be more efficient in mediating important cellular processes. To support this, acetylation of microtubules via NAT10 has previous been shown to be inversely regulated to cell contractility (70). These studies have revealed that an overexpression of an acetyl-mimetic caused lower traction force generation. As tubulin is a known substrate of NAT10, we speculate NAT10 to have an important role in decreasing actomyosin activity. Our data, however, presented inverse findings. We show that inhibition of NAT10 results in rescue from VSMC hypertrophy on the stiffer environment. Previously, this was shown with actomyosin inhibition and therefore this suggests a reduction in microtubule acetylation may mirror these changes. As a result, we speculate that the network reorganisation that is induced from microtubule acetylation may evoke differential responses, and these may be cell-type specific. Further work is now needed to investigate the mechanisms by which these two cytoskeletal structures may coordinate with each other within quiescent VSMCs.

6.5.2 Regulation of nuclear morphology via NAT10 activity

Dysregulation of nuclear morphology typically occurs during CVD development. Misshapen nuclei have previously been observed within laminopathies, which are caused via mutations in the LMNA gene (372-374). This can accelerate the progression of CVD and ageing via atherosclerotic formation and electrophysiological alterations, and prior studies have shown Remodelin to rescue nuclear morphology under these conditions (150, 375). Remodelin works by targeting NAT10 to induce microtubule reorganisation, and our data shows that this can prevent nuclear hypertrophy when VSMCs were stimulated to contract within the rigid environment. Further studies have expanded on the therapeutic benefits of Remodelin by demonstrating how this inhibitor can expand the lifespan of mice with Hutchinson-Gilford progeria syndrome (376). This could be due to improved genomic stability as Remodelin has been shown to reduce DNA damage accumulation within VSMCs (151). Our results fall in agreement with this as they show that inhibition of NAT10 can reduce the γH2AX foci levels within quiescent VSMCs. Previously, we had shown that actomyosin inhibition had no positive effects in attenuating nuclear spreading or DNA damage accumulation. As a result, our findings indicate that NAT10 may present itself as a separate regulatory component of nuclear morphology within quiescent VSMCs. Future studies will be required to clarify the mechanisms in which NAT10 exerts its effects upon the nuclei of quiescent VSMCs.

6.5.3 Chapter Six conclusions

Within this study, we confirm that inhibition of microtubule N-acetyltransferases, specifically NAT10, to attenuate aberrant volume and γH2AX foci levels within dysregulated VSMCs. Importantly, we highlight its effect on cell hypertrophy to be identical to actomyosin inhibition, contradicting previous findings that present an inverse relationship between the two cytoskeletal networks (70). Much like SACs inhibitors, we show a decoupling with the actin cytoskeleton within nuclear morphology, as inhibition of NAT10 was found to attenuate the aberrant changes in nuclear structure. In summation, this chapter highlights a new regulatory component of VSMC function within the stiffer environment.

6.5.4 Limitations and future work

6.5.4.1 Role of NAT10 in VSMC traction force

Our work shows NAT10 to regulate numerous actomyosin-induced processes within VSMCs. As mentioned before, microtubules are a known target of NAT10 (150). Previously, it was speculated that the microtubule and actin cytoskeletal networks may coordinate function due to mediating mutual cellular processes (54, 55). Alongside this, earlier studies have demonstrated how an increase in microtubule acetylation resulted in a decrease in fibroblast traction force generation (70). Our work, however, shows that a reduction in NAT10 and actomyosin activity present similar effects within quiescent VSMCs. As a result, we speculate that NAT10 inhibition will result in decreased VSMC traction force generation, and further TFM work will be required to clarify this.

6.5.4.2 NAT10 targets within VSMCs

Whilst our work shows the effects of NAT10 inhibition on quiescent VSMCs, we do not confirm the substrates that it targets. Previously, it has been shown that NAT10 targets tubulin, and therefore further work will be required to clarify its role with the microtubule network within VSMCs. Whilst we hypothesise that these effects may be mediated via the microtubule network, it is important to note that it could be via other substrates, such as the vimentin intermediate filament network. Vimentin has previously been shown to regulate actin stress fibre assembly and contractility within VSMCs (143, 144, 152-155) and earlier

work reveals acetylation to reorganise the vimentin network, which we speculate could be facilitated via NAT10 (377).

6.5.4.3 Role of NAT10 in gene regulation

Our study has so far focused on NAT10's role in microtubule reorganisation, however earlier work has shown it to also act on histone proteins. Within VSMCs, changes in gene expression are regulated via crucial epigenetic markers such as HK39 acetylation, and this may be mediated through NAT10 activity (165). During CVD development, there are alterations in the expression of key contractile marker proteins (10), and future work will focus on NAT10's implication within this.

Chapter 7: General Discussion & Conclusions

7.1 Regulation of vessel tone in response to decreased aortic compliance

The primary function of VSMCs, within the medial layer of the arterial wall, is to regulate vessel tone via contractile function (10). This allows for efficient regulation of blood pressure as the arterial network transports blood away from the heart (378). Within normal physiology, the arterial structure is compliant due to its highly elastic nature, and this allows VSMCs to perform simple vasoconstriction/dilation (22). Our work has supported this showing clear deformation of the ECM within the physiological stiffness range, along with a reduction in VSMC area with increasing contractile stimulation. However, during CVD development, there is a pathological remodelling which results in increased arterial stiffness (14-16). This hinders control of blood flow from the left ventricle as the stiffer ECM becomes more difficult to manipulate (11).

Key VSMC mechanosensors such as SACs and focal adhesions are able to detect the altered mechanical environment, and previous work has shown matrix stiffness to trigger increased actomyosin activity and formation of larger cell-matrix adhesion complexes (142, 197). Our work has expanded on previous studies by employing substrates that are representative of both physiological (12 kPa) and pathological (72 kPa) environments, and within this project, we have shown that even a six-fold increase in substrate stiffness can cause alterations in VSMC morphology and contractility. Under healthy settings, VSMCs exist in a quiescent contractile phenotype where they perform their role by exerting actomyosin-derived forces (36). Within stiffened conditions, this function can become aberrant. Our results corroborated with earlier studies revealing that VSMCs exert higher levels of traction force in response to matrix rigidity (142). Despite this, there was an absence of substrate deformation on the rigid substrate indicating the ECM had become too stiff to physically pull. Therefore, we speculate that the increased force generation may create tension that is held at the cell membrane, and this may be sufficient to open SACs. Typically, blood flow expands the aortic wall causing the opening of SACs via transient stretch signals, and this allows regulation of the myogenic response via calcium entry (177). However, earlier studies have implicated a variety of SACs within muscle pathology (327, 328). We show that SAC activity is involved within the dysregulated traction force response discussed (**Figure 7.1**), and therefore speculate that the reduction in elasticity may cause a switch between transient stretch signals to more persistent stiffness signals.

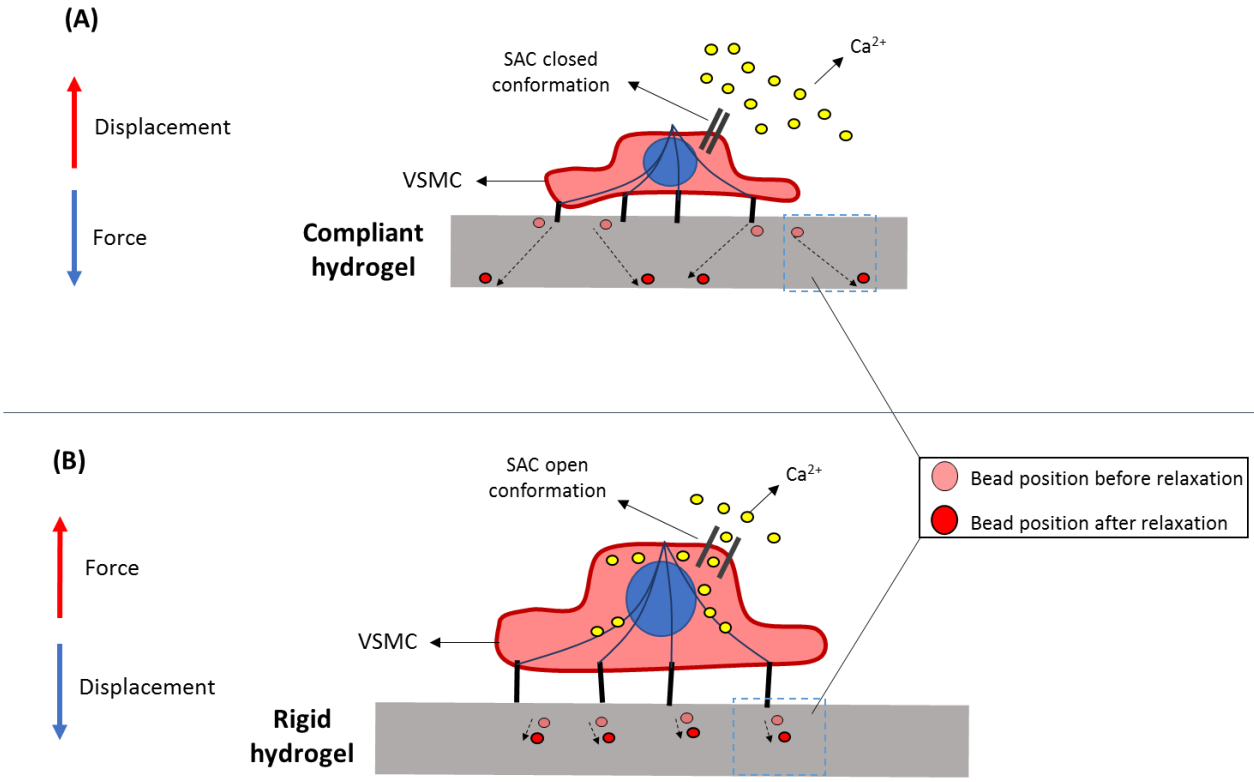

Figure 7.1: Working model revealing the mechanism behind VSMC traction force generation within the stiffer environment. **(A)** shows VSMCs seeded on a physiological matrix. SACs are shown to be closed due to less mechanical tension on the cell membrane. This results in decreased force generation due to blocked calcium entry. The force generated, however, causes larger displacements in bead movement as the matrix is more compliant. **(B)** illustrates VSMCs seeded on a rigid matrix. In this case, SACs are illustrated to be open due to augmented membrane tension mediated via matrix stiffness. This allows calcium into the cell facilitating higher force generation. However, due to the rigid ECM, bead displacement is minimised indicating a reduction in compliancy. SAC: Stretch-activated channel; VSMC: Vascular smooth muscle cell.

Excitingly, we propose a novel candidate within our study, known as Piezo1, that may potentially drive increased force generation within VSMCs. Piezo1 has previously been implicated in arterial remodelling within hypertensive models, and our data shows an upregulation in its expression within the stiffer environment (189). However, prior studies have presented findings determining SAC activation alone to be inadequate in driving VSMC contraction. Previously, it's been shown that calcium permeability is low via SAC entry and therefore opening of Piezo1 may be incapable of independently increasing VSMC force generation (358). Due to this, it was speculated that SAC opening may instead serve to depolarise VGCCs present on the cell membrane, which can facilitate increased calcium entry to enable this (359, 360). Despite this, other researchers have revealed that SACs can

in fact significantly enhance calcium concentration independently, and as a result, further work is required to clarify the role of Piezo1 within quiescent VSMCs (177).

Our study primarily focused on actin-dependent processes as this cytoskeletal network is responsible for facilitating actomyosin activity. However, more recently, the microtubule network has presented a novel role in actin cytoskeletal regulation. Prior studies using fibroblast cells have shown an inverse relationship between tubulin acetylation via NAT10 and cellular contractility, however, our study shows a differential trend between both factors via inhibition of the acetyl-transferase NAT10 (70). We show inhibition of NAT10 within the stiffer environment to induce effects similar to actomyosin inhibition, indicating the effects of this filamentous component to be cell-type specific. Importantly, during aortic remodelling, VSMCs begin to migrate to the tunica intima and both cytoskeletal networks have previously been shown to share mutual roles in adhesion turnover. Earlier work has revealed microtubules to induce endocytosis of integrin molecules as well degradation of other components, such as talin, via proteolysis. The actin cytoskeleton also removes rear-end adhesions, however, it does it via sheer force, as detachment can occur when the force of the non-muscle myosin II exceeds the strength of the VSMC-ECM adhesion (54, 55, 69, 368-371). Due to this, we speculate that these filamentous components may carefully coordinate their function in order to regulate VSMC force generation. Further work will now be required to assess the capability in which these filamentous structures maintain vessel tone when the compliancy of the aortic wall diminishes.

The overall aim of this thesis was to investigate the effects of matrix stiffness on VSMC contractile function, as well as its underlying mechanism. Our findings revealed that the cytoskeletal networks are dynamic and can carefully coordinate their function to effectively respond to changes in the mechanical environment. We show that SAC activation is necessary to facilitate higher force generation, and its inhibition could impede any actin-dependent processes. VSMC contractility is a critical regulator of the aortic structure, and any aberrant effects that arise from unrestrained actomyosin activity could possibly accelerate vessel degeneration and ageing. Our work was performed within a 2D system, in which we could isolate the contractile pathway of the VSMCs to further understand the mechanism behind it. However, previous work has shown that using 2D substrates could elicit responses that deviate from an accurate *in vivo* representation (248-250). For instance, within the aortic wall, the intimal layer can induce vasodilation of the vessel via nitric oxide-mediated relaxation of the VSMCs (304, 305). As a result, we must consider external cues outside of our system to better understand the relationship between aortic compliance, VSMC function and vessel tone regulation.

7.2 VSMC hypertrophy and vessel wall remodelling

During hypertension, the vessel wall undergoes unregulated thickening and this was shown to be partially caused via an increase of smooth muscle cell mass (336-339). VSMC hypertrophy can be a chronic consequence of the mechanical stress placed by the pathological environment, and we show actomyosin activity to induce a significant increase in VSMC volume in response to matrix stiffness (379). In agreement with our findings, Angiotensin II, a common contractile agonist, has previously presented elevated levels within CVD models and been implicated in VSMC hypertrophy, ultimately causing increased vascular resistance (260, 351-354). Interestingly, we show that we can intervene this response by inhibiting SAC activity, indicating that the hypertrophic response observed within VSMCs is via the opening of these mechanical-gated channels.

The dogmatic view originally stated that VSMCs contributed to vessel wall stiffness via their contractile activity, however recent insights have focused on the inherent mechanical properties of these cells (31). It is established that cells respond to a rigid environment by becoming stiffer, and we speculate that an increase in VSMC size via SAC opening facilitates this augmentation of cell rigidity (380). Earlier studies using atomic force microscopy (AFM) support this as they show an increase in VSMC stiffness when isolating cells from aging primates as well as SHR models (31). Within a mature vessel, VSMCs exist in an organised fibrous helix and we hypothesise that cell hypertrophy may increase the hydrostatic pressure placed upon the arterial wall, as shown by **Figure 7.2**. Importantly, the vessel wall also faces hydrostatic pressure from the lumen side of the vessel as blood pressure increases via vessel remodelling (31, 379). Typically, within normal physiology, the pulse pressure from blood flow expands the arterial wall, which causes a decline in blood velocity via kinetic energy transfer. However, due to an increase in arterial stiffness, control of blood pressure becomes unmanageable and the resulting increase in blood velocity causes damage to the microcirculation of different organs (17). Our work therefore identifies a potential hydrostatic balancing system between blood pressure, matrix stiffness and VSMC volume.

In addition, a key change observed in response to stiffness-induced cell hypertrophy within our study was the dysregulation of VSMC nuclear integrity. When seeded on the 72 kPa polyacrylamide hydrogel, we found the nuclei to present similar hypertrophic effects as the cytosol. Importantly, these changes were shown to be induced from short 30 minute stimulations with contractile agonists. Within normal physiology, the opening of ion channels are rapid responses and can occur within milliseconds (381). If the contractile signal is

sustained for a larger length of time, however, it may cause longer term transcriptional changes which may maintain the hypertrophic morphology of the quiescent VSMCs in response to matrix stiffness. As a result, future research focusing on the long-term implications of matrix stiffness and VSMC hypertrophy will allow us to better understand the sustained changes occurring during CVD in the microenvironment of the VSMCs and the larger scale organisation of the vessel wall.

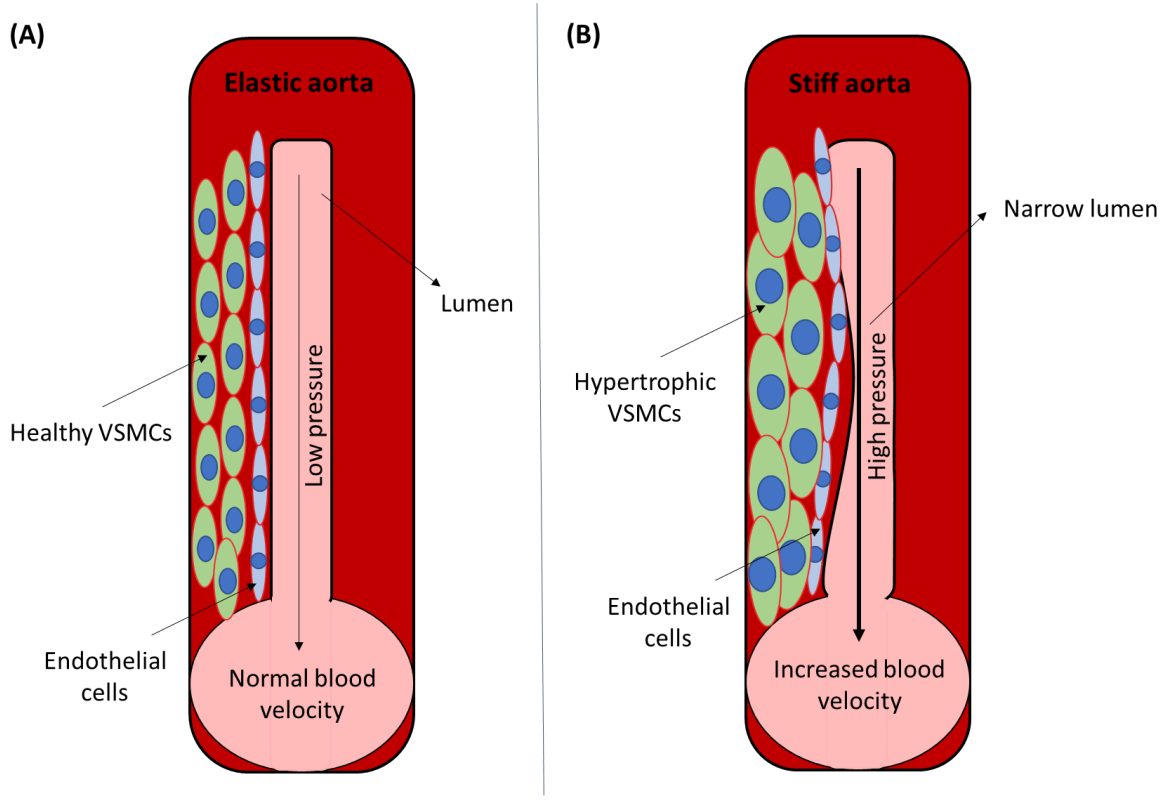

Figure 7.2: Schematic diagram showing the effect of VSMC mechanical properties on the arterial wall. **(A)** shows an elastic arterial wall possessing endothelial cells neighboured by healthy VSMCs and the arterial lumen. Due to the elasticity of the arterial wall, there is low pressure within the artery enabling controlled blood velocity. **(B)** depicts stiff arterial wall which illustrates hypertrophic VSMCs inflicting mechanical pressure on neighbouring endothelial cells. This results in a narrowing of the lumen causing increased pressure within the vessel. As a result, the arterial wall becomes more resistant to expansion from blood flow, causing increased blood velocity. VSMC: Vascular smooth muscle cell.

7.3 DNA damage and VSMC ageing

Our study revealed VSMCs seeded on the 72 kPa hydrogels have a significant increase in DNA damage accumulation. Earlier studies have shown that overexpression of myosin II can induce DNA damage accumulation, indicating the cause to be increased contractility (134). Importantly, it has been shown that DNA damage is one of the most common causes of VSMC ageing (135). Earlier work has shown that VSMCs derived from atherosclerotic plaques present an increase in DNA damage with disease severity, and VSMCs, under these conditions, were also shown to undergo premature senescence (136-138). DNA damage occurs via a variety of factors such as intracellular metabolism and unrestrained actomyosin activity (140, 382), however our study potentially identifies two novel regulatory components that mediate this; SAC activation and microtubule acetylation. We speculate that SAC opening increases cytosolic volume via an influx of ions and solutes, and this creates mechanical overload for the nuclei. The microtubule network has previously been considered to effectively regulate actin-dependent processes, however cell/nuclear hypertrophy leading to a subsequent increase in VSMC stiffness may dysregulate this (54, 55, 69, 70, 368-371). This could potentially result in further mechanical tension placed upon the nuclei, via the filamentous components, leading to disruption of the nuclear integrity.

Current literature is limited in understanding the cause of aberrant vessel remodelling, and the extent in which VSMCs contribute to it. Our work provides a new mechanistic insight where we identify new components that may contribute to this pathological process. It has been shown that DNA damage affects VSMC ageing, and VSMC ageing can trigger a switch to the synthetic proliferative phenotype (126). Within CVD, VSMCs typically transition to the proliferative phenotype where they migrate to the tunica intima to contribute to intimal-medial thickening (38, 130). We hypothesise that mechanical pressure placed by the smaller ECM pores within matrix stiffness could potentially induce further DNA damage, and this could facilitate dysregulated remodelling of the vessel wall. As a result, our findings provide an important perspective, however further work investigating the cross talk between DNA damage, phenotypic modulation and vessel wall remodelling would contribute further clarification to this.

7.4 Differential VSMC contractile mechanism during phenotypic switching

VSMCs display remarkable plasticity between both phenotypes, and we expanded our study by utilising synthetic VSMCs in order to also investigate potential mechanistic insights within the proliferative state. As mentioned before, VSMCs normally exist in the quiescent contractile state, however during vessel damage, they can undergo de-differentiation back to the synthetic proliferative phenotype (37, 38). This is commonly observed during the pathological remodelling of the vessel wall, where VSMCs participate in a multicellular response, via migration, to initiate repair of neighbouring cells (383). Therefore, despite a downregulation of key proteins that enhance contractile function, synthetic VSMCs still rely on traction force generation to propel the cell forward during migration (193, 384). Our study interestingly found key mechanisms that drive VSMC traction force generation within both phenotypes. Within the synthetic proliferative state, we observe an inverse relationship between actomyosin activity and adhesion density. When utilising synthetic VSMCs, we show matrix stiffness to reduce mean pMLC levels whilst enhancing the number of adhesion anchor points. As a result, we speculate that this facilitates efficient force distribution, which may prevent actomyosin-induced tension at the membrane from opening SACs. In this case, our work revealed VSMC spreading due to increased filamentous actin density, however further work will be required to confirm whether there is also a hypertrophic effect via SAC opening within synthetic VSMCs.

Earlier, we hypothesised that hypertrophy-induced mechanical overload can cause DNA damage within quiescent VSMCs, and we speculate that this balancing mechanism in synthetic VSMC force generation may be a compensatory mechanism to prevent this (**Figure 7.3**). Typically, within atherosclerosis, synthetic VSMCs migrate to the tunica intima where they proliferate within the fatty streak and form a cap around the soft-core region. To do this, they squeeze via small pores as a result of ECM remodelling, and our work proposes a new method that may minimise mechanical tension during this (130, 385, 386). We speculate that efficient force distribution may enhance adhesion turnover during migration, preventing unrestrained actomyosin activity from inducing aberrant effects within synthetic VSMCs. This is crucial as when VSMC dysfunction occurs, they fail to switch back to the contractile phenotype following repair, and begin to induce pathological vascular remodelling (387-389).

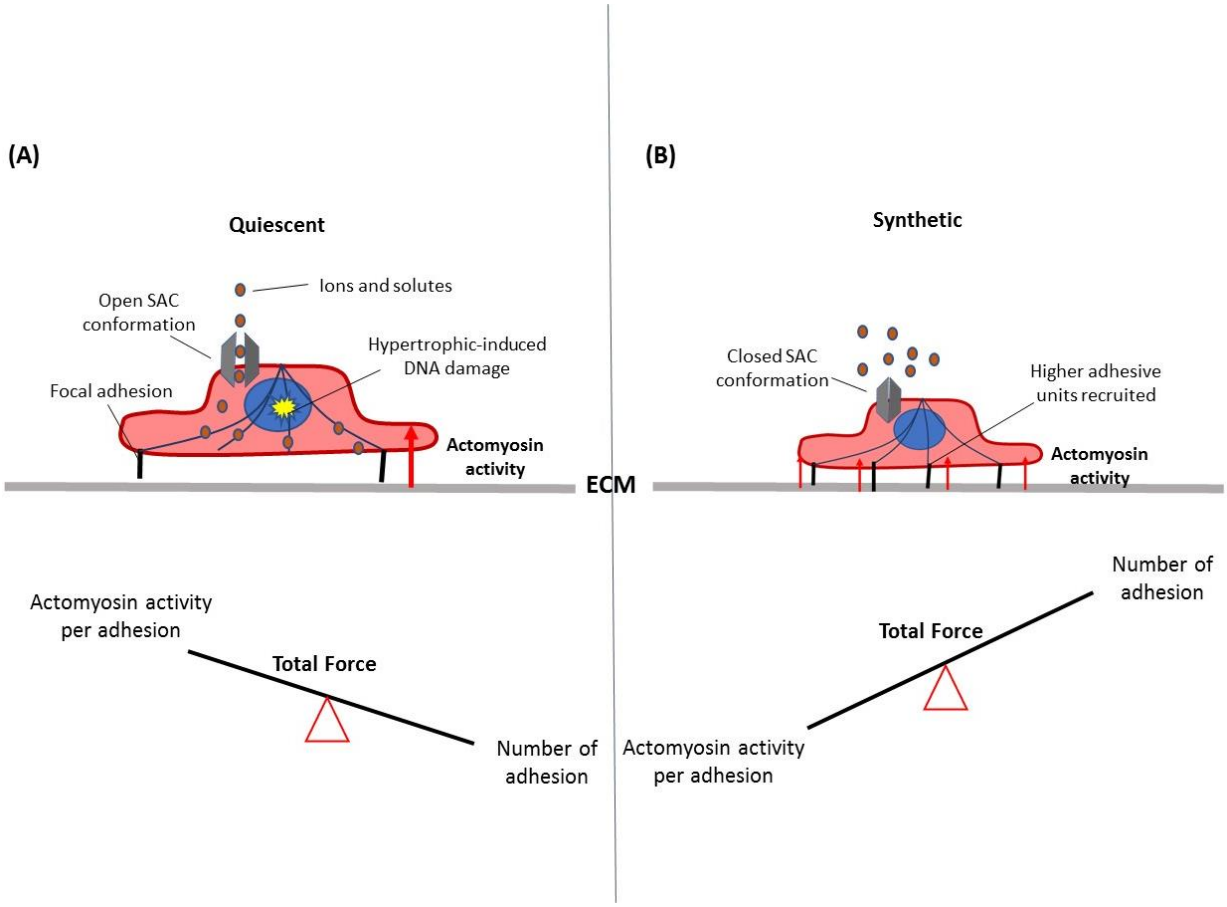

Figure 7.3: Model showing traction force mechanism of both phenotypes in response to matrix stiffness. **(A)** show quiescent VSMC traction force generation. Here, SACs open in response to membrane tension allowing ions within the cell. This causes a swelling of the VSMC, creating mechanical pressure on the nuclei that induces DNA damage. Due to a higher concentration of calcium, the quiescent VSMC is capable of transmitting higher levels of force per individual adhesion molecules. **(B)** shows the mechanism of the synthetic VSMC. In this case, SACs are closed and do not contribute to force generation. Rather, we see a higher recruitment of matrix-adhesion complexes. As a result, the synthetic VSMC can efficiently distribute force to each adhesive unit to maximise transmission to the ECM. ECM: Extracellular matrix; SAC: Stretch-activated channel; VSMC: Vascular smooth muscle cell. Adapted from (390).

7.5 Final conclusions

VSMC contraction works to maintain vessel tone, but also mediates other biological processes such as cell migration, survival and proliferation. Matrix stiffness has emerged as an important biomarker within CVD and our data investigates the actomyosin-induced effects within cellular morphology and mechanosensing, via key proteins including cell-matrix adhesions and SACs. Interestingly, we show an aberrant opening of SACs within quiescent VSMCs as a response to the rigid environment, and how this is implicated in increased cell hypertrophy and force generation. Our work also shows augmented DNA damage as a result of stiffness, and we reveal SAC inhibition to attenuate this. Importantly, we identify novel contractile mechanisms within both phenotypes, and indicate how focal adhesion reorganisation may facilitate transmission of higher forces within synthetic VSMCs. The aberrant changes observed within VSMC structure and function may ultimately drive dysregulated vessel wall remodelling and enable the pathogenesis of multiple age-related vascular diseases. As a result, building on our current understanding on the role of matrix stiffness in VSMC contractile function may highlight novel strategies that will abolish the chronic changes observed within the vessel wall during CVD development.

References

1. Ness AR, Powles JW. Fruit and vegetables, and cardiovascular disease: a review. International Journal of epidemiology. 1997;26(1):1-13.
2. Bhatnagar P, Wickramasinghe K, Wilkins E, Townsend N. Trends in the epidemiology of cardiovascular disease in the UK. Heart. 2016:heartjnl-2016-309573.
3. Stewart J, Manmathan G, Wilkinson P. Primary prevention of cardiovascular disease: A review of contemporary guidance and literature. JRSM cardiovascular disease. 2017;6:2048004016687211.
4. Sun L-y, Lee E-w, Zahra A, Park J-h. Risk Factors of Cardiovascular Disease and Their Related Socio-Economical, Environmental and Health Behavioral Factors: Focused on Low-Middle Income Countries-A Narrative Review Article. Iranian journal of public health. 2015;44(4):435.
5. North BJ, Sinclair DA. The intersection between aging and cardiovascular disease. Circulation research. 2012;110(8):1097-108.
6. Fleg JL, Aronow WS, Frishman WH. Cardiovascular drug therapy in the elderly: benefits and challenges. Nature Reviews Cardiology. 2011;8(1):13.
7. Heidenreich PA, Trogdon JG, Khavjou OA, Butler J, Dracup K, Ezekowitz MD, et al. Forecasting the future of cardiovascular disease in the United States: a policy statement from the American Heart Association. Circulation. 2011;123(8):933-44.
8. Södergren M. Lifestyle predictors of healthy ageing in men. Maturitas. 2015;81(1):117.
9. Papaioannou TG, Protogerou AD, Stergiopulos N, Vardoulis O, Stefanadis C, Safar M, et al. Total arterial compliance estimated by a novel method and all-cause mortality in the elderly: the PROTEGER study. Age. 2014;36(3):1555-63.
10. Ahmed S, Warren DT. Vascular smooth muscle cell contractile function and mechanotransduction. Vessel Plus. 2018;2(11).
11. Cecelja M, Chowienczyk P. Role of arterial stiffness in cardiovascular disease. JRSM cardiovascular disease. 2012;1(4):1-10.
12. Strait JB, Lakatta EG. Aging-associated cardiovascular changes and their relationship to heart failure. Heart failure clinics. 2012;8(1):143-64.
13. LEVY D, ANDERSON KM, SAVAGE DD, KANNEL WB, CHRISTIANSEN JC, Castelli WP. Echocardiographically detected left ventricular hypertrophy: prevalence and risk factors: the Framingham Heart Study. Annals of internal medicine. 1988;108(1):7-13.
14. Palombo C, Kozakova M. Arterial stiffness, atherosclerosis and cardiovascular risk: pathophysiologic mechanisms and emerging clinical indications. Vascular pharmacology. 2016;77:1-7.

15. Mitchell GF. Arterial stiffness and hypertension. Hypertension. 2014;64(1):13-8.
16. Safar ME, Czernichow S, Blacher J. Obesity, arterial stiffness, and cardiovascular risk. Journal of the American Society of Nephrology. 2006;17(4 suppl 2):S109-S11.
17. Mitchell GF, Hwang S-J, Vasan RS, Larson MG, Pencina MJ, Hamburg NM, et al. Arterial stiffness and cardiovascular events: the Framingham Heart Study. Circulation. 2010;121(4):505-11.
18. Ungvari Z, Kaley G, De Cabo R, Sonntag WE, Csiszar A. Mechanisms of vascular aging: new perspectives. Journals of Gerontology Series A: Biomedical Sciences and Medical Sciences. 2010;65(10):1028-41.
19. Cavalcante JL, Lima JA, Redheuil A, Al-Mallah MH. Aortic stiffness: current understanding and future directions. Journal of the American College of Cardiology. 2011;57(14):1511-22.
20. Munakata M. Brachial-ankle pulse wave velocity in the measurement of arterial stiffness: recent evidence and clinical applications. Current hypertension reviews. 2014;10(1):49-57.
21. Steed MM, Tyagi N, Sen U, Schuschke DA, Joshua IG, Tyagi SC. Functional consequences of the collagen/elastin switch in vascular remodeling in hyperhomocysteinemic wild-type, eNOS−/−, and iNOS−/− mice. American Journal of Physiology-Lung Cellular and Molecular Physiology. 2010;299(3):L301-L11.
22. Wagenseil JE, Mecham RP. Vascular extracellular matrix and arterial mechanics. Physiological reviews. 2009;89(3):957-89.
23. Chow M-J, Turcotte R, Lin CP, Zhang Y. Arterial extracellular matrix: a mechanobiological study of the contributions and interactions of elastin and collagen. Biophysical journal. 2014;106(12):2684-92.
24. Bezie Y, Lacolley P, Laurent Sp, Gabella G. Connection of smooth muscle cells to elastic lamellae in aorta of spontaneously hypertensive rats. Hypertension. 1998;32(1):166-9.
25. Koffi I, Lacolley P, Kirchengaast M, Pomiès J-P, Laurent S, Benetos A. Prevention of arterial structural alterations with verapamil and trandolapril and consequences for mechanical properties in spontaneously hypertensive rats. European journal of pharmacology. 1998;361(1):51-60.
26. Koffi I, Safar M, Labat C, Lacolley P, Benetos A, Mourad J. Arterial structural changes with verapamil in spontaneously hypertensive rats. American journal of hypertension. 1999;12(7):732-8.
27. van Gorp AW, Schenau DSVI, Hoeks AP, Boudier HAS, de Mey JG, Reneman RS. In spontaneously hypertensive rats alterations in aortic wall properties precede development

of hypertension. American Journal of Physiology-Heart and Circulatory Physiology. 2000;278(4):H1241-H7.
28. Sehgel NL, Sun Z, Hong Z, Hunter WC, Hill MA, Vatner DE, et al. Augmented vascular smooth muscle cell stiffness and adhesion when hypertension is superimposed on aging. Hypertension. 2015;65(2):370-7.
29. Cox RH. Basis for the altered arterial wall mechanics in the spontaneously hypertensive rat. Hypertension. 1981;3(4):485-95.
30. Mizutani K, Ikeda K, Kawai Y, Yamori Y. Biomechanical properties and chemical composition of the aorta in genetic hypertensive rats. Journal of hypertension. 1999;17(4):481-7.
31. Sehgel NL, Vatner SF, Meininger GA. "Smooth muscle cell stiffness syndrome"—revisiting the structural basis of arterial stiffness. Frontiers in physiology. 2015;6:335.
32. Jufri NF, Mohamedali A, Avolio A, Baker MS. Mechanical stretch: physiological and pathological implications for human vascular endothelial cells. Vascular cell. 2015;7(1):8.
33. Grant CA, Twigg PC. Pseudostatic and dynamic nanomechanics of the tunica adventitia in elastic arteries using atomic force microscopy. ACS nano. 2013;7(1):456-64.
34. Tsamis A, Krawiec JT, Vorp DA. Elastin and collagen fibre microstructure of the human aorta in ageing and disease: a review. Journal of the Royal Society Interface. 2013;10(83):20121004.
35. Haga JH, Li Y-SJ, Chien S. Molecular basis of the effects of mechanical stretch on vascular smooth muscle cells. Journal of biomechanics. 2007;40(5):947-60.
36. Miano JM. Vascular smooth muscle cell differentiation–2010. Journal of biomedical research. 2010;24(3):169-80.
37. Alexander MR, Owens GK. Epigenetic control of smooth muscle cell differentiation and phenotypic switching in vascular development and disease. Annual review of physiology. 2012;74:13-40.
38. Owens GK, editor Molecular control of vascular smooth muscle cell differentiation and phenotypic plasticity. Novartis Foundation symposium; 2007: Wiley Online Library.
39. Fritz K, Jarmolych J, Daoud A. Association of DNA synthesis and apparent dedifferentiation of aortic smooth muscle cells in vitro. Experimental and Molecular Pathology. 1970;12(3):354-62.
40. Manderson JA, Mosse P, Safstrom JA, Young SB, Campbell GR. Balloon catheter injury to rabbit carotid artery. I. Changes in smooth muscle phenotype. Arteriosclerosis: An Official Journal of the American Heart Association, Inc. 1989;9(3):289-98.
41. Campbell GR, Campbell JH. Smooth muscle phenotypic changes in arterial wall homeostasis: implications for the pathogenesis of atherosclerosis. Experimental and molecular pathology. 1985;42(2):139-62.

42. Rensen S, Doevendans P, Van Eys G. Regulation and characteristics of vascular smooth muscle cell phenotypic diversity. Netherlands Heart Journal. 2007;15(3):100-8.
43. Somlyo AP. Myosin isoforms in smooth muscle: how may they affect function and structure? Journal of Muscle Research & Cell Motility. 1993;14(6):557-63.
44. Syamaladevi DP, Spudich JA, Sowdhamini R. Structural and functional insights on the Myosin superfamily. Bioinformatics and biology insights. 2012;6:BBI. S8451.
45. Eddinger TJ, Meer DP. Myosin II isoforms in smooth muscle: heterogeneity and function. American Journal of Physiology-Cell Physiology. 2007;293(2):C493-C508.
46. Löfgren M, Ekblad E, Morano I, Arner A. Nonmuscle myosin motor of smooth muscle. The Journal of general physiology. 2003;121(4):301-10.
47. Peng H, Zhang K, Liu Z, Xu Q, You B, Li C, et al. VPO1 modulates vascular smooth muscle cell phenotypic switch by activating extracellular signal-regulated kinase 1/2 (ERK 1/2) in abdominal aortic aneurysms. Journal of the American Heart Association. 2018;7(17):e010069.
48. Frank ED, Warren L. Aortic smooth muscle cells contain vimentin instead of desmin. Proceedings of the National Academy of Sciences. 1981;78(5):3020-4.
49. Gabbiani G, Schmid E, Winter S, Chaponnier C, De Ckhastonay C, Vandekerckhove J, et al. Vascular smooth muscle cells differ from other smooth muscle cells: predominance of vimentin filaments and a specific alpha-type actin. Proceedings of the National Academy of Sciences. 1981;78(1):298-302.
50. Johansson B, Eriksson A, Virtanen I, Thornell LE. Intermediate filament proteins in adult human arteries. The Anatomical Record: An Official Publication of the American Association of Anatomists. 1997;247(4):439-48.
51. Brouhard GJ, Rice LM. Microtubule dynamics: an interplay of biochemistry and mechanics. Nature reviews Molecular cell biology. 2018;19(7):451-63.
52. Yamin R, Morgan KG. Deciphering actin cytoskeletal function in the contractile vascular smooth muscle cell. The Journal of physiology. 2012;590(17):4145-54.
53. Platts SH, Martinez-Lemus LA, Meininger GA. Microtubule-dependent regulation of vasomotor tone requires Rho-kinase. Journal of vascular research. 2002;39(2):173-82.
54. Ezratty EJ, Partridge MA, Gundersen GG. Microtubule-induced focal adhesion disassembly is mediated by dynamin and focal adhesion kinase. Nature cell biology. 2005;7(6):581-90.
55. Lauffenburger DA, Horwitz AF. Cell migration: a physically integrated molecular process. cell. 1996;84(3):359-69.
56. Dominguez R, Holmes KC. Actin structure and function. 2011.

57. Touré F, Fritz G, Li Q, Rai V, Daffu G, Zou YS, et al. Formin mDia1 mediates vascular remodeling via integration of oxidative and signal transduction pathways. Circulation research. 2012;110(10):1279-93.
58. Weise-Cross L, Taylor JM, Mack CP. Inhibition of diaphanous formin signaling in vivo impairs cardiovascular development and alters smooth muscle cell phenotype. Arteriosclerosis, thrombosis, and vascular biology. 2015;35(11):2374-83.
59. Ning Y, Sun Q, Dong Y, Xu W, Zhang W, Huang H, et al. Slit2-N inhibits PDGF-induced migration in rat airway smooth muscle cells: WASP and Arp2/3 involved. Toxicology. 2011;283(1):32-40.
60. Watanabe N, Higashida C. Formins: processive cappers of growing actin filaments. Experimental cell research. 2004;301(1):16-22.
61. Weaver AM, Young ME, Lee W-L, Cooper JA. Integration of signals to the Arp2/3 complex. Current opinion in cell biology. 2003;15(1):23-30.
62. Campbell G, Campbell J, Manderson J, Horrigan S, Rennick R. Arterial smooth muscle. A multifunctional mesenchymal cell. Archives of pathology & laboratory medicine. 1988;112(10):977-86.
63. Tabas I, García-Cardeña G, Owens GK. Recent insights into the cellular biology of atherosclerosis. Journal of Cell Biology. 2015;209(1):13-22.
64. Gerthoffer WT. Mechanisms of vascular smooth muscle cell migration. Circulation research. 2007;100(5):607-21.
65. Kim HR, Gallant C, Leavis PC, Gunst SJ, Morgan KG. Cytoskeletal remodeling in differentiated vascular smooth muscle is actin isoform dependent and stimulus dependent. American Journal of Physiology-Cell Physiology. 2008;295(3):C768-C78.
66. Fatigati V, Murphy R. Actin and tropomyosin variants in smooth muscles. Dependence on tissue type. Journal of Biological Chemistry. 1984;259(23):14383-8.
67. Gallant C, Appel S, Graceffa P, Leavis P, Lin JJ-C, Gunning PW, et al. Tropomyosin variants describe distinct functional subcellular domains in differentiated vascular smooth muscle cells. American Journal of Physiology-Cell Physiology. 2011;300(6):C1356-C65.
68. Papakonstanti E, Stournaras C. Cell responses regulated by early reorganization of actin cytoskeleton. FEBS letters. 2008;582(14):2120-7.
69. Afewerki T, Ahmed S, Warren D. Emerging regulators of vascular smooth muscle cell migration. Journal of muscle research and cell motility. 2019;40(2):185-96.
70. Joo EE, Yamada KM. MYPT1 regulates contractility and microtubule acetylation to modulate integrin adhesions and matrix assembly. Nature communications. 2014;5(1):1-13.
71. Guilluy C, Osborne LD, Van Landeghem L, Sharek L, Superfine R, Garcia-Mata R, et al. Isolated nuclei adapt to force and reveal a mechanotransduction pathway in the nucleus. Nature cell biology. 2014;16(4):376-81.

72. Woodrum DA, Brophy CM. The paradox of smooth muscle physiology. Molecular and cellular endocrinology. 2001;177(1-2):135-43.
73. Martinsen A, Dessy C, Morel N. Regulation of calcium channels in smooth muscle: New insights into the role of myosin light chain kinase. Channels. 2014;8(5):402-13.
74. Alexander RW, Brock TA, Gimbrone Jr MA, Rittenhouse SE. Angiotensin increases inositol trisphosphate and calcium in vascular smooth muscle. Hypertension. 1985;7(3_pt_1):447-51.
75. Fridlyand LE, Philipson LH. Pancreatic beta cell G-protein coupled receptors and second messenger interactions: a systems biology computational analysis. PloS one. 2016;11(5):e0152869.
76. Inagami T, Eguchi S, Tsuzuki S, Ichiki T. Angiotensin II receptors AT1 and AT2: new mechanisms of signaling and antagonistic effects of AT1 and AT2. Angiotensin II Receptor Blockade Physiological and Clinical Implications: Springer; 1998. p. 129-39.
77. Klee CB, Vanaman TC. Calmodulin. Advances in protein chemistry. 35: Elsevier; 1982. p. 213-321.
78. Adelstein RS, Sellers JR. Effects of calcium on vascular smooth muscle contraction. The American journal of cardiology. 1987;59(3):B4-B10.
79. Lee S, Kumar S. Actomyosin stress fiber mechanosensing in 2D and 3D. F1000Research. 2016;5.
80. Webb RC. Smooth muscle contraction and relaxation. Advances in physiology education. 2003;27(4):201-6.
81. Li Z, Dong X, Wang Z, Liu W, Deng N, Ding Y, et al. Regulation of PTEN by Rho small GTPases. Nature cell biology. 2005;7(4):399-404.
82. Van Aelst L, D'Souza-Schorey C. Rho GTPases and signaling networks. Genes & development. 1997;11(18):2295-322.
83. Fukata Y, Kaibuchi K, Amano M. Rho–Rho-kinase pathway in smooth muscle contraction and cytoskeletal reorganization of non-muscle cells. Trends in pharmacological sciences. 2001;22(1):32-9.
84. Gohla A, Offermanns S, Wilkie TM, Schultz G. Differential involvement of Gα12 and Gα13 in receptor-mediated stress fiber formation. Journal of Biological Chemistry. 1999;274(25):17901-7.
85. Fukuhara S, Chikumi H, Gutkind JS. RGS-containing RhoGEFs: the missing link between transforming G proteins and Rho? Oncogene. 2001;20(13):1661-8.
86. Amano M, Nakayama M, Kaibuchi K. Rho-kinase/ROCK: a key regulator of the cytoskeleton and cell polarity. Cytoskeleton. 2010;67(9):545-54.
87. Loirand G, Guérin P, Pacaud P. Rho kinases in cardiovascular physiology and pathophysiology. Circulation research. 2006;98(3):322-34.

88. Nakagawa O, Fujisawa K, Ishizaki T, Saito Y, Nakao K, Narumiya S. ROCK-I and ROCK-II, two isoforms of Rho-associated coiled-coil forming protein serine/threonine kinase in mice. FEBS letters. 1996;392(2):189-93.
89. Maekawa M, Ishizaki T, Boku S, Watanabe N, Fujita A, Iwamatsu A, et al. Signaling from Rho to the actin cytoskeleton through protein kinases ROCK and LIM-kinase. Science. 1999;285(5429):895-8.
90. Murányi A, Derkach D, Erdődi F, Kiss A, Ito M, Hartshorne DJ. Phosphorylation of Thr695 and Thr850 on the myosin phosphatase target subunit: inhibitory effects and occurrence in A7r5 cells. FEBS letters. 2005;579(29):6611-5.
91. Burute M, Thery M. Spatial segregation between cell–cell and cell–matrix adhesions. Current opinion in cell biology. 2012;24(5):628-36.
92. Sun Z, Parrish AR, Hill MA, Meininger GA. N-cadherin, A Vascular Smooth Muscle Cell–Cell Adhesion Molecule: Function and Signaling for Vasomotor Control. Microcirculation. 2014;21(3):208-18.
93. Lyon CA, Johnson JL, White S, Sala-Newby GB, George SJ. EC4, a truncation of soluble N-cadherin, reduces vascular smooth muscle cell apoptosis and markers of atherosclerotic plaque instability. Molecular Therapy-Methods & Clinical Development. 2014;1:14004.
94. Lyon CA, Wadey KS, George SJ. Soluble N-cadherin: A novel inhibitor of VSMC proliferation and intimal thickening. Vascular pharmacology. 2016;78:53-62.
95. Lodish H, Berk A, Zipursky SL, Matsudaira P, Baltimore D, Darnell J. Cell-cell adhesion and communication. Molecular Cell Biology 4th edition: WH Freeman; 2000.
96. Lyon CA, Koutsouki E, Aguilera CM, Blaschuk OW, George SJ. Inhibition of N-cadherin retards smooth muscle cell migration and intimal thickening via induction of apoptosis. Journal of vascular surgery. 2010;52(5):1301-9.
97. Perez T, Nelson W. Cadherin adhesion: mechanisms and molecular interactions. Cell adhesion: Springer; 2004. p. 3-21.
98. Shapiro L, Weis WI. Structure and biochemistry of cadherins and catenins. Cold Spring Harbor perspectives in biology. 2009;1(3):a003053.
99. Weis WI, Nelson WJ. Re-solving the cadherin-catenin-actin conundrum. Journal of biological chemistry. 2006;281(47):35593-7.
100. Gomez GA, McLachlan RW, Yap AS. Productive tension: force-sensing and homeostasis of cell–cell junctions. Trends in cell biology. 2011;21(9):499-505.
101. Leckband DE, le Duc Q, Wang N, de Rooij J. Mechanotransduction at cadherin-mediated adhesions. Current opinion in cell biology. 2011;23(5):523-30.
102. Yonemura S. Cadherin–actin interactions at adherens junctions. Current opinion in cell biology. 2011;23(5):515-22.

103. Jackson TY, Sun Z, Martinez-Lemus LA, Hill MA, Meininger GA. N-Cadherin and integrin blockade inhibit arteriolar myogenic reactivity but not pressure-induced increases in intracellular Ca2+. Frontiers in physiology. 2010;1:165.
104. Jones M, Sabatini PJ, Lee FS, Bendeck MP, Langille BL. N-cadherin upregulation and function in response of smooth muscle cells to arterial injury. Arteriosclerosis, thrombosis, and vascular biology. 2002;22(12):1972-7.
105. Berrier AL, Yamada KM. Cell–matrix adhesion. Journal of cellular physiology. 2007;213(3):565-73.
106. Bachir AI, Zareno J, Moissoglu K, Plow EF, Gratton E, Horwitz AR. Integrin-associated complexes form hierarchically with variable stoichiometry in nascent adhesions. Current Biology. 2014;24(16):1845-53.
107. Galbraith CG, Yamada KM, Sheetz MP. The relationship between force and focal complex development. The Journal of cell biology. 2002;159(4):695-705.
108. Sun Z, Guo SS, Fässler R. Integrin-mediated mechanotransduction. Journal of Cell Biology. 2016;215(4):445-56.
109. Romer LH, Birukov KG, Garcia JG. Focal adhesions: paradigm for a signaling nexus. Circulation research. 2006;98(5):606-16.
110. Suki B, Parameswaran H, Imsirovic J, Bartolák-Suki E. Regulatory roles of fluctuation-driven mechanotransduction in cell function. Physiology. 2016;31(5):346-58.
111. Chorev DS, Volberg T, Livne A, Eisenstein M, Martins B, Kam Z, et al. Conformational states during vinculin unlocking differentially regulate focal adhesion properties. Scientific reports. 2018;8(1):1-14.
112. Mierke CT. The role of vinculin in the regulation of the mechanical properties of cells. Cell biochemistry and biophysics. 2009;53(3):115-26.
113. Carisey A, Ballestrem C. Vinculin, an adapter protein in control of cell adhesion signalling. European journal of cell biology. 2011;90(2-3):157-63.
114. Wong VW, Rustad KC, Akaishi S, Sorkin M, Glotzbach JP, Januszyk M, et al. Focal adhesion kinase links mechanical force to skin fibrosis via inflammatory signaling. Nature medicine. 2012;18(1):148-52.
115. Calderwood DA, Fujioka Y, de Pereda JM, García-Alvarez B, Nakamoto T, Margolis B, et al. Integrin β cytoplasmic domain interactions with phosphotyrosine-binding domains: a structural prototype for diversity in integrin signaling. Proceedings of the National Academy of Sciences. 2003;100(5):2272-7.
116. Geiger B, Bershadsky A, Pankov R, Yamada KM. Transmembrane crosstalk between the extracellular matrix and the cytoskeleton. Nature reviews Molecular cell biology. 2001;2(11):793-805.

117. Bouzid T, Kim E, Riehl BD, Esfahani AM, Rosenbohm J, Yang R, et al. The LINC complex, mechanotransduction, and mesenchymal stem cell function and fate. Journal of Biological Engineering. 2019;13(1):1-12.
118. Crisp M, Liu Q, Roux K, Rattner J, Shanahan C, Burke B, et al. Coupling of the nucleus and cytoplasm: role of the LINC complex. The Journal of cell biology. 2006;172(1):41-53.
119. Haque F, Lloyd DJ, Smallwood DT, Dent CL, Shanahan CM, Fry AM, et al. SUN1 interacts with nuclear lamin A and cytoplasmic nesprins to provide a physical connection between the nuclear lamina and the cytoskeleton. Molecular and cellular biology. 2006;26(10):3738-51.
120. Warren DT, Zhang Q, Weissberg PL, Shanahan CM. Nesprins: intracellular scaffolds that maintain cell architecture and coordinate cell function? Expert reviews in molecular medicine. 2005;7(11):1-15.
121. Burke B, Ellenberg J. Remodelling the walls of the nucleus. Nature reviews molecular cell biology. 2002;3(7):487-97.
122. Porter LJ, Holt MR, Soong D, Shanahan CM, Warren DT. Prelamin A accumulation attenuates Rac1 activity and increases the intrinsic migrational persistence of aged vascular smooth muscle cells. Cells. 2016;5(4):41.
123. Schwartz C, Fischer M, Mamchaoui K, Bigot A, Lok T, Verdier C, et al. Lamins and nesprin-1 mediate inside-out mechanical coupling in muscle cell precursors through FHOD1. Scientific reports. 2017;7(1):1-14.
124. Chancellor T, Lee J, Thodeti CK, Lele T. Actomyosin tension exerted on the nucleus through nesprin-1 connections influences endothelial cell adhesion, migration, and cyclic strain-induced reorientation. Biophysical journal. 2010;99(1):115-23.
125. Thakar K, May CK, Rogers A, Carroll CW. Opposing roles for distinct LINC complexes in regulation of the small GTPase RhoA. Molecular biology of the cell. 2017;28(1):182-91.
126. Trache A, Massett MP, Woodman CR. Vascular smooth muscle stiffness and its role in aging. 2020.
127. Ross R, Glomset JA. Atherosclerosis and the arterial smooth muscle cell. Science. 1973;180(4093):1332-9.
128. Swift J, Ivanovska IL, Buxboim A, Harada T, Dingal PDP, Pinter J, et al. Nuclear lamin-A scales with tissue stiffness and enhances matrix-directed differentiation. Science. 2013;341(6149).
129. Yang Y-l, Leone LM, Kaufman LJ. Elastic moduli of collagen gels can be predicted from two-dimensional confocal microscopy. Biophysical journal. 2009;97(7):2051-60.

130. Bacakova L, Travnickova M, Filova E, Matějka R, Stepanovska J, Musilkova J, et al. The role of vascular smooth muscle cells in the physiology and pathophysiology of blood vessels. Muscle Cell Tissue Curr Status Res Field. 2018;229.
131. Harada T, Swift J, Irianto J, Shin J-W, Spinler KR, Athirasala A, et al. Nuclear lamin stiffness is a barrier to 3D migration, but softness can limit survival. Journal of Cell Biology. 2014;204(5):669-82.
132. Pfeifer CR, Alvey CM, Irianto J, Discher DE. Genome variation across cancers scales with tissue stiffness–An invasion-mutation mechanism and implications for immune cell infiltration. Current opinion in systems biology. 2017;2:103-14.
133. Tamiello C, Kamps MA, van den Wijngaard A, Verstraeten VL, Baaijens FP, Broers JL, et al. Soft substrates normalize nuclear morphology and prevent nuclear rupture in fibroblasts from a laminopathy patient with compound heterozygous LMNA mutations. Nucleus. 2013;4(1):61-73.
134. Xia Y, Ivanovska IL, Zhu K, Smith L, Irianto J, Pfeifer CR, et al. Nuclear rupture at sites of high curvature compromises retention of DNA repair factors. Journal of Cell Biology. 2018;217(11):3796-808.
135. Chi C, Li D-J, Jiang Y-J, Tong J, Fu H, Wu Y-H, et al. Vascular smooth muscle cell senescence and age-related diseases: State of the art. Biochimica et Biophysica Acta (BBA)-Molecular Basis of Disease. 2019;1865(7):1810-21.
136. Bennett MR, Evan GI, Schwartz SM. Apoptosis of human vascular smooth muscle cells derived from normal vessels and coronary atherosclerotic plaques. The Journal of clinical investigation. 1995;95(5):2266-74.
137. O'brien E, Alpers C, Stewart D, Ferguson M, Tran N, Gordon D, et al. Proliferation in primary and restenotic coronary atherectomy tissue. Implications for antiproliferative therapy. Circulation Research. 1993;73(2):223-31.
138. Gray K, Kumar S, Figg N, Harrison J, Baker L, Mercer J, et al. Effects of DNA damage in smooth muscle cells in atherosclerosis. Circulation research. 2015;116(5):816-26.
139. Herraiz C, Calvo F, Pandya P, Cantelli G, Rodriguez-Hernandez I, Orgaz JL, et al. Reactivation of p53 by a cytoskeletal sensor to control the balance between DNA damage and tumor dissemination. JNCI: Journal of the National Cancer Institute. 2016;108(1).
140. Takaki T, Montagner M, Serres MP, Le Berre M, Russell M, Collinson L, et al. Actomyosin drives cancer cell nuclear dysmorphia and threatens genome stability. Nature communications. 2017;8(1):1-13.
141. Shanahan CM. Mechanisms of vascular calcification in CKD—evidence for premature ageing? Nature Reviews Nephrology. 2013;9(11):661.

142. Sazonova OV, Isenberg BC, Herrmann J, Lee KL, Purwada A, Valentine AD, et al. Extracellular matrix presentation modulates vascular smooth muscle cell mechanotransduction. Matrix Biology. 2015;41:36-43.
143. Tang DD, Bai Y, Gunst SJ. Silencing of p21-activated kinase attenuates vimentin phosphorylation on Ser-56 and reorientation of the vimentin network during stimulation of smooth muscle cells by 5-hydroxytryptamine. Biochemical Journal. 2005;388(3):773-83.
144. Li J, Wang R, Gannon OJ, Rezey AC, Jiang S, Gerlach BD, et al. Polo-like kinase 1 regulates vimentin phosphorylation at Ser-56 and contraction in smooth muscle. Journal of Biological Chemistry. 2016;291(45):23693-703.
145. Kong R, Zhang L, Hu L, Peng Q, Han W, Du X, et al. hALP, a novel transcriptional U three protein (t-UTP), activates RNA polymerase I transcription by binding and acetylating the upstream binding factor (UBF). Journal of Biological Chemistry. 2011;286(9):7139-48.
146. Shen Q, Zheng X, McNutt MA, Guang L, Sun Y, Wang J, et al. NAT10, a nucleolar protein, localizes to the midbody and regulates cytokinesis and acetylation of microtubules. Experimental cell research. 2009;315(10):1653-67.
147. Fu D, Collins K. Purification of human telomerase complexes identifies factors involved in telomerase biogenesis and telomere length regulation. Molecular cell. 2007;28(5):773-85.
148. Chi Y-H, Haller K, Peloponese Jr J-M, Jeang K-T. Histone acetyltransferase hALP and nuclear membrane protein hsSUN1 function in de-condensation of mitotic chromosomes. Journal of Biological Chemistry. 2007;282(37):27447-58.
149. Li Q, Liu X, Jin K, Lu M, Zhang C, Du X, et al. NAT10 is upregulated in hepatocellular carcinoma and enhances mutant p53 activity. BMc cancer. 2017;17(1):1-10.
150. Larrieu D, Britton S, Demir M, Rodriguez R, Jackson SP. Chemical inhibition of NAT10 corrects defects of laminopathic cells. Science. 2014;344(6183):527-32.
151. Cobb AM, Larrieu D, Warren DT, Liu Y, Srivastava S, Smith AJ, et al. Prelamin A impairs 53 BP 1 nuclear entry by mislocalizing NUP 153 and disrupting the Ran gradient. Aging cell. 2016;15(6):1039-50.
152. Li Q-F, Spinelli AM, Wang R, Anfinogenova Y, Singer HA, Tang DD. Critical role of vimentin phosphorylation at Ser-56 by p21-activated kinase in vimentin cytoskeleton signaling. Journal of Biological Chemistry. 2006;281(45):34716-24.
153. Wang R, Li Q-F, Anfinogenova Y, Tang DD. Dissociation of Crk-associated substrate from the vimentin network is regulated by p21-activated kinase on ACh activation of airway smooth muscle. American Journal of Physiology-Lung Cellular and Molecular Physiology. 2007;292(1):L240-L8.

154. Jia L, Tang DD. Abl activation regulates the dissociation of CAS from cytoskeletal vimentin by modulating CAS phosphorylation in smooth muscle. American Journal of Physiology-Cell Physiology. 2010;299(3):C630-C7.
155. Li J, Wang R, Tang DD. Vimentin dephosphorylation at ser-56 is regulated by type 1 protein phosphatase in smooth muscle. Respiratory research. 2016;17(1):1-11.
156. Guo D, Song X, Guo T, Gu S, Chang X, Su T, et al. Vimentin acetylation is involved in SIRT5-mediated hepatocellular carcinoma migration. American journal of cancer research. 2018;8(12):2453.
157. Wu J, Zhu H, Wu J, Chen W, Guan X. Inhibition of N-acetyltransferase 10 using remodelin attenuates doxorubicin resistance by reversing the epithelial-mesenchymal transition in breast cancer. American journal of translational research. 2018;10(1):256.
158. Slatkin M. Epigenetic inheritance and the missing heritability problem. Genetics. 2009;182(3):845-50.
159. Manolio TA, Collins FS, Cox NJ, Goldstein DB, Hindorff LA, Hunter DJ, et al. Finding the missing heritability of complex diseases. Nature. 2009;461(7265):747-53.
160. Handy DE, Castro R, Loscalzo J. Epigenetic modifications: basic mechanisms and role in cardiovascular disease. Circulation. 2011;123(19):2145-56.
161. Kouzarides T. Chromatin modifications and their function. Cell. 2007;128(4):693-705.
162. Martin C, Zhang Y. The diverse functions of histone lysine methylation. Nature reviews Molecular cell biology. 2005;6(11):838-49.
163. Nan X, Ng H-H, Johnson CA, Laherty CD, Turner BM, Eisenman RN, et al. Transcriptional repression by the methyl-CpG-binding protein MeCP2 involves a histone deacetylase complex. Nature. 1998;393(6683):386-9.
164. Wade PA, Gegonne A, Jones PL, Ballestar E, Aubry F, Wolffe AP. Mi-2 complex couples DNA methylation to chromatin remodelling and histone deacetylation. Nature genetics. 1999;23(1):62-6.
165. McDonald OG, Wamhoff BR, Hoofnagle MH, Owens GK. Control of SRF binding to CArG box chromatin regulates smooth muscle gene expression in vivo. The Journal of clinical investigation. 2006;116(1):36-48.
166. Campbell G, Campbell J. The Phenotypes of Smooth Muscle Expressed in Human Atheroma a. Annals of the New York Academy of Sciences. 1990;598(1):143-58.
167. Uryga AK, Bennett MR. Ageing induced vascular smooth muscle cell senescence in atherosclerosis. The Journal of physiology. 2016;594(8):2115-24.
168. Sahar S, Reddy MA, Wong C, Meng L, Wang M, Natarajan R. Cooperation of SRC-1 and p300 with NF-κB and CREB in angiotensin II-induced IL-6 expression in vascular smooth muscle cells. Arteriosclerosis, thrombosis, and vascular biology. 2007;27(7):1528-34.

169. Damodaran K, Venkatachalapathy S, Alisafaei F, Radhakrishnan A, Sharma Jokhun D, Shenoy VB, et al. Compressive force induces reversible chromatin condensation and cell geometry–dependent transcriptional response. Molecular biology of the cell. 2018;29(25):3039-51.
170. Martino F, Perestrelo AR, Vinarský V, Pagliari S, Forte G. Cellular mechanotransduction: from tension to function. Frontiers in physiology. 2018;9:824.
171. Alonso JL, Goldmann WH. Cellular mechanotransduction. transport. 2016;1(7).
172. Martinac B. The ion channels to cytoskeleton connection as potential mechanism of mechanosensitivity. Biochimica et Biophysica Acta (BBA)-Biomembranes. 2014;1838(2):682-91.
173. Wrighton KH. Cell adhesion: the'ins' and'outs' of integrin signalling. Nature Reviews Molecular Cell Biology. 2013;14(12):752.
174. Ye GJ, Nesmith AP, Parker KK. The role of mechanotransduction on vascular smooth muscle myocytes cytoskeleton and contractile function. The Anatomical Record. 2014;297(9):1758-69.
175. Anwar M, Shalhoub J, Lim C, Gohel M, Davies A. The effect of pressure-induced mechanical stretch on vascular wall differential gene expression. Journal of vascular research. 2012;49(6):463-78.
176. Ducret T, El Arrouchi J, Courtois A, Quignard J-F, Marthan R, Savineau J-P. Stretch-activated channels in pulmonary arterial smooth muscle cells from normoxic and chronically hypoxic rats. Cell calcium. 2010;48(5):251-9.
177. Zou H, Lifshitz LM, Tuft RA, Fogarty KE, Singer JJ. Visualization of Ca2+ entry through single stretch-activated cation channels. Proceedings of the National Academy of Sciences. 2002;99(9):6404-9.
178. Schubert R, Brayden JE. Stretch-activated cation channels and the myogenic response of small arteries. Mechanosensitivity in Cells and Tissues: Academia; 2005.
179. Nilius B, Szallasi A. Transient receptor potential channels as drug targets: from the science of basic research to the art of medicine. Pharmacological reviews. 2014;66(3):676-814.
180. Earley S, Brayden JE. Transient receptor potential channels in the vasculature. Physiological reviews. 2015;95(2):645-90.
181. Bulley S, Fernández-Peña C, Hasan R, Leo MD, Muralidharan P, Mackay CE, et al. Arterial smooth muscle cell PKD2 (TRPP1) channels regulate systemic blood pressure. ELife. 2018;7:e42628.
182. Narayanan D, Bulley S, Leo MD, Burris SK, Gabrick KS, Boop FA, et al. Smooth muscle cell transient receptor potential polycystin-2 (TRPP2) channels contribute to the myogenic response in cerebral arteries. The Journal of physiology. 2013;591(20):5031-46.

183. Welsh DG, Morielli AD, Nelson MT, Brayden JE. Transient receptor potential channels regulate myogenic tone of resistance arteries. Circulation research. 2002;90(3):248-50.
184. Nishioka K, Nishida M, Ariyoshi M, Jian Z, Saiki S, Hirano M, et al. Cilostazol suppresses angiotensin II–induced vasoconstriction via protein kinase A–mediated phosphorylation of the transient receptor potential canonical 6 channel. Arteriosclerosis, thrombosis, and vascular biology. 2011;31(10):2278-86.
185. Zhao Q, Wu K, Geng J, Chi S, Wang Y, Zhi P, et al. Ion permeation and mechanotransduction mechanisms of mechanosensitive piezo channels. Neuron. 2016;89(6):1248-63.
186. Coste B, Mathur J, Schmidt M, Earley TJ, Ranade S, Petrus MJ, et al. Piezo1 and Piezo2 are essential components of distinct mechanically activated cation channels. Science. 2010;330(6000):55-60.
187. Li J, Hou B, Tumova S, Muraki K, Bruns A, Ludlow MJ, et al. Piezo1 integration of vascular architecture with physiological force. Nature. 2014;515(7526):279-82.
188. Ranade SS, Qiu Z, Woo S-H, Hur SS, Murthy SE, Cahalan SM, et al. Piezo1, a mechanically activated ion channel, is required for vascular development in mice. Proceedings of the National Academy of Sciences. 2014;111(28):10347-52.
189. Retailleau K, Duprat F, Arhatte M, Ranade SS, Peyronnet R, Martins JR, et al. Piezo1 in smooth muscle cells is involved in hypertension-dependent arterial remodeling. Cell reports. 2015;13(6):1161-71.
190. Bennett MR, Sinha S, Owens GK. Vascular smooth muscle cells in atherosclerosis. Circulation research. 2016;118(4):692-702.
191. Kher N, Marsh JD. Pathobiology of atherosclerosis. Semin Thromb Hemost. 2004;30:665-72.
192. Tracqui P, Broisat A, Toczek J, Mesnier N, Ohayon J, Riou L. Mapping elasticity moduli of atherosclerotic plaque in situ via atomic force microscopy. Journal of structural biology. 2011;174(1):115-23.
193. Isenberg BC, DiMilla PA, Walker M, Kim S, Wong JY. Vascular smooth muscle cell durotaxis depends on substrate stiffness gradient strength. Biophysical journal. 2009;97(5):1313-22.
194. Hartman CD, Isenberg BC, Chua SG, Wong JY. Vascular smooth muscle cell durotaxis depends on extracellular matrix composition. Proceedings of the National Academy of Sciences. 2016;113(40):11190-5.
195. Timraz SB, Rezgui R, Boularaoui SM, Teo JC. Stiffness of extracellular matrix components modulates the phenotype of human smooth muscle cells in vitro and allows for the control of properties of engineered tissues. Procedia Eng. 2015;110:29-36.

196. Chaterji S, Kim P, Choe SH, Tsui JH, Lam CH, Ho DS, et al. Synergistic effects of matrix nanotopography and stiffness on vascular smooth muscle cell function. Tissue Engineering Part A. 2014;20(15-16):2115-26.
197. Hytönen VP, Wehrle-Haller B. Mechanosensing in cell–matrix adhesions–Converting tension into chemical signals. Experimental cell research. 2016;343(1):35-41.
198. Qiu H, Zhu Y, Sun Z, Trzeciakowski JP, Gansner M, Depre C, et al. Vascular smooth muscle cell stiffness as a mechanism for increased aortic stiffness with agingnovelty and significance. Circulation research. 2010;107(5):615-9.
199. McDaniel DP, Shaw GA, Elliott JT, Bhadriraju K, Meuse C, Chung K-H, et al. The stiffness of collagen fibrils influences vascular smooth muscle cell phenotype. Biophysical journal. 2007;92(5):1759-69.
200. Seawright JW, Sreenivasappa H, Gibbs HC, Padgham S, Shin SY, Chaponnier C, et al. Vascular smooth muscle contractile function declines with age in skeletal muscle feed arteries. Frontiers in physiology. 2018;9:856.
201. Kohn JC, Lampi MC, Reinhart-King CA. Age-related vascular stiffening: causes and consequences. Frontiers in genetics. 2015;6:112.
202. Minaisah R-M, Cox S, Warren DT. The use of polyacrylamide hydrogels to study the effects of matrix stiffness on nuclear envelope properties. The Nuclear Envelope: Springer; 2016. p. 233-9.
203. Tse JR, Engler AJ. Preparation of hydrogel substrates with tunable mechanical properties. Current protocols in cell biology. 2010;47(1):10.6. 1-.6. 6.
204. Bretschneider F, De Weille JR. Introduction to electrophysiological methods and instrumentation: Academic Press; 2018.
205. van Popele NM, Mattace-Raso FU, Vliegenthart R, Grobbee DE, Asmar R, van der Kuip DA, et al. Aortic stiffness is associated with atherosclerosis of the coronary arteries in older adults: the Rotterdam Study. Journal of hypertension. 2006;24(12):2371-6.
206. Gauthier-Bastien A, Ung R-V, Larivière R, Mac-Way F, Lebel M, Agharazii M. Vascular remodeling and media calcification increases arterial stiffness in chronic kidney disease. Clinical and Experimental Hypertension. 2014;36(3):173-80.
207. Porter L, Minaisah R-M, Ahmed S, Ali S, Norton R, Zhang Q, et al. SUN1/2 Are Essential for RhoA/ROCK-Regulated Actomyosin Activity in Isolated Vascular Smooth Muscle Cells. Cells. 2020;9(1):132.
208. Galmiche G, Labat C, Mericskay M, Aissa KA, Blanc J, Retailleau K, et al. Inactivation of serum response factor contributes to decrease vascular muscular tone and arterial stiffness in mice. Circulation research. 2013;112(7):1035-45.
209. Ehrlicher AJ, Nakamura F, Hartwig J, Weitz D, Stossel T. Mechanical strain in actin networks regulates FilGAP and integrin binding to filamin A. Nature. 2011;478(7368):260-3.

210. Friedland JC, Lee MH, Boettiger D. Mechanically activated integrin switch controls α5β1 function. Science. 2009;323(5914):642-4.
211. Wang Y-K, Wang Y-H, Wang C-Z, Sung J-M, Chiu W-T, Lin S-H, et al. Rigidity of collagen fibrils controls collagen gel-induced down-regulation of focal adhesion complex proteins mediated by α2β1 integrin. Journal of Biological Chemistry. 2003;278(24):21886-92.
212. Wei W-C, Lin H-H, Shen M-R, Tang M-J. Mechanosensing machinery for cells under low substratum rigidity. American Journal of Physiology-Cell Physiology. 2008;295(6):C1579-C89.
213. Lo C-M, Wang H-B, Dembo M, Wang Y-l. Cell movement is guided by the rigidity of the substrate. Biophysical journal. 2000;79(1):144-52.
214. Sun M, Chi G, Li P, Lv S, Xu J, Xu Z, et al. Effects of matrix stiffness on the morphology, adhesion, proliferation and osteogenic differentiation of mesenchymal stem cells. International journal of medical sciences. 2018;15(3):257.
215. Yeh Y-C, Ling J-Y, Chen W-C, Lin H-H, Tang M-J. Mechanotransduction of matrix stiffness in regulation of focal adhesion size and number: reciprocal regulation of caveolin-1 and β1 integrin. Scientific reports. 2017;7(1):1-14.
216. Gupta M, Sarangi BR, Deschamps J, Nematbakhsh Y, Callan-Jones A, Margadant F, et al. Adaptive rheology and ordering of cell cytoskeleton govern matrix rigidity sensing. Nature communications. 2015;6(1):1-9.
217. Ragnauth CD, Warren DT, Liu Y, McNair R, Tajsic T, Figg N, et al. CLINICAL PERSPECTIVE. Circulation. 2010;121(20):2200-10.
218. Kraning-Rush CM, Califano JP, Reinhart-King CA. Cellular traction stresses increase with increasing metastatic potential. PloS one. 2012;7(2).
219. Califano JP, Reinhart-King CA. Substrate stiffness and cell area predict cellular traction stresses in single cells and cells in contact. Cellular and molecular bioengineering. 2010;3(1):68-75.
220. Han SJ, Bielawski KS, Ting LH, Rodriguez ML, Sniadecki NJ. Decoupling substrate stiffness, spread area, and micropost density: a close spatial relationship between traction forces and focal adhesions. Biophysical journal. 2012;103(4):640-8.
221. Amano M, Chihara K, Kimura K, Fukata Y, Nakamura N, Matsuura Y, et al. Formation of actin stress fibers and focal adhesions enhanced by Rho-kinase. Science. 1997;275(5304):1308-11.
222. Raoul A, Mgrditchian T, Regnault V, Lacolley P. Role of focal adhesions of vascular smooth muscle cells in thrombin generation. Archives of Cardiovascular Diseases Supplements. 2020;12(1):145.

223. Shemesh T, Geiger B, Bershadsky AD, Kozlov MM. Focal adhesions as mechanosensors: a physical mechanism. Proceedings of the National Academy of Sciences. 2005;102(35):12383-8.
224. Moiseeva EP. Adhesion receptors of vascular smooth muscle cells and their functions. Cardiovascular research. 2001;52(3):372-86.
225. Yeung T, Georges PC, Flanagan LA, Marg B, Ortiz M, Funaki M, et al. Effects of substrate stiffness on cell morphology, cytoskeletal structure, and adhesion. Cell motility and the cytoskeleton. 2005;60(1):24-34.
226. Gorenne I, Kavurma M, Scott S, Bennett M. Vascular smooth muscle cell senescence in atherosclerosis. Cardiovascular research. 2006;72(1):9-17.
227. Hall A. Rho GTPases and the actin cytoskeleton. Science. 1998;279(5350):509-14.
228. Mayanagi T, Sobue K. Diversification of caldesmon-linked actin cytoskeleton in cell motility. Cell adhesion & migration. 2011;5(2):150-9.
229. Fletcher DA, Mullins RD. Cell mechanics and the cytoskeleton. Nature. 2010;463(7280):485-92.
230. Engler A, Bacakova L, Newman C, Hategan A, Griffin M, Discher D. Substrate compliance versus ligand density in cell on gel responses. Biophysical journal. 2004;86(1):617-28.
231. Ghosh K, Pan Z, Guan E, Ge S, Liu Y, Nakamura T, et al. Cell adaptation to a physiologically relevant ECM mimic with different viscoelastic properties. Biomaterials. 2007;28(4):671-9.
232. Choi CK, Vicente-Manzanares M, Zareno J, Whitmore LA, Mogilner A, Horwitz AR. Actin and α-actinin orchestrate the assembly and maturation of nascent adhesions in a myosin II motor-independent manner. Nature cell biology. 2008;10(9):1039-50.
233. Wang N, Tytell JD, Ingber DE. Mechanotransduction at a distance: mechanically coupling the extracellular matrix with the nucleus. Nature reviews Molecular cell biology. 2009;10(1):75-82.
234. Buxboim A, Swift J, Irianto J, Spinler KR, Dingal PDP, Athirasala A, et al. Matrix elasticity regulates lamin-A, C phosphorylation and turnover with feedback to actomyosin. Current Biology. 2014;24(16):1909-17.
235. Vicente-Manzanares M, Ma X, Adelstein RS, Horwitz AR. Non-muscle myosin II takes centre stage in cell adhesion and migration. Nature reviews Molecular cell biology. 2009;10(11):778-90.
236. Polte TR, Eichler GS, Wang N, Ingber DE. Extracellular matrix controls myosin light chain phosphorylation and cell contractility through modulation of cell shape and cytoskeletal prestress. American Journal of Physiology-Cell Physiology. 2004;286(3):C518-C28.

237. Wells RG. The role of matrix stiffness in regulating cell behavior. Hepatology. 2008;47(4):1394-400.
238. Sazonova OV, Lee KL, Isenberg BC, Rich CB, Nugent MA, Wong JY. Cell-cell interactions mediate the response of vascular smooth muscle cells to substrate stiffness. Biophysical journal. 2011;101(3):622-30.
239. Gallant ND, García AJ. Quantitative analyses of cell adhesion strength. Adhesion protein protocols: Springer; 2007. p. 83-95.
240. Thyberg J, Blomgren K, Roy J, Tran PK, Hedin U. Phenotypic modulation of smooth muscle cells after arterial injury is associated with changes in the distribution of laminin and fibronectin. Journal of Histochemistry & Cytochemistry. 1997;45(6):837-46.
241. Thyberg J, Blomgren K, Hedin U, Dryjski M. Phenotypic modulation of smooth muscle cells during the formation of neointimal thickenings in the rat carotid artery after balloon injury: an electron-microscopic and stereological study. Cell and tissue research. 1995;281(3):421-33.
242. Shi N, Chen SY. Smooth muscle cell differentiation: model systems, regulatory mechanisms, and vascular diseases. Journal of cellular physiology. 2016;231(4):777-87.
243. Eddinger TJ, Meer DP, Miner AS, Meehl J, Rovner AS, Ratz PH. Potent inhibition of arterial smooth muscle tonic contractions by the selective myosin II inhibitor, blebbistatin. Journal of Pharmacology and Experimental Therapeutics. 2007;320(2):865-70.
244. Rhee AY, Ogut O, Brozovich FV. Nonmuscle myosin, force maintenance, and the tonic contractile phenotype in smooth muscle. Pflügers Archiv. 2006;452(6):766-74.
245. Gaudet C, Marganski WA, Kim S, Brown CT, Gunderia V, Dembo M, et al. Influence of type I collagen surface density on fibroblast spreading, motility, and contractility. Biophysical journal. 2003;85(5):3329-35.
246. Zhang Y, Ng SS, Wang Y, Feng H, Chen WN, Chan-Park MB, et al. Collective cell traction force analysis on aligned smooth muscle cell sheet between three-dimensional microwalls. Interface focus. 2014;4(2):20130056.
247. Müller C, Pompe T. Distinct impacts of substrate elasticity and ligand affinity on traction force evolution. Soft matter. 2016;12(1):272-80.
248. Baker BM, Chen CS. Deconstructing the third dimension–how 3D culture microenvironments alter cellular cues. Journal of cell science. 2012;125(13):3015-24.
249. Bonnier F, Keating M, Wrobel TP, Majzner K, Baranska M, Garcia-Munoz A, et al. Cell viability assessment using the Alamar blue assay: a comparison of 2D and 3D cell culture models. Toxicology in vitro. 2015;29(1):124-31.
250. Gauvin R, Chen Y-C, Lee JW, Soman P, Zorlutuna P, Nichol JW, et al. Microfabrication of complex porous tissue engineering scaffolds using 3D projection stereolithography. Biomaterials. 2012;33(15):3824-34.

251. Del Álamo JC, Meili R, Álvarez-González B, Alonso-Latorre B, Bastounis E, Firtel R, et al. Three-dimensional quantification of cellular traction forces and mechanosensing of thin substrata by fourier traction force microscopy. PloS one. 2013;8(9).
252. Brozovich F, Nicholson C, Degen C, Gao YZ, Aggarwal M, Morgan KG. Mechanisms of vascular smooth muscle contraction and the basis for pharmacologic treatment of smooth muscle disorders. Pharmacological reviews. 2016;68(2):476-532.
253. Halka AT, Turner NJ, Carter A, Ghosh J, Murphy MO, Kirton JP, et al. The effects of stretch on vascular smooth muscle cell phenotype in vitro. Cardiovascular Pathology. 2008;17(2):98-102.
254. Poliseno L, Cecchettini A, Mariani L, Evangelista M, Ricci F, Giorgi F, et al. Resting smooth muscle cells as a model for studying vascular cell activation. Tissue and Cell. 2006;38(2):111-20.
255. Han M, Wen J-K, Zheng B, Cheng Y, Zhang C. Serum deprivation results in redifferentiation of human umbilical vascular smooth muscle cells. American Journal of Physiology-Cell Physiology. 2006;291(1):C50-C8.
256. Kato M, Kyogoku M. Competence growth factors evoke the phenotypic transition of arterial smooth muscle cells. Annals of the New York Academy of Sciences. 1990;598:232-7.
257. Patel MK, Clunn GF, Lymn JS, Austin O, Hughes AD. Effect of serum withdrawal on the contribution of L-type calcium channels (CaV1. 2) to intracellular Ca2+ responses and chemotaxis in cultured human vascular smooth muscle cells. British journal of pharmacology. 2005;145(6):811-7.
258. Elliott D, Peart W. Amino-acid sequence in a hypertensin. Nature. 1956;177(4507):527-8.
259. Campbell-Boswell M, Robertson Jr AL. Effects of angiotensin II and vasopressin on human smooth muscle cells in vitro. Experimental and molecular pathology. 1981;35(2):265-76.
260. Geisterfer A, Peach MJ, Owens GK. Angiotensin II induces hypertrophy, not hyperplasia, of cultured rat aortic smooth muscle cells. Circulation research. 1988;62(4):749-56.
261. Berk BC, Vekshtein V, Gordon HM, Tsuda T. Angiotensin II-stimulated protein synthesis in cultured vascular smooth muscle cells. Hypertension. 1989;13(4):305-14.
262. Kato H, Suzuki H, Tajima S, Ogata Y, Tominaga T, Sato A, et al. Angiotensin II stimulates collagen synthesis in cultured vascular smooth muscle cells. Journal of hypertension. 1991;9(1):17-22.
263. Kim JS, Lee G-J, Lee TW, Ihm CG, Lee YH, Kim YG, et al. Observations of the Effects of Angiotensin II Receptor Blocker on Angiotensin II-Induced Morphological and

Mechanical Changes in Renal Tubular Epithelial Cells Using Atomic Force Microscopy. BioMed research international. 2018;2018.
264. Xu T, Zhu H, Li D, Lang Y, Cao L, Liu Y, et al. Luteolin inhibits angiotensin II-stimulated VSMC proliferation and migration through downregulation of Akt phosphorylation. Evidence-Based Complementary and Alternative Medicine. 2015;2015.
265. Cantwell H, Nurse P. Unravelling nuclear size control. Current genetics. 2019:1-5.
266. von Schrenck T, Mackensen B, Mende U, Schmit W, Sievers J, Mirau S, et al. Signal transduction pathway of the muscarinic receptors mediating gallbladder contraction. Naunyn-Schmiedeberg's Archives of Pharmacology. 1994;349(4):346-54.
267. Thompson AM, Martin KA, Rzucidlo EM. Resveratrol induces vascular smooth muscle cell differentiation through stimulation of SirT1 and AMPK. PloS one. 2014;9(1):e85495.
268. Herbert J-M, Delisée C, Dol F, Schaeffer P, Cazaubon C, Nisato D, et al. Effect of SR 47436, a novel angiotensin II AT1 receptor antagonist, on human vascular smooth muscle cells in vitro. European journal of pharmacology. 1994;251(2-3):143-50.
269. Hoffmann M, Chen X, Hirano M, Arimitsu K, Kimura H, Higuchi T, et al. 18F-Labeled Derivatives of Irbesartan for Angiotensin II Receptor PET Imaging. ChemMedChem. 2018;13(23):2546-57.
270. Katzung B. Acetylcholine receptor antagonists. Basic and clinical pharmacology Appleton and Lange, Norwalk. 1987:75-83.
271. Gardner A, Choo L, Mitchelson F. Comparison of the effects of some muscarinic agonists on smooth muscle function and phosphatidylinositol turnover in the guinea-pig taenia caeci. British journal of pharmacology. 1988;94(1):199-211.
272. Kovács M, Tóth J, Hetényi C, Málnási-Csizmadia A, Sellers JR. Mechanism of blebbistatin inhibition of myosin II. Journal of Biological Chemistry. 2004;279(34):35557-63.
273. Goldstein JL, Brown MS. Regulation of the mevalonate pathway. Nature. 1990;343(6257):425-30.
274. Bruder-Nascimento T, Callera GE, Montezano AC, de Chantemele EJB, Tostes RC, Touyz RM. Atorvastatin inhibits pro-inflammatory actions of aldosterone in vascular smooth muscle cells by reducing oxidative stress. Life sciences. 2019;221:29-34.
275. Huang X, Yang N, Fiore VF, Barker TH, Sun Y, Morris SW, et al. Matrix stiffness–induced myofibroblast differentiation is mediated by intrinsic mechanotransduction. American journal of respiratory cell and molecular biology. 2012;47(3):340-8.
276. Vega FM, Fruhwirth G, Ng T, Ridley AJ. RhoA and RhoC have distinct roles in migration and invasion by acting through different targets. Journal of Cell Biology. 2011;193(4):655-65.

277. Paszek MJ, Zahir N, Johnson KR, Lakins JN, Rozenberg GI, Gefen A, et al. Tensional homeostasis and the malignant phenotype. Cancer cell. 2005;8(3):241-54.
278. Schwartz SM, Campbell GR, Campbell JH. Replication of smooth muscle cells in vascular disease. Circulation Research. 1986;58(4):427-44.
279. Campbell JH, Campbell GR. Smooth muscle phenotypic modulation—a personal experience. Arteriosclerosis, thrombosis, and vascular biology. 2012;32(8):1784-9.
280. Babij P, Kawamoto S, White S, Adelstein RS, Periasamy M. Differential expression of SM1 and SM2 myosin isoforms in cultured vascular smooth muscle. American Journal of Physiology-Cell Physiology. 1992;262(3):C607-C13.
281. Tang M, Zhao L, Chen Y, Wang L, Zhang X. Angiotensin II protects cortical neurons against oxygen-glucose deprivation-induced injury in vitro. Biomedical reports. 2014;2(1):112-6.
282. Laflamme L, de Gasparo M, Gallo J-M, Payet MD, Gallo-Payet N. Angiotensin II Induction of Neurite Outgrowth by AT2 Receptors in NG108-15 Cells EFFECT COUNTERACTED BY THE AT1 RECEPTORS. Journal of Biological Chemistry. 1996;271(37):22729-35.
283. Matthew J, Khromov A, McDuffie M, Somlyo A, Somlyo A, Taniguchi S, et al. Contractile properties and proteins of smooth muscles of a calponin knockout mouse. The Journal of physiology. 2000;529(3):811-24.
284. Warton A, Goldie RG, Papadimitriou JM, Paterson JW. Effects of adrenaline and carbachol on the morphology of alveolar contractile cells in the lung of the toad (Bufo marinus). Comparative biochemistry and physiology C, Comparative pharmacology and toxicology. 1984;77(2):283-8.
285. Thijssen DH, Carter SE, Green DJ. Arterial structure and function in vascular ageing: are you as old as your arteries? The Journal of physiology. 2016;594(8):2275-84.
286. Denac M, Kümin G, Scharrer E. Effect of noradrenaline on smooth muscle strips from the reticular groove of adult cattle. Journal of Veterinary Medicine Series A. 1991;38(1-10):383-8.
287. Sjölund M, Madsen K, von der Mark K, Thyberg J. Phenotype modulation in primary cultures of smooth-muscle cells from rat aorta: Synthesis of collagen and elastin. Differentiation. 1986;32(2):173-80.
288. Touyz RM, He G, El Mabrouk M, Schiffrin EL. p38 Map kinase regulates vascular smooth muscle cell collagen synthesis by angiotensin II in SHR but not in WKY. Hypertension. 2001;37(2):574-80.
289. Guibert C, Ducret T, Savineau J-P. Voltage-independent calcium influx in smooth muscle. Progress in biophysics and molecular biology. 2008;98(1):10-23.

290. Folgering JH, Sharif-Naeini R, Dedman A, Patel A, Delmas P, Honoré E. Molecular basis of the mammalian pressure-sensitive ion channels: focus on vascular mechanotransduction. Progress in biophysics and molecular biology. 2008;97(2-3):180-95.
291. Weiss P, Garber B. Shape and movement of mesenchyme cells as functions of the physical structure of the medium: contributions to a quantitative morphology. Proceedings of the National Academy of Sciences of the United States of America. 1952;38(3):264.
292. Maciejowski J, Li Y, Bosco N, Campbell PJ, de Lange T. Chromothripsis and kataegis induced by telomere crisis. Cell. 2015;163(7):1641-54.
293. Lammerding J, Schulze PC, Takahashi T, Kozlov S, Sullivan T, Kamm RD, et al. Lamin A/C deficiency causes defective nuclear mechanics and mechanotransduction. The Journal of clinical investigation. 2004;113(3):370-8.
294. Lee JS, Hale CM, Panorchan P, Khatau SB, George JP, Tseng Y, et al. Nuclear lamin A/C deficiency induces defects in cell mechanics, polarization, and migration. Biophysical journal. 2007;93(7):2542-52.
295. Stewart-Hutchinson P, Hale CM, Wirtz D, Hodzic D. Structural requirements for the assembly of LINC complexes and their function in cellular mechanical stiffness. Experimental cell research. 2008;314(8):1892-905.
296. Muhamed I, Chowdhury F, Maruthamuthu V. Biophysical tools to study cellular mechanotransduction. Bioengineering. 2017;4(1):12.
297. Ribeiro AJ, Denisin AK, Wilson RE, Pruitt BL. For whom the cells pull: Hydrogel and micropost devices for measuring traction forces. Methods. 2016;94:51-64.
298. Redden RA, Doolin EJ. Collagen crosslinking and cell density have distinct effects on fibroblast-mediated contraction of collagen gels. Skin research and technology. 2003;9(3):290-3.
299. Gullberg D, Tingström A, Thuresson A-C, Olsson L, Terracio L, Borg TK, et al. β1 integrin-mediated collagen gel contraction is stimulated by PDGF. Experimental cell research. 1990;186(2):264-72.
300. Timpson P, Mcghee EJ, Erami Z, Nobis M, Quinn JA, Edward M, et al. Organotypic collagen I assay: a malleable platform to assess cell behaviour in a 3-dimensional context. JoVE (Journal of Visualized Experiments). 2011(56):e3089.
301. Chen H-C, Yang T-H, Thoreson AR, Zhao C, Amadio PC, Sun Y-N, et al. Automatic and quantitative measurement of collagen gel contraction using model-guided segmentation. Measurement Science and Technology. 2013;24(8):085702.
302. Kim J, Jones CA, Groves NS, Sun B. Three-dimensional reflectance traction microscopy. PloS one. 2016;11(6):e0156797.

303. Bogunovic N, Meekel JP, Micha D, Blankensteijn JD, Hordijk PL, Yeung KK. Impaired smooth muscle cell contractility as a novel concept of abdominal aortic aneurysm pathophysiology. Scientific reports. 2019;9(1):1-14.
304. Forstermann U, Munzel T. Endothelial nitric oxide synthase in vascular disease: from marvel to menace. Circulation. 2006;113(13):1708-14.
305. Lincoln TM, Cornwell TL, Komalavilas P, Macmillan-Crow LA, Boerth N. The Nitric Oxide–Cyclic GMP Signaling System. Biochemistry of smooth muscle contraction: Elsevier; 1996. p. 257-68.
306. Schwarz US, Soiné JR. Traction force microscopy on soft elastic substrates: A guide to recent computational advances. Biochimica et Biophysica Acta (BBA)-Molecular Cell Research. 2015;1853(11):3095-104.
307. Jonas O, Duschl C. Force propagation and force generation in cells. Cytoskeleton. 2010;67(9):555-63.
308. Tee S-Y, Fu J, Chen CS, Janmey PA. Cell shape and substrate rigidity both regulate cell stiffness. Biophysical journal. 2011;100(5):L25-L7.
309. Wilkinson IB, MacCallum H, Flint L, Cockcroft JR, Newby DE, Webb DJ. The influence of heart rate on augmentation index and central arterial pressure in humans. The Journal of physiology. 2000;525(Pt 1):263.
310. Ebina M, Yaegashi H, Chiba R, Takahashi T, Motomiya M, Tanemura M. Hyperreactive site in the airway tree of asthmatic patients revealed by thickening of bronchial muscles: a morphometric study. American Review of Respiratory Disease. 1990;141(5_pt_1):1327-32.
311. Regamey N, Ochs M, Hilliard TN, Mühlfeld C, Cornish N, Fleming L, et al. Increased airway smooth muscle mass in children with asthma, cystic fibrosis, and non-cystic fibrosis bronchiectasis. American journal of respiratory and critical care medicine. 2008;177(8):837-43.
312. Guo M, Pegoraro AF, Mao A, Zhou EH, Arany PR, Han Y, et al. Cell volume change through water efflux impacts cell stiffness and stem cell fate. Proceedings of the National Academy of Sciences. 2017;114(41):E8618-E27.
313. Zhou E, Trepat X, Park C, Lenormand G, Oliver M, Mijailovich S, et al. Universal behavior of the osmotically compressed cell and its analogy to the colloidal glass transition. Proceedings of the National Academy of Sciences. 2009;106(26):10632-7.
314. Moeendarbary E, Valon L, Fritzsche M, Harris AR, Moulding DA, Thrasher AJ, et al. The cytoplasm of living cells behaves as a poroelastic material. Nature materials. 2013;12(3):253-61.
315. Tzur A, Kafri R, LeBleu VS, Lahav G, Kirschner MW. Cell growth and size homeostasis in proliferating animal cells. Science. 2009;325(5937):167-71.

316. Padovan-Merhar O, Nair GP, Biaesch AG, Mayer A, Scarfone S, Foley SW, et al. Single mammalian cells compensate for differences in cellular volume and DNA copy number through independent global transcriptional mechanisms. Molecular cell. 2015;58(2):339-52.
317. Irianto J, Swift J, Martins RP, McPhail GD, Knight MM, Discher DE, et al. Osmotic challenge drives rapid and reversible chromatin condensation in chondrocytes. Biophysical journal. 2013;104(4):759-69.
318. Kim D-H, Li B, Si F, Phillip JM, Wirtz D, Sun SX. Volume regulation and shape bifurcation in the cell nucleus. Journal of cell science. 2015;128(18):3375-85.
319. Kobayashi T, Sokabe M. Sensing substrate rigidity by mechanosensitive ion channels with stress fibers and focal adhesions. Current opinion in cell biology. 2010;22(5):669-76.
320. Xie K, Yang Y, Jiang H. Controlling cellular volume via mechanical and physical properties of substrate. Biophysical journal. 2018;114(3):675-87.
321. Narumiya S, Ishizaki T, Watanabe N. Rho effectors and reorganization of actin cytoskeleton. FEBS letters. 1997;410(1):68-72.
322. Nilius B, Voets T, Prenen J, Barth H, Aktories K, Kaibuchi K, et al. Role of Rho and Rho kinase in the activation of volume-regulated anion channels in bovine endothelial cells. The Journal of physiology. 1999;516(Pt 1):67.
323. Doolin MT, Ornstein TS, Stroka KM. Nuclear deformation in response to mechanical confinement is cell type dependent. Cells. 2019;8(5):427.
324. Park KS, Kim Y, Lee Y-H, Earm YE, Ho W-K. Mechanosensitive cation channels in arterial smooth muscle cells are activated by diacylglycerol and inhibited by phospholipase C inhibitor. Circulation research. 2003;93(6):557-64.
325. Morita H, Honda A, Inoue R, Ito Y, Abe K, Nelson MT, et al. Membrane stretch-induced activation of a TRPM4-like nonselective cation channel in cerebral artery myocytes. Journal of pharmacological sciences. 2007;103(4):417-26.
326. Copp SW, Kim JS, Ruiz-Velasco V, Kaufman MP. The mechano-gated channel inhibitor GsMTx4 reduces the exercise pressor reflex in decerebrate rats. The Journal of physiology. 2016;594(3):641-55.
327. Venkatachalam K, Montell C. TRP channels. Annu Rev Biochem. 2007;76:387-417.
328. Friedrich O, Wagner S, Battle AR, Schürmann S, Martinac B. Mechano-regulation of the beating heart at the cellular level–mechanosensitive channels in normal and diseased heart. Progress in biophysics and molecular biology. 2012;110(2-3):226-38.
329. Bowman CL, Gottlieb PA, Suchyna TM, Murphy YK, Sachs F. Mechanosensitive ion channels and the peptide inhibitor GsMTx-4: history, properties, mechanisms and pharmacology. Toxicon. 2007;49(2):249-70.

330. Bae C, Sachs F, Gottlieb PA. The mechanosensitive ion channel Piezo1 is inhibited by the peptide GsMTx4. Biochemistry. 2011;50(29):6295-300.
331. Dryer SE, Roshanravan H, Kim EY. TRPC channels: Regulation, dysregulation and contributions to chronic kidney disease. Biochimica et Biophysica Acta (BBA)-Molecular Basis of Disease. 2019;1865(6):1041-66.
332. De Vos WH, Houben F, Kamps M, Malhas A, Verheyen F, Cox J, et al. Repetitive disruptions of the nuclear envelope invoke temporary loss of cellular compartmentalization in laminopathies. Human molecular genetics. 2011;20(21):4175-86.
333. Redon C, Pilch D, Rogakou E, Sedelnikova O, Newrock K, Bonner W. Histone H2a variants H2AX and H2AZ. Current opinion in genetics & development. 2002;12(2):162-9.
334. Gupta A, Hunt CR, Chakraborty S, Pandita RK, Yordy J, Ramnarain DB, et al. Role of 53BP1 in the regulation of DNA double-strand break repair pathway choice. Radiation research. 2014;181(1):1-8.
335. Suchyna TM, Johnson JH, Hamer K, Leykam JF, Gage DA, Clemo HF, et al. Identification of a peptide toxin from Grammostola spatulata spider venom that blocks cation-selective stretch-activated channels. Journal of General Physiology. 2000;115(5):583-98.
336. Furuyama M. Histometrical investigations of arteries in reference to arterial hypertension. The Tohoku Journal of Experimental Medicine. 1962;76(4):388-414.
337. Ichijima K. Morphological studies on the peripheral small arteries of spontaneously hypertensive rats. japanese Circulation journal. 1969;33(8):785-813.
338. FOLKOW B, Hallbäck M, Lundgren Y, Sivertsson R, Weiss L. Importance of adaptive changes in vascular design for establishment of primary hypertension, studied in man and in spontaneously hypertensive rats. Circulation Research. 1973;32(5).
339. Lundgren Y, Hallback M, Weiss L, Folkow B. Rate and extent of adaptive cardiovascular changes in rats during experimental renal hypertension. Acta Physiologica Scandinavica. 1974;91(1):103-15.
340. Wiener J, Loud A, Giacomelli F, Anversa P. Morphometric analysis of hypertension-induced hypertrophy of rat thoracic aorta. The American Journal of Pathology. 1977;88(3):619.
341. Warshaw DM, Mulvany MJ, Halpern W. Mechanical and morphological properties of arterial resistance vessels in young and old spontaneously hypertensive rats. Circulation research. 1979;45(2):250-9.
342. Crane W, Dutta L. The utilisation of tritiated thymidine for deoxyribonucleic acid synthesis by the lesions of experimental hypertension in rats. The Journal of Pathology and Bacteriology. 1963;86(1):83-97.
343. Fernandez D, Crane W. New cell formation in rats with accelerated hypertension due to partial aortic constriction. The Journal of pathology. 1970;100(4):307-16.

344. Bevan RD. An autoradiographic and pathological study of cellular proliferation in rabbit arteries correlated with an increase in arterial pressure. Journal of Vascular Research. 1976;13(1-2):100-28.
345. Bevan R, van Marthens E, Bevan J. Hyperplasia of vascular smooth muscle in experimental hypertension in the rabbit. Circulation Research. 1976;38(6):58-62.
346. Bevan RD, Eggena P, Hume WR, Van Marthens E, Bevan JA. Transient and persistent changes in rabbit blood vessels associated with maintained elevation in arterial pressure. Hypertension. 1980;2(1):63-72.
347. Olivetti G, Anversa P, Melissari M, Loud A. Morphometry of medial hypertrophy in the rat thoracic aorta. Laboratory Investigation; a Journal of Technical Methods and Pathology. 1980;42(5):559-65.
348. Owens GK, Schwartz SM. Alterations in vascular smooth muscle mass in the spontaneously hypertensive rat. Role of cellular hypertrophy, hyperploidy, and hyperplasia. Circulation research. 1982;51(3):280-9.
349. Owens GK, Rabinovitch PS, Schwartz SM. Smooth muscle cell hypertrophy versus hyperplasia in hypertension. Proceedings of the National Academy of Sciences. 1981;78(12):7759-63.
350. Walsh K, Shiojima I, Gualberto A. DNA replication and smooth muscle cell hypertrophy. The Journal of clinical investigation. 1999;104(6):673-4.
351. Romero JC, Reckelhoff JF. Role of angiotensin and oxidative stress in essential hypertension. Hypertension. 1999;34(4):943-9.
352. Griendling KK, Minieri CA, Ollerenshaw JD, Alexander RW. Angiotensin II stimulates NADH and NADPH oxidase activity in cultured vascular smooth muscle cells. Circulation research. 1994;74(6):1141-8.
353. Taubman MB. Angiotensin II: a vasoactive hormone with ever-increasing biological roles. Am Heart Assoc; 2003.
354. Andrawis N, Ruley E, Abernethy D. Angiotensin II regulates human vascular smooth muscle α-actin gene expression. Biochemical and biophysical research communications. 1993;196(2):962-8.
355. Higashi M, Shimokawa H, Hattori T, Hiroki J, Mukai Y, Morikawa K, et al. Long-term inhibition of Rho-kinase suppresses angiotensin II–induced cardiovascular hypertrophy in rats in vivo: effect on endothelial NAD (P) H oxidase system. Circulation research. 2003;93(8):767-75.
356. Shi J, Zhang Y-W, Summers LJ, Dorn II GW, Wei L. Disruption of ROCK1 gene attenuates cardiac dilation and improves contractile function in pathological cardiac hypertrophy. Journal of molecular and cellular cardiology. 2008;44(3):551-60.

357. Zeidan A, Javadov S, Karmazyn M. Essential role of Rho/ROCK-dependent processes and actin dynamics in mediating leptin-induced hypertrophy in rat neonatal ventricular myocytes. Cardiovascular Research. 2006;72(1):101-11.
358. Kirber MT, Walsh JV, Singer JJ. Stretch-activated ion channels in smooth muscle: a mechanism for the initiation of stretch-induced contraction. Pflügers Archiv-European Journal of Physiology. 1988;412(4):339-45.
359. Benham C, Hess P, Tsien R. Two types of calcium channels in single smooth muscle cells from rabbit ear artery studied with whole-cell and single-channel recordings. Circulation Research. 1987;61(4).
360. Matsuda J, Volk K, Shibata E. Calcium currents in isolated rabbit coronary arterial smooth muscle myocytes. The Journal of Physiology. 1990;427(1):657-80.
361. Dingal PDP, Bradshaw AM, Cho S, Raab M, Buxboim A, Swift J, et al. Fractal heterogeneity in minimal matrix models of scars modulates stiff-niche stem-cell responses via nuclear exit of a mechanorepressor. Nature materials. 2015;14(9):951-60.
362. Getts RC, Stamato TD. Absence of a Ku-like DNA end binding activity in the xrs double-strand DNA repair-deficient mutant. Journal of Biological Chemistry. 1994;269(23):15981-4.
363. Taccioli GE, Gottlieb TM, Blunt T, Priestley A, Demengeot J, Mizuta R, et al. Ku80: product of the XRCC5 gene and its role in DNA repair and V (D) J recombination. Science. 1994;265(5177):1442-5.
364. Stern CS, Lebowitz J. Latest drug developments in the field of cardiovascular disease. The International journal of angiology: official publication of the International College of Angiology, Inc. 2010;19(3):e100.
365. Nagareddy P, Smyth SS. Inflammation and thrombosis in cardiovascular disease. Current opinion in hematology. 2013;20(5):457.
366. Rzucidlo EM, Martin KA, Powell RJ. Regulation of vascular smooth muscle cell differentiation. Journal of vascular surgery. 2007;45(6):A25-A32.
367. Nogales E. Structural insights into microtubule function. Annual review of biochemistry. 2000;69(1):277-302.
368. Caswell PT, Vadrevu S, Norman JC. Integrins: masters and slaves of endocytic transport. Nature reviews Molecular cell biology. 2009;10(12):843-53.
369. Franco SJ, Rodgers MA, Perrin BJ, Han J, Bennin DA, Critchley DR, et al. Calpain-mediated proteolysis of talin regulates adhesion dynamics. Nature cell biology. 2004;6(10):977-83.
370. Wu X, Kodama A, Fuchs E. ACF7 regulates cytoskeletal-focal adhesion dynamics and migration and has ATPase activity. Cell. 2008;135(1):137-48.

371. Kaverina I, Krylyshkina O, Small JV. Microtubule targeting of substrate contacts promotes their relaxation and dissociation. The Journal of cell biology. 1999;146(5):1033-44.
372. Galiová G, Bártová E, Raška I, Krejčí J, Kozubek S. Chromatin changes induced by lamin A/C deficiency and the histone deacetylase inhibitor trichostatin A. European journal of cell biology. 2008;87(5):291-303.
373. De Sandre-Giovannoli A, Bernard R, Cau P, Navarro C, Amiel J, Boccaccio I, et al. Lamin a truncation in Hutchinson-Gilford progeria. Science. 2003.
374. Eriksson M, Brown WT, Gordon LB, Glynn MW, Singer J, Scott L, et al. Recurrent de novo point mutations in lamin A cause Hutchinson–Gilford progeria syndrome. Nature. 2003;423(6937):293-8.
375. Hamczyk MR, del Campo L, Andrés V. Aging in the cardiovascular system: lessons from Hutchinson-Gilford progeria syndrome. Annual review of physiology. 2018;80:27-48.
376. Balmus G, Larrieu D, Barros AC, Collins C, Abrudan M, Demir M, et al. Targeting of NAT10 enhances healthspan in a mouse model of human accelerated aging syndrome. Nature communications. 2018;9(1):1700.
377. Rathje L-SZ, Nordgren N, Pettersson T, Rönnlund D, Widengren J, Aspenström P, et al. Oncogenes induce a vimentin filament collapse mediated by HDAC6 that is linked to cell stiffness. Proceedings of the National Academy of Sciences. 2014;111(4):1515-20.
378. Tucker WD, Mahajan K. Anatomy, blood vessels. 2017.
379. Li C, Xu Q. Mechanical stress-initiated signal transductions in vascular smooth muscle cells. Cellular signalling. 2000;12(7):435-45.
380. Solon J, Levental I, Sengupta K, Georges PC, Janmey PA. Fibroblast adaptation and stiffness matching to soft elastic substrates. Biophysical journal. 2007;93(12):4453-61.
381. Alberts B, Johnson A, Lewis J, Raff M, Roberts K, Walter P. Ion channels and the electrical properties of membranes. Molecular Biology of the Cell 4th edition: Garland Science; 2002.
382. Williamson EA, Wray JW, Bansal P, Hromas R. Overview for the histone codes for DNA repair. Progress in molecular biology and translational science. 2012;110:207-27.
383. Louis SF, Zahradka P. Vascular smooth muscle cell motility: From migration to invasion. Experimental & Clinical Cardiology. 2010;15(4):e75.
384. Yaghini FA, Song CY, Lavrentyev EN, Ghafoor HU, Fang XR, Estes AM, et al. Angiotensin II–induced vascular smooth muscle cell migration and growth are mediated by cytochrome P450 1B1–dependent superoxide generation. Hypertension. 2010;55(6):1461-7.
385. Ionita MG, Arslan F, De Kleijn DP, Pasterkamp G. Endogenous inflammatory molecules engage Toll-like receptors in cardiovascular disease. Journal of innate immunity. 2010;2(4):307-15.

386. Maier KG, Han X, Sadowitz B, Gentile KL, Middleton FA, Gahtan V. Thrombospondin-1: a proatherosclerotic protein augmented by hyperglycemia. Journal of vascular surgery. 2010;51(5):1238-47.
387. Schaper W, Ito WD. Molecular mechanisms of coronary collateral vessel growth. Circulation research. 1996;79(5):911-9.
388. Wolf C, Cai W-J, Vosschulte R, Koltai S, Mousavipour D, Scholz D, et al. Vascular remodeling and altered protein expression during growth of coronary collateral arteries. Journal of molecular and cellular cardiology. 1998;30(11):2291-305.
389. Ridley AJ, Schwartz MA, Burridge K, Firtel RA, Ginsberg MH, Borisy G, et al. Cell migration: integrating signals from front to back. Science. 2003;302(5651):1704-9.
390. Ahmed S, Mabeza P, Warren DT. A model for estimating traction force magnitude reveals differential regulation of actomyosin activity and matrix adhesion number in response to smooth muscle cell spreading. BioRxiv. 2019:612267.